



**CORROSION OF TI-BASED BULK METALLIC GLASSES FOR SMALL
DIAMETER DENTAL IMPLANTS**

By

Qi Wei

**A thesis submitted to University of Birmingham for the degree of
DOCTOR OF PHILOSOPHY**

School of Metallurgy and Materials
College of Engineering and Physical Sciences
University of Birmingham
September 2019

UNIVERSITY OF
BIRMINGHAM

University of Birmingham Research Archive

e-theses repository

This unpublished thesis/dissertation is copyright of the author and/or third parties. The intellectual property rights of the author or third parties in respect of this work are as defined by The Copyright Designs and Patents Act 1988 or as modified by any successor legislation.

Any use made of information contained in this thesis/dissertation must be in accordance with that legislation and must be properly acknowledged. Further distribution or reproduction in any format is prohibited without the permission of the copyright holder.

Abstract

Ti-based bulk metallic glasses (BMGs) have been proposed to be an alternative to conventional Ti alloys to be used to manufacture small dental implants. For this application, it is important to determine whether they have suitable corrosion resistance. The corrosion behaviour of BMGs and the alloy, Ti6Al4V was tested in physiological saline (PS), with and without the addition of albumin and hydrogen peroxide. Albumin is the main protein in extracellular fluid, and peroxide (H_2O_2) is a transient biological species used here to simulate the presence of reactive oxygen species (ROS) that can be formed during infection or inflammation.

Electrochemical tests on BMG_Sn2 showed that addition of albumin to PS suppresses the cathodic reaction and enhances the pitting resistance of BMG_Sn2, while H_2O_2 decreases the pitting resistance of BMG_Sn2. The addition of albumin to H_2O_2 -containing PS suppresses both anodic and cathodic reactions.

Most Ti-based BMGs contain a high content of Cu. However, Cu is potentially less biocompatible compared with other elements which can be used to enhance the glass forming potential. In this case, Ga was used to partly replace Cu, up to 10 at.%. Experiments were conducted to check that this partial substitution does not have a detrimental effect on corrosion resistance. It was found that substitution of 10 at.% Ga did not modify the corrosion resistance of Ti-based BMGs in 0.9 wt.% NaCl solution. It was also found that some degree of structural relaxation can slightly improve the corrosion resistance.

Mechanically-assisted crevice corrosion (MACC) is a corrosion process associated with abrasive damage to test surfaces. The abrasion causes damage to the passive surface film, leading to a burst of metal dissolution from the bare metal surface. The metal ions hydrolyse and result in local acidity in the crevice. The acid environment delays the repassivation of Ti and can eventually cause severe corrosion. Such wear damage and local acidity have been found for cemented femoral stems and modular orthopaedic Ti implants. There is concern that MACC may also be a risk for dental implants, so it is important to be able to evaluate risk in quantitative way. A new device was developed that can retain the local acidity produced by MACC. A series of parallel tests on BMGs and Ti6Al4V using this device were conducted to compare their MACC resistance. The results have shown that Ti-based BMGs show better MACC resistance than Ti6Al4V evidenced by lower MACC currents, associated with milder local chemistry changes and less wear and corrosion products generated. It has also been shown that MACC gets increasingly worse for Ti6Al4V with time but this was not observed for BMGs in the current test period (16 ks). This can be explained by the fact that Ti-based BMGs possess greater wear resistance than Ti6Al4V, which means the passive film may be better preserved under the abrasive conditions.

Acknowledgment

Foremost, I would like to express my deep and sincere gratitude to my supervisors: Prof. Alison Davenport, Prof. Owen Addison and Dr. Petre Flaviu Gostin for their continuous support of my study and research, for their patience, motivation, and knowledge. Their guidance and support have greatly helped me throughout my laboratory experiments, paper and thesis writing. It is a great fortune to have them as my supervisors. Three years ago, my initial plan was just completing a Master's degree, I was so hesitating about doing a PhD. It was their encouragement that helped me to do the right decision.

My thanks also go to the people who offered technical support to this PhD work: Dr. Daniel Reed for the XRD work, Prof. Mariana Calin, Dr. Supriya Bera and Dr. Parthiban Ramasamy to design and fabricate metallic glasses as experimental specimens, and Dr. Nicolas Courtois to machine MACC samples. Dr. Jiayun Jiang for the Keyence microscopy work.

Thanks to all my colleagues: George, Sarah, Sophie, Angus, Steven, Berenika, and my friends: Shanshan, Yulin, Jinsen, Johnny C, and Gerald. I feel grateful to have their company in the days in England. The friendship will stay with me forever.

Last but not the least, I would like to thank my parents and grandparents for their continued love, spiritual and financial support.

Contents

1	Introduction	1
2	Literature review.....	4
2.1	Small diameter implants	4
2.2	Fluid surrounding dental implants.....	5
2.2.1	Saliva, crevicular fluid and extracellular fluid.....	5
2.2.2	Inflammatory reactions (reactive oxygen species)	8
2.3	Ti alloys and Ti-based BMGs for dental implants	9
2.3.1	Materials & mechanical properties.....	9
2.3.2	Passivation and localised corrosion of Ti	11
2.4	Effect of albumin and/or H ₂ O ₂ on corrosion of Ti	12
2.4.1	Effect of albumin	12
2.4.2	Effect of hydrogen peroxide.....	16
2.4.3	Synergistic effect of H ₂ O ₂ and albumin	16
2.5	Mechanically-assisted crevice corrosion (MACC).....	18
2.5.1	MACC concept and clinical observation.....	18
2.5.2	Tribocorrosion and MACC	21
2.5.3	MACC of Ti	23
2.5.4	Effect of albumin on tribocorrosion	26
2.5.5	Adverse in-vivo biological effect caused by Ti.....	27

2.6	Ti-based metallic glass	28
2.6.1	Ti ₄₀ Zr ₁₀ Cu ₃₆ Pd ₁₄	28
2.6.2	Corrosion of Ti-based metallic glasses in simulated body fluid	29
2.6.3	Effect of fabrication (structural states) on corrosion of metallic glasses	32
2.6.4	Minor additions to BMG system	35
2.6.5	Corrosion of other constituent elements under physiological conditions	36
2.7	Summary.....	41
3	Materials and Methods.....	42
3.1	Crystalline alloys	42
3.2	Metallic glasses	43
3.3	Electrolyte	44
3.4	Sample preparation	45
3.5	Electrochemical measurements	47
3.6	Characterisation.....	49
3.7	MACC device and tests	50
3.8	Calculation of charge transfer	53
3.9	Statistical analysis	53
4	Effect of albumin and H ₂ O ₂ on corrosion of Ti ₄₀ Zr ₁₀ Cu ₃₄ Pd ₁₄ Sn ₂	54
4.1	Introduction	54
4.2	Characterisation of as-received materials	55

4.3	OCP and repassivation	57
4.4	Effect of albumin on $Ti_{40}Zr_{10}Cu_{34}Pd_{14}Sn_2$	58
4.5	Effect of H_2O_2 on BMG_Sn2	61
4.6	Effect of albumin in H_2O_2 -containing solution.....	65
4.7	Effect of peroxide ±albumin on main constituent elements.....	68
4.7.1	Titanium and zirconium.....	68
4.7.2	Copper	72
4.7.3	Palladium	76
4.7.4	Tin.....	77
4.7.5	Corrosion potentials of constituent elements	78
4.8	Pitting morphology and dealloying process	80
4.9	Discussion	88
4.9.1	Corrosion of Ti-Zr-Cu-Pd-Sn.....	88
4.9.2	Alloying elements induce pitting.....	89
4.9.3	Effect of albumin	91
4.9.4	Effect of H_2O_2	91
4.9.5	Effect of albumin + H_2O_2	92
4.10	Conclusion.....	95
5	The influence of partial replacement of Cu with Ga on the corrosion behaviour of $Ti_{40}Zr_{10}Cu_{36}Pd_{14}$ metallic glasses.....	96

5.1	Introduction	96
5.2	Characterisation before corrosion.....	98
5.3	Electrochemical measurements on $Ti_{40}Zr_{10}Cu_{36-x}Pd_{14}Ga_x$ ($x=0-10$) in 0.9% NaCl....	100
5.3.1	OCP and potentiodynamic polarisation curves of rods.....	100
5.3.2	OCP and anodic polarisation curves of ribbons	103
5.3.3	Potentiostatic measurements	109
5.3.4	Electrochemical measurement of Cu and Ga.....	111
5.4	Pitting morphology and chemical composition.....	113
5.4.1	Rods	113
5.4.2	Ribbon.....	115
5.5	Discussion	118
5.5.1	Effect of replacement of Cu with Ga on corrosion behaviour of $Ti_{40}Zr_{10}Cu_{36-x}Pd_{14}Ga_x$	118
5.5.2	Comparison between as-cast rod and as-spun ribbon	119
5.6	Conclusion.....	121
6	Mechanically-Assisted Crevice Corrosion (MACC).....	122
6.1	Introduction	122
6.2	Observation on retrieved dental implant.....	124
6.3	As-received materials	127
6.3.1	Chemical composition	127

6.3.2	Polarisation curves	127
6.3.3	Hardness	128
6.4	MACC polarisation curves	129
6.5	Potentiostatic measurements	134
6.6	Effect of load and speed on MACC of Ti6Al4V and metallic glasses	136
6.6.1	Typical OCP behaviour	136
6.6.2	Effect of load and rotation speed on MACC	137
6.6.3	Time-dependence of MACC potential	143
6.7	MACC current	149
6.8	pH variation	151
6.9	Abrasion damage	153
6.10	Wear debris	157
6.11	MACC resistance	161
6.12	Effect of albumin	168
6.13	Discussion	173
6.13.1	MACC device	173
6.13.2	Acidity in cavity for Ti6Al4V	174
6.13.3	Comparison of MACC resistance between BMGs and Ti6Al4V	175
6.13.4	Effect of albumin	176
6.14	Conclusion	177

7	General discussion and future work	178
7.1	General discussion	178
7.1.1	Use of bulk metallic glasses to replace Ti Alloys for small dental implants	178
7.1.2	MACC testing	178
7.1.3	Structural relaxation and elemental substitution	179
7.2	Future work.....	180
7.2.1	MACC products characterisation followed by cell culture.....	180
7.2.2	Effect of albumin and H ₂ O ₂	181
8	References.....	183
9	Appendix	198

TABLE OF SYMBOLS AND ABBREVIATIONS

SDI (s)	Small diameter implant(s)
MACC	Mechanically-assisted crevice corrosion
BMG(s)	Bulk metallic glass(es)
PIF	Peri-implant 'cervicular' fluid
GCF	Gingival crevicular fluid
BSA	Bovine serum albumin
H ₂ O ₂	Hydrogen peroxide
BMG_Sn2	Ti ₄₀ Zr ₁₀ Cu ₃₄ Pd ₁₄ Sn ₂
DI water	Deionised water
PS	Physiological saline / 0.9 wt.% NaCl
PS+A	Physiological saline / 0.9 wt.% NaCl + 4 wt.% bovine serum albumin
PS+P	Physiological saline / 0.9 wt.% NaCl + 0.1 wt.% hydrogen peroxide
PS+A+P	Physiological saline / 0.9 wt.% NaCl + 4 wt.% bovine serum albumin + 0.1 wt.% hydrogen peroxide
OCP	Open circuit potential

E_{corr}	Corrosion potential
E_{pit}	Pitting potential
SEM	Scanning electron microscope
EDX	Energy dispersive X-ray spectroscopy
TEM	Transmission electron microscope
XPS	X-ray photoelectron spectroscopy
AES	Auger electron spectroscopy
WE	Working electrode
CE	Counter electrode
RE	Reference electrode
SHE	Standard hydrogen electrode
SCE	Saturated calomel electrode
rpm	Revolution per minute
GFA	Glass forming ability

1 Introduction

Titanium and its alloys have been widely used as implant materials due to their good combination of mechanical properties, biocompatibility and corrosion resistance [1]. Mechanical failure of dental implants made of CP-Ti and Ti6Al4V has frequently been reported clinically [2]. Therefore, there is clinical need of developing new materials with better mechanical properties, e.g. higher strength and better fatigue resistance. To achieve better properties, Ti-based bulk metallic glasses have been developed [3, 4]. The alloy system $\text{Ti}_{40}\text{Zr}_{10}\text{Cu}_{36}\text{Pd}_{14}$ proposed by Zhu et. al [5] has drawn our attention because of its good glass forming ability and superior mechanical properties [6, 7].

Albumin is the most abundant protein found in extracellular environment (~ 4 wt.%), and it shows quick absorption on metallic implants [8]. Reactive oxygen species (ROS) are a by-product of inflammatory reactions [9]. For dental implants, chronic peri-implant inflammatory reactions have been shown to take place at interfaces between dental implant components [10-12]. Albumin and H_2O_2 (one form of ROS) have been shown to act synergistically to modify the corrosion behaviour of Ti, and Ti alloys [13, 14]. Also, characterisation of passive oxide films on Ti-based BMGs also show the enrichment of Ti [15, 16], which implies these two species in combination also affect the corrosion of Ti-based BMGs. In this work, the corrosion behaviour of a Ti-based BMG, $\text{Ti}_{40}\text{Zr}_{10}\text{Cu}_{34}\text{Pd}_{14}\text{Sn}_2$ (BMG_Sn2), was tested firstly in 0.9 wt.% NaCl solution (physiological saline, PS), then with presence of albumin and/or H_2O_2 to investigate how albumin and H_2O_2 affect the corrosion behaviour of BMG_Sn2.

The base alloy studied in this work was $\text{Ti}_{40}\text{Zr}_{10}\text{Cu}_{36}\text{Pd}_{14}$. Among the constituent elements, Cu (in high concentration) is less biocompatible than the others. However, Cu is also an indispensable element for achieving good glass-forming ability [17], which is necessary for further processing. In this work, Ga is chosen as the alternative element for partial replacement of Cu, with the purpose of further enhancing glass forming ability, improving the strength and achieving better biocompatibility [18]. The substitution of Cu with Ga up to 10 at.% was performed on $\text{Ti}_{40}\text{Zr}_{10}\text{Cu}_{36-x}\text{Pd}_{14}\text{Ga}_x$ alloy system. The corrosion behaviour of Ga-containing metallic glasses was tested in physiological saline.

The two main methods to fabricate metallic glasses are melt spinning, which produces thin ribbons and mould casting which produces bulk rods. These two fabrication methods provide different cooling rates during solidification of the molten alloys, leading to different levels of structural relaxation. [19] Structural relaxation may alter the chemical ordering of metallic glasses, which can modify their corrosion resistance [20-22]. In this work, the corrosion behaviour of as-cast bulk and as-spun ribbons with same composition were also investigated.

Ti and its alloys are very resistant to aqueous corrosion due to their chemically inert oxide film. As long as the oxide film is undamaged, pitting is not observed at potentials as high as 10V vs Ag/AgCl [23, 24]. Although Ti possesses good corrosion resistance, discoloration and evidence of severe corrosion attack (etching, delamination and surface cracking) at the connection surfaces on retrieved Ti orthopaedic modular prostheses has been observed [25, 26], and elevated concentration of Ti ions in peri-implant tissues have been consistently

reported [27, 28]. Compared with one-piece implants, implants with a modular design in which components are press-fit together generate higher levels of acidity in surrounding tissue [29]. This behaviour is consistent with the mechanism of mechanically-assisted crevice corrosion (MACC) proposed by Gilbert et. al [25, 30]. However, there is currently no standard apparatus to test alloy susceptibility to MACC. Most devices that are routinely used to simulate tribocorrosion do not maintain the necessary local acidic chemistry in the crevice that is critical for MACC for any sustained period [31]. In this work, a new apparatus is demonstrated which can conserve the local chemistry developed by MACC, quantifies the MACC current, and captures wear debris and corrosion products that are produced. The MACC behaviour of Ti6Al4V and several Ti-based BMGs was tested. Both short-term and long-term MACC behaviour was investigated, as well as how the MACC behaviour changes with time. The MACC products were also collected and characterized.

2 Literature review

2.1 Small diameter implants

Figure 2-1 (a) illustrates a typical three-component dental implant consisting of the implant body, abutment and superstructure. The implant body is 'screw-shaped' and is the part that is surgically inserted into the bone and supports the attached components. Its surface is designed with macroscopic and microscopic surface features to provide an intimate interface with the surrounding bone. An abutment is inserted into the hollow core of the implant body and secured using an internal screw. Abutments are available in a wide range of geometries and material, and span the thickness of the gingival tissue (the gums) providing the connection between the implant body and the superstructure. The superstructure is usually a prosthesis mimicking the anatomy of a single tooth, known colloquially as a 'crown'. The crown is typically fabricated from entirely ceramic or ceramic fused to metal. The structure and design of implants varies depending on the manufacturer and can differ considerably. Some systems separate the abutment into a screw and a pedestal/abutment to provide the clinician with more flexibility during reconstruction, as shown in Figure 2-1 (b). Clinically the diameter of the implant body selected is limited by the dimensions of the bone into which it is inserted. To avoid bone grafting (to increase the volume of available bone at the implantation site) small diameter implants have been increasingly advocated and new alloys sought to provide the pre-requisite mechanical properties. [32, 33] Defined by U.S Food and Drug Administration (FDA), small diameter

implants (SDIs) refer to the implants which have implant body diameter ranging from 1.8 to 2.9 mm [34].



Figure 2-1 (a) Regular three-component dental implant; (b) Some implants separate the abutment into two parts (abutment and screw).

2.2 Fluid surrounding dental implants

2.2.1 Saliva, crevicular fluid and extracellular fluid

Dental implants are exposed to a complex physiological environment as shown in Figure 2-2. The fluids coming into contact with dental implant components include saliva for the parts which protrude into the oral cavity; peri-implant 'crevicular' fluid contacts components below the gum, and extracellular fluids contact the implant surface at its interface with bone. [35]



Figure 2-2 Diagram showing the fluids surrounding a dental implant

Human saliva comprises of -99.5% water, electrolytes, proteins, mucins, antibacterial compounds and various enzymes. The electrolyte contains 13.9 mmol/L sodium, 26.2 mmol/L potassium, 12.7 mmol/L chloride, 5.6 mmol/L phosphate and 7.4 mmol/L carbonate [36]. Peri-implant 'crevicular' fluid (PIF) flows into the gingival sulcus (the gap between the gum tissues and the implant) and is similar to gingival crevicular fluid (GCF) which is released into the sulcus between the gum and natural teeth. PIF flow is minimal but increases with inflammation and hence its volume and contents can act as biomarker of peri-implant disease, e.g. the intensity of inflammation [37]. The composition of GCF is summarised in Table 2-1. Sodium is the dominant species in inorganic ions, and the amount of albumin exceeds all other proteins. Note that the composition of GCF is dynamic but the dominant species are not normally changed [38].

Table 2-1 Components of gingival crevicular fluid [39]

Cellular components	Inorganic ions (mmol/lit)	Organic ions (g/l)	Enzymes	Bacterial products
neutrophils	sodium (91.6± 31.1)	albumins (35)	acid phosphatase	endotoxins
lymphocytes	potassium (17.4± 11.7)	gammaglobulin (7.5)	cathepsin B. D	
monocytes	calcium (5.0± 1.8)	immunoglobins		
Epithelial cell	phosphate (1.3± 1.0)			
...

The electrolytic constituents in extracellular fluid are sodium ions (150 mM), potassium ions (5 mM), calcium ions (1 mM), magnesium ions (1.5 mM), chloride (110 mM), hydrogencarbonate ions (24 mM) and phosphorus ions (2 mM) [40]. Extracellular fluid also consists of various proteins, among which, albumin is the most abundant, with a concentration ranging from 35 to 50 g/L [41, 42]. Hence albumin is often chosen as a representative protein to study the effects of protein on the behaviour of implanted materials [43]. Serum albumin is a single polypeptide consisting of 585 amino acid residues having 17 pairs of disulphide bridges and one free cysteine residue [44, 45].

2.2.2 Inflammatory reactions (reactive oxygen species)

The human immune system comprises the cells that can defend the host from infection of foreign invaders, e.g. pathogens, damaged cells and toxic compounds. The inflammatory reaction is part of the complex biological response which involves immune cells [46, 47].

Bacteria, Ti particles and Ti ions have been shown to be recognised as foreign by immune cells, which can then trigger the peri-implant inflammatory reaction [48-50]. For dental implants, chronic peri-implant inflammatory reactions have been shown to happen in tissues adjacent to interfaces between implant components (implant/ abutment/ crown) independent of whether the interface is above or below the alveolar bone crest [10-12]. The generation of reactive oxygen species (ROS) is key to the progression of inflammatory reactions. ROS, including peroxide and superoxide radicals ($\cdot O^{2-}$), are produced directly or indirectly by the immune cells such as polymorphonuclear neutrophils (PMNs) and accumulate in the extracellular space [51]. During in-vitro corrosion tests, H_2O_2 is commonly selected to represent ROS [46, 51]. H_2O_2 can act as both oxidiser and reducer at certain potentials, as indicated in Figure 2-3, it can be doubly unstable and chemically decomposed to water and oxygen.

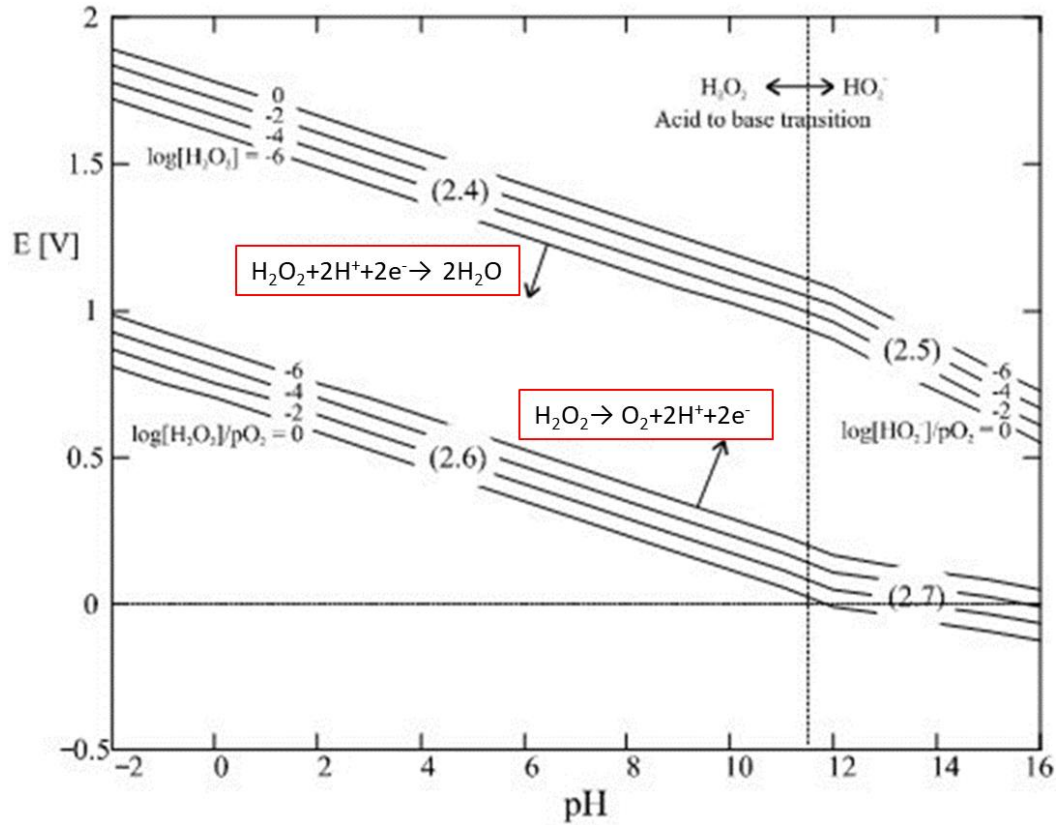


Figure 2-3 E-pH (Pourbaix) diagram for H_2O/H_2O_2 system at room temperature [52]

2.3 Ti alloys and Ti-based BMGs for dental implants

2.3.1 Materials & mechanical properties

Commercially pure titanium (CP-Ti), grade I to grade IV, and Ti6Al4V are commonly used as materials for dental implants. They are also the certificated materials by the American Society for Testing and Materials (ASTM) as implant materials [53].

For small diameter implants, improved mechanical properties such as a lower Young's modulus and increased fatigue resistance are required when compared with CP-Ti, especially

for patients with high masticatory loading forces, known as parafunction. A Ti-based metallic glass with composition $Ti_{40}Zr_{10}Cu_{36}Pd_{14}$ has been reported as having superior mechanical properties when compared with CP-Ti and Ti6Al4V. Some key mechanical properties of $Ti_{40}Zr_{10}Cu_{36}Pd_{14}$, CP-Ti and Ti6Al4V are listed in Table 2-2. The lower Young's modulus, higher compressive strength, higher yield strength and better fracture resistance of $Ti_{40}Zr_{10}Cu_{36}Pd_{14}$ have all been proposed to make it an attractive composition for a biomedical application. [54, 55]

Table 2-2 Comparison of some key mechanical properties as SDIs of $Ti_{40}Zr_{10}Cu_{36}Pd_{14}$ [56], CP-Ti and Ti6Al4V [57]

	Young's modulus (GPa)	Compressive strength (MPa)	Yield strength (MPa)	Fatigue Endurance Limit (MPa)
$Ti_{40}Zr_{10}Cu_{36}Pd_{14}$	82	1950	2050 [4]	762 * ¹
CP-Ti (G4)	105	170	830	223
Ti6Al4V	114	970	1430	535

*¹Data are acquired from $Ti_{40}Zr_{10}Cu_{34}Pd_{14}Sn_2$ [58]

According to the American Academy of Implant Dentistry, approximately 3 million people have dental implants, this number is expected to grow annually by 500,000 [59]. The literature indicates that various complications were observed for more than 30% patients with dental implants over a 5-year period [60]. The most common restorative complication is screw loosening, fracture and cracking of the dental implant components. Mechanical failure of dental implants made of CP-Ti and Ti6Al4V has frequently been reported clinically [2]. The fracture and fatigue morphologies of retrieved implants made of Ti alloys have been

illustrated by SEM in previous works [61, 62]. Therefore, the clinical need of developing new materials is desirable.

2.3.2 Passivation and localised corrosion of Ti

The excellent corrosion resistance of Ti and Ti alloys derives from the formation of a thin surface oxide layer. The oxide film, which is $\sim 20 \text{ \AA}$ thick in the native state, is chemically inert in air and in most aqueous solutions. However, general corrosion of Ti still can happen at a very slow rate if Ti is immersed in concentrated reducing acids [63-65]. The dissolution occurs either by direct chemical dissolution [65] or by electrochemical dissolution [64]. When Ti is in a fully passive condition, the corrosion rate is usually less than 0.02 mm per year which is well below the 0.13 mm per year maximum corrosion rate accepted for biomaterial applications [66]. Therefore, general corrosion is not a significant concern for Ti implants. Stable pitting corrosion of Ti can only happen in Cl⁻-containing solution when the applied potential reaches $>10 \text{ V vs Ag/AgCl}$ [23, 24]. Burstein has reported metastable pits for Ti in Cl⁻-containing solution using microelectrodes, however, the current was in -pA and pits were not able to propagate [67]. It is possible that the observed behaviour was as a consequence of dissolution of localised impurities such as Fe in the commercially pure substrate [30]. Crevice corrosion of Ti can only take place at physiologically irrelevant temperatures. The temperature reported for crevice corrosion to take place on Ti was $65 \text{ }^\circ\text{C}$ [68], boiling chloride solutions [69], or in 25% NaCl solution at $100 \text{ }^\circ\text{C}$ [70]. It can therefore be concluded that pitting and crevice corrosion of Ti is unlikely to happen at body temperatures as long as the passive film remains intact. In general, Ti has good passivation

ability, and the physiological environment does not allow localised corrosion to take place. However, Ti ions, and particles of a size and speciation indicative of a corrosion source have been found in fluids and tissues associated with Ti implants [27, 71, 72]. It has been hypothesized that chemical species in physiological fluids, such as proteins and reactive oxygen species may modify the Ti dissolution rate (section 2.4) and circumstances may arise where the passive oxide film becomes persistently disrupted leading to mechanically-assisted crevice corrosion (section 2.5).

2.4 Effect of albumin and/or H₂O₂ on corrosion of Ti

2.4.1 Effect of albumin

Electrostatic repulsion plays an important role on the adsorption of proteins on a metallic surfaces. It was reported that albumin strongly adsorbs on the Ti surface by chemisorption through carboxylate/amino groups or through electrostatic interactions [8, 73]. The IEP (isoelectric point) of human serum albumin is 4.7 and the point of zero charge (PZC) of TiO₂ in NaCl solution is about 6.0. Thereby, the maximal amount of absorption is under pH of 4.7 to 5.0 where albumin is negatively charged and TiO₂ is positively charged. In 0.1 M NaCl, the maximum adsorption pH is 4.7. Surface saturation of human serum albumin on TiO₂ surface in 0.1 M NaCl is 0.2 g/L, above this value, the amount of adsorption would not increase with time. [74]

This albumin-layer impedes the electrons gained by the oxidizer e.g. oxygen, thereby albumin serves as cathodic inhibitor [13, 75]. Albumin was reported to block charge transfer

at metal/solution interface because lower passive current density was observed [76, 77]. This adsorbed layer has been shown to slow down the attack on the passive film from other anions such as fluoride [77, 78]. However, it has also been reported that proteins can accelerate the metal dissolution either by abstracting metal ions, forming stable complexes (known as 'chelating effect') [73] [79, 80]. Due to the uncertainty of the anodic reaction of Ti caused by albumin, the specific influence on Ti alloys is still in debate, either increasing the corrosion resistance of Ti alloys [13, 77, 78, 81, 82], decreasing it [83-85] or having little effect [79, 86, 87]. How albumin affects Ti alloys, mainly Ti6Al4V, as well as the experimental conditions are summarized in Table 2-3.

Table 2-3 Effect of albumin on corrosion of Ti alloys in simulated body fluid

Material	Increased or decreased corrosion resistance	Evidence	Solution	pH	Other findings	Refs
Ti6Al4V	Increased	Smaller difference between breakdown potential and repassivation potential in PBS+ albumin	PBS ± 1 mg/ml bovine albumin	5-9	The addition of albumin to the PBS reduced the influence of pH on the corrosion behaviour of Ti6Al4V.	[81]
Ti6Al4V	Increased	Potentiodynamic scans show that addition of albumin to the SIP solution lowers the dissolution of the Ti alloy.	SIP ± 37.7 mg/cm ³ crystallized bovine albumin	7.4		[82]
Ti6Al4V	Increased	Addition of BSA decreases the potentiostatic current at both anodic and cathodic potentials.	0.9 wt.% NaCl ± 4 wt.% BSA	6.7-7	BSA significantly inhibits the cathodic reaction in 0.9 % NaCl.	[13]
Ti6Al4V	Increased	The corrosion current and passive current decreases, and polarisation resistance increases with the presence of albumin in NaF-containing media.	Artificial saliva and 0.1% NaF ± (0.01 – 0.2) % BSA	5	Albumin layer on metal surface can protect the metal from attack by fluoride ions.	[77]
CP-Ti			0.9 wt.% NaCl + 0.2 wt.% NaF ± (0.1- 1.0) g/l albumin			[78]
Ti6Al4V	Decreased	Addition of BSA pushes OCP negative. Addition of BSA decreases impedance by approximately 10 times.	Deaerated PBS, 1 wt.% H ₂ O ₂ ± 1 wt. % BSA	3	Deaeration destabilises the Ti oxide film in PBS. H ₂ O ₂ destabilises the Ti oxide film in deaerated PBS.	[83]

Ti6Al4V	Decreased	The amount of Ti release became larger in the HSA–PBS solutions with 8 weeks immersion, measured by ICP-OES.	PBS+ (0-4) g/L \pm HSA	7.4	BSA reduces the vanadium ion release from Ti6Al4V up to 22 weeks.	[84]
Ti6Al4V	Decreased	Protein and cells adhered on surface decreases repassivation rate and increases charge density.	α -MEM+10 % FBS		The adhered protein and cells block the diffusion, producing an occluded space with low pH.	[85]
Ti6Al4V	Little effect	Same impedance values for Ti6Al4V in solution with different concentration of BSA.	Artificial saliva \pm (0.01-0.5) % BSA	5	Change of polarization resistance shows an irregular change with BSA concentration.	[86]
Ti6Al4V ELI	Little effect	No difference can be detected on anodic polarisation curves.	PBS with N ₂ gas \pm 10% BSA	7.4	The passive film mainly consists of TiO ₂ , Al ₂ O ₃ , and small amount of V oxides by anodic polarisation in deaerated serum solution.	[87]
Pure Ti	Little effect	No changes of concentration of Ti metal ions in the solution with and without albumin, measured by atomic absorption spectrophotometer.	0.1% crystallized bovine albumin in 0.1 M sodium chloride and 0.01 M sodium phosphate	7.4		[79]

*PBS: Phosphate-buffered saline SIP: Simulated inorganic plasma HSA: human serum albumin α -MEM: Minimum Essential Medium which is widely used for mammalian cell culture. FBS: Fetal bovine serum BSA: Bovine serum albumin

*All experiments in the table were carried out at 37 °C.

2.4.2 Effect of hydrogen peroxide

Ti ion release is always increased in the presence of reactive oxygen species (ROS) compared with conditions without these species [50, 83, 88]. This can be explained by the change of oxide film in the presence of H_2O_2 . Pan et al. [89] found that CP-Ti immersed in PBS with H_2O_2 developed a duplex surface film consisting of a dense inner layer and a porous outer layer, consistent with observation of two time- constants from EIS results. The passive film growing on Ti in PBS was observed to be thinner than that growing in PBS with H_2O_2 due to the existence of the additional outer porous layer. The dissolution of Ti is enhanced at this stage, however the authors also observed that following extended time periods, corrosion resistance increased again in H_2O_2 -containing PBS solution. The explanation given was that hydrates or precipitates incorporate with the outer film and fill in the pores. The outer layer has a transition from porous at early stage to dense at later stage. The two-layer model was also confirmed by XPS as TiO_2 , TiO and Ti_2O_3 were detected in Hanks solution with H_2O_2 while only TiO_2 and TiO were detected in absence of H_2O_2 [90, 91].

2.4.3 Synergistic effect of H_2O_2 and albumin

The effect of H_2O_2 and BSA on the corrosion of Ti6Al4V has been systematically studied by F. Yu [13]. The main findings can be schematically shown in Figure 2-4. An active dissolution is seen at low potentials, then the alloy undergoes passivation at higher potentials. The 'active dissolution' was supported by ICP-MS measurements showing

that Ti ion release at 90 mV vs SCE was higher than that at 200 mV vs SCE [14]. The existence of this active peak explains that corrosion current densities increase with a suppressed cathodic reaction with albumin. Figure 2-4 shows that the anodic reaction was suppressed in PS+P on addition of albumin, and this was also confirmed with potentiostatic measurements. However, the effect was subsequently reported to be time dependent. The suppression effect lasted for approximately 22 hours, after which, albumin starts to progressively dissolve the Ti-H₂O₂ corrosion product layer, causing a thinner oxide film and more metal dissolution [14].

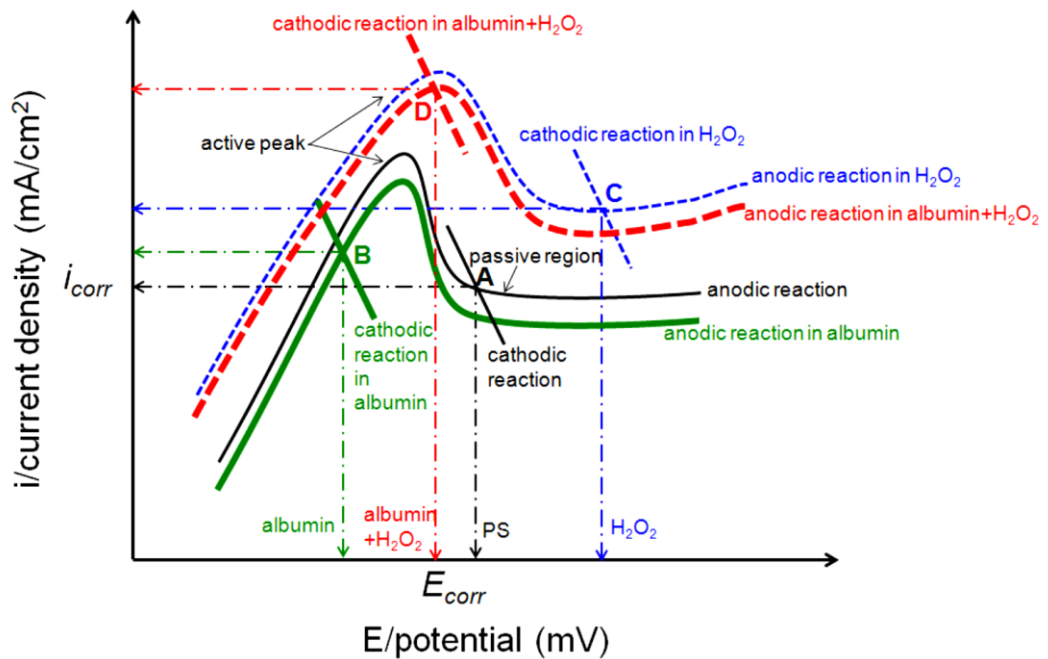


Figure 2-4 Hypothesis of synergistic effect of H₂O₂ and albumin on corrosion of Ti6Al4V, presented by Evans diagram (mixed potential theory) [13].

2.5 Mechanically-assisted crevice corrosion (MACC)

2.5.1 MACC concept and clinical observation

The term 'mechanically assisted crevice corrosion (MACC)' was proposed by Gilbert et al., and was first observed in a biomedical context associated with devices for hip arthroplasty [25]. The mechanism of MACC was also proposed by Gilbert, which is shown in Figure 2-5. Loading on implants causes a fretting motion between components, leading to damage of oxide film. The repassivation and hydrolysis of Ti consumes oxygen in the cavity and generates H^+ . More chloride ions are drawn into cavity, and local acidity will be developed gradually. Local acidity is adverse for the oxide film stability, and at some point the oxide film will become too thin/unstable to protect underlying metal and active corrosion attack will occur. [30, 92]

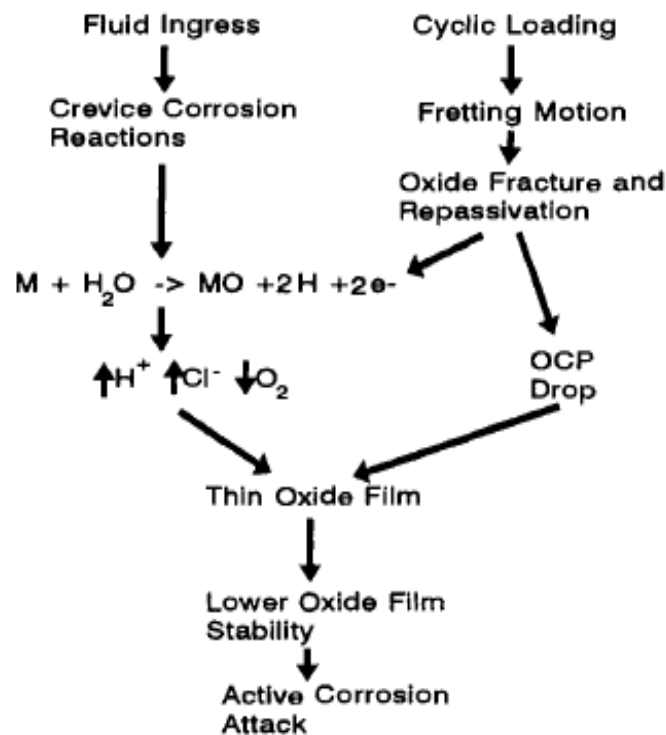


Figure 2-5 Schematic diagram of mechanically-assisted crevice corrosion [93]

Direct evidence of corrosion on retrieved dental implants has been infrequently reported. However, Danieli C. Rodrigues [94] reported images consistent with corrosion that are reproduced here in Figure 2-6. Evidence of pitting attack (red arrows on (a)) can be clearly seen on the outer surface of a retrieved abutment. A yellow and violet colour on the surface of another abutment suggests that oxidation of titanium (to Ti^{3+} or Ti^{4+}) has taken place. As previously mentioned, pitting is not predicted under physiological conditions and the lack of clinical history provided for the explant samples limits exclusion of external factors (e.g. intraoral use of H_2O_2 or HF is conceivable). Despite this corrosion-assisted fracture on dental implants has been frequently reported [95]. The occurrence of MACC in Ti dental implants would not be

surprising as there is strong evidence to show that cyclical masticatory forces cause relative motion between components. The mastication force of an adult is about 70 N-150 N [33], and the micromotion can be simulated depending on the stress distribution [96] [97]. In the literature, an interfacial discrepancy between components of between 2.5 μm - 60 μm in implant fixture-abutment gaps has been reported [98].

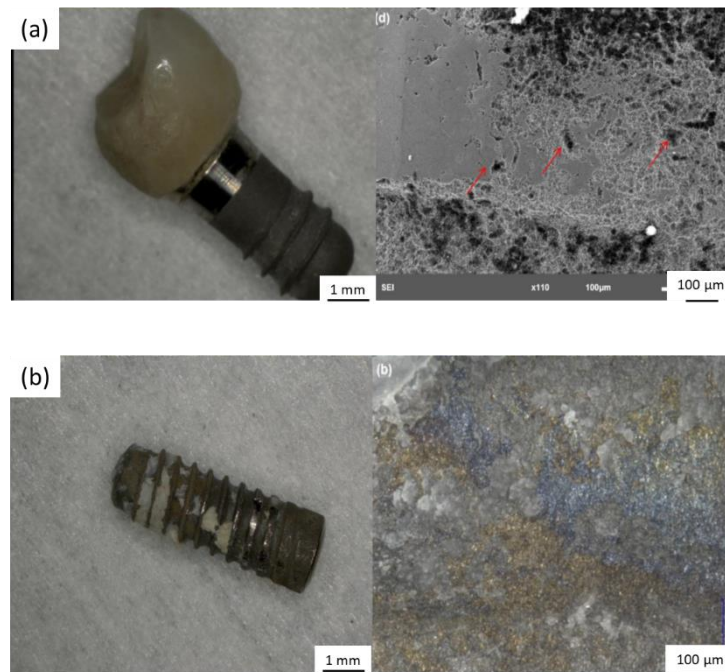


Figure 2-6 (a) Surface condition of a retrieved dental implant, some pits can be seen on the surface. (b) Surface condition of another dental implant, surface showing violet and yellow discoloration. [94]

There is a clinical study indicating that pH of peri-implant crevicular fluid around a modular dental implant shows more acidity than a one-piece dental implant [29]. This also gives the indication that MACC happens more dramatically in modular implants leading to more acidity.

2.5.2 Tribocorrosion and MACC

The combined effect of wear and corrosion is generally called 'tribocorrosion'. An example of tribocorrosion in a biomedical context is the process that takes place at the two acetabular surfaces of a hip implant. As the two surfaces rub together, there is abrasion and the passive film on the metal surface is disturbed, leading to a burst of metal dissolution from the bare metal surface. However, the movement of the two surfaces is relatively large, and fresh neutral solution is pumped into the gap flushing the surfaces, so that the passive film is able to regrow. MACC can be seen as a special case of tribocorrosion that takes place where there is a crevice geometry with limited motion, for example in a modular implant where two metal components are press-fit together. When small relative movements of the two metal surfaces take place, again the passive film is removed, and a burst of dissolution takes place on the surface. However, because of the crevice geometry, the metal ions that have been generated cannot diffuse away, but instead undergo hydrolysis, creating a concentrated anodic solution, which makes regrowth of passive film very difficult.

For conventional tribocorrosion testing, the measurements are usually made with 'pin-on-disc [99, 100]' including other contacting forms: ball-on-disc [101], roll-on-disc [102], block-on-block/ flat-on-flat [103]. However, these measurements typically involve macroscopic movement between the two surfaces so that neutral test solution is flushed into the test surfaces, which facilitates repassivation [104, 105].

Figure 2-7 shows how possible corrosion happens in a cemented total hip joint prosthesis system. Both tribocorrosion and MACC can exist in one hip prosthesis system, the acetabular cup and femoral head [106, 107] are designed to endure a large range of sliding motion, so body fluid between them is refreshed with each motion, thereby the corrosion between them is tribocorrosion. While corrosion between femoral head and stem [108-110] and corrosion between stem and cement [111, 112] is more likely to be MACC. This is due to these components not being exposed to large relative motions. The micro motion creates little perturbation of the body fluid in between, moreover, the narrow gap and complex geometry are not favourable for flushing the fluid away.

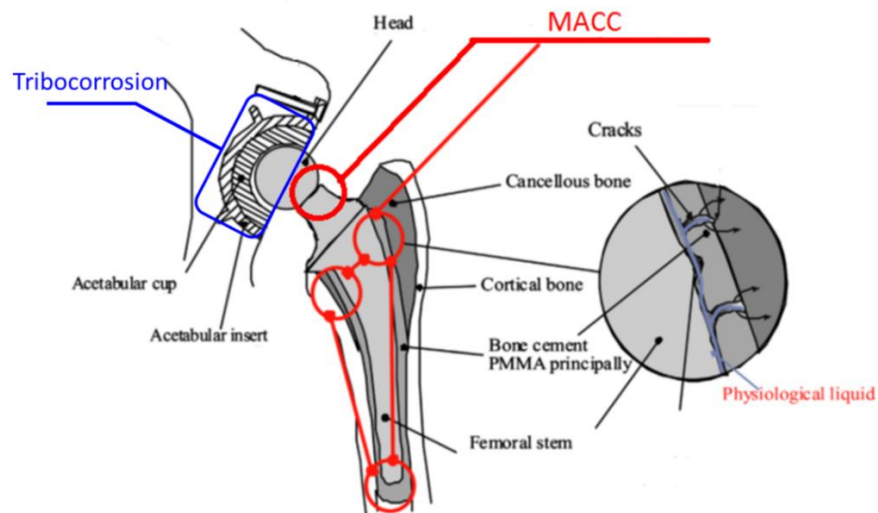
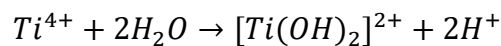
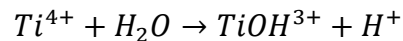


Figure 2-7 Total hip joint cemented prosthesis components [113], with the red circles to show the vulnerable places for MACC and the blue box to show where tribocorrosion could happen if it is metal-on-metal (MoM) contact. The figure was re-edited by the author.

2.5.3 MACC of Ti

MACC is associated with removal of the oxide film, hydrolysis of metal ions and repassivation. The first stage of MACC is damage to the oxide film that occurs due to fretting, which itself is highly dependent on the tribological properties of the metal. The surface layer of the Ti alloy is brittle, tending to be continuously fragmented and poorly adhered to the substrate, so Ti deforms badly in an unlubricated system [114, 115]. The poor wear resistance determines that the passive Ti film will be easily removed under fretting condition.

Once the top layer/ passive film is damaged, Ti ions will be released into aqueous solution. Hydrolysis of Ti in chloride media can be written as [116]:



Under occluded crevice conditions, cation hydrolysis and the development of local acidity will follow. Repassivation of Ti has been studied extensively using tribocorrosion simulation devices. Most simulations use classic pin-on-disc devices [99, 101, 102, 117-120]. The common approach involves removing the surface oxide film and electrochemically measuring the 'healing' process. Damage to the oxide film is instigated by scratching the specimen with a ceramic tube [118, 119], diamond tip [120], grinding paper [121], or fracturing the thin surface film on a non-conductive

substrate [120]. Although the local chemistry in such devices cannot be maintained, the effect of the local environment on repassivation of Ti can still be examined by utilising electrolytes with different pH. As shown in Figure 2-8, the fracture of the passive film causes a burst of metal ion release, which is reflected in the electrochemical measurement as a sudden sharp increase in the anodic current. Repassivation then follows, characterised by a progressive decrease of anodic current. The whole depassivation and repassivation process occurs in a very short time scale as shown, only lasting less than 100 μs for Ti in 0.6 M NaCl solution [120] or 0.5 ms- 2.5 ms tested by scratching test [92].

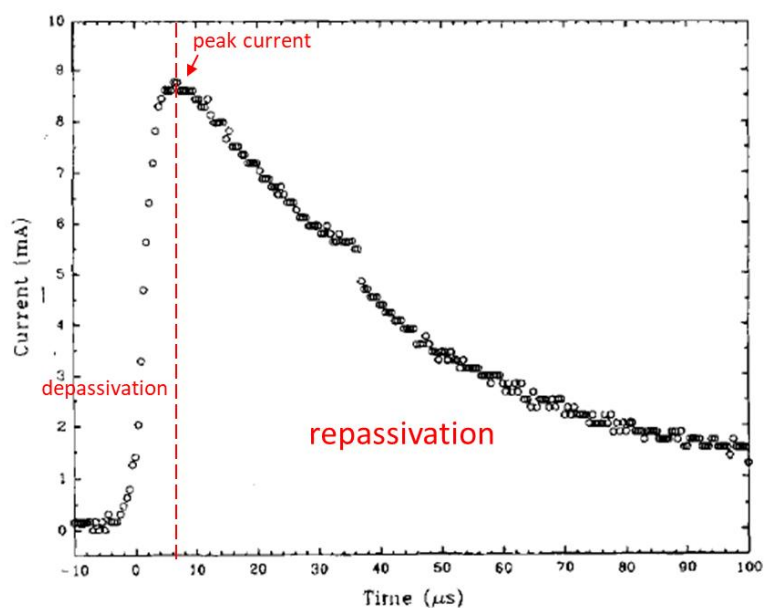


Figure 2-8 Measured current repassivation transient for a fractured titanium thin film electrode exposed to 0.6 M NaCl at 0 V vs. SCE [120].

Repassivation of Ti would be depressed in low-pH solutions from both thermodynamic and kinetics standpoints. The equilibrium potential-pH diagram of Ti shows that the stable state is Ti^{3+} in acid solution rather than its oxidation state (TiO , Ti_2O_3 and TiO_2) in neutral and alkaline solution. The current decay during repassivation can be fitted with different expressions based on experimental data, for example, it can be fitted as [120]:

$$i = i_0 \left(\frac{t}{t_0} \right)^{-m}$$

Where: i is current density, i_0 is the peak bare surface current density, t is elapsed time, and t_0 and m are constants.

Or [92]:

$$I(t) = I_{peak} e^{\frac{-(t-t_0)}{\tau}} - I_{\infty}$$

Where: I_{peak} is peak current, t_0 is the time to initiate the scratch, I_{∞} is steady state current and τ is the time constant for relaxation.

As illustrated from either expression of the current decay, a longer time would be required to pull the current back to steady state from higher peak current. And the peak current has been found to be larger in low-pH solution [92, 120], which corresponds to slower repassivation rate. On depassivation, OCP exhibits a sharp drop

because of abrupt anodic current increasing and then as mechanical disruption stops, repassivation follows and OCP will automatically recover. The rate of this recovery represents the rate of repassivation. The faster the OCP recovers, the larger degree of repassivation that happens. It was found that OCP recovery in a low-pH buffer solution (pH=4) is slower than in neutral buffer solution [119]. Briefly, local acidity is unfavourable for the repassivation of Ti.

2.5.4 Effect of albumin on tribocorrosion

The effect of albumin on MACC behaviour of Ti6Al4V has previously been evaluated with MACC device by Yu et al., [122], and it was found the addition of 4 wt.% albumin into physiological saline reduced the charge transfer of Ti6Al4V.

As stated in 2.4.1, the effect of the presence of albumin on general corrosion of Ti is ambiguous, which brings the complexity of studying the role of albumin in tribocorrosion because tribocorrosion is the synergistic combination of mechanical wear and corrosion processes [123]. Wear damage can be significantly reduced in PBS with the addition of albumin because a tribofilm consisting of Ti-albumin complexes reduces the friction coefficient of fretting, known as a lubrication effect [124].

Regarding corrosion, it has been reported that the fretting current of Ti6Al4V ELI was lower in PBS+ BSA when compared with PBS alone [125, 126]. However, the protection provided by albumin does not apply to all conditions. Runa et. al reported that it can be modified by the passive state of the Ti6Al4V, at lower potential (just slightly higher

than OCP), the presence of albumin in PBS decreases the fretting current. However, at higher potential where Ti6Al4V is in passivation, albumin will decay the repassivation rate and increase the charge transfer [127]. It is worth noting that more studies on the effect of albumin on tribocorrosion of metals have focused on Co-Cr(-Mo) alloy rather than Ti alloys because the former alloy is widely used as a bearing surface in total hip arthroplasty due to its excellent wear resistance. Neville et. al proposed that the tribofilm consisting of denatured proteins and a complex mixture of Co species was present on the fretting surface in bovine serum solution. This tribofilm, again, can reduce friction coefficient and decrease the level of ion release and total material loss. [100, 128-130]

2.5.5 Adverse in-vivo biological effect caused by Ti

In-vitro studies have shown that Ti ions and particles can stimulate both the adaptive and innate immune responses [131]. Chronic inflammation (usually assumed as a response to pathogens) is linked to alveolar bone loss surrounding teeth and dental implants [11, 12, 132]. Interestingly, the rate of alveolar bone loss can be more dramatic surrounding implants when compared with natural teeth and it has been hypothesized that implant related products may act as inflammatory modifiers [41]. Persistent chronic peri-implant inflammation leads to implant loosening due to loss of osseointegration and ultimately a need for revision surgeries or implant loss [71, 133-136].

2.6 Ti-based metallic glass

Concerns regarding the in-vivo corrosion of Ti implant materials leading to adverse biological outcomes or mechanical failures of implants [137-139] have led to a search for alloys with improved mechanical properties and corrosion resistance. Previous studies have identified Ti-based bulk metallic glasses as possible candidate materials to be used to fabricate dental implants [17, 54, 56, 140, 141].

2.6.1 $Ti_{40}Zr_{10}Cu_{36}Pd_{14}$

The mechanical properties of $Ti_{40}Zr_{10}Cu_{36}Pd_{14}$ are described in section 2.3.1. In addition, the good glass forming ability (GFA) and reported biocompatibility of $Ti_{40}Zr_{10}Cu_{36}Pd_{14}$ make it potentially useful as a dental implant material. $Ti_{40}Zr_{10}Cu_{36}Pd_{14}$ exhibits good GFA, characterised by a wide supercooled liquid region ($\Delta T=49$ K). It can be cast into rods with maximum dimension of 6 mm in diameter. Good GFA is essential for future commercialisation opportunities because less demanding solidification conditions are required to achieve a fully amorphous structure, and the reasonable size (6 mm) makes machining easier. [142-144]

Cell proliferation and differentiation studies performed on Ti-based metallic glasses ($Ti_{44}Zr_{10}Pd_{10}Cu_6Co_{23}Ta_7$, $Ti_{44}Zr_{10}Pd_{10}Cu_{10}Co_{19}Ta_7$ and $Ti_{44}Zr_{10}Pd_{10}Cu_{14}Co_{15}Ta_7$) showed similar results to those observed on control samples (glass substrate and Ti6Al4V),

indicating no cytotoxicity of the test metallic glasses to human osteoblast-like cells (SaOS-2). In addition, compared with Ti6Al4V, these cells cultured on metallic glasses exhibited greater levels of calcium deposition, indicating favourable osseointegration ability [141] [145]. In vivo evaluations have shown that these compositions have good biological compatibility and osseointegration. [146].

2.6.2 Corrosion of Ti-based metallic glasses in simulated body fluid

It is known that the corrosion resistance of metallic glasses is better than their crystalline counterparts because of the absence of structural defects, e.g. precipitates, segregates and grain boundaries, and the presence of a more homogeneous passive film [147, 148]. The corrosion resistance of $Ti_{47.5}Zr_{2.5+x}Cu_{37.5-x}Pd_{7.5}Sn_5$ (with $x = 0, 5,$ and 7.5 at.%) glassy alloy rods was investigated in Hanks solution at $pH = 7.4$ and at $37\text{ }^{\circ}C$. The potentiodynamic polarization curves of these alloys showed a passive region where the current density was lower than that of CP-Ti and much lower than high purity Cu (Figure 2-9). Significant pitting was observed with sweeping potential. The pitting potential for these metallic glasses varies from $0.18\text{-}0.4\text{ V vs SCE}$ depending on the different x value (Zr/ Cu ratio) [16]. Similar measurements were conducted on $Ti_{40}Zr_{10}Cu_{36}Pd_{14}$ also in Hanks solution at $37\text{ }^{\circ}C$, as shown in Figure 2-10, and show similar results [54, 140, 147]. Both the corrosion and passive current densities were lower than CP Ti and Ti6Al4V. Significant pitting did occur on $Ti_{40}Zr_{10}Cu_{36}Pd_{14}$, at potentials of 0.35 V vs SCE [147] or 0.5 V vs SCE [140].

It has been shown that the chemical composition and structure of the passive film plays an important role in the corrosion resistance of metallic glasses. After extended immersion in Hanks solution, the elemental variation in the oxide film of $Ti_{47.5}Zr_{2.5+x}Cu_{37.5-x}Pd_{7.5}Sn_5$ (with $x = 0, 5,$ and 7.5 at.%) and $Ti_{40}Zr_{10}Cu_{36}Pd_{14}$ glassy alloys measured by X-ray photoelectron spectroscopy (XPS) or auger electron spectroscopy (AES) was similar and showed that Ti and Zr were enriched while Cu, Pd and Sn were deficient [16, 147].

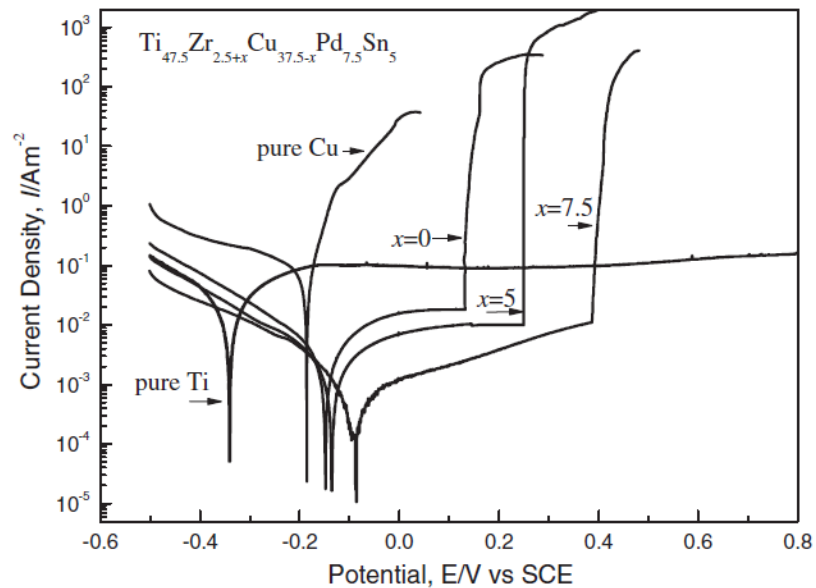


Figure 2-9 Anodic and cathodic polarization curves of the $Ti_{47.5}Zr_{2.5+x}Cu_{37.5-x}Pd_{7.5}Sn_5$ (with $x = 0, 5,$ and 7.5 at.%) bulk glassy alloys in Hanks solution at $37\text{ }^\circ\text{C}$ [16].

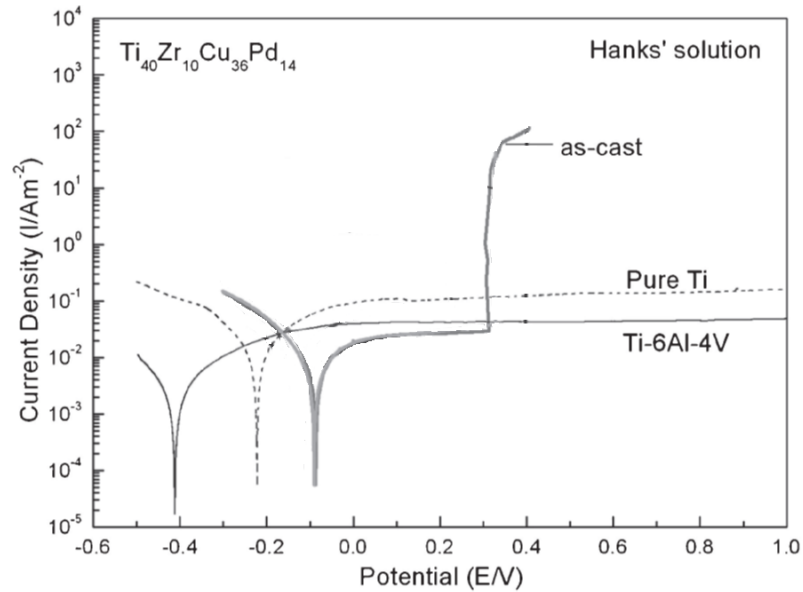


Figure 2-10 Anodic polarization curves of the as-cast and annealed $Ti_{40}Zr_{10}Cu_{36}Pd_{14}$ bulk glassy alloy immersed in Hanks solution at 310 K. The curves of pure Ti and Ti6Al4V alloy are also shown for comparison [147].

Minor changes to the elemental composition of metallic glass has been shown to affect the corrosion behaviour significantly. In a $Ti_{47.5}Cu_{37.5}Ni_{7.5}Zr_{2.5}M_5$ ($M = Cu, Co, Nb$ or Ta) alloy system, 5 at.% addition of Nb or Ta could lower the corrosion current by one order of magnitude compared with that of the base alloy. The addition of Nb or Ta facilitates the enrichment of Ti, and certain amounts of Nb or Ta existing in the surface film result in higher corrosion resistance [15]. After pitting, the dealloying process in the pitting area should be studied, which allows the amount and species of corrosion products to be determined. This has clinical relevance to the species which will be potentially released after implantation. This is an important aspect to take into

account when considering metallic glasses as a biomaterial because the different metal compounds could have remarkably different interactions with surrounding biological tissues [137]. For $\text{Ti}_{40}\text{Zr}_{10}\text{Cu}_{36}\text{Pd}_{14}$ after pitting has occurred in Hanks solution, Ti and Zr were deficient and Cu and Pd were enriched compared with the nominal composition. Meanwhile, some white corrosion products were deposited in the pit. The corrosion products of $\text{Ti}_{40}\text{Zr}_{10}\text{Cu}_{34}\text{Pd}_{14}\text{Sn}_2$ in 0.9% NaCl were studied by in-situ synchrotron XRD, and it was found that Pd nanoparticles had formed in the interior of the pits, and a salt layer consisting of CuCl, PdCl₂, ZrOCl₂·8H₂O, Cu and Cu₂O formed just below the active dissolution surface [149].

2.6.3 Effect of fabrication (structural states) on corrosion of metallic glasses

Copper-mould casting is the most common and popular method to produce BMGs in different alloy systems. Figure 2-11 (a) shows a schematic of the equipment normally used for copper mould casting of BMGs. Briefly, the alloy is melted and poured into a copper mould where it solidifies quickly because of the rapid heat extraction conferred by the Cu mould [150]. To produce metallic glass in the form of ribbons, melt-spinning is the most common method. Figure 2-11 (b) shows a schematic diagram of the melt spinning process. The master alloy is heated and melted by induction coils and pushed by ejection pressure, in a jet through a small nozzle in the crucible over the rotating wheel where it is rapidly cooled to form the ribbon of metallic glass typically of 40-50 μm thickness [151].

Compared with melt spinning, the product formed by bulk casting is usually in dimensions of several millimetres. Apart from the size, the main difference between these two fabrication methods is the cooling rate, which is 10^5 - 10^6 K/s for melt-spun ribbon and approximately 10^2 - 10^3 K/s for mould-casted bulk [152]. Illekova et al. produced an amorphous alloy with composition of $Zr_{55}Ni_{25}Al_{20}$ using these two approaches. They found that the ribbon sample exhibited a higher degree of short-range order than the bulk sample [153]. In other words, both ribbon and rod samples are in the glassy state, but the bulk formed glass possesses a more relaxed structure than the compositionally equivalent ribbon [19]. The corrosion behaviour of amorphous alloys with different structurally relaxed states has been previously studied [20-22, 154-159]. Generally, structural relaxation below T_g can increase the corrosion resistance, which was evidenced by decreased anodic or passive current densities [20, 22, 154, 158]. The passivation ability of amorphous alloys can be enhanced by the reduction of free volume accompanied with structural relaxation [20, 155]. It was also proposed that the corrosion resistance of the Al-Co-Ce alloy was enhanced after long-time exposure (up to 4 h) due to the preferential dissolution of Al leaving a surface enriched in Co and Ce [20]. Pitting behaviour of Zr-based metallic glasses in different structural states has also been studied. It was proposed that the relaxed specimen possessed a lower pitting potential than the as-cast equivalent due to the formation of chemical clusters/inhomogeneities [159]. When studying the corrosion behaviour of metallic glasses after different degrees of structural relaxation, a common approach has been to make a specimen that was partial devitrificated/ crystallised and compare

it with the fully amorphous alloy. With no exception, the corrosion resistance was significantly reduced once crystallites had formed and this is consistent with the general idea that inhomogeneities in crystalline alloys (e.g. grain boundary) have high corrosion susceptibility [20-22, 157].

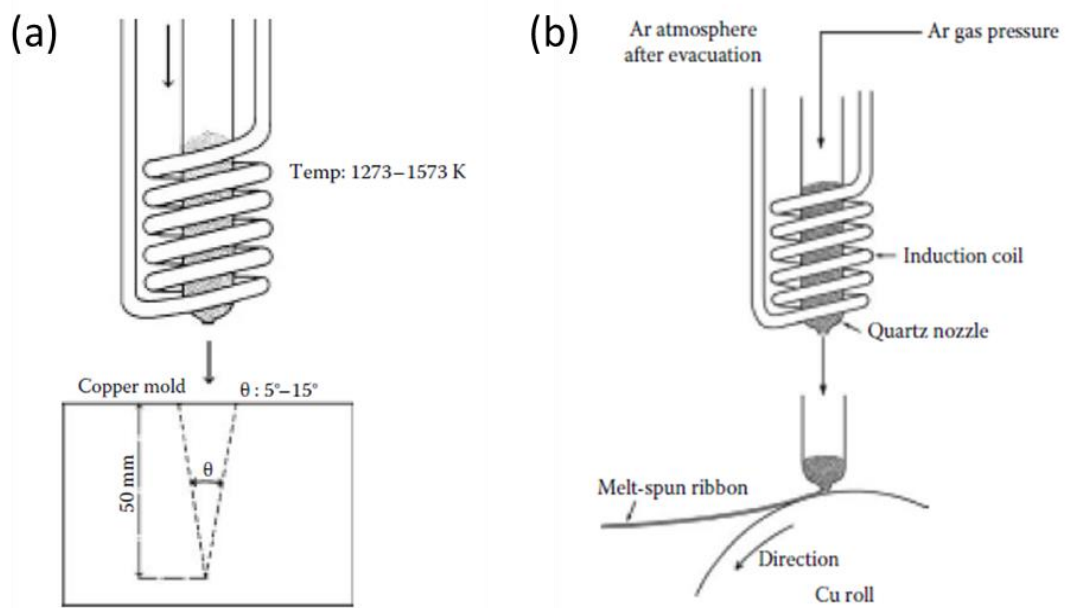


Figure 2-11 Schematic diagram of the manufacturing process of (a) rods by copper-mould casting technique [150], (b) ribbons by melt spinning [160].

2.6.4 Minor additions to BMG system

It has been reported that increasing the number of constituent elements is an effective way to improve the glass forming ability (GFA). The addition of 2 at.% Sn to $\text{Ti}_{40}\text{Zr}_{10}\text{Cu}_{36}\text{Pd}_{14}$ alloy system improves the GFA significantly [142, 144], by suppressing the precipitation of CuTi and $\text{Cu}_{10}\text{Zr}_7$ phases, enlarging negative mixing heat with Ti, Zr and Pd, and inducing more atomic mismatch [161]. 2 at.% Sn decreases the Young's modulus considerably [144] which could facilitate a potential biomedical application by diminishing the 'stress shielding' effect, and it increases the compressive strength from 1950 to 2050 MPa [142].

Recently, a new series of Ti metallic glasses, with a composition of $\text{Ti}_{40}\text{Zr}_{10}\text{Cu}_{36-x}\text{Pd}_{14}\text{Ga}_x$ ($x = 1, 2, 4, 8, 10$ at.%) [18], has been developed from the $\text{Ti}_{40}\text{Zr}_{10}\text{Cu}_{36}\text{Pd}_{14}$ alloy first described by Zhu et al. [56]. Ga partially replaces Cu improving ductility and enhances glass-forming ability (up to 4 at.%) whilst maintaining biological compatibility. The addition of Ga has also been proposed to be potentially biologically beneficial as Ga^{3+} possesses antimicrobial properties and has been used therapeutically to treat osteoporosis. [162, 163]

Compared with $\text{Ti}_{40}\text{Zr}_{10}\text{Cu}_{40}\text{Pd}_{10}$, $\text{Ti}_{40}\text{Zr}_{10}\text{Cu}_{40}\text{Pd}_{10}\text{Si}_2$ has a larger supercooled region, lower Young's modulus, however, 2 at.% Si also reduces the compressive strength from 2012 MPa to 1935 MPa [164].

2.6.5 Corrosion of other constituent elements under physiological conditions

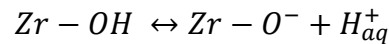
Corrosion resistance of metallic glasses is determined by the electrochemical properties of all constituent elements. The electrochemical behaviours of other constituent elements (Zr, Cu, Pd, Sn and Ga) are also reviewed here.

2.6.5.1 Zirconium

Roxolid is the tradename of a commercial alloy used by Straumann (Basel, Switzerland) for dental implant manufacture. The alloy is composed of ~15 at. % Zr and ~85 at. % Ti and was specifically designed for use in dental implantology and in particular for narrow diameter implants. TiZr alloys are stronger than pure titanium and have excellent osseointegration properties. The progressive addition of Zr enhances the oxide film stability of Ti and improves the corrosion resistance in acid and inflammatory (H₂O₂-containing) environments. However, Zr is very susceptible to pitting and once the atomic percentage of Zr into Ti exceeds 50%, the alloys showed significant pitting in 0.9% NaCl solution [165].

Commercially pure Zr has been shown to pit in 2 M HCl and 0.9% NaCl solution with a pitting potential of 0.2 V vs SCE and 0.8 V vs SCE in HCl and NaCl solutions respectively. The addition of Zr to Ti (up to 50 at.%) increases the passivity of Ti in both HCl and the oxidative (NaCl+ H₂O₂) environment. However, when the addition of Zr reaches 50 at.%, similar pitting behaviour as pure Zr took place. No pitting was shown on Ti alloys with 5 at.% and 15 at.% Zr until 1.5 V vs SCE [165]. The pitting mechanism of pure Zr in

Cl⁻-containing solution is different depending on the pH of electrolyte. In acidic solutions, pitting may be induced either by flaking or weakening of the oxide film by H₃O⁺, resulting in a porous oxide film. In basic solutions, the amorphous zirconium oxyhydroxide layer is in an acid–base equilibrium:

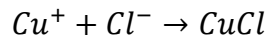


In the base solution, hydroxyl ions accelerate the reaction to generate more ZrO⁻ and H_{aq}⁺. It has been experimentally shown that a linear increase in current density occurs with increasing hydroxyl concentration in solution suggesting that the concentration of structural ZrO⁻ increases linearly with concentration of hydroxyl. The negatively charged ZrO⁻ increases the overpotential between metal-oxide and oxide-solution and it will reach the potential of oxygen evolution. The production of oxygen beneath the oxide film will eventually cause rupture, so pitting occurs. [166, 167]

2.6.5.2 Copper

Cu is an element which is necessary to achieve good glass forming ability for Ti-based metallic glasses due to the large atomic mismatch and its negative entropy with Ti and Zr [17, 168]. However, chloride ion environments are very aggressive to copper and its alloys, due to the tendency of the chloride ion to form an unstable surface film (CuCl) and soluble chloride complexes (CuCl₂⁻ or CuCl₃²⁻) [169, 170]. The anodic reaction has generally been taken to be reversible, mainly due to the rapid, highly thermodynamically favourable complexation of the cuprous ion by the chloride ion.

The cathodic reaction is usually dominated by oxygen reduction [171]. In neutral chloride solutions, the main, initial corrosion product of copper is cuprous chloride, $CuCl$ formed via the reaction:



It has been proposed that cuprous chloride, which has low solubility in dilute sodium chloride, reacts to produce cuprous oxide (Cu_2O), and Cu_2O is the main chemical species of the visible thick scale on the surface. Cu_2O can be further oxidised over time to other compounds depending on the pH and Cl^{-} concentration [171, 172]. Compared with $Ti_{47.5}Zr_{10}Cu_{30}Pd_{7.5}Sn_5$, the anodic and corrosion current of pure Cu is considerably larger, indicating the active dissolution of it in Hanks solution (Figure 2-9). The surface composition of Cu-based metallic glasses ($(Cu_{0.6}Hf_{0.25}Ti_{0.15})_{90}Nb_{10}$) after immersion in HCl, NaCl and H_2SO_4 solution has been studied and compared with its nominal composition. It was found that Ti and Hf were enriched and Cu was deficient [173]. Cu is a potentially toxic element and its toxicity is attributed to its potential as a catalyst for oxidative damage to human tissues through redox cycling between Cu(I) and Cu(II), particularly in the presence of H_2O_2 [174]. In vitro cell culture assays have indicated that the Cu-based dental alloys are associated with Cu ion release which causes a reduction in cellular proliferation [175-177].

Interactions between BSA protein and copper have been evaluated by EIS and using quartz crystal microbalance measurements [178]. Adsorption occurred most

dramatically when a positive potential was applied (187 mV vs. SCE) on Cu in the presence of O₂. The resistance of the oxide film was also the highest in this case when compared with lower potentials and the absence of O₂. The presence of albumin in artificial seawater has been shown to significantly reduce the formation of CuO, Cu₂O and Ni(OH)₂ for a 70Cu–30Ni alloy [179]. The corrosion inhibition by amino acids has also been reported [180-185]. For example, the polarisation and chronoamperometry tests showed that cysteine (10⁻⁶-10⁻² M) in a 0.5 M Na₂SO₄ solution consistently decreased the anodic current density, and the corrosion current of Cu [186]. Similar results showing that cysteine significantly decreases the anodic current of Cu have been confirmed by other authors [182]. The reason for the corrosion inhibition was proposed as the adsorption of the amino acid blocks the active corrosion sites of Cu [183].

2.6.5.3 Palladium

Palladium is a noble metal, which is highly resistant to corrosion and oxidation in moist air. As shown in the Pourbaix diagram [52], the potential needs to be raised to 0.5 V vs SHE to oxidise Pd to Pd(OH)₂ at neutral pH. In a Ti-Pd alloy, Pd was found to be enriched on the alloy surface, due to the preferential dissolution of Ti [187]. In acid environments, Pd was also reported to accelerate proton reduction. For Pd-containing alloys, proton reduction occurs with smaller Tafel slopes (50 mV⁻¹ to 65 mV⁻¹) compared with CP-Ti which possess a Tafel slope of >120 mV⁻¹ [188]. According to mixed potential theory, the increase of cathodic reaction with addition of (0.1-2.0)

wt.% Pd shifts the cross-point from 'active transition' to passivated stage on anodic curve in acid solution, so the Ti-Pd alloy has higher OCP and lower corrosion current [189]. Similar results have been reported showing that the alloying addition of Pd to Ti can improve the corrosion resistance in PBS with H₂O₂ [190]. SEM micrographs have also shown the surface of a Ti-Pd alloy to be much less affected by the attack of fluoride ions, which further confirms the better corrosion resistance of Ti-Pd than Ti and its alloys (Ti6Al4V and Ti6Al7Nb) [189].

2.6.5.4 Gallium

As mentioned above, the main constituent elements (Ti, Zr, Cu and Pd) in metallic glasses are very susceptible to chloride ions. In general, the presence of Cl⁻ ions can badly affect the corrosion resistance of these metals, and the corrosion products are normally metal-chlorides. However, it has been shown that the amount of Ga ions released into NaCl-containing solution (0.1% to 1%) is lower than that into deionised water after 28 days. This is contradictory to other constituent elements that the presence of Cl⁻ can reduce the level of ion release. The corrosion product for solid Ga in deionised water is likely to be Ga₂O which is then hydrolysed to GaO(OH). No detectable GaCl_x has been shown to form in 1% NaCl solution. [191] Note that these findings are based on solid Ga and the corrosion tests were carried out at (24± 2) °C which is lower than the melting point (29°C).

2.7 Summary

The overall purpose of this project is to evaluate the potential of Ti-based bulk metallic glass (based on $\text{Ti}_{40}\text{Zr}_{10}\text{Cu}_{34}\text{Pd}_{14}$) to be used as small diameter dental implants.

Ti and its alloys are the most commonly used material for dental implants, and they are very resistant to localized corrosion in simulated body fluids (e.g. physiological saline). Previous work points out that H_2O_2 and albumin can significantly accelerate the corrosion of Ti6Al4V in physiological saline. In this case, how H_2O_2 and serum albumin affect the corrosion of Ti-based metallic glass should also be understood.

There is a biological motivation to explore the replacement of Cu in the $\text{Ti}_{40}\text{Zr}_{10}\text{Cu}_{36}\text{Pd}_{14}$ metallic glass system. Nevertheless, Cu is an unavoidable element to attain good glass forming ability. Optimising the composition to achieve a combination of desired properties is the current emphasis in developing metallic glasses. In this work, gallium is used to partly substitute copper with an expectation of achieving better mechanical properties whilst not compromising corrosion resistance.

Corrosion has been observed at the interfaces of modular Ti implants. It has been proposed that MACC is contributory and Ti may be particularly susceptible to MACC due to its poor wear resistance. The MACC behaviour of Ti-based BMGs needs to be investigated as part of an evaluation before considering application as an implant material.

3 Materials and Methods

3.1 Crystalline alloys

The crystalline alloys used in this work were commercially pure titanium (CP-Ti), Ti6Al4V, commercially pure zirconium, copper, tin, gallium and palladium. All materials were commercially sourced. Nominal compositions and manufacturer details are given in Table 3-1.

Table 3-1 Crystalline alloys (G refers to ASTM standard Grades)

Metal	Source	Manufacturer's compositional certificate
CP-Ti (G4)	Titanium Products Ltd	wt.%, 0.006 N, 0.007 C, 0.002 H, 0.22 Fe, 0.30 O and Ti Bal.
Ti6Al4V (G5)		wt.%, N 0.05, C 0.08, H 0.015, Fe 0.3, O 0.2 max, Al 5.5-6.8, V 3.5-4.5, Ti Bal
CP-Zr (G702)	Goodfellow	wt.%, 0.07 Fe, 2.36 Hf, 0.01 Cr, 0.015 C, 0.11 O, 0.007 N, 0.0002 H and Zr Bal.
Cu	Advent Research Materials	ppm: As 5, Bi 1, Cd 1, Fe 10, Mn 0.5, Ni 10 O 5, P 3, Pb 5, S 15, Sb 4, Sae 3, Sn 2 Te 2 Zn 1 and Cu 9.99+%.
Sn		ppm: Pb 340, Sb 130, As 50, Fe 40, In 50, Bi 10, Cu 10, Ag <10, Cd <2, Zn 4, Ni <5, Al <2. Balance Sn 99.93+%
Pt		ppm: Rh< 50, Si< 50, Fe< 50, Au< 50, Ir< 50, Pd< 50, Mo< 40, Te< 40, Al< 40 etc. Total impurities < 100ppm. Purity 99.99%.
Pd	Alfa Aesar	ppm: Pt 22, Au 13, Ca 19, Zn 1, Cu 3, Fe 8, Cr 2, Al 2 and Pd 99.99+%
Ga	Sigma-Aldrich	99.999% based on trace metals analysis

3.2 Metallic glasses

Fabrication of metallic glasses was carried out at the Leibniz Institute for Solid State and Materials Research (IFW) Dresden, Germany. The nominal alloy compositions of rods and ribbons were $\text{Ti}_{40}\text{Zr}_{10}\text{Cu}_{34}\text{Pd}_{14}\text{Sn}_2$ and $\text{Ti}_{40}\text{Zr}_{10}\text{Cu}_{36-x}\text{Pd}_{14}\text{Ga}_x$ ($x = 0, 1, 2, 4, 8$ and 10 at. %). Master alloys with the nominal compositions were prepared by arc melting the elements Ti, Zr, Cu, Pd, Sn and Ga (purity of 99.99% or higher) under a Ti gettered Ar 99.998% atmosphere with an Edmund Bühler GmbH Arc Melter. All ingots were flipped and re-melted at least five times to achieve good chemical homogeneity. To make rod metallic glasses, the molten alloy was then injected into a water-cooled copper mould. The mould was cylinder-shaped for Ga-containing rods, or plate-shaped for $\text{Ti}_{40}\text{Zr}_{10}\text{Cu}_{34}\text{Pd}_{14}\text{Sn}_2$.

Metallic glass ribbons were produced using a single roller Bühler melt spinner. In common with the production process for BMG rods, master alloy ingots were prepared with high purity metals using arc melting. The process was repeated three times under a titanium-gettered argon atmosphere to ensure good homogeneity. The alloys were melted by inductive heating at 1973 K and ejected onto a high speed (35 m/s) rotating Cu wheel under a 400 mbar Argon atmosphere to prevent oxidation. The cooling rate was approximately 10^6 K/s and the dimensions of melt-spun ribbons were 5 mm (width) \times 45 μm -50 μm (thickness).

To identify whether inhomogeneity existed in the bulk metallic glass samples which could cause variation in the chemical composition, nine areas (100 μm \times 100 μm each),

were randomly selected from the test surface and mapped using EDX. The mean and standard deviation values of the chemical composition of all bulk and ribbon metallic glasses were given by the software (INCA suite, V 4.13).

The materials used in MACC experiments were Ti6Al4V (G5) and three metallic glasses with compositions: $\text{Ti}_{40}\text{Zr}_{10}\text{Cu}_{36}\text{Pd}_{14}$ (BMG_Pd14), $\text{Ti}_{40}\text{Zr}_{10}\text{Cu}_{34}\text{Pd}_{14}\text{Sn}_2$ (BMG_Sn2), $\text{Ti}_{40}\text{Zr}_{10}\text{Cu}_{33}\text{Pd}_{14}\text{Sn}_2\text{Si}$ (BMG_Sn2Si). For MACC experiments close fitting paired pin and cup components made of same material were used in one test throughout to avoid galvanic corrosion. Materials for pin and cup were also fabricated at IFW Dresden, Germany and machined by the commercial implant manufacturer Anthogyr SAS, France. Components were machined using the same procedures and nominally had the same surface finish.

3.3 Electrolyte

Four simplified electrolytes were prepared to simulate different environments surrounding the implanted materials. The abbreviations and compositions of them are listed in Table 3-2. The chemical reagents used were: NaCl (Sigma Aldrich, UK), hydrogen peroxide (30 wt.% in H_2O , Sigma Aldrich, UK) and Bovine serum albumin ($\geq 98\%$, lyophilized powder, Sigma Aldrich). The electrolytes were made by dissolving proportioned reagents into deionised water ((DI water), 15 M Ω cm, Millipore, USA). Note that H_2O_2 - and albumin-containing solutions were refrigerated (4 ± 2) °C to

minimise decomposition. The activity of H₂O₂-containing solutions was tested by electrochemical methods to ensure the concentration of H₂O₂ was correct before carrying on the corrosion tests, more specifically, the current densities should be consistent when using a Pt electrode to decompose H₂O₂-containing solutions.

Table 3-2 List of abbreviations and compositions of all tested solutions (all in wt.%)

Abbreviation	Composition
PS	0.9% NaCl
PS+P	0.9% NaCl+ 0.1% H ₂ O ₂
PS+A	0.9% NaCl+ 4% albumin
PS+A+P	0.9% NaCl+ 0.1% H ₂ O ₂ + 4% albumin

3.4 Sample preparation

To prepare the samples for metallographic characterisation, the metals were hot-mounted in Bakelite resin (Struers Ltd. UK), followed by grinding with 400, 800, 1200, 2500, and 4000 grit SiC abrasive paper and polishing with a MD-Chem polishing cloth (Struers Ltd. UK) lubricated with 0.04 µm OP-S Colloidal Silica suspension (Struers Ltd. UK) to achieve a mirror surface. Samples were then ultrasonically cleaned with DI water (15 MΩ cm) for 5 minutes.

To prepare samples for electrochemical tests, all alloys, including all pure metals (except Ga) and metallic glasses, were cold-mounted in epoFix resin (Struers Ltd. UK) and an electrical connection was made to the metal surface not exposed to solution.

To minimise the risk of crevice corrosion for ribbon samples, a small amount of adhesive (Araldite Rapid Tubes Epoxy, UK) was beaded to the ribbon edges prior to embedding in epoxy resin. The cross section of the ribbon samples is schematically shown in Figure 3-1. Due to the good adhesion between Araldite and the ribbon samples, a peripheral crevice was minimised and the estimation of surface area was improved.

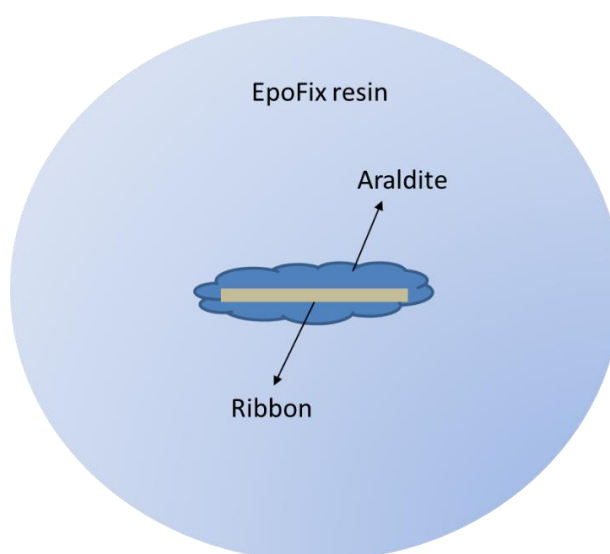


Figure 3-1 Schematic illustration of the cross section of ribbon samples used for electrochemical measurements.

All metallic glass samples and pure elements were prepared using the same approach. However, as the melting point of Ga is low, it is in a liquid state when immersed in a 37 °C solution. To prepare the Ga sample, a small amount of epofix resin was placed at bottom of a rigid plastic tube (\varnothing 5 mm) with a Cu wire passing through the resin. After the resin was set, the Ga was heated to a liquid state and poured into the tube. The

surface in contact with the resin made an electrical connection with the Cu wire, whilst the contralateral surface was exposed to solution used for measurements.

3.5 Electrochemical measurements

Electrochemical tests were controlled by a Gill AC potentiostat (ACM Instruments, Cumbria, UK). The electrochemical cell was a three-electrode system with a saturated calomel electrode (SCE) as the reference electrode (RE), a Pt mesh as the counter electrode (CE) and the sample under investigation as the working electrode (WE). Figure 3-2 illustrates the layout of all the electrodes and sensor in the cell. The electrolyte temperature (37 °C) was controlled by pumping water at the required temperature around the jacket of the electrochemical cell. A sensor connected with an electronic thermocouple (YC-727UD data logger thermometer, Taiwan) was used to monitor the temperature variation in the cell and a temperature variation within 1 °C was deemed acceptable.

Each electrochemical experiment consisted of monitoring the open circuit potential (OCP) for 1 h and potentiodynamic sweeps, which were carried out at a sweep rate of 1 mV/s. Anodic sweeps were initiated at 50 mV below OCP, and cathodic sweeps were initiated at 50 mV above OCP. The anodic polarisation test was stopped if the current density exceeded 10 mA/cm² while no current limit was applied for the cathodic test. An anodic current density limit was set in case the samples corroded excessively.

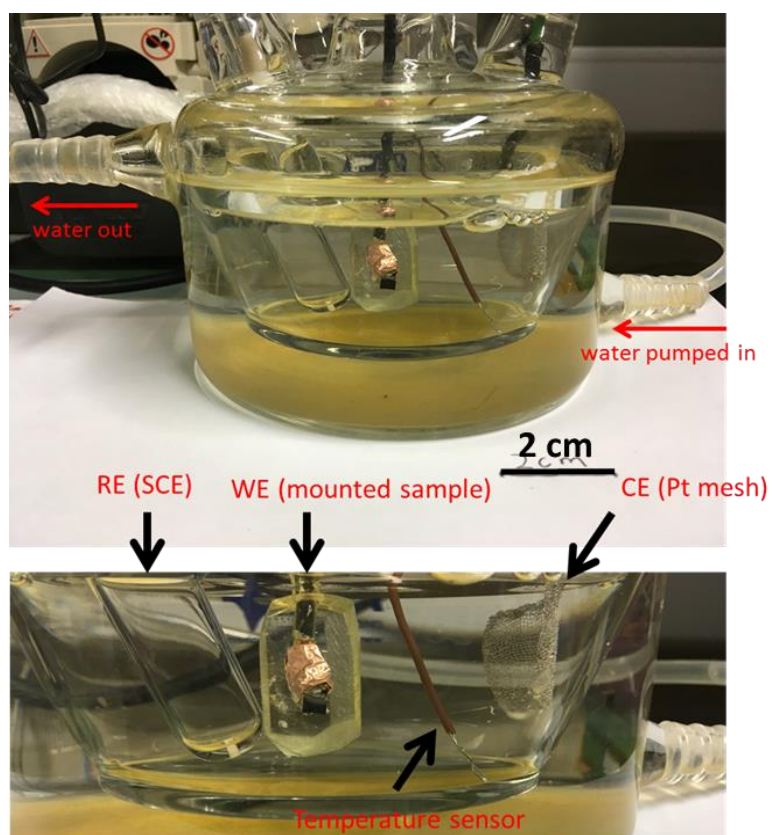


Figure 3-2 Illustration of the standard three-electrode electrochemical cell with water jacket: mounted sample as working electrode (WE), platinum mesh as counter electrode (CE) and saturated calomel electrode as reference electrode (RE).

3.6 Characterisation

The samples were observed using optical microscopy (DFC420, Leica, Germany) before the corrosion test to make sure there were no discernible defects e.g. scratches, holes, crevices along the resin etc. After the corrosion test, the sample surface was re-examined to identify the location and size of any pits. A Schott KL 1500 LCD cold light source was used to illuminate samples from side on.

X-ray diffraction (XRD) was used to confirm the amorphous structure of the metallic glasses. The equipment used in this work was either a D8 Advance diffractometer (Bruker, USA) for BMG_Sn2 or Rigaku Miniflex 600 diffractometer (Rigaku, Japan) for Ga-containing metallic glasses due to availability. Both instruments used $\text{CuK}\alpha$ radiation ($\lambda=1.54 \text{ \AA}$), under an accelerating voltage of 40 kV and a current of 40 mA with an angular range of 20° - 100° .

Pitting morphology was imaged using scanning electron microscopy (SEM) with either a JEOL 7000 or JEOL 6060 instrument (Japan Electron Optics Laboratory, Japan). The accelerating voltage used was 20 kV and the working distance was 10 mm. The composition analysis of the specimen surfaces was carried out using Energy dispersive X-ray spectroscopy (EDX, Oxford Instruments, UK) and the data analysed in INCA suite (V 4.13) software. A transmission electron microscope (Tecnai F20, FEI), was used to characterise the wear debris generated by MACC.

After corrosion tests, the gallium in the rigid tube turned to liquid. The surface area of liquid gallium was determined by confocal microscopy (LEXT OLS3100, Olympus). The

resolution of the microscopy is 0.12 μm . The microscope is equipped with a 408 nm violet optical system. The magnification used to observe the samples was 10 \times , with a working distance 10.1 mm.

The hardness of the MACC samples was tested with a Micro-Vickers hardness testing machine (MKV-H1, Mitutoyo, UK). The load applied was 500 g and 15 points on sample surface were randomly picked.

A digital optical microscope (VHX-6000, Keyence, UK) was used to observe MACC sample surfaces in section 6.11.

3.7 MACC device and tests

The device shown in Figure 3-3 (a), was established to study MACC. The core part is a three-electrode cell. The working electrode was a metal rod made of the test material. The counter electrode was a platinum wire with an area of 30 mm^2 , and a silver chloride (Ag/AgCl) electrode was used as the reference electrode due to the dimensional limitation of the cell. The counter reference had to be positioned carefully to avoid direct contact with the working electrode when MACC simulation was in operation. All MACC experiments were carried out at room temperature.

Figure 3-3 (b) shows the pin and cup components which make up the couple. The cup had an outer diameter of 4.8 mm and an inner diameter of 4.3 mm. The inner diameter of the cup was matched to that of the pin. Both have a conical contact area and the cone pitch angle was 45°, simulating the connection between a dental implant

and abutment. The pin can rotate at certain speed (0.1 rpm, 0.5 rpm, 5 rpm, 10 rpm (revolutions per minute)), whilst the cup was mechanically pressed into a PEEK container and kept fixed using an anti-rotation notch. The rotation of the pin was driven by a separated motor (Powermax II®, Pacific scientific, USA) which is not shown in this diagram. The weight of the plate above the pin provides control of a normal applied force. In this work a maximum of 634 g and minimum 50 g were applied to the plate. A compact potentiostat (Ivium Technologies, Eindhoven, Netherlands) was connected to the MACC device to monitor the electrochemical process. Figure 3-3 (c) shows the cross-section of the pin and cup when they are coupled. The nominal contact area is the lateral surface of a truncated cone, which is $\approx 20 \text{ mm}^2$. The small groove ($\varnothing 0.75 \text{ mm}$) located at the bottom of the cup is designed for the collection of the wear debris and corrosion products after experiments.

In the MACC experiments, one experimental condition is named 'static', under this condition, the pin keeps fixed. The other condition is named 'fretting' or 'rotation', which indicates that the pin rotates at a certain speed in the cup. Under both conditions, there was always some load applied on the weight plate. The back of pin (not the end for MACC experiments) was sealed with araldite when conducting the electrochemical tests in section 6.3.2.

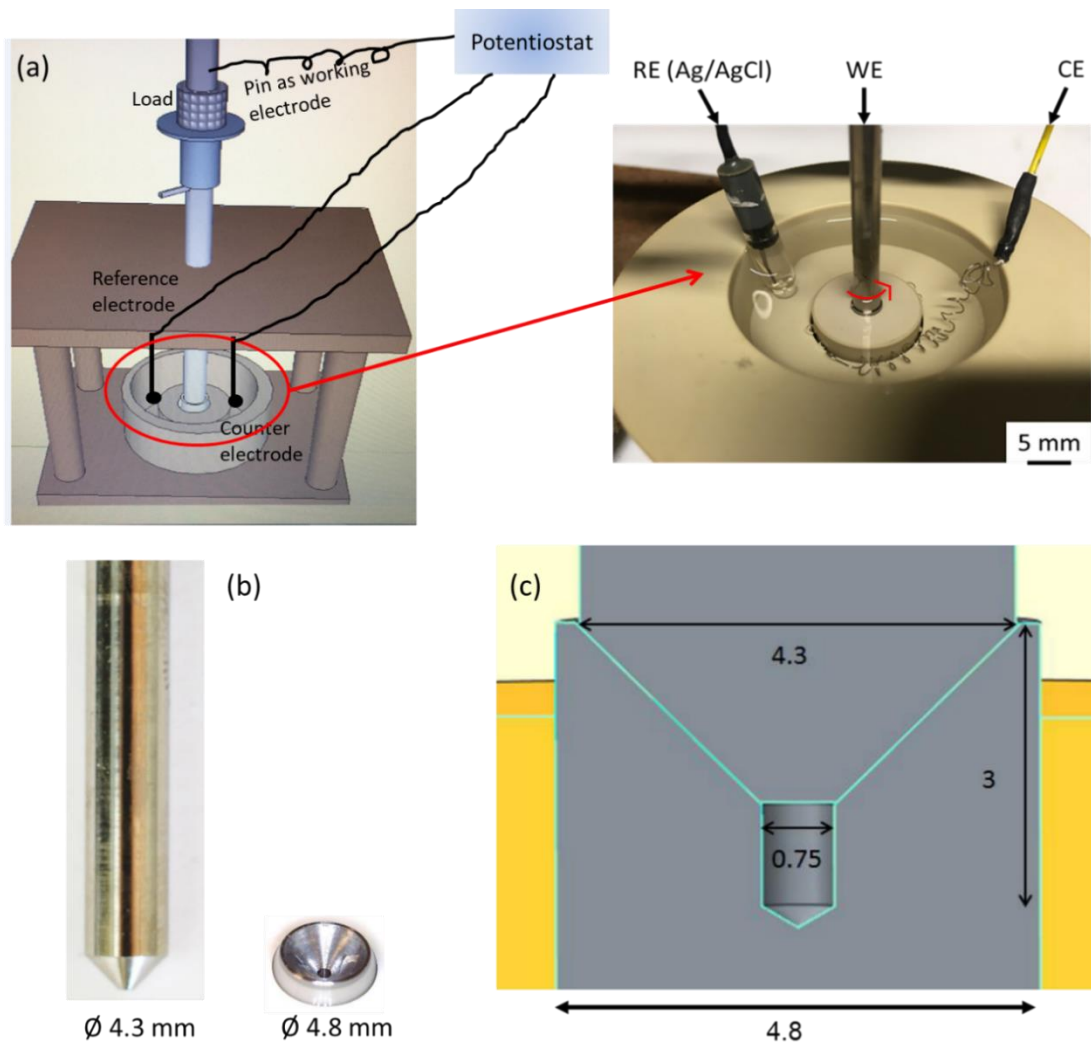


Figure 3-3 (a) Schematic diagram of MACC device and photograph of the electrochemical cell. (b) Photograph of separate pin and cup. (c) The cross-section drawn of coupled pin and cup.

3.8 Calculation of charge transfer

The charge passing through the sample surface was calculated from potentiostatic measurements by integration of the current with time ($Q = \int_0^t I dt$). Because the data are individual points rather than a continuous function, the integration method used is trapezoidal numerical integration. The calculation was performed in Matlab R2018a, and the script can be found in Appendix.

3.9 Statistical analysis

A two-way analysis of variance (ANOVA) was used to identify differences in E_{corr} and E_{pit} between sample groups where the factors were Ga content (at 6 levels) and manufacturing route (at two levels). Subsequently two-sample t-tests were used to identify significant differences in E_{corr} and E_{pit} between samples of identical composition but manufactured by melt-spinning or mould-casting. The statistical method to evaluate the effect of albumin addition during MACC simulation was a repeated measure ANOVA with a Greenhouse-Geisser correction. Statistical analyses were conducted in SPSS v25 software (IBM Corp, USA) at $\alpha = 0.05$.

4 Effect of albumin and H₂O₂ on corrosion of

Ti₄₀Zr₁₀Cu₃₄Pd₁₄Sn₂

4.1 Introduction

Serum albumin is the most common protein in extracellular fluid, and it adheres to metallic implants quickly [192, 193]. Hydrogen peroxide (H₂O₂) can be used to simulate the reactive oxygen species that are produced by immune cells during inflammation, which is associated with local infection or implantation surgery [9]. Previous studies illustrate that both H₂O₂ and albumin have effects on corrosion of Ti [13, 194] and Cu [178]. Based on this, it is likely that the presence of H₂O₂ and albumin may also modify the corrosion behaviour of BMG_Sn2 (Ti₄₀Zr₁₀Cu₃₄Pd₁₄Sn₂). It is imperative to understand how the corrosion resistance would be modified by these chemical species before implantation. In this chapter, BMG_Sn2 was tested electrochemically in NaCl solutions containing H₂O₂ and/or albumin. Subsequently, all the constituent elements were tested with same procedures. Although it has been reported that Ti and Zr tend to passivate the metal surface [15, 140], it is still necessary to study all constituent elements for the sake of understanding of its dealloying process once the passive film is ruptured.

4.2 Characterisation of as-received materials

Figure 4-1 shows only one single broad peak at 43° indicating the amorphous structure of BMG_Sn2. The SEM image in Figure 4-2 is a typical area on the as-polished sample surface, where no phases or crystalline features can be observed. The scratch or sunken points were left by grinding and polishing.

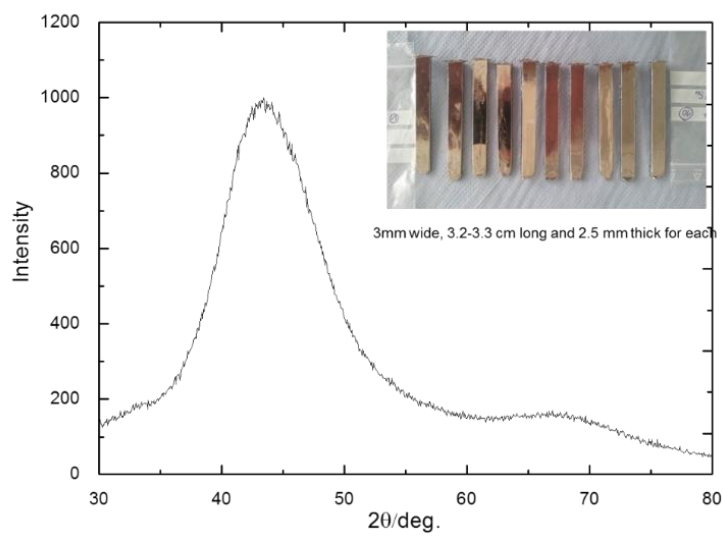


Figure 4-1 XRD pattern of as-polished BMG_Sn2, with CuK α radiation ($\lambda=1.54 \text{ \AA}$). The insert picture is the appearance of as-sectioned BMG_Sn2.

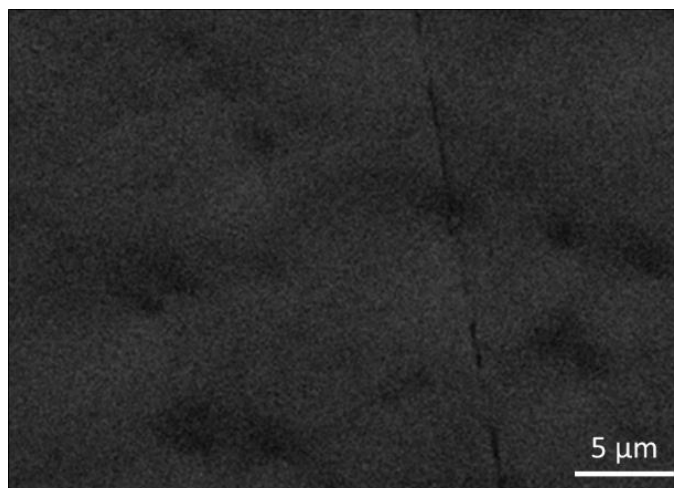


Figure 4-2 SEM image of the as-polished surface of BMG_Sn2, some sunken points and scratches were left by polishing.

Table 4-1 shows the measured composition of as-polished surface of BMG_Sn2. The compositions of the sample were deemed acceptable for this study.

Table 4-1 Nominal composition and surface composition measured by EDX of BMG_Sn2 samples, all values are in at.%

Sample code	Composition	Ti	Zr	Cu	Pd	Sn
BMG_Sn2	Ti40Zr10Cu34Pd14Sn2	39 ± 1.5	10 ± 1	32 ± 1	17 ± 2	2 ± 0.3

4.3 OCP and repassivation

Figure 4-3 shows the OCP of BMG_Sn2 in 0.9 wt.% NaCl solution, one measurement lasted for 5 hours and the other one only lasted for 1 hour. It shows the OCP increases with time at the first 3600s then the potential varies in a narrow range (≈ 30 mV vs SCE) due to the passive film reaches a relatively stable state in this situation. Thereby, the period of OCP measurements hereafter was set as 3600s.

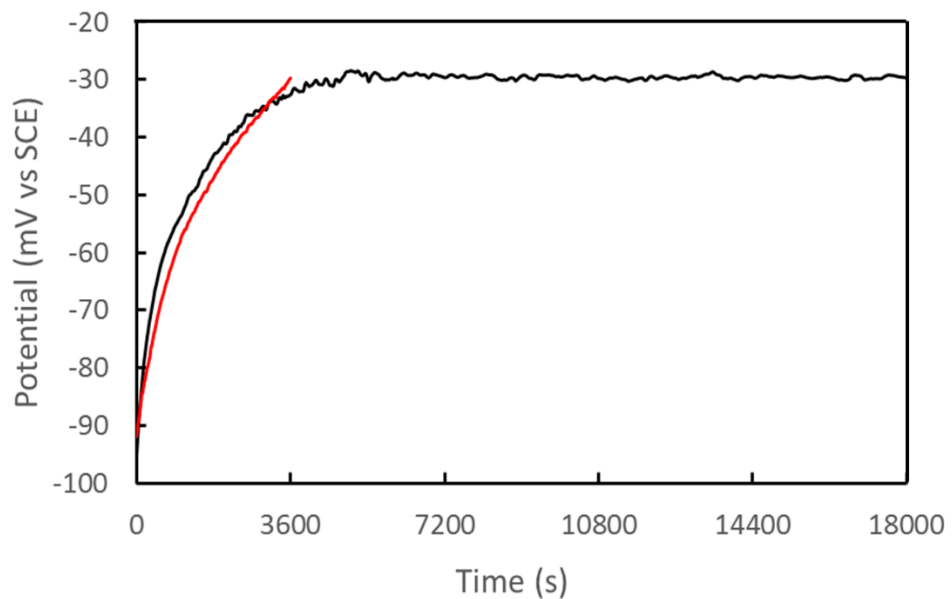


Figure 4-3 OCP measurements of BMG_Sn2 in 0.9 wt.% NaCl at 37 °C lasting for 3600s and 18000s.

Figure 4-4 shows the anodic polarisation curve of BMG_Sn2 in 0.9 wt.% NaCl solution. The sweep potential, as indicated by the arrows, started at -50 mV vs OCP, then it reversed from pitting potential (426 mV vs SCE) and was terminated at repassivation potential (81 mV vs SCE).

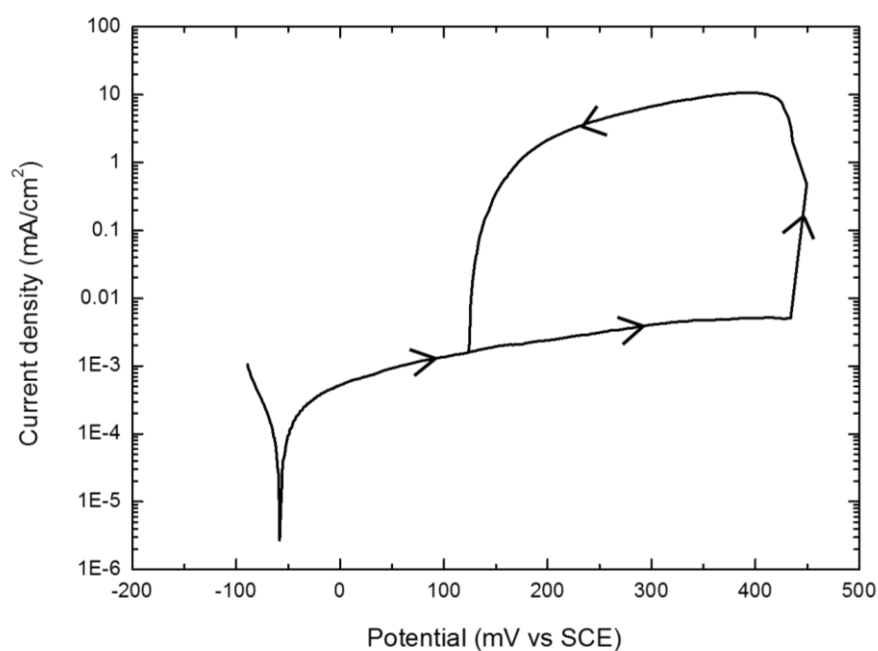


Figure 4-4 Anodic cyclic potentiodynamic polarization curve of BMG_Sn2 in 0.9 wt.% NaCl at 37 °C. Arrows indicate the direction of the scan.

4.4 Effect of albumin on $\text{Ti}_{40}\text{Zr}_{10}\text{Cu}_{34}\text{Pd}_{14}\text{Sn}_2$

Figure 4-5 (a) shows the OCP values of BMG_Sn2 in 0.9 wt.% NaCl (PS) and 0.9 wt.% NaCl+4 wt.% bovine serum albumin (PS+A) solution at 37 °C. Each experimental condition was tested three times to attain good reproducibility. The presence of albumin consistently decreases OCP in PS.

Immediately after the OCP measurement, anodic or cathodic polarisation tests were carried out. Figure 4-5 (b) and (c) show the anodic and cathodic polarisation curves of BMG_Sn2 respectively. (b) shows the anodic current density in PS+A is larger than that in PS at early stage, then the difference gets increasingly smaller with increasing potential.

The cathodic polarisation curves of BMG_Sn2 are shown in Figure 4-5 (c). In PS, the cathodic current firstly increases with a more negative potential, and then it approaches a plateau, where the current density is approximately 0.1 mA/cm², consistent with reduction of oxygen under diffusion control. A further current density increase appears around -900 mV vs SCE, which is hydrogen evolution.

Figure 4-5 (c) also shows the cathodic current density in PS+A is smaller than that in PS from OCP to the plateau region, this is consistent with the idea that albumin suppresses the cathodic reaction of BMG_Sn2 so increases the net anodic current density close to OCP. The significantly smaller cathodic current density in PS+A also explains the smaller OCP in PS+A.

The pitting potential (E_{pit}) difference in PS and PS+A is noticeable, as shown in Figure 4-5 (b), the E_{pit} in PS+A is consistently higher than that in PS. One hypothesis could be made that albumin inhibits both the anodic and cathodic reactions of BMG_Sn2, but the inhibition on cathodic reaction is more significant than that on anodic reaction. This can explain that the net anodic reaction in PS+A seems to be higher, but the presence of albumin still postpones the occurrence of pitting.

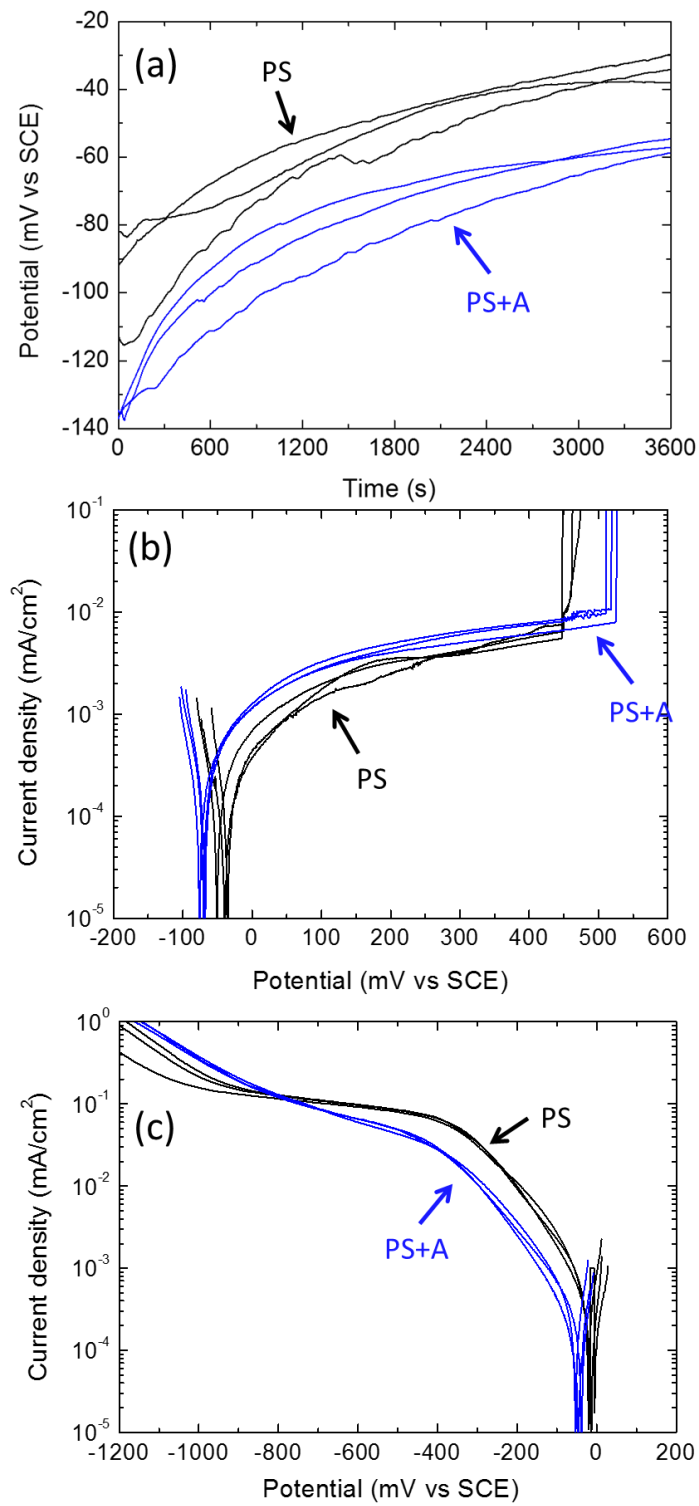


Figure 4-5 (a) OCP (b) Anodic (c) Cathodic polarisation curves of BMG_Sn2 measured in PS (0.9% NaCl) and PS+A (0.9% NaCl+4% albumin). Sweep rate: 1 mV/s.

4.5 Effect of H₂O₂ on BMG_Sn2

Figure 4-6 (a) shows the effect of H₂O₂ on corrosion of BMG_Sn2 by conducting measurements in 0.9 wt.% NaCl (PS) and 0.9 wt.% NaCl+ 0.1 wt.% H₂O₂ (PS+P). Figure 4-6 (a) shows the OCP of BMG_Sn2 in PS and PS+P is significantly different. The OCP in PS+P is much more positive than that in PS.

Figure 4-6 (b) and (c) show the anodic and cathodic polarisation curves respectively. The cathodic polarisation curves show that the cathodic current density in PS+P is substantially higher than that in PS. The cathodic reaction in PS+P is dominated by the H₂O₂ reduction reaction, while the cathodic reaction in PS is dominated by the O₂ reduction followed by H₂O reduction. It is clear that reduction of H₂O₂ happened more readily than that of O₂. The larger cathodic current in PS+P is consistent with the higher OCP.

The anodic current density of BMG_Sn2 in PS+P shows a sharper increase than that in PS. This is the same as we expected because from the thermodynamic view oxidation of H₂O₂ in the current potential range should happen. Thereby, it is not reasonable to draw the conclusion that peroxide increases the anodic reaction of BMG_Sn2 (oxidation of BMG_Sn2) because of the strong effect of the oxidation and reduction of peroxide itself. It is very interesting to observe that H₂O₂ does not modify the E_{pit} of BMG_Sn2 since H₂O₂ has such significant effect on anodic and cathodic reactions.

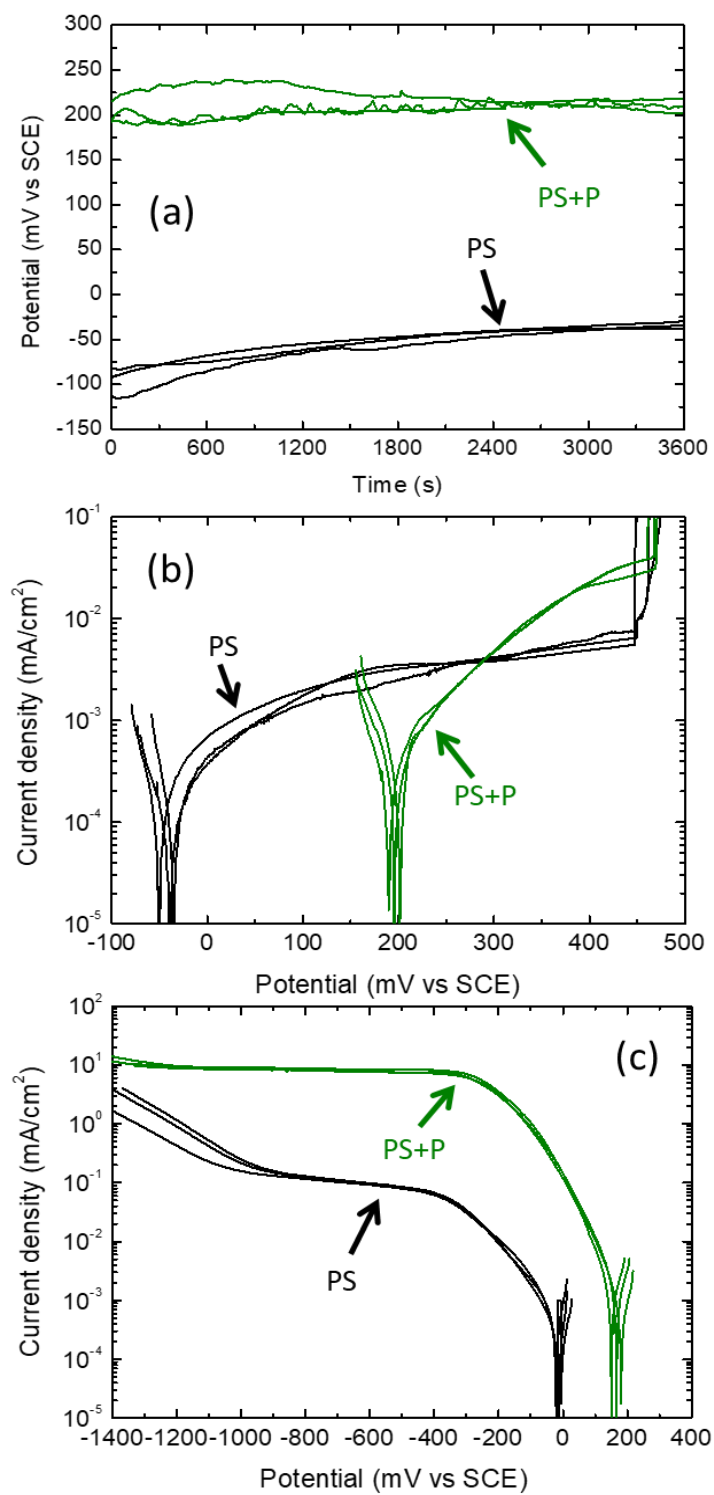


Figure 4-6 (a) OCP, (b) Anodic (c) Cathodic polarisation curves of BMG_Sn2 measured in PS (0.9% NaCl) and PS+P (0.9% NaCl+0.1% hydrogen peroxide). Sweep rate: 1 mV/s.

In order to examine the oxidation and reduction of peroxide on an inert surface, Pt was used as the working electrode to study the decomposition process of H_2O_2 . The anodic and cathodic polarisation curves are shown in Figure 4-7. It is interesting to note that the net anodic current density of BMG_Sn2 is larger than that of Pt. This may suggest that both oxidation of BMG_Sn2 and H_2O_2 may be taking place on BMG_Sn2 in PS+P. However, it is also possible that Pt is a better cathode for the reduction of H_2O_2 , so the apparently lower current density on Pt may be the sum of the anodic reaction and the enhanced cathodic reaction.

Figure 4-7 (b) shows the cathodic curves of Pt and BMG_Sn2 in PS+P. The net cathodic current of Pt is larger than that of BMG_Sn2 at the beginning then reaches the same plateau from -300 mV vs SCE. The larger cathodic current on Pt may indicate it is a better catalyst than BMG_Sn2 for H_2O_2 .

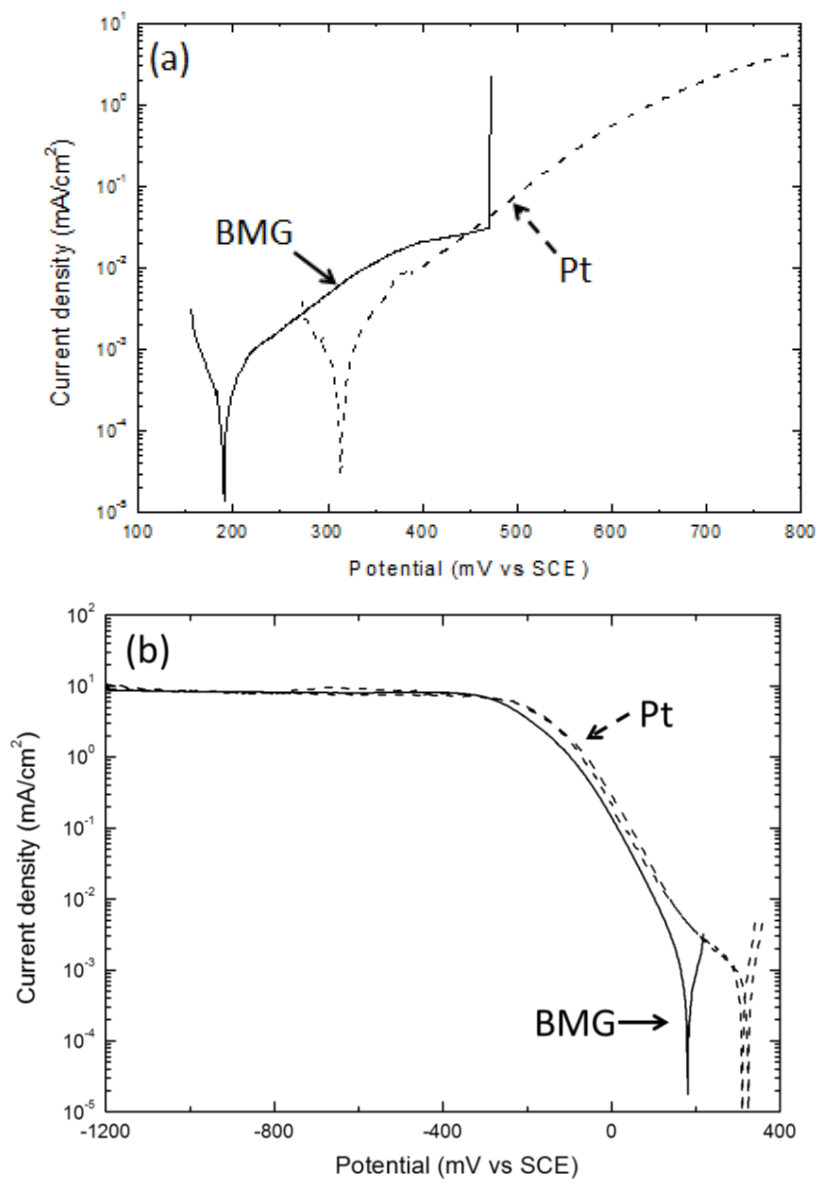


Figure 4-7 (a) Anodic and (c) cathodic polarisation curves of Pt (dashed line) and BMG_Sn2 (solid line) in PS+P (0.9% NaCl+0.1% hydrogen peroxide). Sweep rate: 1 mV/s.

4.6 Effect of albumin in H₂O₂-containing solution

In the solution containing both albumin and H₂O₂ (PS+A+P) (Figure 4-8 a), the OCP of BMG_Sn2 showed a gradual increase from -170 mV to -250 mV vs SCE. The OCP values were similar to those of PS+P at early stages but by the end of the test, the OCP for (PS+A+P) was slightly higher than that for (PS+P). The higher OCP in the presence of albumin can also be seen in the anodic polarisation curve (Figure 4-8 b) and the cathodic polarisation curve (Figure 4-8 c).

The anodic polarisation curves shown in Figure 4-8 b show a higher pitting potential for (PS+A+P) compared with (PS+P), suggesting that albumin inhibits pitting, and is consistent with the effect shown in Figure 4-5 b for PS with and without albumin in the absence of peroxide. The current density just below the pitting potential is lower in the presence of albumin.

Figure 4-8 (b) shows that the presence of albumin suppresses the anodic current. This is different from Figure 4-5 which shows that albumin seems to increase the anodic current. As stated, this was attributed to the effect of albumin in suppressing the cathodic reaction, leading to a higher net anodic current.

Figure 4-8 (c) shows the cathodic current density in PS+A+P is slightly lower than that in PS+P in the diffusion-limited plateau, which indicates albumin may inhibit the cathodic reaction of H₂O₂ and/or BMG_Sn2. However, closer to OCP, net cathodic current in PS+P is lower than that in PS+A+P. This may be explained by the fact that in

the presence of H_2O_2 , albumin inhibits both anodic and cathodic reactions of H_2O_2 and/or BMG_Sn2, but close to OCP, inhibition of anodic reaction dominates, leading to a higher net cathodic reaction and slightly higher OCP.

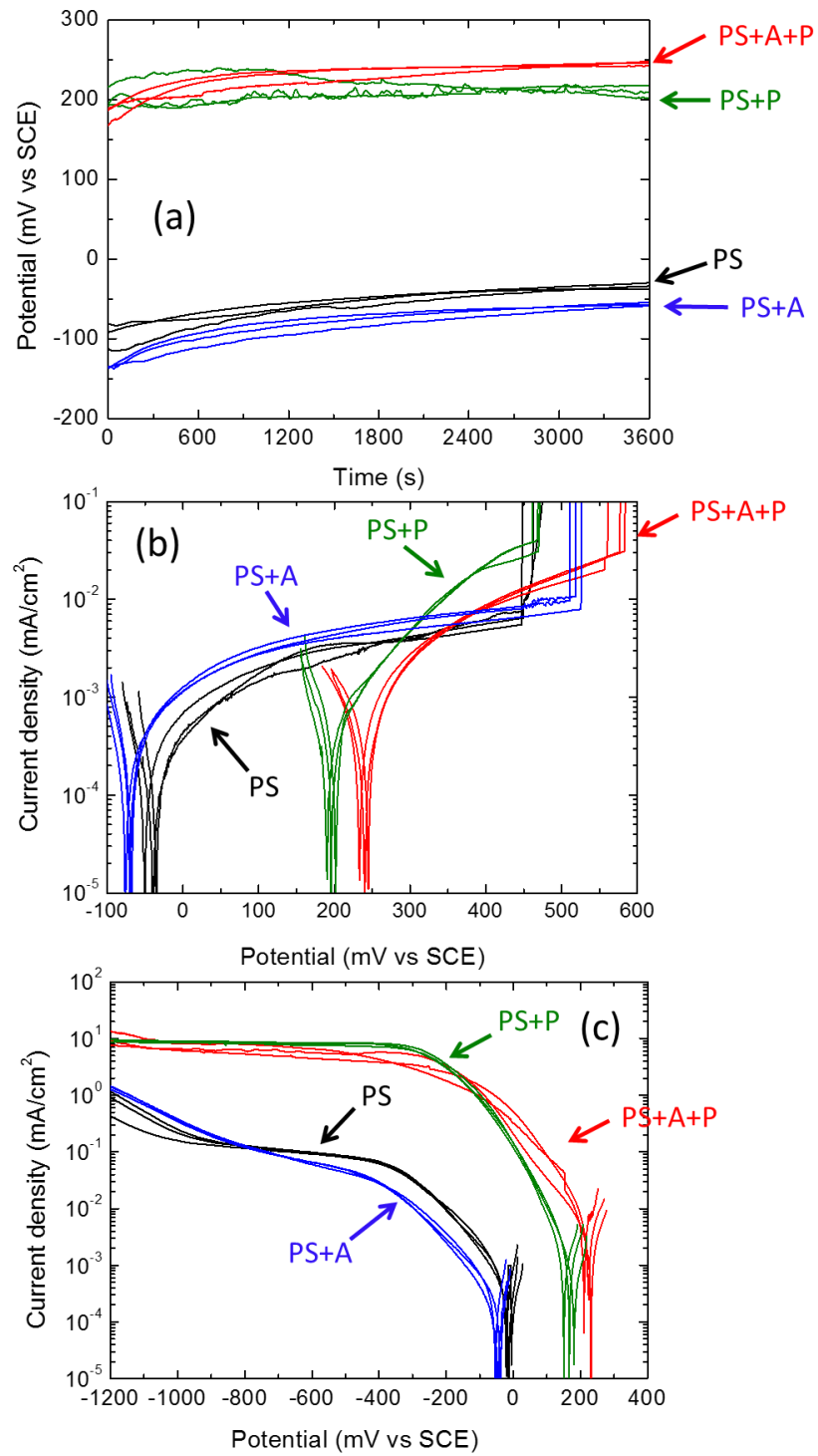


Figure 4-8 OCP measurement for BMG_Sn2 measured in PS (0.9% NaCl), PS+P (0.9% NaCl+0.1% hydrogen peroxide), PS+A (0.9% NaCl+4% albumin) and PS+A+P (0.9% NaCl+4% albumin+0.1% hydrogen peroxide). Sweep rate: 1 mV/s.

4.7 Effect of peroxide ±albumin on main constituent elements

4.7.1 Titanium and zirconium

Anodic and cathodic polarisation curves of CP-Ti were also measured followed by OCP (Figure 4-9). The presence of albumin in PS does not alter the anodic reaction, whereas it suppresses the cathodic reaction significantly. Clearly, the lower OCP with presence of albumin is caused by the slower cathodic reaction.

Again, the presence of albumin in PS+P suppresses both the anodic reaction and cathodic reaction of H_2O_2 and/or Ti. The net anodic current just above OCP in PS+A+P is larger, which may be due to the inhibition of cathodic reaction dominating, leading to a larger net anodic reaction and lower OCP.

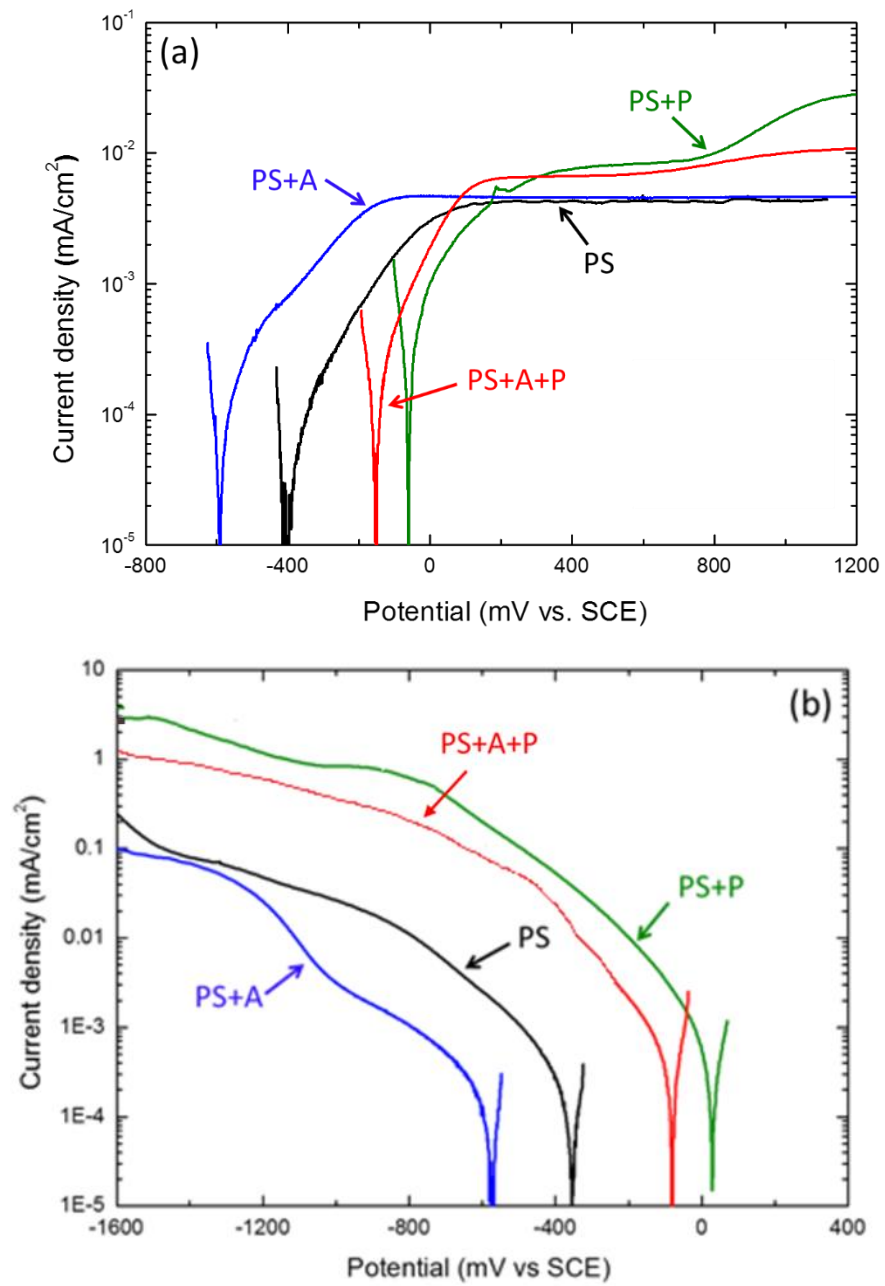


Figure 4-9 (a) Anodic (b) Cathodic polarisation curves of CP-Ti in PS (0.9% NaCl), PS+P (0.9% NaCl+0.1% hydrogen peroxide), PS+A (0.9% NaCl+4% albumin) and PS+A+P (0.9% NaCl+4% albumin+0.1% hydrogen peroxide). Sweep rate: 1 mV/s.

Anodic and cathodic polarisation curves of CP-Zr are shown in Figure 4-10 (a) and (b) respectively. The presence of albumin suppressed cathodic reaction significantly in PS, which is similar to Ti. However, it seems that the presence of albumin had a very little effect in PS+P. Both anodic and cathodic curves in PS+P and PS+A+P are similar.

In addition, significant pitting (E_{pit}) takes place on Zr in the potential range of 400 mV to 800 mV vs SCE in all test solutions. It worth noting that albumin in PS decreases the pitting susceptibility of Zr.

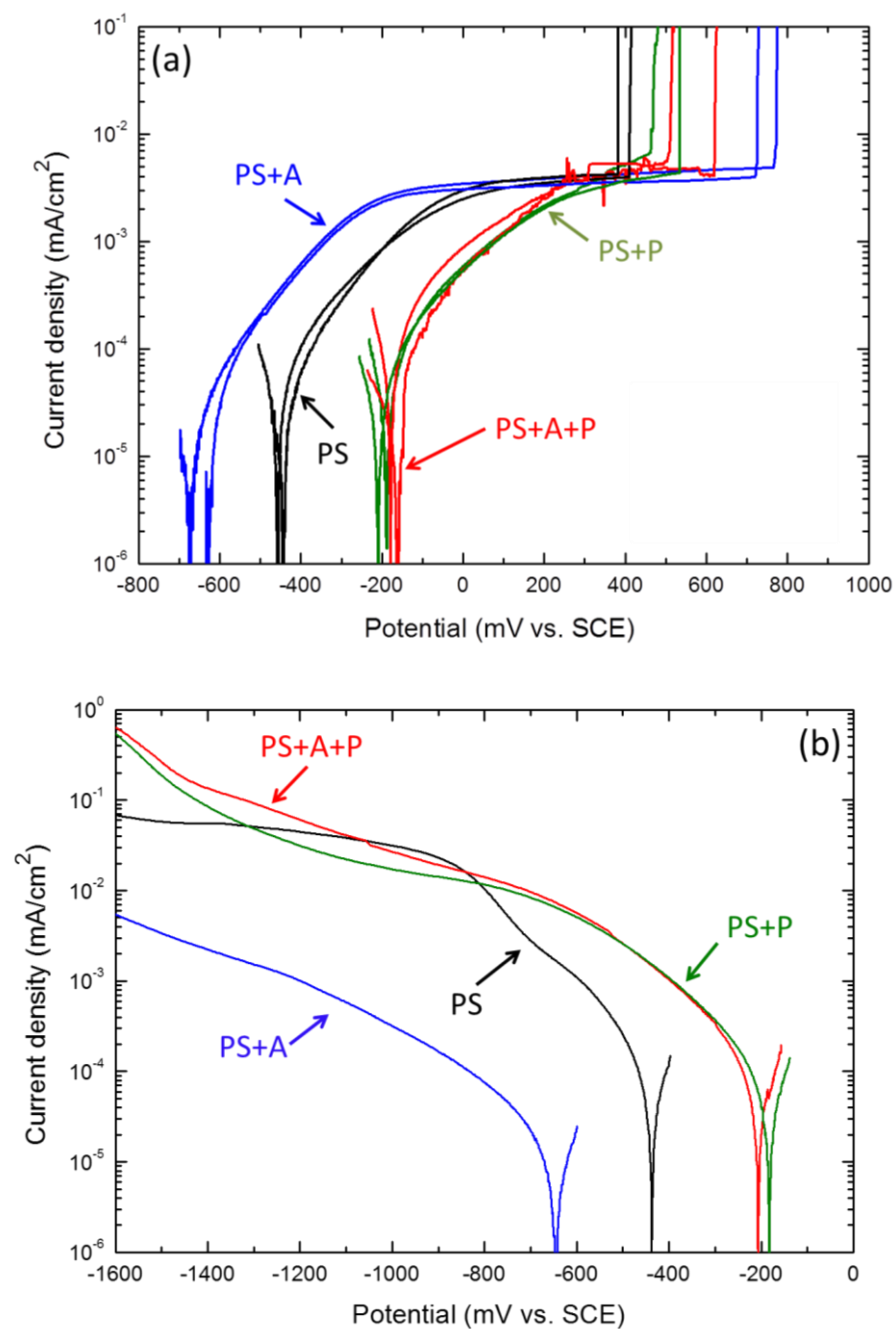


Figure 4-10 (a) Anodic (b) Cathodic polarisation curves of CP-Zr in PS (0.9% NaCl), PS+P (0.9% NaCl+0.1% hydrogen peroxide), PS+A (0.9% NaCl+4% albumin) and PS+A+P (0.9% NaCl+4% albumin+0.1% hydrogen peroxide). Sweep rate: 1 mV/s.

4.7.2 Copper

Figure 4-11 shows the anodic and cathodic curves of Cu in test solutions.

The anodic current densities of Cu were 1 mA/cm²- 10 mA/cm², which were hundreds of times larger than that of Ti or Zr (10⁻³ mA/cm²- 10⁻² mA/cm²). The presence of peroxide in PS did not give significant increase of anodic current, but it increased cathodic current due to the reduction reaction of peroxide. The presence of albumin reduced anodic current in both PS and PS+P, and addition of albumin and peroxide reduced anodic current densities further compared with that in PS only.

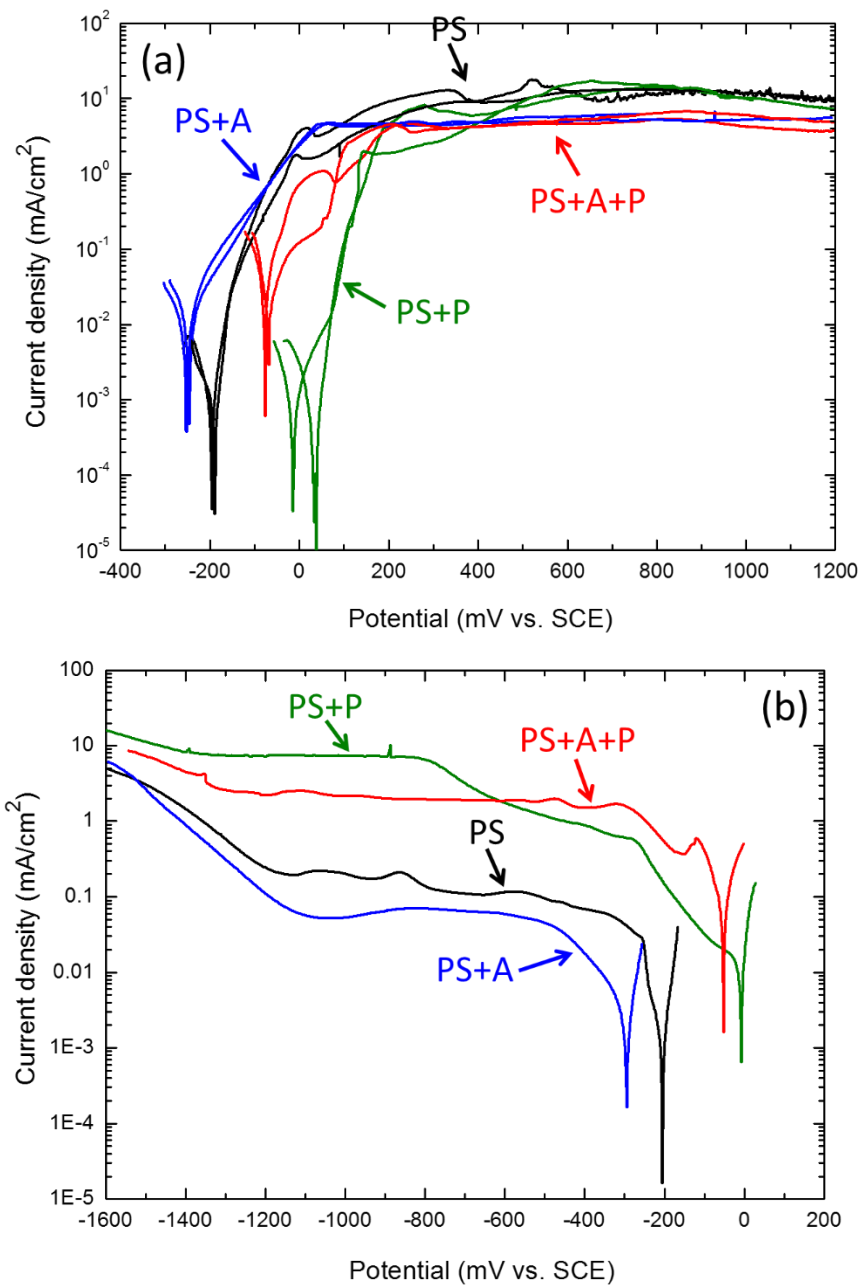


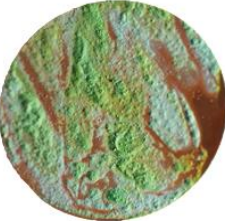



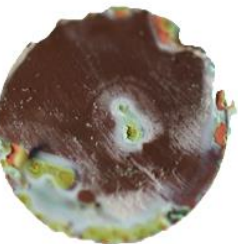


Figure 4-11 (a) Anodic (b) Cathodic polarisation curves of pure Cu in PS (0.9% NaCl), PS+P (0.9% NaCl+0.1% hydrogen peroxide), PS+A (0.9% NaCl+4% albumin) and PS+A+P (0.9% NaCl+4% albumin+0.1% hydrogen peroxide). Sweep rate: 1 mV/s.

Apart from the polarisation tests, the surface changes after being tested in different solutions also drew our attention. As seen in Table 4-2, the as-polished copper showed a reddish-brown colour. After being tested in PS, the surface colour of copper became darker and slightly green. Some corrosion products as well as pits were discernible on the surface. The solution (PS) turned to light green from clear. After being tested in PS+P, the surface of copper also showed a significant change with most of the surface covered with a green scale, which was hard to rinse off. At same time, PS+P also turned from clear to green. For the sample tested in PS+A, the surface of copper seemed to be covered by a loose white layer, most of which could be easily flushed away by DI water. The solution became clear from light yellow, which makes sense as quite a large amount of albumin was adhering on metal surface. In this case, the copper surface was well-protected under this albumin layer since no trace of corrosion products or pits could be observed on Cu surface. This white layer may be some Cu(II)-amino acid complex [195, 196]. In the solution containing albumin and peroxide, the surface condition seemed to be the combination of that in PS+A and PS+P. It was, on the one hand, attacked by peroxide and on the other, protected by albumin. Thereby the surface was heterogeneous, possessing regions with an albumin layer and regions with evidence of corrosion attack.

Table 4-2 Surface morphology of Cu-rod after being anodically polarised (-50 mV vs OCP to 1200 mV vs SCE) in different solutions, surface area is 2 cm².

Solution	Surface morphology after anodic polarisation	Wash the adherent foam off	Solution colour
As-polished			
PS			Clear to light green
PS+P			Clear to green
PS+A			Light yellow to clear
PS+A+P			Light yellow to clear

4.7.3 Palladium

Figure 4-12 shows the OCPs of Pd are much higher than those of BMGs, indicating the high thermodynamic stability of Pd in test solutions.

It seems albumin suppresses the cathodic reaction of H_2O_2 , which gives higher net anodic reaction at low potential, but albumin suppresses H_2O_2 oxidation at higher potential.

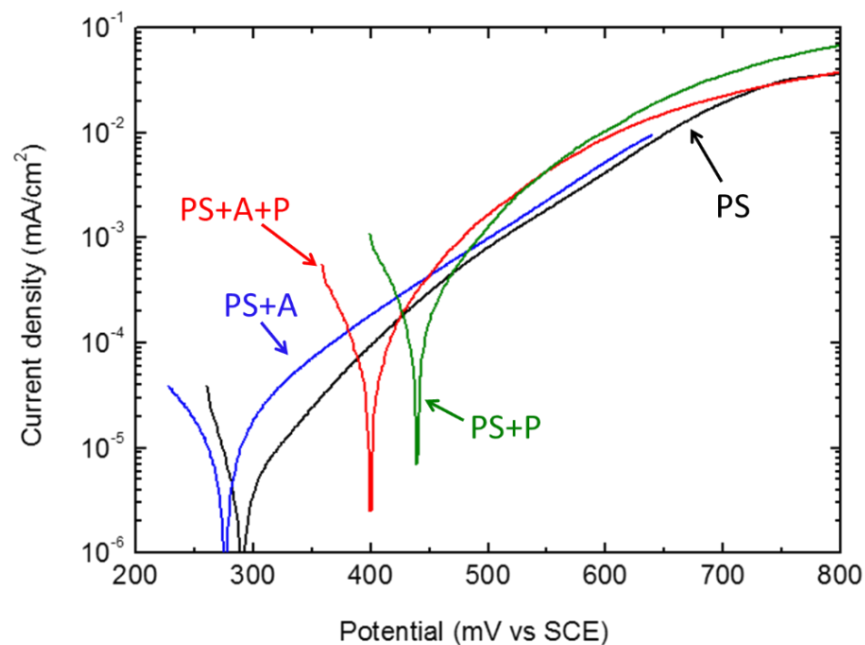


Figure 4-12 Anodic polarisation curves of Pd in PS (0.9% NaCl), PS+P (0.9% NaCl+0.1% hydrogen peroxide), PS+A (0.9% NaCl+4% albumin) and PS+A+P (0.9% NaCl+4% albumin+0.1% hydrogen peroxide). Sweep rate: 1 mV/s.

4.7.4 Tin

In contrast, as shown in Figure 4-13, the OCPs of Sn are much lower than those of BMGs, indicating that Sn is in active dissolution state at OCP of BMG_Sn2.

The current densities after pitting are not accurate since the surface of tin was corroded badly and the areas of the rough surfaces were difficult to estimate precisely.

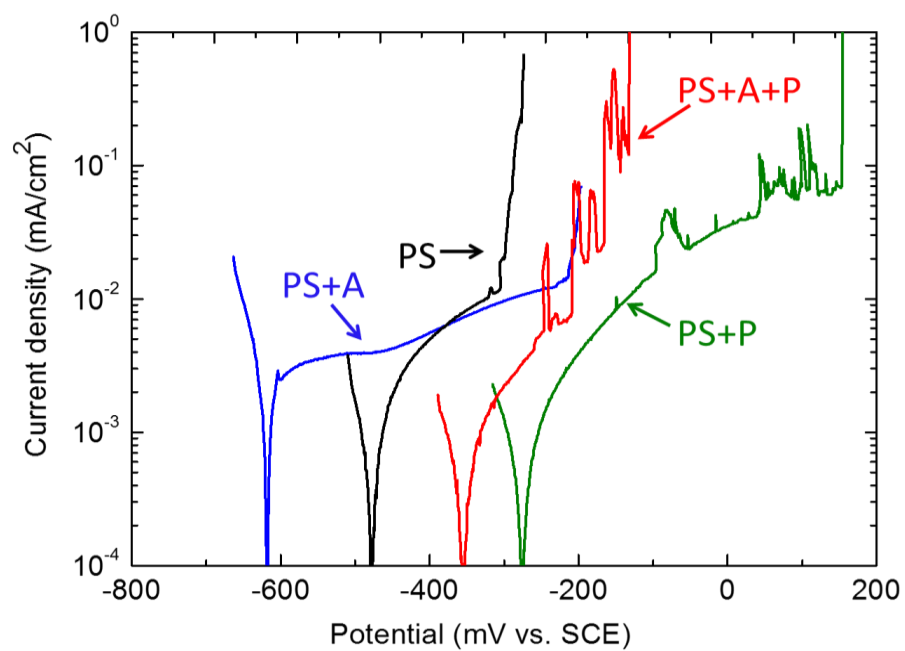


Figure 4-13 Anodic polarisation curves of Sn in PS (0.9% NaCl), PS+P (0.9% NaCl+0.1% hydrogen peroxide), PS+A (0.9% NaCl+4% albumin) and PS+A+P (0.9% NaCl+4% albumin+0.1% hydrogen peroxide). Sweep rate: 1 mV/s.

4.7.5 Corrosion potentials of constituent elements

The open circuit potential of all constituent elements (Ti, Zr, Cu, Pd and Sn) was extracted from their polarisation curves and shown in Figure 4-14. For comparison, the corrosion potential of BMG_Sn2 was also put in the same figure. It shows that in the potential range of BMG_Sn2, Ti and Zr are in the passive state but Cu and Sn are in active dissolution due to lower corrosion potentials compared with BMG_Sn2. Pd stays as metallic Pd or slightly dissolves due to its higher corrosion potential.

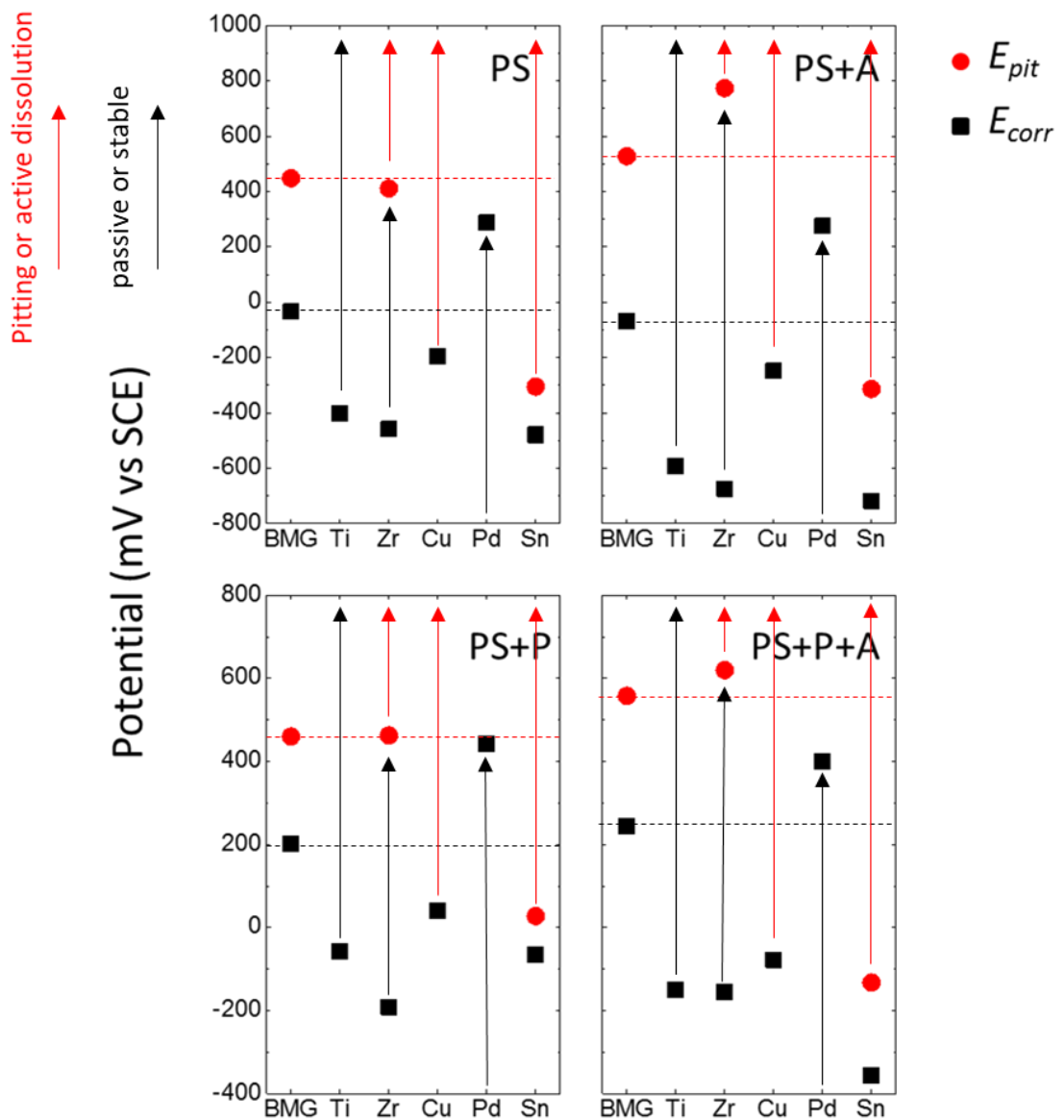


Figure 4-14 Corrosion and pitting potentials of all constituent elements, together with BMG_Sn2 in four test solutions (PS, PS+A, PS+P, PS+A+P). Dashed lines indicate the potential range of interest (E_{corr} to E_{pit}) of BMG_Sn2. Arrows indicate the state of constituent elements, the black arrows indicate the metals are in passive or stable state, and the red arrows indicate the metal are in pitting or active dissolution. The potential values (E_{corr} and E_{pit}) are extracted from anodic polarisation curves.

4.8 Pitting morphology and dealloying process

In order to view the morphology of pits at their early stage, the anodic current was stopped at a relatively low level, 2-3 mA/cm² in the anodic polarisation test. Figure 4-15, Figure 4-17, Figure 4-16 and Figure 4-18 show the pits at the initial stage in each test solution: PS, PS+A, PS+P and PS+A+P respectively.

In general, the pitting morphologies in different solutions are very similar. Inside the pit, the alloy was not uniformly corroded, and the remaining alloys are flake-shaped with micro-sized cracks (as shown by red arrows in Figure 4-15 c). There are also some micro-scale alloy clusters presented in the pits (as shown by red arrows in Figure 4-15 d). In the pits formed in PS+A and PS+P (shown in Figure 4-17 and Figure 4-16), more metal clusters can be seen, and in the pits formed in PS+A+P, the flakes with cracks can be seen more clearly.

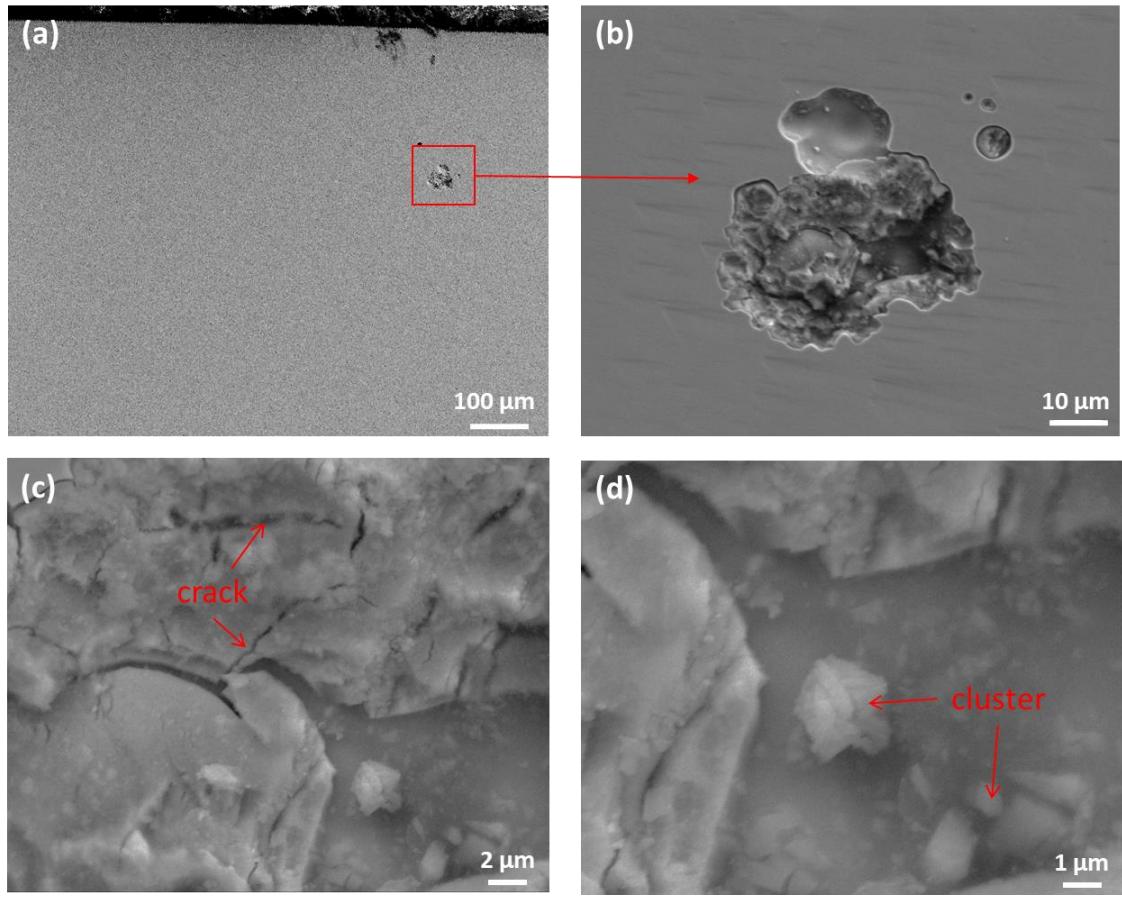


Figure 4-15 (a) Surface morphology of BMG_Sn2 after anodic polarisation test in PS at 37 °C, scanning rate: 1 mV/s, current was stopped at 3 mA/cm², (b)-(d) are the magnified view of pit in (a).

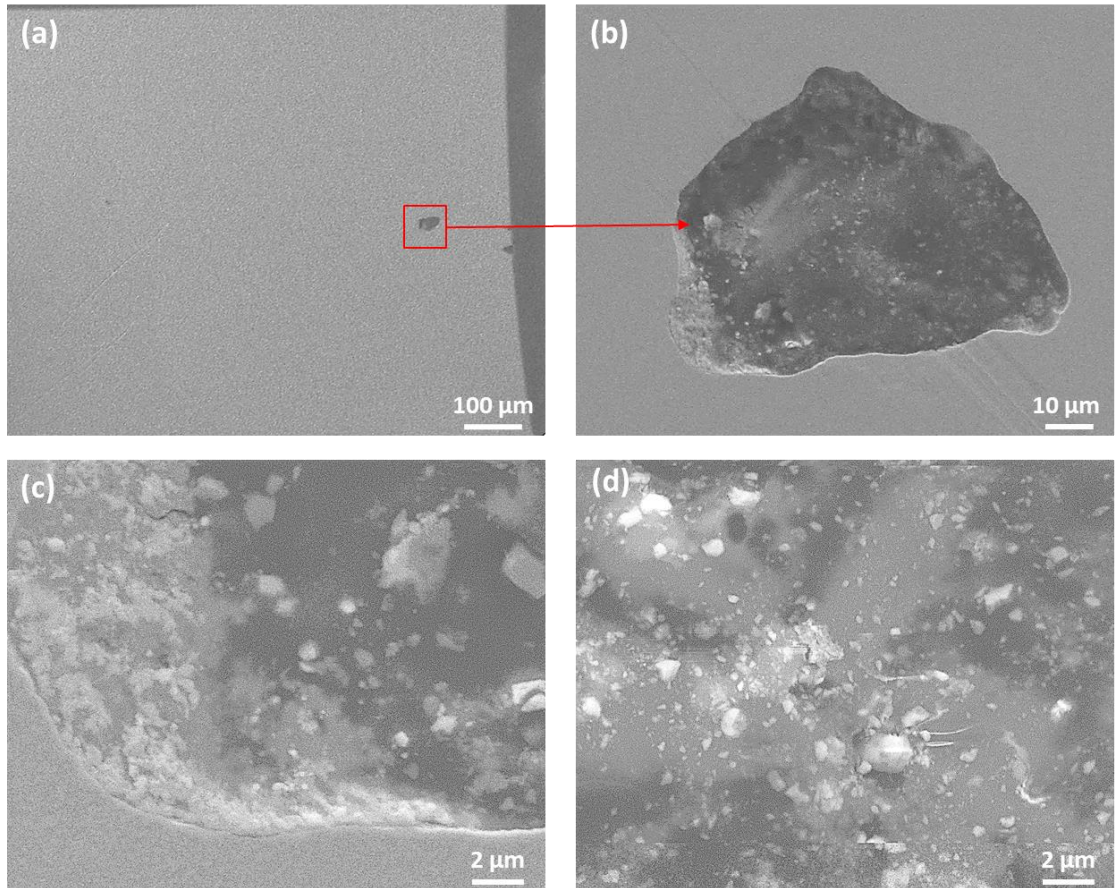


Figure 4-16 (a) Surface morphology of BMG_Sn2 after anodic polarisation test in PS+A at 37 °C, scanning rate: 1 mV/s, current was stopped at 3 mA/cm², (b)-(d) are the magnified view of pit in (a).

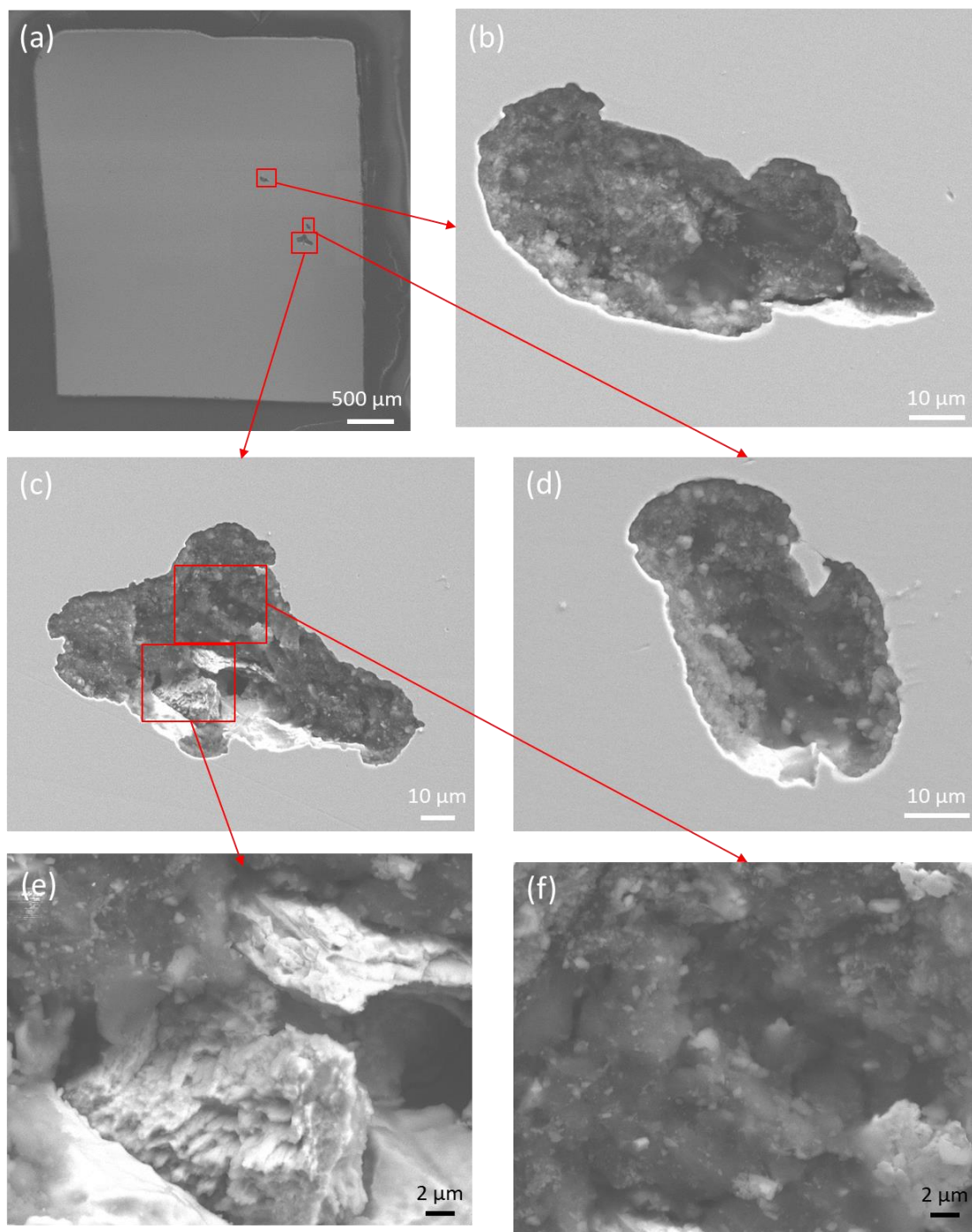


Figure 4-17 (a) Surface morphology of BMG_Sn2 after anodic polarisation test in PS+P at 37 °C, scanning rate: 1 mV/s, current was stopped at 3 mA/cm², (b)-(f) are the magnified view of pit in (a).

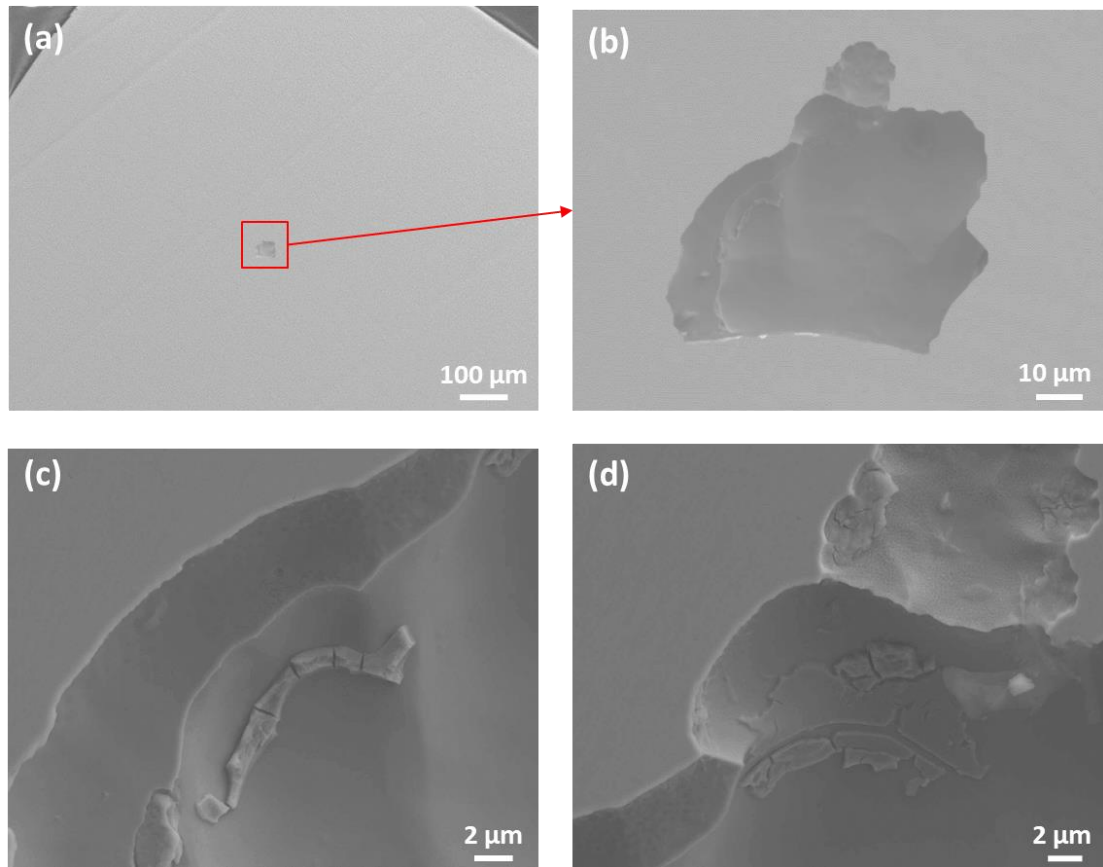


Figure 4-18 (a) Surface morphology of BMG_Sn2 after anodic polarisation test in PS+A+P at 37 °C, scanning rate: 1 mV/s, current was stopped at 2 mA/cm², (b)-(d) are the magnified view of pit in (a).

After viewing the pit morphologies, EDX was performed inside the pits to study the dealloying process at early stages of pitting. The compositional changes of the pit were identified by EDX and nine points were randomly picked in the pits shown in Figure 4-15 to Figure 4-18. The compositional changes inside the pits formed in different solutions are presented by the bar charts in Figure 4-19. The nominal composition is also shown by dashed bars for comparison. It shows that the elemental variation in the pits have the same trend in all test solutions in that Pd was enriched, O appeared and Ti, Zr, Cu were deficient. Sn did not give a consistent trend here, which is likely to be caused by its low atomic percentage. The average percentages of Ti and Cu in albumin-containing solution are higher than those not containing albumin. If we compare PS and PS+A or compare PS+P and PS+A+P. It implies that the presence of albumin, both in PS and PS+P, can stabilise Ti and Cu after pitting occurred. Figure 4-20 shows the normalised composition in absence of oxygen. Even more clearly, Cu content in PS+A+P is substantially higher than that in PS+P.

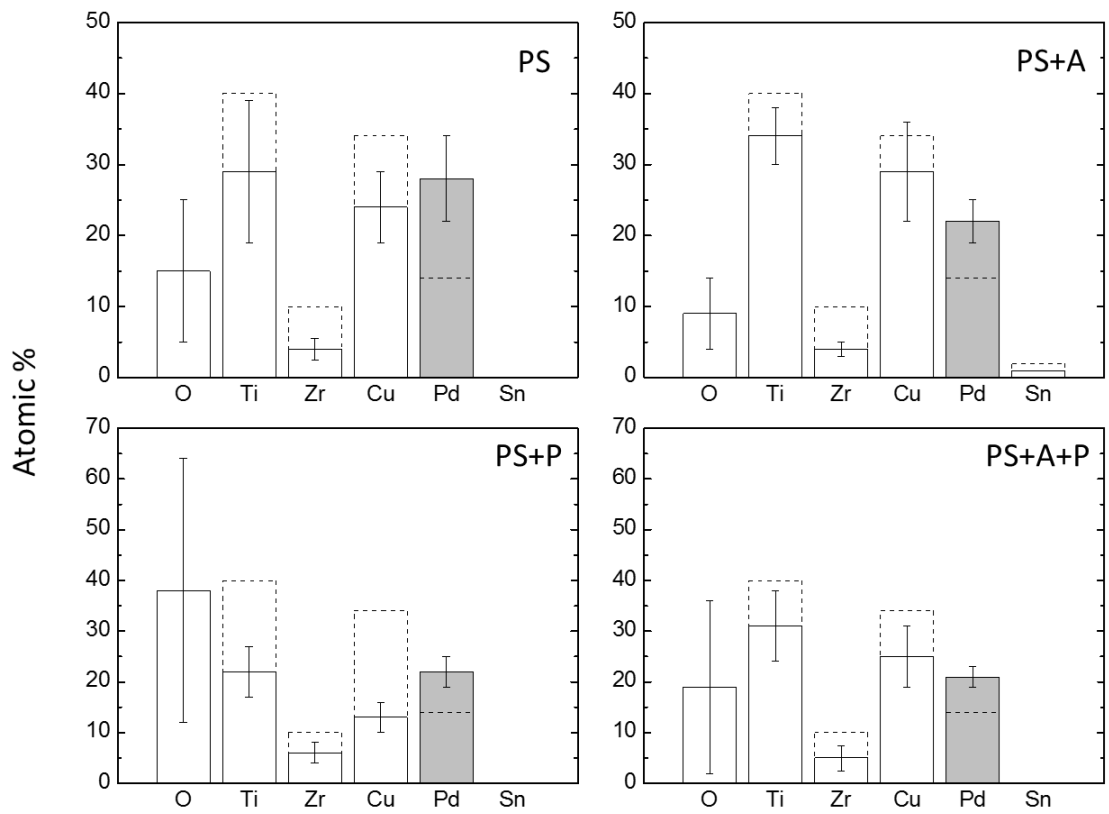


Figure 4-19 Elemental changes of BMG_Sn2 in the pit in different test solution after anodic polarisation test, stopped at 2-3 mA/cm². Dashed bar indicates the nominal composition and solid bar indicates the composition in the pit. Error bar is obtained by the standard deviation of nine EDX point-measurements. In all the test solutions, only Pd shows enrichment while other elements all show deficiency.

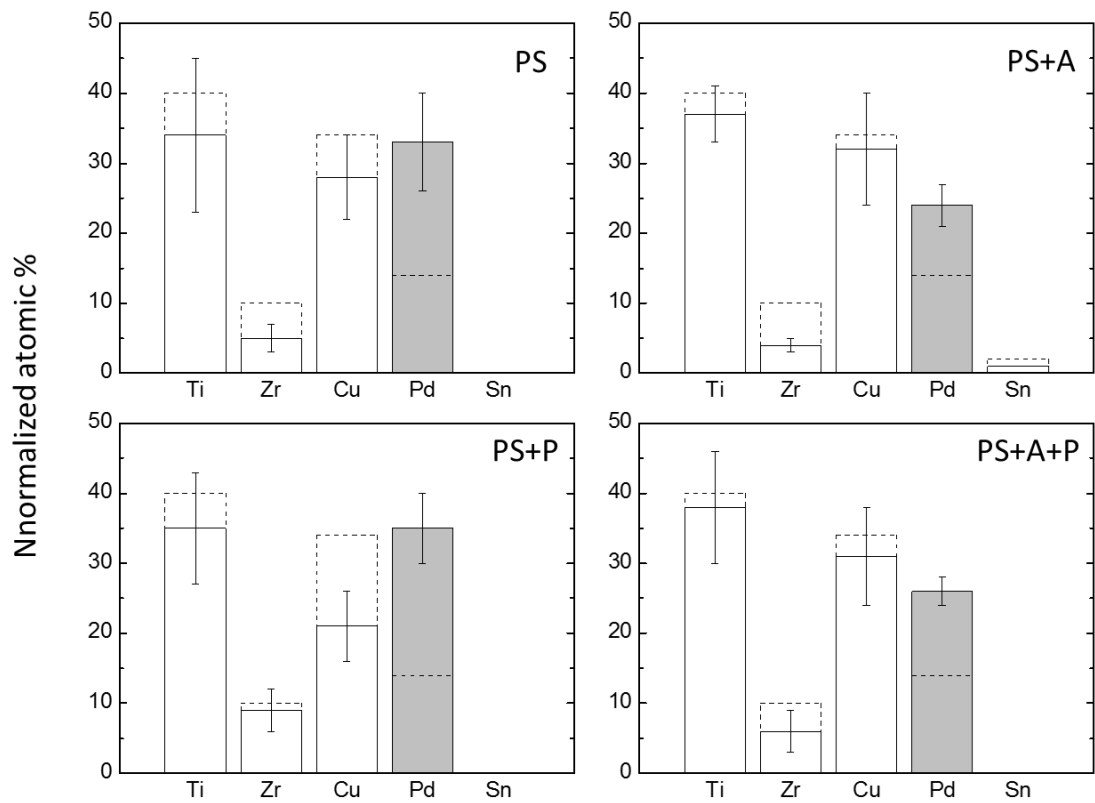


Figure 4-20 Normalised elemental changes (with oxygen ruling out) of BMG_Sn2 in the pit in different test solution after anodic polarisation test, stopped at 2-3 mA/cm². Raw data are extracted from Figure 4-19. Dashed bar indicates the nominal composition and solid bar indicates the composition in the pit. Error bar is obtained by the standard deviation of nine EDX point-measurements.

4.9 Discussion

4.9.1 Corrosion of Ti-Zr-Cu-Pd-Sn

As shown in Figure 4-14, Ti and Zr are in a passive state at the potential, while Cu and Sn suffer from massive dissolution, and Pd stays as Pd due to its high equilibrium potential [52], and the states of all these elements are consistent in all test solutions. The electrochemical diversity of the constituent elements results in BMG_Sn2 neither possessing the stable passive region like Ti nor suffering from massive metal dissolution like Cu. The current density of BMG_Sn2 before pitting is in the same magnitude as Ti and Zr, which is 10^{-3} - 10^{-2} mA/cm², but it keeps rising. This is probably due to the fact that active elements (Cu, Sn) destabilise the passive film, and accelerate the anodic reaction. The dominant elements at the interface however, should still be Ti and Zr, so the overall anodic current is limited to a low level. Similar finding was also reported in [197], in which, the metallic glass $Ti_{46}Cu_{27.5}Zr_{11.5}Co_7Sn_3Si_1Ag_4$ (A4) also possessed an unstable passive region in 0.9 wt.% NaCl. The nature of the amorphous structure benefits the formation of a uniform passive film, however, the addition of less noble elements may raise the anodic current by dissolving more. Consequently, the anodic current of metallic glass is dominated by passivation and is modified by other elements especially the active elements.

The cathodic reaction rate of BMG_Sn2 is higher than that of Ti, which may be due to the modification of the surface oxide layer by alloying elements. The passive film on $Ti_{40}Zr_{10}Cu_{36}Pd_{14}$ in air, measured by XPS was reported to be TiO_2 , ZrO_2 and a low

amount of Cu_2O [140]. AES profiles also indicate the enrichment of Ti and Zr in the oxide film after immersing in Hanks solution for 168 h [148]. It can be speculated that the alloying elements, and especially Cu, make the passive film less dense and more conductive so it allows easier access for oxygen to get electrons compared with the passive film of CP-Ti which predominantly consists of TiO_2 [198].

4.9.2 Alloying elements induce pitting

BMG_Sn2 is more susceptible to pitting compared with pure Ti. Among the constituent elements, only Zr gives similar pitting behaviour as the metallic glass, showing an abrupt large current with sweep potential. Consistent with previous work, Ti has quite a high pitting resistance, i.e. the E_{pit} of can reach as high as 10 V in 3% NaCl [199].

Based on the electrochemical behaviour of all the constituent elements, a reasonable assumption can be made that Zr and Cu inlay in Ti-oxides, forming the weak points in the passive film, which with the attack of chloride ions become the focus of breakdown, firstly occurring in areas with enriched Zr- and Cu-compounds. For a better comparison, the E_{pit} of Zr and the BMG in different solutions are summarised in Figure 4-21. It shows that E_{pit} of BMG and Zr correlate well, although some deviation is present in PS+A solutions. The deviation in PS+A may be owing to the amount of adsorbed albumin on the different metal surfaces, e.g. it was reported that only half the amount of albumin (100 ng/cm^2) can be adsorbed onto a ZrO_2 surface compared with a Ti surface (200 ng/cm^2) in PBS (pH=7.4) solution [200].

The elemental changes after pitting in the four solutions show good consistency. Ti, Zr and Cu were deficient and Pd was enriched. Similarly, Gostin et al. found that artificial pits on the bulk metallic glass $\text{Ti}_{40}\text{Zr}_{10}\text{Cu}_{34}\text{Pd}_{14}\text{Sn}_2$ in 0.9% NaCl were also enriched in Pd [149]. The in situ XRD and ex situ TEM/EDX revealed that the Pd enrichment was due to the presence of loose crystalline Pd rich nanoparticles which had accumulated inside the artificial pits, e.g. $80\pm 5\%$ Pd, 16 ± 10 nm particle size at 0.7 V vs Ag/AgCl. In our study, we did not attempt to resolve potential Pd nanoparticles.

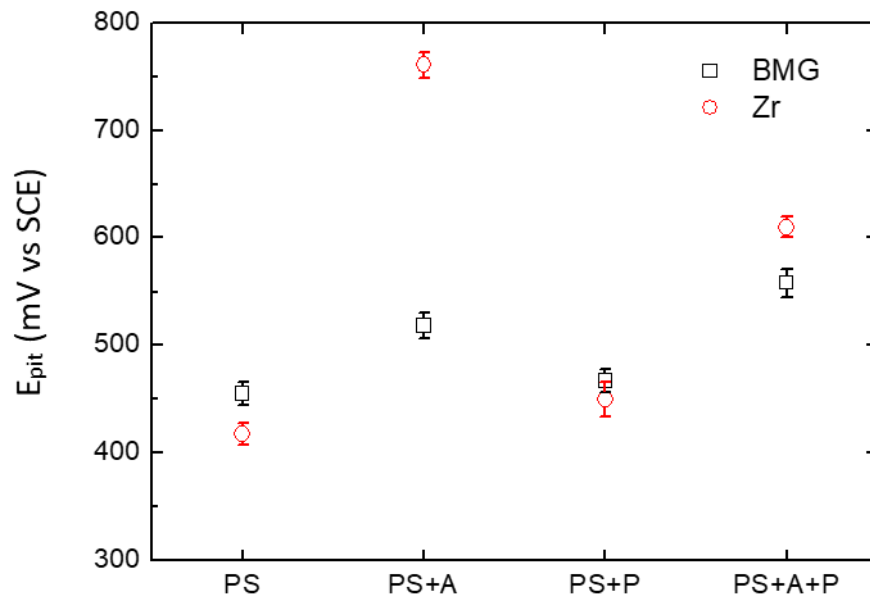


Figure 4-21 Comparison of pitting potential of BMG and CP-Zr in all test solutions. Values of E_{pit} are extracted from polarisation curve.

4.9.3 Effect of albumin

Albumin suppresses the cathodic reaction of BMG_Sn2 in physiological saline, causing a lower corrosion potential. The suppression of the cathodic reaction of BMG_Sn2 shows good agreement with that observed on Ti and Zr [76, 201] given the fact that the passive film of BMG_Sn2 predominately consists of Ti and Zr oxides [15, 140, 147]. Albumin adsorbs on the Ti and Zr surface and blocks the cathodic reaction [13, 75]. The increase in net anodic current density may have resulted from a significantly suppressed cathodic reaction, together with the fact that albumin causes little effect on the anodic reaction on Ti and Zr [202] (also seen in section 4.6.1). The presence of albumin in PS reduces the pitting susceptibility of BMG_Sn2 by enlarging the potential difference between corrosion potential and pitting potential.

4.9.4 Effect of H₂O₂

The presence of H₂O₂ in PS increased the pitting susceptibility of BMG_Sn2 by decreasing the potential difference between corrosion potential and pitting potential. Due to the oxidation of H₂O₂ in the anodic potential range of BMG_Sn2, Figure 4-6 (b) is not able to give a clear indication of how H₂O₂ affects the oxidation of BMG_Sn2. It can be hypothesized that H₂O₂ increases the oxidation of BMG_Sn2 based on the effects seen on constituent elements. H₂O₂ increases the anodic reaction of Ti by complexing with it and forming a more defective oxide film [64, 194, 203] [204, 205].

In this case, the underlying metal has more chance to be oxidised. Once more Cu is oxidized, the anodic reaction would be more dramatic due to the high dissolution rate of Cu. In H₂O₂-containing solution, the cathodic reaction is dominated by reduction of H₂O₂ which is much higher than the reduction of O₂ in H₂O₂-absent solutions.

Here, it is thought that H₂O₂ induces higher pitting susceptibility, increases the corrosion rate of BMG_Sn2 by enhancing both the anodic and cathodic reaction.

4.9.5 Effect of albumin + H₂O₂

The effect of albumin on BMG_Sn2 in PS+P is different to that observed in PS. The presence of albumin decreased the OCP in PS but increased OCP in PS+P. According to mixed potential theory, the smaller OCP value in PS+A+P was more likely to be attributed to the smaller anodic current density. The anodic current suppression by albumin in PS+P of BMG_Sn2 has not been reported yet. For a clear view, the anodic current densities of CP-Ti, CP-Zr and Cu together with BMG_Sn2 at the same potential range are summarised in Figure 4-22. It shows that the only possible element taking account for the anodic reaction inhibition by albumin is Cu. Accordingly, a reasonable assumption can be given here. The presence of peroxide weakens the passive film of BMG_Sn2 and this process may be similar to how peroxide reacts with Ti. Then Cu atoms have a greater chance to react with albumin. Due to its high affinity with BSA

(Table 4-2 and previous studies [184]), Cu takes over the reaction with albumin. It was previously reported that a higher concentration of albumin (>1 g/L) can inhibit the further formation of Cu₂O [206]. In addition the strong adsorption between Cu and albumin inhibits the further dissolution of Cu ions [178]. The mechanism was reported as the formation of an insoluble complex between the metal ions (e.g. Cu⁺ ions) and the amino acid via functional groups (e.g. mercapto group (-SH) in cysteine) [182, 186]. It is worth noting that the amount of Cu atoms interacting with albumin is still restrained by the passive film and this is reflected in the anodic current densities of BMG_Sn2 which are still in the same order of magnitude as those of Ti and Zr, which are much less than Cu (indicated by red circle in Figure 4-22).

The addition of albumin in PS+P also increased the pitting resistance of BMG_Sn2. It is known that for a pit to grow stably the rate of metal ion production has to be greater than that of metal ion escape [207]. The presence of albumin may increase the pitting resistance of BMG_Sn2 by decreasing the metal ion production compared with in PS+P.

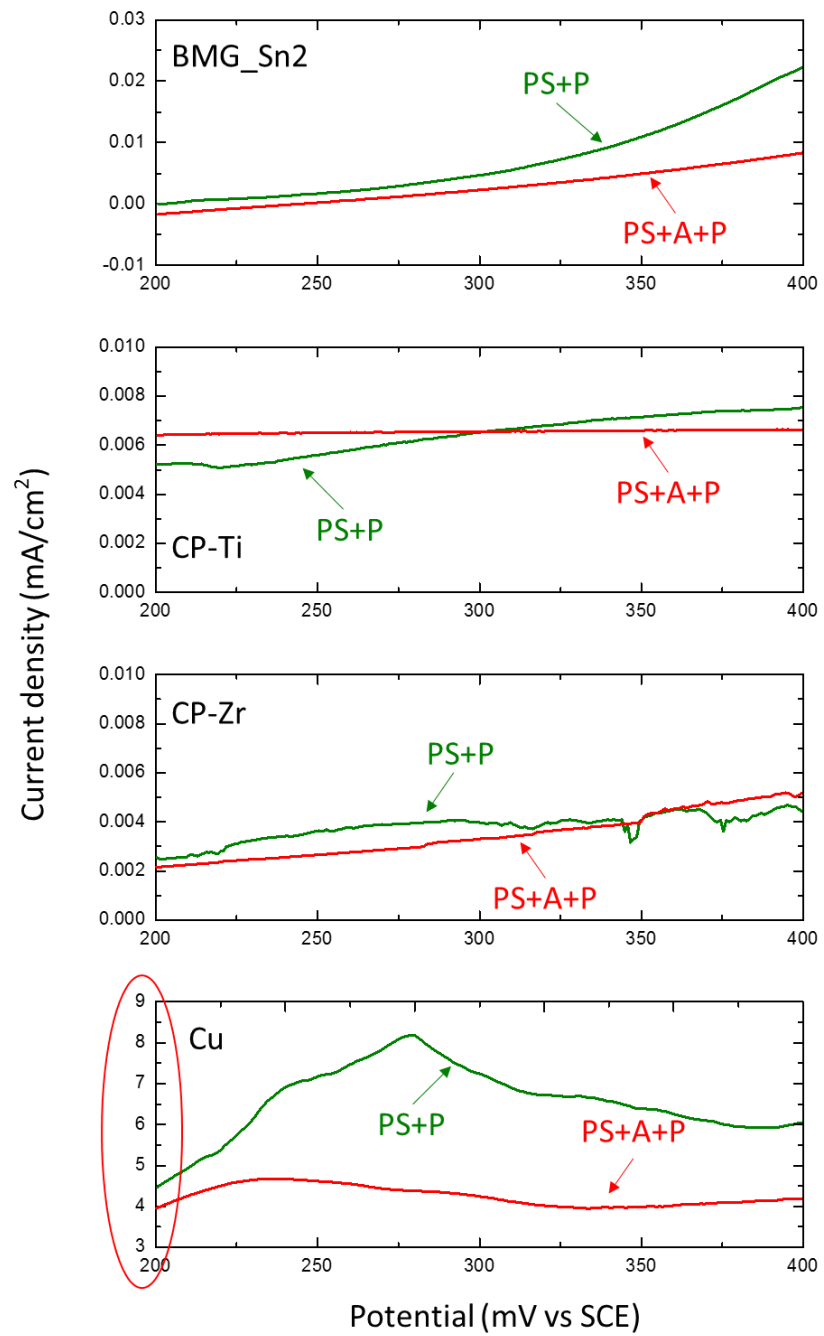


Figure 4-22 Potential (200 mV- 400 mV vs SCE) vs. current densities of BMG_Sn2, CP-Ti, CP-Zr and Cu in PS+P and PS+A+P. All curves are extracted from polarisation curves measured above.

4.10 Conclusion

Alloying elements induce pitting for $\text{Ti}_{40}\text{Zr}_{10}\text{Cu}_{34}\text{Pd}_{14}\text{Sn}_2$ in 0.9 wt.% NaCl \pm H_2O_2 \pm albumin. Zirconium and copper are the main elements accounting for pitting. Inside the pits, the content of Ti, Zr and Cu reduce, O appears, while Pd enriches, and the elemental variation in all test solutions is consistent.

The addition of albumin to NaCl solution inhibits the cathodic reaction and increases the pitting potential of BMG_Sn2.

The addition of H_2O_2 to NaCl solution increases the pitting susceptibility of BMG_Sn2. H_2O_2 increases both the anodic and cathodic current density of BMG_Sn2 in NaCl solution. The increase in cathodic reaction is due to the reduction of H_2O_2 , but the reason of the increase in anodic reaction is unclear. It is hard to tell the increase is derived from oxidation of H_2O_2 and/or more dissolution of BMG_Sn2.

The addition of albumin to H_2O_2 -containing NaCl solution decreases anodic current density, so it seems that the net cathodic reaction is enhanced at a low potential. The inhibition of anodic reaction may be attributed to Cu. It has been proposed that H_2O_2 increases the solubility of the Ti oxide film by complexation. Therefore Cu can have more chance to react with albumin. Albumin suppresses the anodic reaction significantly by decreasing the rate of Cu dissolution.

5 The influence of partial replacement of Cu with Ga on the corrosion behaviour of $\text{Ti}_{40}\text{Zr}_{10}\text{Cu}_{36}\text{Pd}_{14}$ metallic glasses

5.1 Introduction

The $\text{Ti}_{40}\text{Zr}_{10}\text{Cu}_{34}\text{Pd}_{16}$ alloy system has been proven that it can be potentially applied in the biomedical field [56, 208]. Recently, a new series of Ti metallic glasses, with a composition of $\text{Ti}_{40}\text{Zr}_{10}\text{Cu}_{36-x}\text{Pd}_{14}\text{Ga}_x$ ($x = 1, 2, 4, 8, 10$ at.%) [18], has been developed from the $\text{Ti}_{40}\text{Zr}_{10}\text{Cu}_{36}\text{Pd}_{14}$ alloy first described by Zhu et al [5]. Ga partially replaces Cu, improving ductility and enhancing glass-forming ability (up to 4 at.%) whilst maintaining biological compatibility [18]. The addition of Ga has also been proposed to be potentially biologically beneficial as Ga^{3+} possesses antimicrobial properties [70] and has been used therapeutically to treat osteoporosis [209].

Melt spinning and mould casting are the two main fabrication methods used to produce metallic glasses. The main difference between the as-cast 'bulk' specimens and as-spun ribbons is that the ribbons possess a higher degree of short-range order [153]. This arises due to the higher cooling rate associated with melt spinning (10^5 - 10^6 K/s) which limits time for atoms in the ribbon to adopt a crystalline conformation [210]. The chemical ordering of metallic glasses was reported to alter their corrosion resistance [20, 155, 156, 211].

In this chapter, Ga was used to progressively replace Cu in the $\text{Ti}_{40}\text{Zr}_{10}\text{Cu}_{36-x}\text{Pd}_{14}\text{Ga}_x$ alloy system from 0 to 10 at.%. The metallic glass with same chemical composition was

fabricated by both methods (mould- casting and melt-spinning). Corrosion behaviours of all alloys were investigated mainly by a series of electrochemical measurements including polarisation tests and potentiostatic tests.

5.2 Characterisation before corrosion

Prior to the corrosion tests, it is necessary to confirm that all alloys are amorphous for the sake of comparison. XRD is a simple and powerful technique to detect whether the test substrates have remaining crystallites in the metallic glass. In this work, XRD was undertaken with Rigaku Miniflex 600 diffractometer using Cu K α radiation. The accelerating voltage and current were 40 kV and 15 mA. No Bragg peaks were seen on diffractograms for all samples, indicating no detectable crystallites.

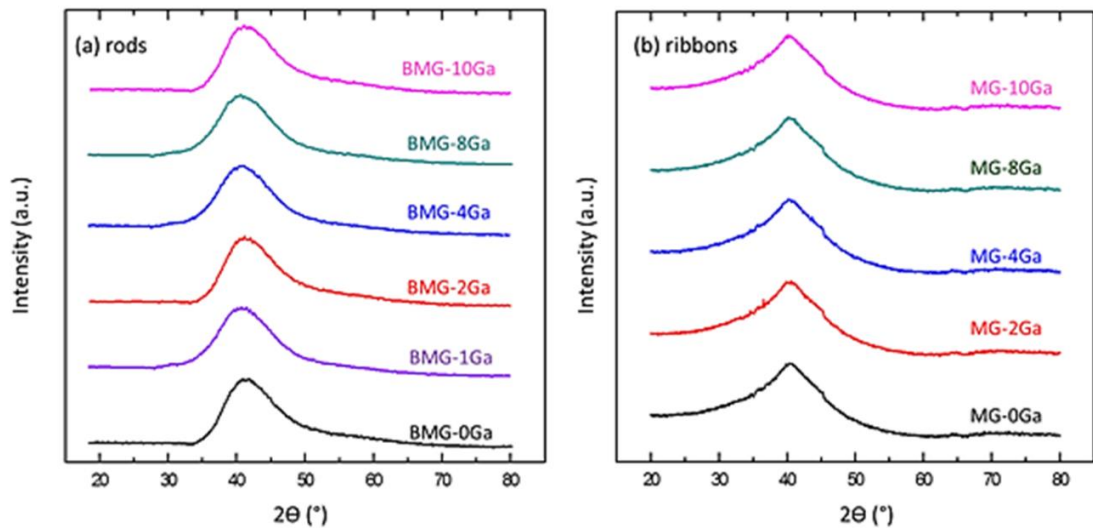


Figure 5-1 XRD patterns of (a) as-cast rods and (b) as-spun ribbons of $Ti_{40}Zr_{10}Cu_{36-x}Pd_{14}Ga_x$ ($x=0-10$) at.%. Red arrow and dashed line indicate the peak position of each sample.

The compositions of as-polished surfaces of rod and ribbon samples were analysed by EDX. The mean values and standard deviations of the chemical compositions of rods and ribbons are shown in Table 5-1 and Table 5-2 respectively. The compositions of all

samples were deemed acceptable. In comparison to rod samples, the homogeneity of ribbon samples is better, which is indicated by less compositional variation.

Table 5-1 Nominal composition and surface composition measured by EDX of all Ga-containing rod samples, all values are in at.%

Sample code	Composition	Ti	Zr	Cu	Pd	Ga
Rod-0Ga	Ti40Zr10Cu36Pd14	41 ± 1	10 ± 2	36 ± 2	13 ± 1	0
Rod-1Ga	Ti40Zr10Cu35Pd14Ga1	41 ± 1	9 ± 2	34 ± 2	14 ± 0.5	1 ± 0.3
Rod-2Ga	Ti40Zr10Cu34Pd14Ga2	43 ± 2	9 ± 2	33 ± 3	13 ± 2	2 ± 0.5
Rod-4Ga	Ti40Zr10Cu32Pd14Ga4	42 ± 2	9 ± 1	34 ± 2	11 ± 2	5 ± 1
Rod-8Ga	Ti40Zr10Cu28Pd14Ga8	40 ± 1	10 ± 1	27 ± 2	13 ± 2	8 ± 1
Rod-10Ga	Ti40Zr10Cu26Pd14Ga10	42 ± 2	9 ± 1	26 ± 3	15 ± 1	10 ± 1

Table 5-2 Nominal composition and composition measured by EDX of all ribbon samples, all values are in at.%

Sample code	Composition	Ti	Zr	Cu	Pd	Ga
Ribbon-0Ga	Ti40Zr10Cu36Pd14	41 ± 0.5	9 ± 0.1	35 ± 0.5	14 ± 0.4	0
Ribbon-2Ga	Ti40Zr10Cu34Pd14Ga2	42 ± 0.5	8 ± 0.2	34 ± 0.5	14 ± 0.4	2 ± 0.1
Ribbon-4Ga	Ti40Zr10Cu32Pd14Ga4	41 ± 0.3	8 ± 0.3	33 ± 0.1	14 ± 0.2	4 ± 0.2
Ribbon-8Ga	Ti40Zr10Cu28Pd14Ga8	42 ± 0.3	8 ± 0.4	30 ± 0.7	13 ± 0.3	8 ± 0.2
Ribbon-10Ga	Ti40Zr10Cu26Pd14Ga10	40 ± 0.4	8 ± 0.1	27 ± 0.5	14 ± 0.1	11 ± 0.5

5.3 Electrochemical measurements on $Ti_{40}Zr_{10}Cu_{36-x}Pd_{14}Ga_x$ ($x=0-10$) in 0.9% NaCl

5.3.1 OCP and potentiodynamic polarisation curves of rods

Figure 5-2 shows the OCP evolution for all the rod samples in 0.9% NaCl at 37°C.

Initially, the OCP values are in the interval -180--60 mV vs SCE. Then, for all alloys the OCP increases gradually with time, finally ending up in a range from -70 to 10 mV vs SCE. Some curves show consistent increases, e.g. Rod-0Ga, while some show a more variable pattern of increase e.g. Rod-2Ga. But clearly, the tendency of all OCP values vs. time is consistently exhibited on all rod samples without exception.

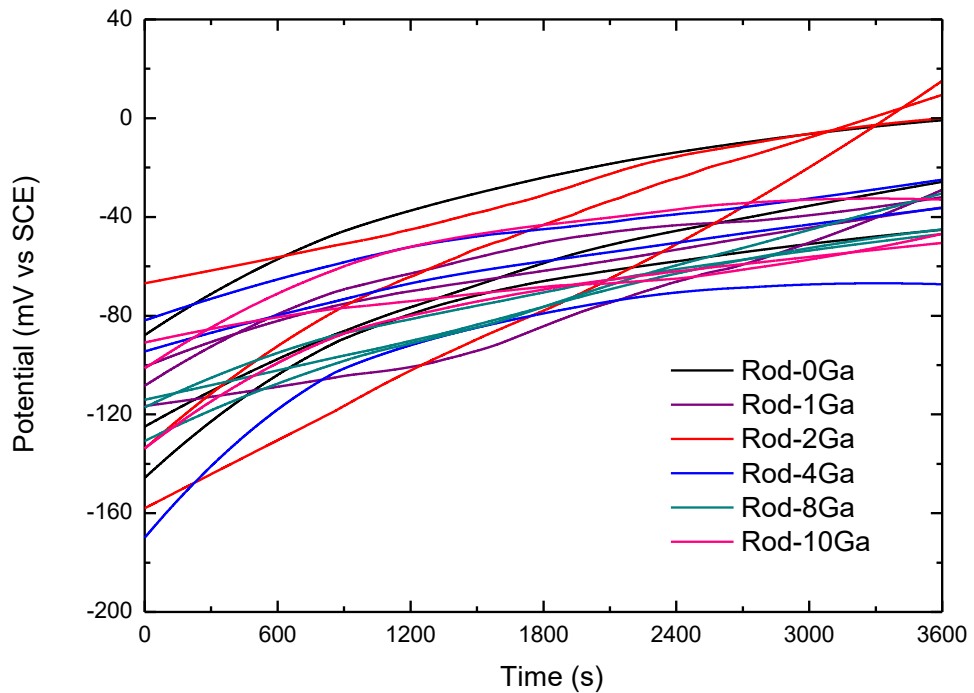


Figure 5-2 OCP measurements of rod samples $Ti_{40}Zr_{10}Cu_{36-x}Pd_{14}Ga_x$ ($x=0, 1, 2, 4, 8, 10$) in 0.9% NaCl at 37 °C.

Following the OCP measurement, the measurement of anodic or cathodic polarisation curves was carried out immediately. Figure 5-3 (a) shows anodic polarisation curves for rod samples. The corrosion potentials are in the interval -50 mV- 5 mV vs. SCE. This interval is similar to the one in which the OCPs are situated, i.e. -70 mV- 10 mV vs. SCE. The corrosion currents are of the order of 10^{-4} mA/cm². The measured anodic current increases with the applied potential before reaching a passive plateau at current density values of -2×10^{-3} mA/cm². For all alloys, with further increase in applied potential there is a sudden increase in current clearly indicating stable pitting corrosion. The pitting potentials (E_{pit}) are in the interval 300 mV- 400 mV vs SCE.

Following the same procedures as for measuring anodic polarisation curves, cathodic polarisation curves were also measured after one-hour OCP and the curves are shown in Figure 5-3 (b). Cathodic polarisation curves are very consistent irrespective of the Ga content. The curves exhibit three stages as indicated by arrows in the figure; namely oxygen reduction at the beginning, oxygen diffusion limitation characterised by a plateau at 0.1 mA/cm² and hydrogen evolution as a final stage.

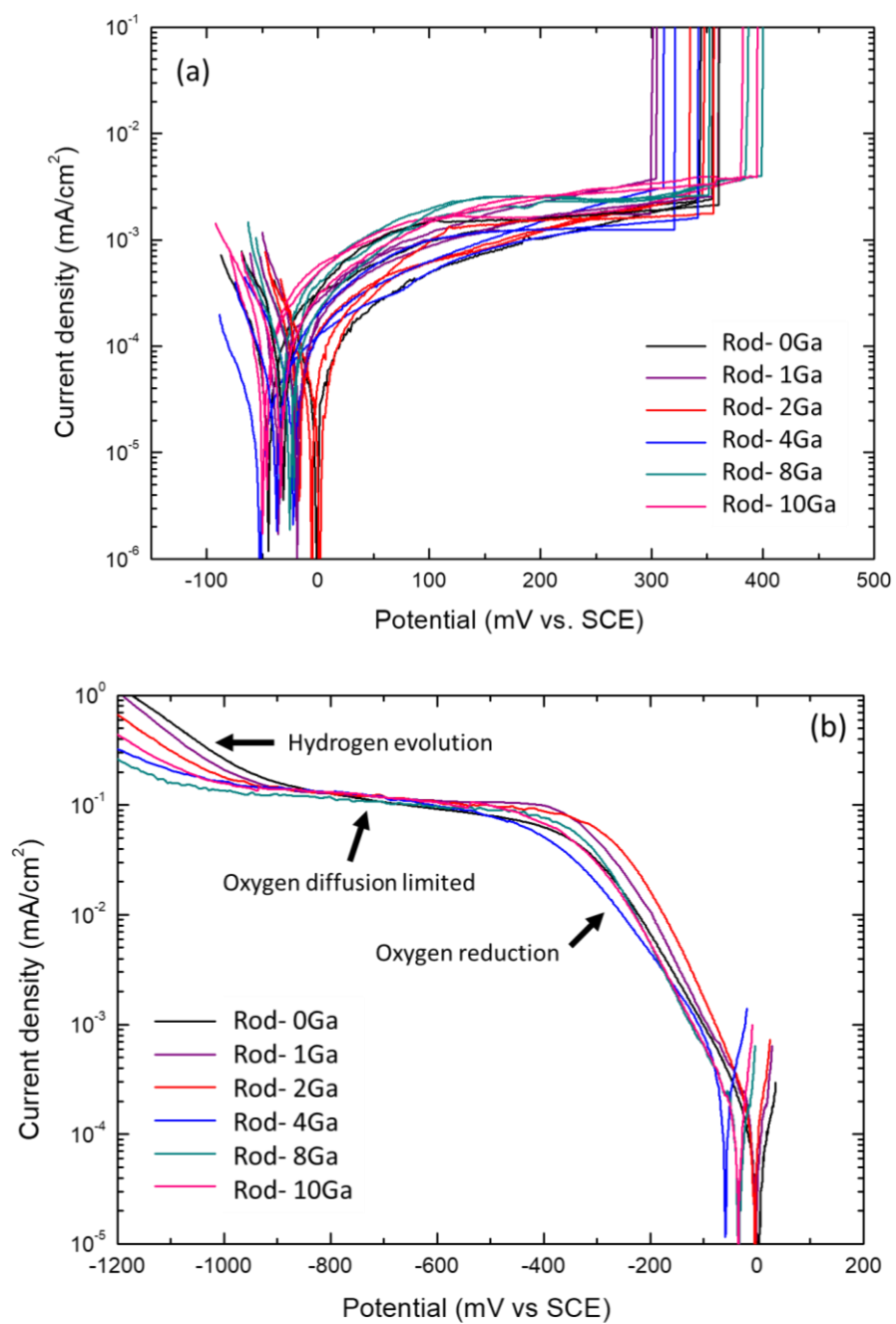


Figure 5-3 (a) Anodic (b) Cathodic polarisation curves of bulk metallic glass $Ti_{40}Zr_{10}Cu_{36-x}Pd_{14}Ga_x$ ($x=0, 1, 2, 4, 8, 10$) in 0.9% NaCl at 37 °C.

5.3.2 OCP and anodic polarisation curves of ribbons

Similar to the measurements on rod samples, the open circuit potentials for ribbon samples were measured in 0.9% NaCl at 37 °C for one hour. OCP curves for all ribbon samples are shown in Figure 5-4. All OCP values show an increasing tendency with time, but with different slopes. The OCP values for the Ribbon-0Ga, -4Ga and -8Ga increase steadily with time before plateauing towards a constant. Whereas the OCPs of Ribbon-2Ga and -8Ga increase throughout the measurement period. The initial values of ribbon samples scatter in a large range (-180--80 mV vs SCE) but end in a smaller potential range (-85--30 mV vs SCE) after 1 hour.

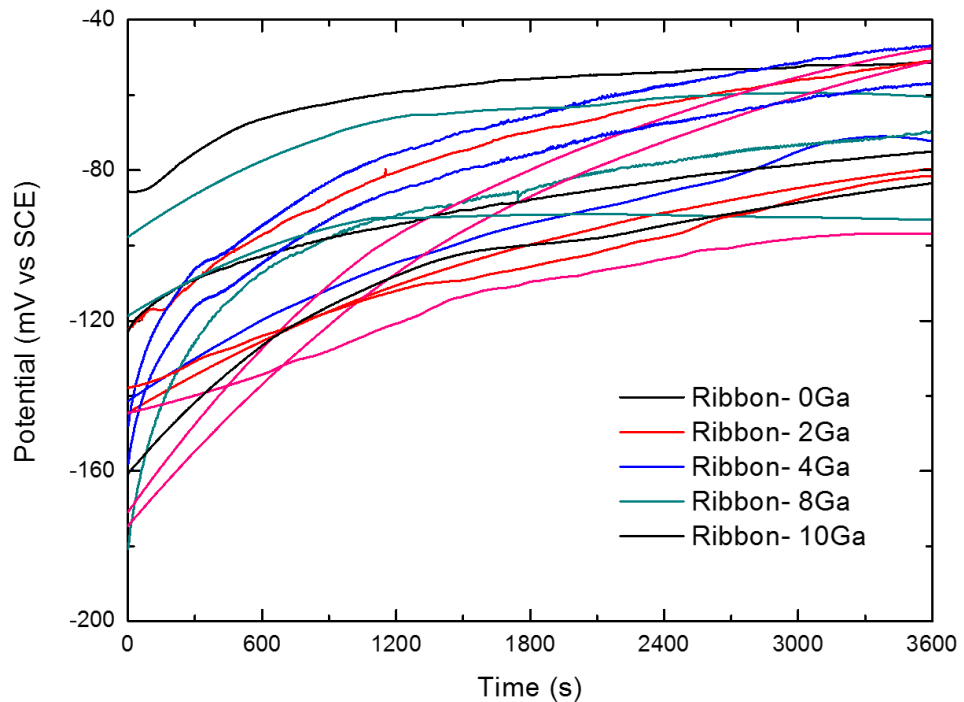


Figure 5-4 OCP measurements of as-spun metallic glass $Ti_{40}Zr_{10}Cu_{36-x}Pd_{14}Ga_x$ ($x=0, 2, 4, 8, 10$) in 0.9% NaCl at 37 °C.

Anodic and cathodic polarisation curves for the ribbon samples are shown in Figure 5-5. From the anodic polarisation curves, it is evident that the corrosion potentials are in the interval -100 mV- -50 mV vs SCE. The corrosion currents are of the same order (10^{-4} mA/cm²) as rod samples. The pitting potentials (E_{pit}) for all ribbon samples are in the interval of 375 mV- 500 mV vs SCE. Cathodic polarisation curves are shown in (b) and show high consistency for all ribbon samples. However, no significant oxygen-diffusion limited stage was observed for ribbons as it was for the rod samples.

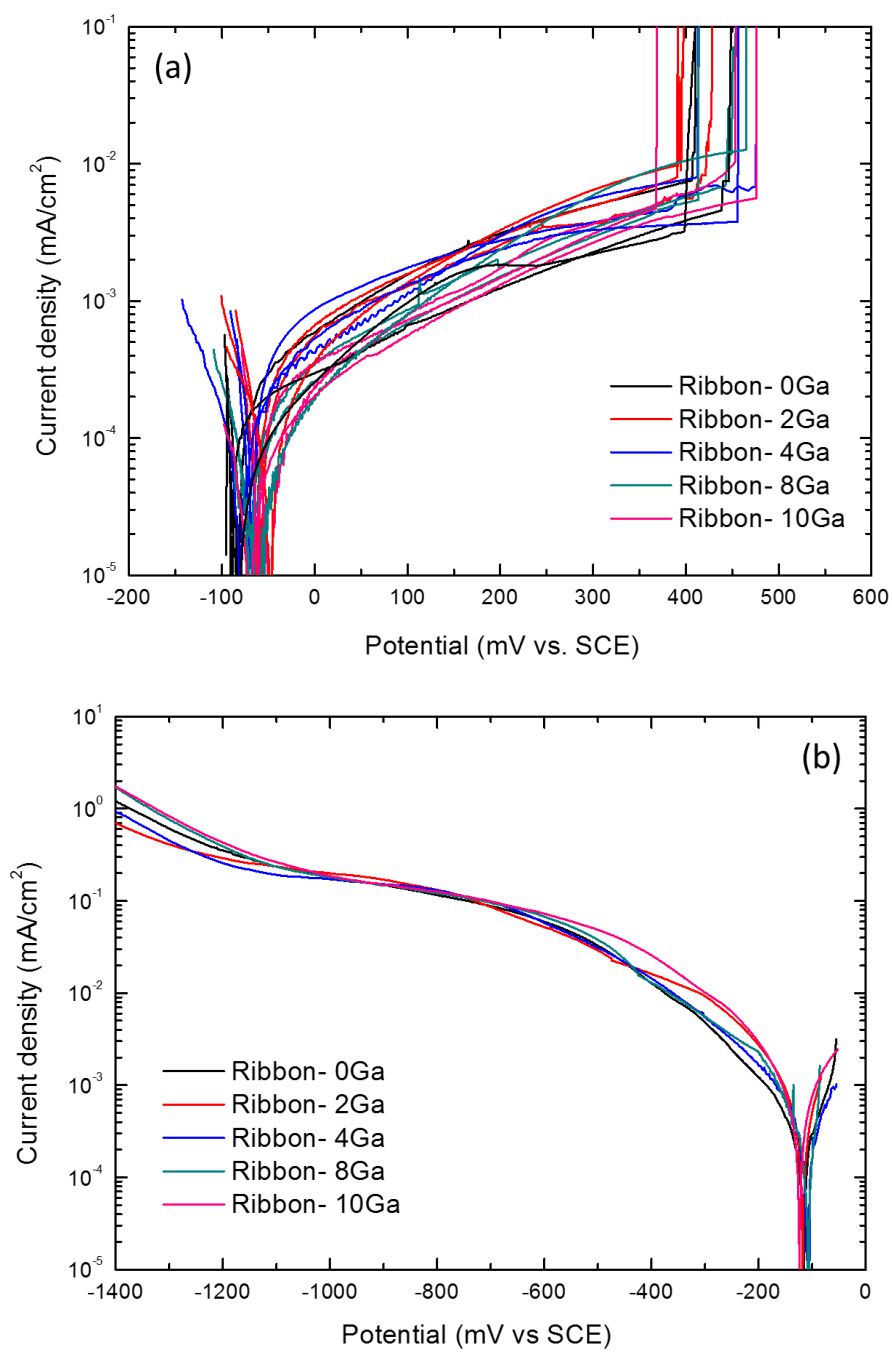


Figure 5-5 (a) Anodic (b) Cathodic polarisation curves of as-spun metallic glass $Ti_{40}Zr_{10}Cu_{36-x}Pd_{14}Ga_x$ ($x=0, 2, 4, 8, 10$) in 0.9% NaCl at 37 °C.

For a clearer view of the comparison between rod and ribbon samples, the characteristic parameters: corrosion potential (E_{corr}), pitting potential (E_{pit}) were summarised in Figure 5-6. Each parameter accords with three data points representing three repeated measurements. For all alloys except for $x = 10$ at.%, E_{corr} is significantly higher for rods than it is for ribbons. For $x = 10$ at.%, the difference in E_{corr} is not as significant as others because one data point of E_{corr} of ribbon overlaps with the data of rod. For all alloys with no exception, E_{pit} is significantly lower for rods than it is for ribbons. It follows that for all alloys the pitting overpotential, i.e. $\eta_{pit} = E_{pit} - E_{corr}$, is significantly higher for ribbons than it is for rods. The larger overpotential indicates that ribbons have a higher pitting resistance than rods.

There is no clear effect of Ga content on E_{corr} or E_{pit} for either rods or ribbons. However, a two-way ANOVA identified a significant effect of fabrication route on mean E_{corr} and E_{pit} ($p < 0.01$) and a significant factorial interaction (between Ga content and fabrication route) on mean E_{corr} ($p = 0.03$) suggests the magnitude in difference in E_{corr} associated with fabrication route is dependent on alloy composition. Independent t-tests show that for all alloys (comparing pairs of equivalent composition) except for 10 at.% Ga, E_{corr} is significantly higher and E_{pit} is significantly lower for rods than for ribbons ($p < 0.05$) (Table 5-3).

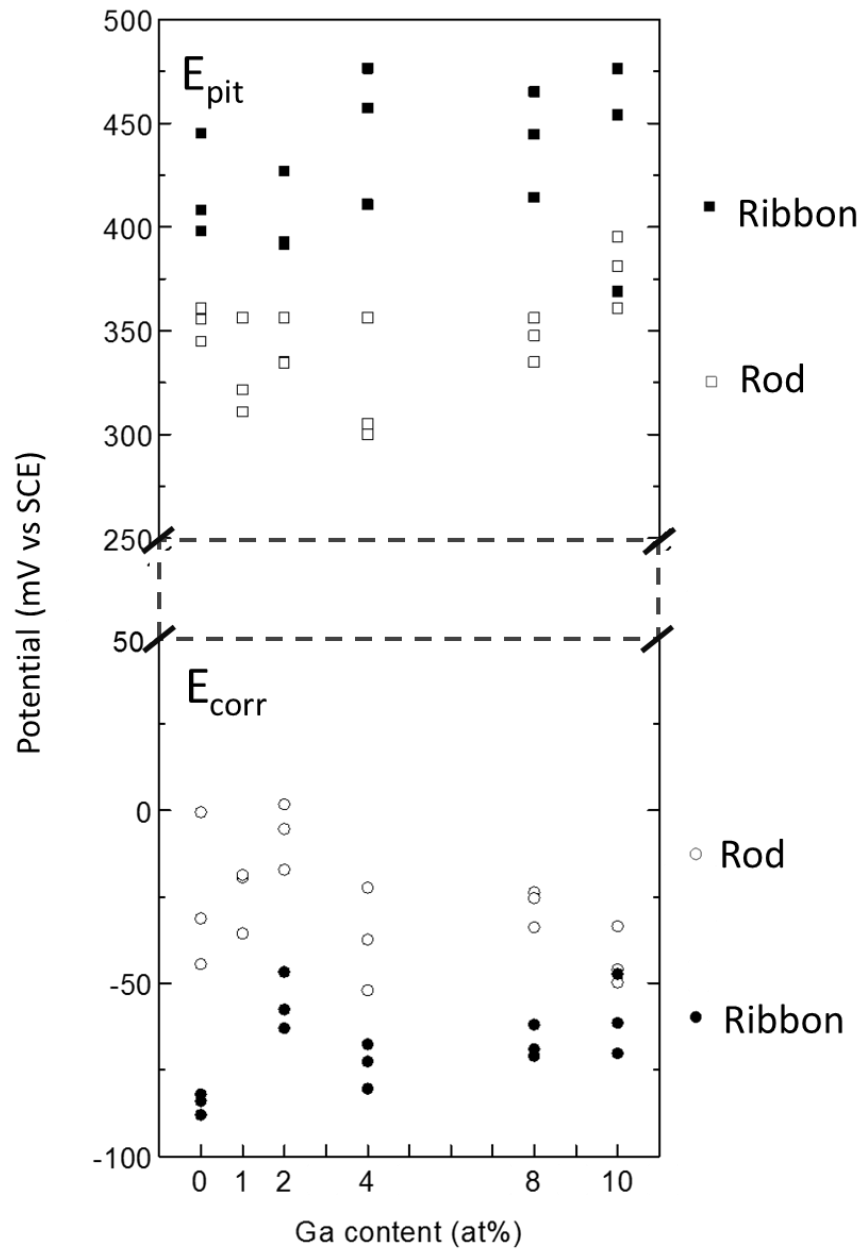


Figure 5-6 The pitting (E_{pit}) and the corrosion (E_{corr}) potential of glassy $Ti_{40}Zr_{10}Cu_{36-x}Pd_{14}Ga_x$ alloy ribbons and rods in 0.9% NaCl at 37 °C for $x = 0, 1, 2, 4, 8$ and 10 at.%. Filled square for E_{pit} of ribbons. Empty square for E_{pit} of rods. Filled circle for E_{corr} of ribbons. Empty circle for E_{corr} of rods.

Table 5-3 Summary of independent sample t-tests comparing E_{corr} and E_{pit} of rods and ribbons of equivalent compositions ($\alpha = 0.05$). Statistically significant differences are annotated (*).

	Ga (at.%)	p-value
E_{corr}	0	0.011*
	2	0.002*
	4	0.017*
	8	0.001*
	10	0.120
E_{pit}	0	0.014*
	2	0.010*
	4	0.008*
	8	0.004*
	10	0.188

5.3.3 Potentiostatic measurements

To further study the effect of Ga content on the electrochemical behaviours, potentiostatic measurements were carried out on rod and ribbon samples. Following 1-hour OCP measurements, 200 mV vs SCE was applied on the samples immediately. OCP values were basically the same as those shown in Figure 5-2 and Figure 5-4, so the data are not shown here. The current responses under 200 mV vs SCE were recorded and shown in Figure 5-7. For all samples, current densities decrease sharply at first then decrease gradually after longer time period. After 120 s, the current densities of ribbons are consistently higher than those of rods. The current density of ribbons decreases from 4.3×10^{-3} to 3.1×10^{-4} mA/cm², while that of rods decreases from 4.3×10^{-3} to 1.04×10^{-4} mA/cm² in 120-5000 s. It also shows some occasional spikes on the curves, which indicates that metastable pits show up at 200 mV vs SCE if this potential is held for long time. For the alloys fabricated using the same methods, the current difference was too small to give a hint of how the potentiostatic current is affected by Ga content. For example, in the first 1500 s, the current density follows the order of Ribbon-8Ga > Ribbon -10Ga > Ribbon -2Ga > Ribbon -0Ga > Ribbon -4Ga, while after 1500 s, all curves are overlapping again. The current responses of rod samples were similar in that there was some order in the first 2000 s then all curves overlap.

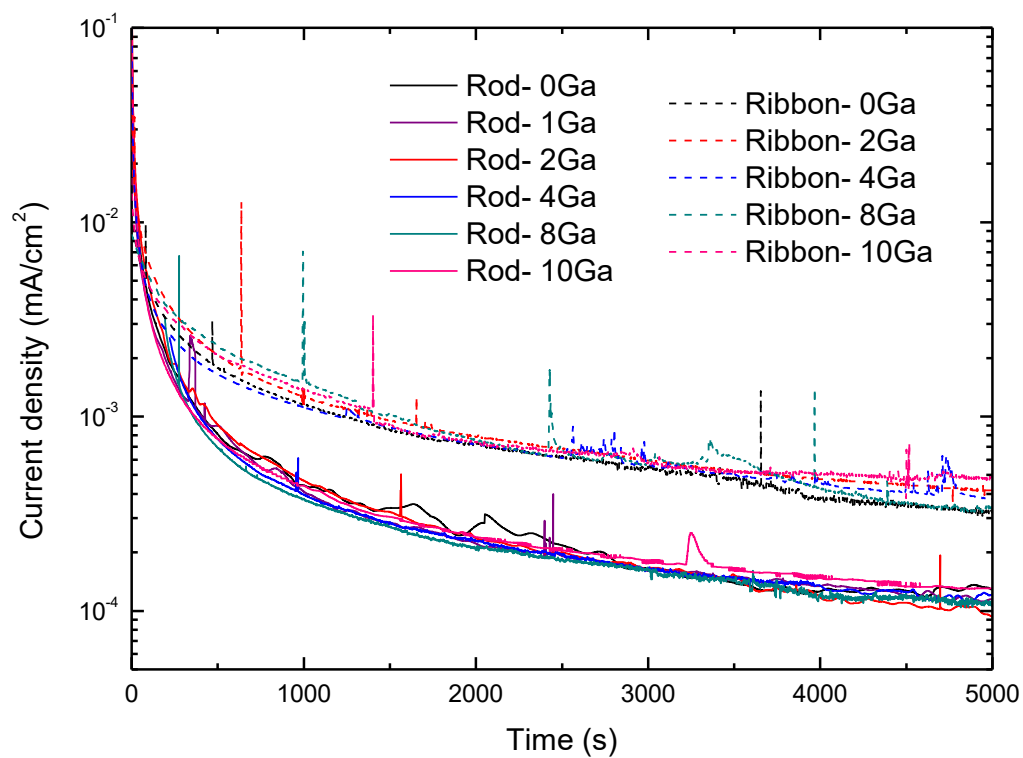


Figure 5-7 Potentiostatic measurement of rod and ribbon samples for 5000 s in 0.9% NaCl at 37 °C, and 200 mV vs SCE following 1 hour at OCP.

5.3.4 Electrochemical measurement of Cu and Ga

Since the only compositional alteration is the replacement of Cu with Ga, an understanding of the electrochemical behaviours of pure Cu and Ga was necessary to understand the behaviours of the metallic glasses. Before the measurement, the surface of Ga was flat with an area about 11.3 mm². Due to the low melting point of Ga (30 °C), it turned into liquid during the measurement at 37 °C. The surface area of the Ga electrode is necessary for the determination of current density. Here, the surface of liquid Ga electrode was scanned by confocal microscopy and as shown in Figure 5-8 exhibited a convex surface. The measured surface area was 12.8 mm², which is larger than if the surface was considered as flat. The current density was calculated based on the surface area of the convex surface however, it should be pointed out this can only be an approximation and hence the calculated current density was an estimate. An in-situ measurement on current vs. the deformed surface of Ga should be developed to attain more accurate current density.

Figure 5-9 shows the polarisation curves of Ga and Cu in 0.9% NaCl at 37 °C. The corrosion potential of Ga (-789 mV vs SCE) is much lower than that of Cu (-190 mV vs SCE). For both metals the current density increases significantly with potential up to very high values, e.g. -5 mA/cm² at 100 mV vs SCE, clearly indicating active dissolution. In the potential range from -100 to 500 mV vs SCE, which includes the corrosion potential and the pitting potential of all Ti₄₀Zr₁₀Cu_{36-x}Ga_x metallic glasses the current density of Cu and Ga is relatively similar.

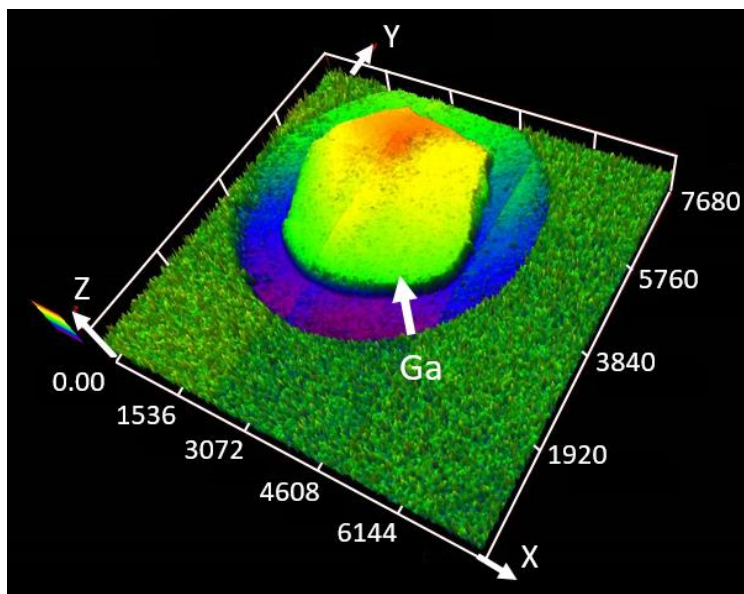


Figure 5-8 Confocal microscope image of convex Ga electrode sample after anodic polarisation test.

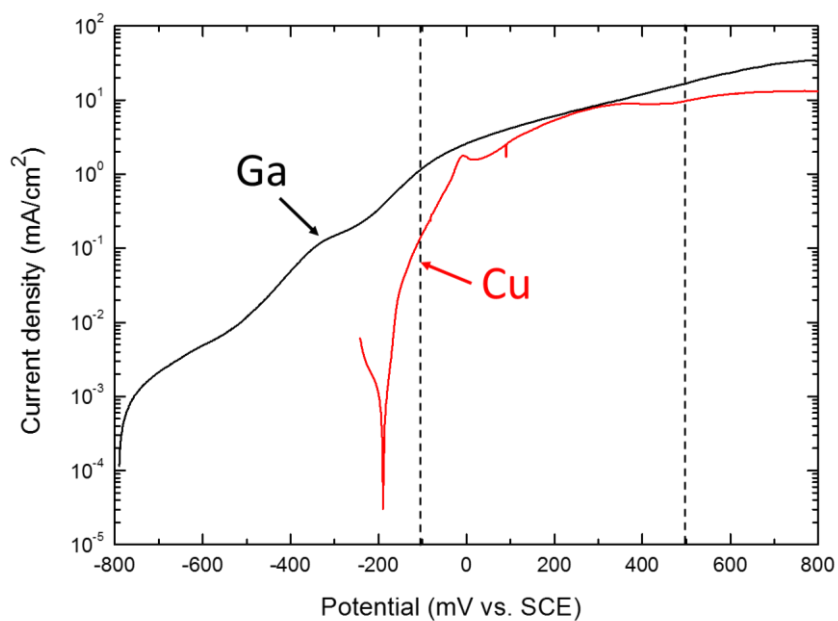


Figure 5-9 Anodic polarisation curve of Cu and Ga in 0.9% NaCl at 37 °C. Two dashed lines indicate the potential range of all metallic glasses from their corrosion potential to pitting potential.

5.4 Pitting morphology and chemical composition

5.4.1 Rods

Figure 5-10 shows the polished cross-section of the Rod-2Ga sample before (a) and after (b) a typical anodic polarisation such as the ones shown in Figure 5-3. The test was stopped at 5 mA/cm² in order to capture pits at an early stage of their propagation. Under an optical microscope, three pits can be seen (Figure 5-10 b). Two of them are located at the specimen edge, in the vicinity of the interface between the sample and the resin. Figure 5-10 (c) and (d) show higher magnification SEM images of the pit marked in (b). The interior structure of pit shows a clear alloy leaching feature with a large number of micro-pores left by metal dissolution. The chemical composition inside the pit was analysed by EDX, which is presented in Table 5-4. The concentration of Pd inside the pit was 32 at.% and is significantly higher than in locations free of pits (13 at.%) and the nominal value (14 at.%), while the concentrations of Ti, Zr, Cu and Ga were lower.

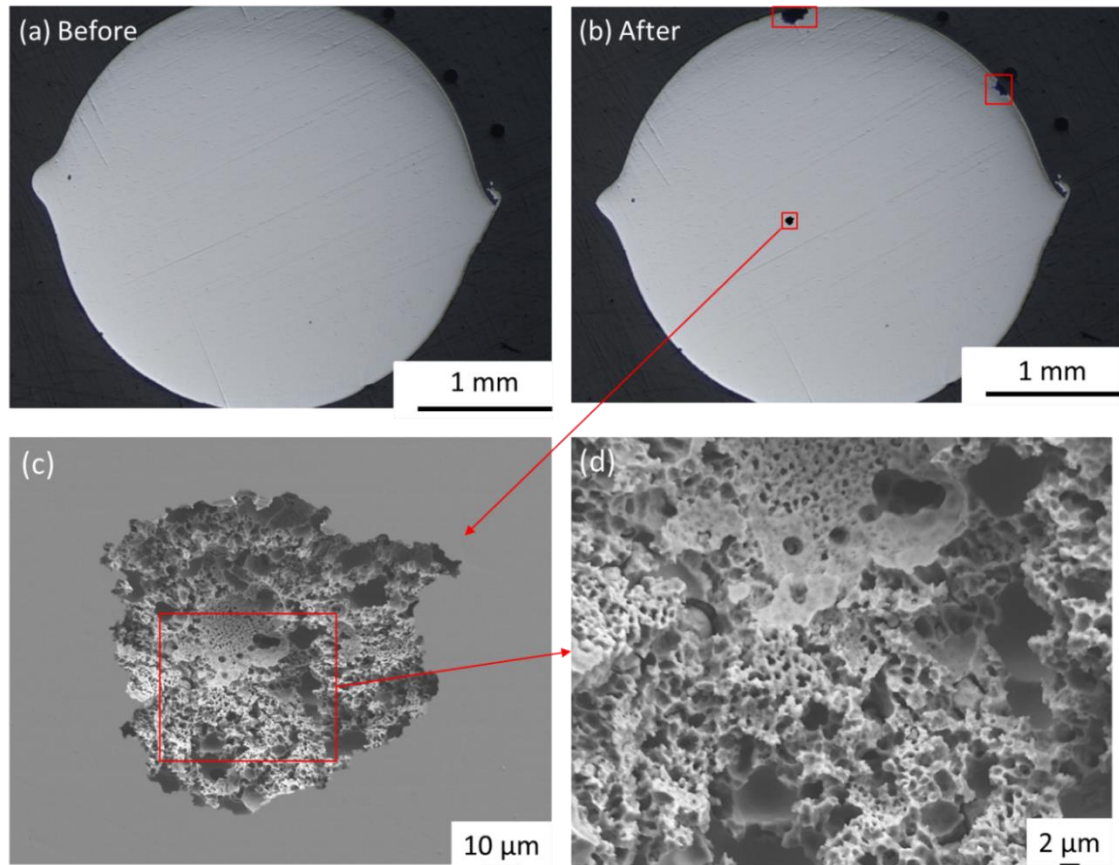


Figure 5-10 Optical microscopic images of surface condition of Rod-2Ga (a) before and (b) after anodic polarisation measurement. (c) SEM images showing pitting morphologies of individual pit in (b). (d) Magnified view of the pit in (c). The measurement was performed in 0.9% NaCl at 37 °C and was stopped immediately when current density reached 5 mA/cm².

Table 5-4 Elemental composition of pits on Rod-2Ga measured by EDX after anodic polarisation corresponding to the images shown in Figure 9, reported as mean values and standard deviation (the number of individual measurements, n = 25). Unit of all numbers is at.%.

Area	O	Na	Cl	Ti	Zr	Cu	Pd	Ga
Corroded	5 ± 3	2 ± 3	1 ± 3	28 ± 10	5 ± 2	27 ± 3	32 ± 6	0
Non-corroded				41 ± 1	9 ± 0.6	35 ± 2	13 ± 1	2 ± 0.3
Nominal				40	10	34	14	2

5.4.2 Ribbon

Figure 5-11 (a) and (b) show optical microscope images of the Ribbon-2Ga before and after potentiodynamic testing, respectively. The anodic current was stopped at 3 mA/cm². One large crevice pit was seen under optical microscopy. SEM images in (c-d) show the microstructure inside of this pit. The appearance of the pit on the ribbon was different from the pit seen on equivalent rod exhibiting some cracks that were distributed irregularly on the lamella. The chemical composition inside the pit was analysed by EDX and it is shown in Table 5-5 and in Figure 5-11. It can be clearly seen that the concentration of Pd inside the pit (30 at.%) is significantly higher than in locations free of pits (14 at.%) and the nominal value (14 at.%), while the concentration of Ti, Zr, Cu and Ga is lower. This is similar to the observation made for the equivalent composition Rod-2Ga sample.

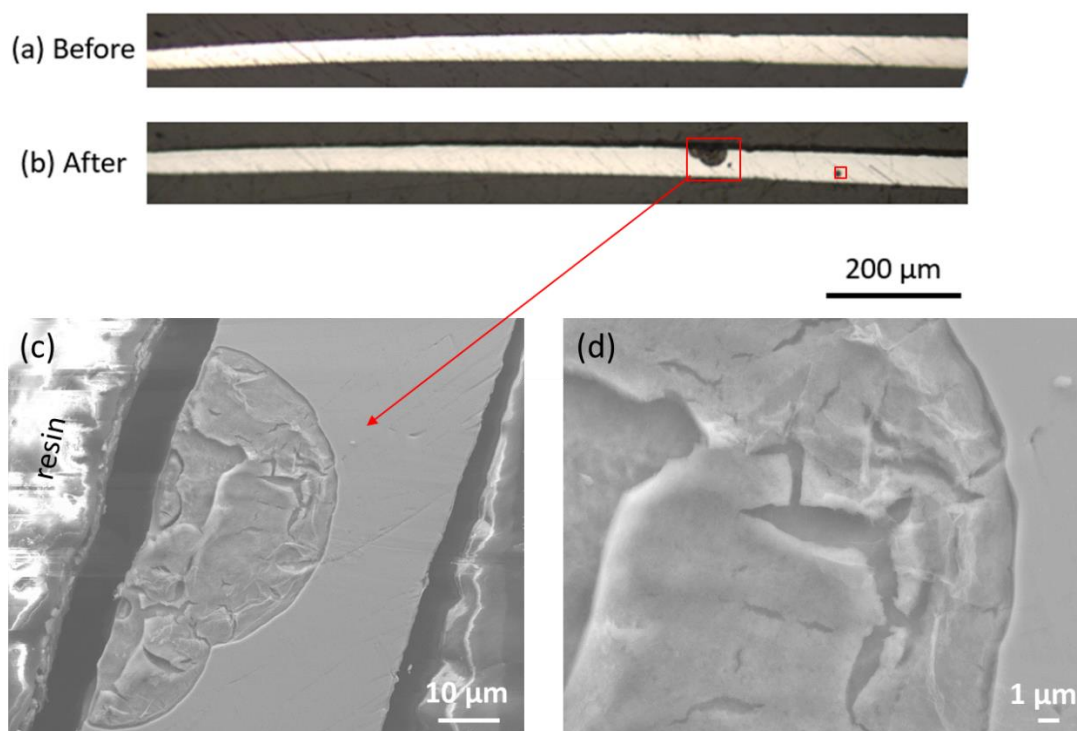


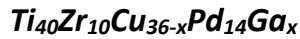
Figure 5-11 Optical microscopic images of surface condition of Ribbon-2Ga (a) before and (b) after anodic polarisation measurement. (c) SEM images showing pitting morphologies of crevice pit in (b). (d) Magnified view of the pit in (c). The measurement was performed in 0.9% NaCl at 37 °C and was stopped immediately when the current density reached 3 mA/cm².

Table 5-5 Elemental composition of pits on Ribbon-2Ga measured by EDX after anodic polarisation corresponding to the images shown in Figure 10, reported as mean values and standard deviation (the number of individual measurements, n = 25). Unit of all numbers is at.%.

Area	O	Na	Cl	Ti	Zr	Cu	Pd	Ga
Corroded	8 ± 7	3 ± 5	5 ± 8	25 ± 5	2 ± 2	27 ± 5	30	0
Non-corroded				39 ± 0.6	9 ± 0.7	36 ± 1	14 ± 0.2	2 ± 0.1
Nominal				40	10	34	14	2

5.5 Discussion

5.5.1 Effect of replacement of Cu with Ga on corrosion behaviour of



The substitution of Ga (up to 10 at.%) did not significantly change the electrochemical parameters (E_{corr} , E_{pit} and anodic current density) for samples with same fabrication method. The main reason could be the very similar electrochemical behaviour between Cu and Ga in the range of E_{corr} to E_{pit} of metallic glasses (Figure 5-9), which means, they have approximately equal contribution to the anodic reaction. However, it should be noted that the method to measure current density for Ga has limited accuracy because the surface area measurement was not conducted in-situ. Under this circumstance, it is believed that the passive film also plays important role to diminish the current fluctuation caused by Ga content. The passive film consists of Ti and Zr oxides, which blocks the dissolution of underlying metal. Due to the high chemical stability of the oxide film, the anodic current is rarely dependent on the underlying metal no matter what it is. Therefore, when substituting Cu with Ga, as long as the oxide film can still cover the specimen surface, a significant change in the electrochemical behaviour of metallic glasses would not be expected.

5.5.2 Comparison between as-cast rod and as-spun ribbon

The specimens fabricated as ribbons or rods can were produced from the same alloy, and neither showed crystalline peaks following XRD characterisation. The production of ribbons is associated with a high cooling rate, expected to lead to a fully glassy structure. However, the production of rods involves a relatively lower cooling rate such that significant structural relaxation may occur. This is often accompanied by the reduction of free volume and changes in chemical and topological short-range order [19]. It is therefore possible that the rod samples had local chemical heterogeneity. This may be the cause of the larger elemental variation (Table 5-1 and Table 5-2). In addition, it is notable that the pits in the ribbon samples had relatively smooth surfaces whereas the pits in the rods had a rougher surface, with smaller areas of local attack (Figure 5-10 and Figure 5-11). It is possible that the heterogeneous dissolution in pits seen on rods may be associated with selective dissolution of reactive elements (Cu and Ga), which leaves a more unreactive surface enriched with Ti and Zr [20]. This may also explain why the passive current densities of rods were significantly lower than those of ribbons (Figure 5-7). Previous work has indicated that the more stable structure which evolves in amorphous alloys during structural relaxation may lead to initial dissolution of the reactive elements from sites where they are locally enriched, leaving behind a surface that is enriched with passivating elements which therefore has chemical stability [20, 156]. A number of amorphous alloy systems, for example, $Zr_{48}Cu_{36}Ag_8Al_8$ [155], $Fe_{78-x}Si_{13}B_9Cr$ ($x=3, 4, 7$) [22] show lower passive current densities after thermal relaxation. These findings are consistent with the passive current

densities shown in Figure 5-7 which demonstrates that the rod samples which are expected to be in a more structurally relaxed state, have lower current densities than the equivalent ribbon.

The pitting potentials for rods were statistically lower than those for ribbons, except the composition with 10 at.% Ga. The exception of 10 at.% Ga may be owing to the reduced glass forming ability compared with the compositions with 0-8 at.% Ga [18]. The reason for this is also likely to be due to the chemical heterogeneity introduced by slower cooling for rods. The initiation of pits is associated with dissolution of metastable pits, which are likely to start at regions enriched with Cu and Ga in rods, compared with the more uniform composition found in the ribbons.

The alloy with 10% Ga did not show a statistically significant difference between the pitting potentials for rod and ribbon samples. This may be associated with the enhanced glass-forming ability of Ga relative to Cu [18], such that it may have not undergone the same level of structural relaxation as the other alloys.

5.6 Conclusion

Partial substitution of Cu with Ga in the metallic glass $\text{Ti}_{40}\text{Zr}_{10}\text{Cu}_{36-x}\text{Pd}_{14}\text{Ga}_x$ ($x \leq 10$ at%) is desirable for small medical implants as Ga can enhance the glass-forming ability and potentially improve biocompatibility. It has been shown that for both rod and ribbon samples, Ga levels up to 8% have no significant effect on the passive current density, pitting potential or cathodic reactivity in 0.9% NaCl at 37 °C.

Different pitting potential and corrosion potential values were found when ribbon and rod samples of the same composition were compared for all compositions apart from the composition containing the highest Ga level (10 at%). This was attributed to structural relaxation occurring as a result of the slower cooling rates during casting of rods compared with melt-spinning ribbons. It is proposed that the structural relaxation leads to local regions with higher Cu and Ga levels that are more susceptible to corrosion, leading to a lower pitting potential and a rougher pit surface for rod samples compared with ribbons. This may also explain the lower passive current density for rod samples.

Rod and ribbon samples containing 10% Ga showed no significant difference in pitting potential. This may be a result of the higher glass-forming ability of Ga, which may reduce levels of structural relaxation during casting of rods.

Substitution of Cu with Ga in these metallic glasses is therefore expected to have no significant effect on corrosion susceptibility.

6 Mechanically-Assisted Crevice Corrosion (MACC)

6.1 Introduction

Ti is known to be susceptible to crevice corrosion at high temperatures but has been shown to be resistant in chloride containing media below a temperature of 65 °C [14]. Gilbert and co-authors proposed that mechanically-assisted crevice corrosion (MACC) can explain the observed corrosion at modular interfaces [25, 30] such as those that are present between dental components. For MACC to occur there must be relative micromotion at the interface of modular surfaces which leads to rupture of the passivating oxide film and bursts of metal dissolution that generate local acidity through hydrolysis of metal ions. MACC will develop only if the relative motion is on a sufficiently small scale for the geometry of the crevice and the chemistry of the acidic solution inside the crevice to be maintained. If the acidic solution is diluted by the neutral solution outside the crevice, then the protective passive oxide will regrow and corrosion will cease. Connections such as Morse tapers in orthopaedic modular joint replacements and implant body-abutment interfaces in dental implants provide the pre-requisite conditions. For example, the micromotion between dental implant body and abutment components under masticatory loading has been frequently simulated and reported between 20 -70 μm [96, 212-214].

There is currently no standard test to simulate MACC. In contrast, several instruments such as pin-on-disk devices are routinely used to simulate tribocorrosion but do not maintain the necessary local acidic chemistry that is critical for MACC for any sustained

period [31, 215]. In this chapter, we demonstrate a new device to quantify MACC that preserves both the local acidic chemistry and corrosion products during electrochemical testing. This device emphasizes the long-term effect of corrosion products on the corrosion of alloys rather than the transient ‘depassivation-repassivation’ process investigated in most tribocorrosion tests. At the same time, steps to mitigate MACC through alloy design are explored. The susceptibility of Ti alloys to MACC has been linked to their poor wear resistance [216, 217]. Ti-based bulk metallic glasses (BMGs) have good corrosion resistance and significantly better wear resistance than Ti alloys [115, 218]. Several Ti-based BMG compositions have been shown to have favourable biological compatibility [17, 54, 219] including the ability to osseointegrate [146]. These properties show the promise of Ti-based BMGs to be used for dental implants. For MACC simulation we consider chloride rich environments and the addition of the serum protein albumin which has been shown to modify the corrosion resistance of Ti alloys in static tests and in tribocorrosion experiments [129, 130].

6.2 Observation on retrieved dental implant

A modular dental implant (Straumann SLA Regular Neck, Basel, Switzerland) was retrieved (after 4 years of service) due to chronic peri-implant inflammation (peri-implantitis). The implant was imaged using micro computerized tomography (25 μm resolution, Milabs, Utrecht, Netherlands). A tomogram image is shown in Figure 6-2 (a), showing an abutment, abutment screw and the implant body. In Figure 6-1 (b) a magnified view of the connection between components shows the contact and non-contact areas. Due to the design and loading conditions, it can be seen that not all of the connection surfaces of the modular implant are tightly opposed.

Subsequently, the abutment and implant body were uncoupled, and sectioned. The as-cut implant was washed with EDTA solution (Sigma-Aldrich, UK) for 24 hours to reduce the amount of organic species on the surface. Two areas (marked with a box) are identified in Figure 6-2 (a) and show the boundary of a contact and non-contact area. It can be seen that there is a clear boundary in Figure 6-2 (b), and SEM imaging revealed morphological variation between the contact and non-contact area, which may be caused by some form of material migration. This variation in contact and non-contact area can be distinguished more clearly in Figure 6-2 (c), the upper side of the crest is the side contacting with screw, and the lower side is the side left clearance. The ditch-like feature on the upper side, as well as the severe plastic deformation illustrates that the relative motion has occurred between implant body and abutment screw.

However, it cannot be discriminated whether this was due to the coupling and uncoupling events or as a result of a cumulative micromotion over time.

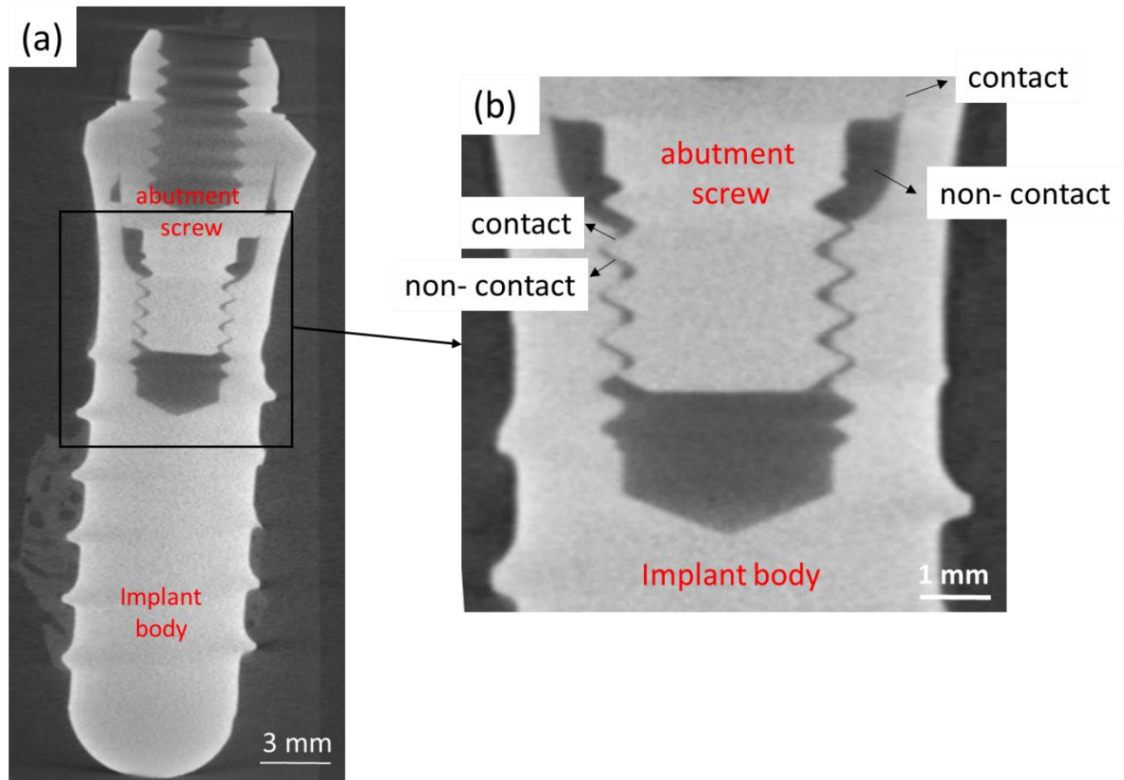


Figure 6-1 (a) Axial views taken from tomographic imaging of a retrieved implant including an abutment screw and an implant body. (b) A magnified view of the junction of abutment screw and implant body, with arrows indicating contact and non-contact area.

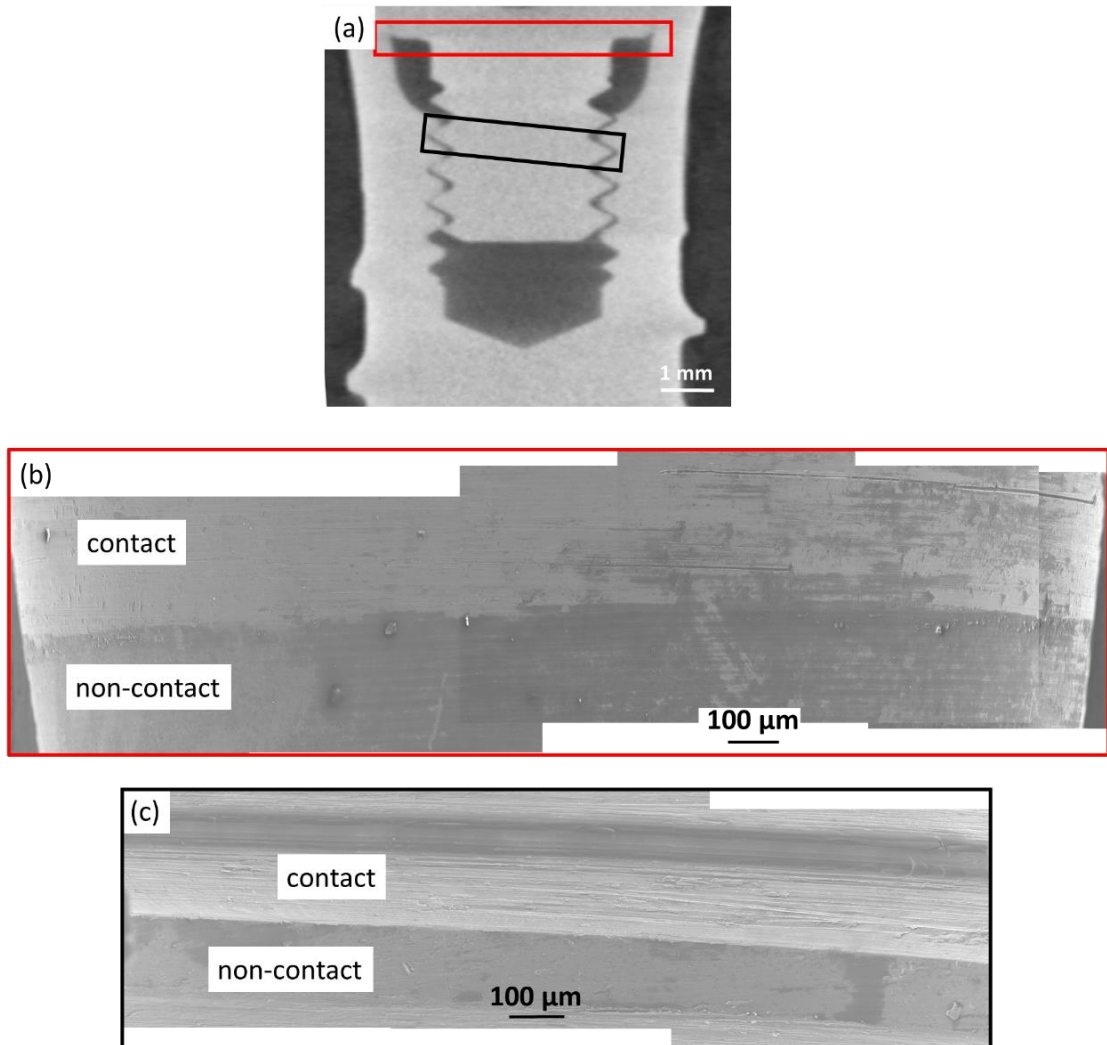


Figure 6-2 (a) CT-scanned tomography showing the abutment and implant when they are coupled. Then abutment and implant were uncoupled, then implant body was cut into half. (b) and (c) are SEM images of inner surface of implant body, they are picked up to reveal the morphology difference of contact and non-contact area.

6.3 As-received materials

6.3.1 Chemical composition

The chemical composition of MACC samples were analysed by EDX, the measured composition, as well as nominal composition, is shown in Table 6-1.

Table 6-1 Materials used in MACC, all values are in at.%

Sample code	Composition	Measured composition
Ti6Al4V	Ti6Al4V	Ti: 89 ± 1.4 Al: 5.9 ± 0.7 V: 4.2 ± 0.2
BMG_Sn2	Ti40Zr10Cu34Pd14Sn2	Ti: 40 ± 1.2 Zr: 11 ± 1 Cu: 34 ± 1.5 Pd: 14 ± 0.6 Sn: 2 ± 0.3
BMG-Pd14	Ti40Zr10Cu36Pd14	Ti: 40 ± 1.5 Zr: 11 ± 0.8 Cu: 35 ± 1.6 Pd: 14 ± 0.8
BMG_Sn2 Si	Ti40Zr10Cu33Pd14Sn2Si	Ti: 40 ± 1.2 Zr: 11 ± 1 Cu: 33 ± 1.5 Pd: 14 ± 0.6 Sn: 2 ± 0.3 Si: 1 ± 0.1

6.3.2 Polarisation curves

Prior to any MACC experiments, the polarisation curves of the as-received materials were studied. To obtain the exact surface area, the back of the pin was sealed with Araldite. Then polarisation curve measurements were carried out in 0.9% NaCl at room temperature. These measurements are not MACC tests, but provide the basic electrochemical information which could be used as the baseline for the following MACC test data. As shown in Figure 6-3, Ti6Al4V stays passive, giving a passive current density of 3×10^{-3} mA/cm². The metallic glasses show clear pitting behaviour with the pitting potential following the order of: $E_{pit}(\text{Sn2Si}) > E_{pit}(\text{Sn2}) > E_{pit}(\text{Pd14})$. The passive

current of Sn2 and Sn2Si is approximately equal to that of Ti6Al4V, while the passive current of Pd14 is higher than all others.

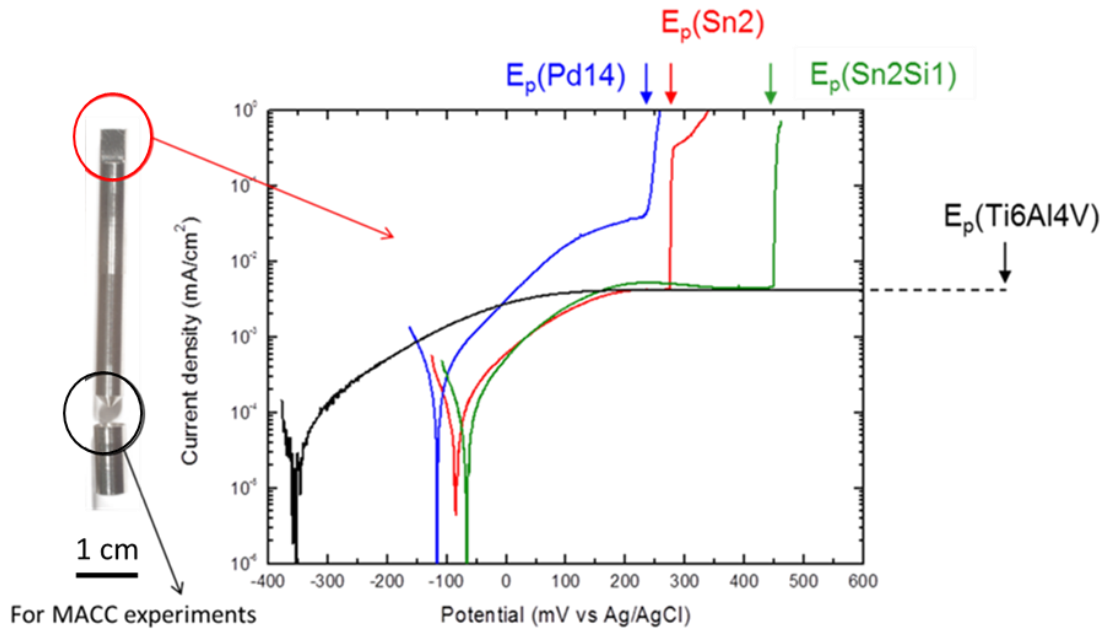


Figure 6-3 Anodic polarisation curves of the as-received materials, Ti6Al4V and three metallic glasses.

6.3.3 Hardness

Table 6-2 shows the hardness of all MACC samples follows the order of: BMG_Sn2Si > BMG_Sn2 ≈ BMG_Pd14 > Ti6Al4V. The hardness for metallic glasses is higher than that of Ti6Al4V.

Table 6-2 Hardness of MACC samples (n=15)

Material	Hardness (Vickers)
Ti6Al4V	349±6
BMG_Sn2 (Ti ₄₀ Zr ₁₀ Cu ₃₄ Pd ₁₄ Sn ₂)	577±8
BMG_Pd14 (Ti ₄₀ Zr ₁₀ Cu ₃₆ Pd ₁₄)	561±7
BMG_Sn2Si (Ti ₄₀ Zr ₁₀ Cu ₃₃ Pd ₁₄ Sn ₂ Si)	624±10

6.4 MACC polarisation curves

The effect of MACC on the electrochemical behaviour of the alloys was evaluated by measuring polarisation curves when the cup and pin were stationary and comparing them with the electrochemical behaviour during rotation between the cup and pin.

Figure 6-4 (a-d) shows a series of experiments (with fresh electrolyte) in which the static OCP was measured, and then a potential of 50 mV below the OCP was applied and the potential was then increased without any rotation (labelled as 'static'). The solution was then replaced, and the same measurement made with continuous rotation (labelled as 'rotation'). Note that the y-axis is current instead of current density because the actual contact area cannot be defined during rotation. The low rotation speed (0.1 rpm) was extensively used in this work because large scale of peripheral motion between implant and bone/tissues does not happen in a clinical situation. In the case of Ti6Al4V (Figure 6-4 a), the static polarisation curve shows an OCP of -200 mV vs. Ag/AgCl, and then a passive region with a small increase in current (growth of the passive film) is seen above 800 mV vs. Ag/AgCl. However, during rotation, the OCP is -600 mV vs. Ag/AgCl, and there is a high current immediately above the OCP.

All of the BMG samples (Figure 6-4 b-d) show a passive region above the OCP that is similar to that of Ti6Al4V for the static measurements. At higher potentials, unlike Ti6Al4V, the BMG samples show a sharp increase in current at a 'pitting potential' that is associated with localised corrosion (pitting). However, during rotation, the BMGs

show significantly lower increase in anodic current. However, rotation does decrease the susceptibility to pitting, which happens at a lower potential.

For biomedical devices, the corrosion potential of an external surface outside any crevice is likely to dominate the corrosion potential of the device, so the risk of corrosion in the crevice can be estimated by looking at the current flowing from the surface during rotation at the OCP in the absence of rotation. In this case, the current flowing from the Ti6Al4V couple is approximately an order of magnitude greater than that of the BMG couples.

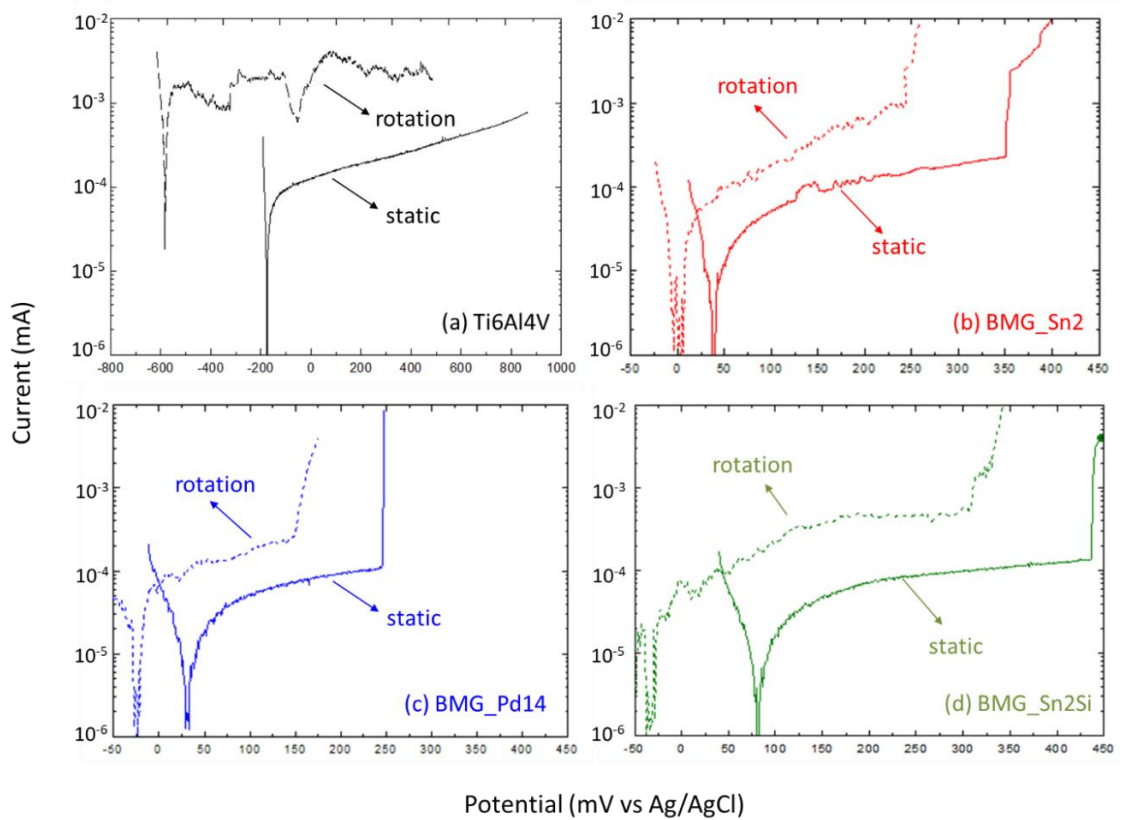


Figure 6-4 Anodic polarization curves for (a) Ti6Al4V, and three metallic glasses: (b) BMG_Sn2, (c) BMG_Pd14, and (d) BMG_Sn2Si. The curves labelled with 'rotation' were measured with 0.1 rpm rotation. The curves labelled with 'static' were measured without rotation. All curves were measured with 634 g load. Fresh solution was supplied for each measurement (curve).

The cathodic polarisation curves (Figure 6-5) measured under 634 g and 0.1 rpm do not show major differences when compared with the ones measured under static conditions, for both Ti6Al4V (a) and metallic glasses (b-d). In theory, stirring the bulk solution may facilitate the access of oxygen, which should accelerate the oxygen reduction reaction, if the reaction is dominated by mass transfer. However, in this case, 0.1 rpm is too slow to cause any measurable differences. Based on mixed potential theory, if the cathodic reaction rate is unchanged at a rotation speed, the shift of OCP is only due to the anodic reaction rate.

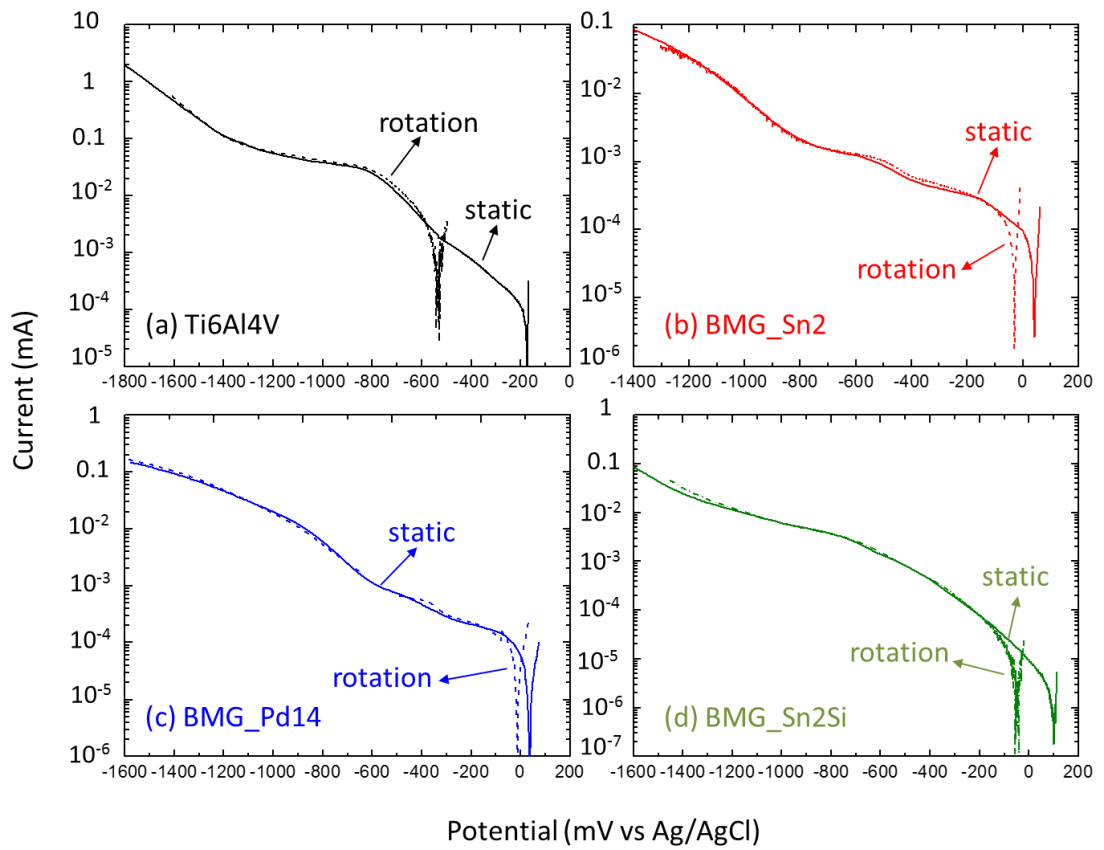


Figure 6-5 Cathodic polarization curves for (a) Ti6Al4V, and three metallic glasses: (b) BMG_Sn2, (c) BMG_Pd14, and (d) BMG_Sn2Si. The curves labelled with 'rotation' were measured with 0.1 rpm rotation. The curves labelled with 'static' were measured without rotation. All curves were measured with 634 g load. Fresh solution was supplied for each measurement (curve).

6.5 Potentiostatic measurements

To evaluate the current response of metallic glasses and Ti6Al4V at constant potential, potentiostatic measurements were carried out. The potential was held at 100 mV vs Ag/AgCl since this potential stays within the passive region for all of the alloys. The load applied was 634 g and rotation speed was 0.1 rpm. The current response is shown in Figure 6-6. Figure 6-6 (b) is the magnified view of (a) to show the potentiostatic current for metallic glasses. It shows the current given by Ti6Al4V is much higher than that of metallic glasses, e.g. the current for Ti6Al4V starts at 1 μ A and gradually increases up to 3 μ A, while the current for metallic glasses is below 0.6 μ A. The overall tendency was that the current of Ti6Al4V increased with time, while the current for BMGs did not give a clear tendency within the test period (16 ks). The reason for this may be the damage to the passive film gets increasingly worse for Ti6Al4V due to its relatively poor wear resistance.

The integrated charge is also shown in Figure 6-7 and is again approximately one order of magnitude greater for Ti6Al4V when compared with the BMGs.

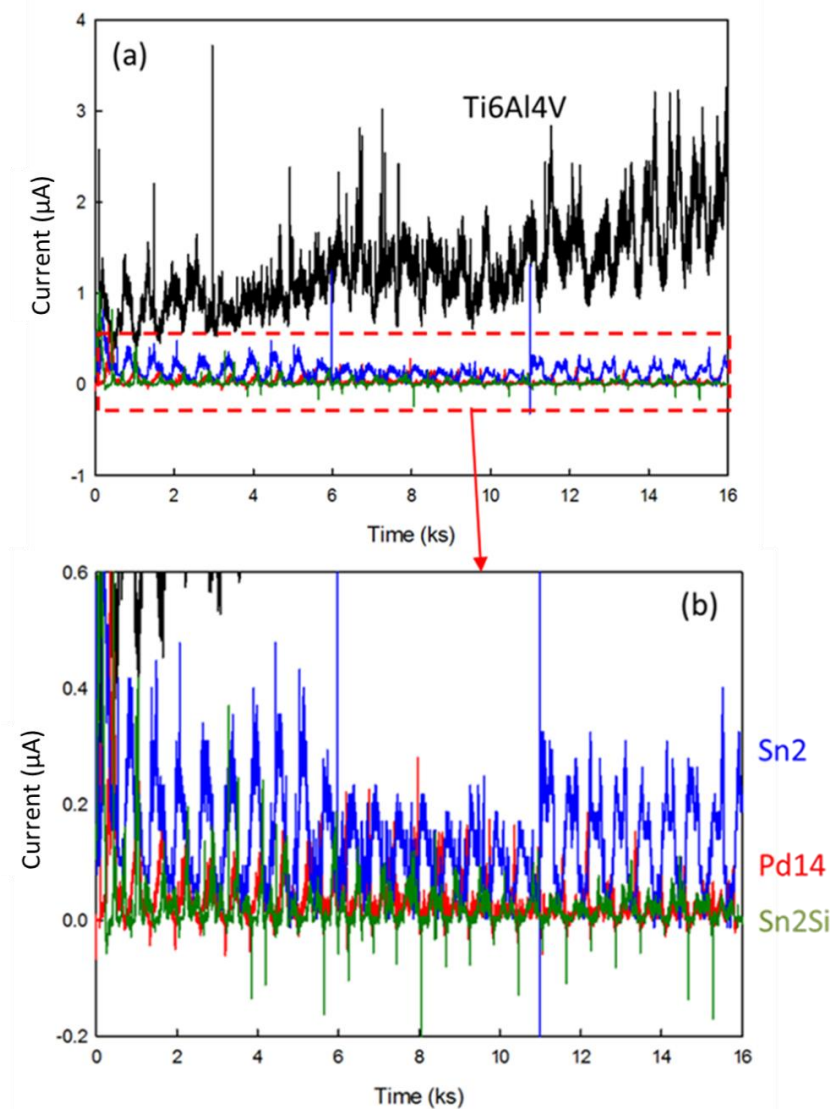


Figure 6-6 (a) Potentiostatic measurement for three metallic glasses and Ti6Al4V. Potential was held at 100 mV vs Ag/AgCl, rotation speed was 0.1 rpm, load applied was 634 g. (b) is the magnified view of three metallic glass samples.

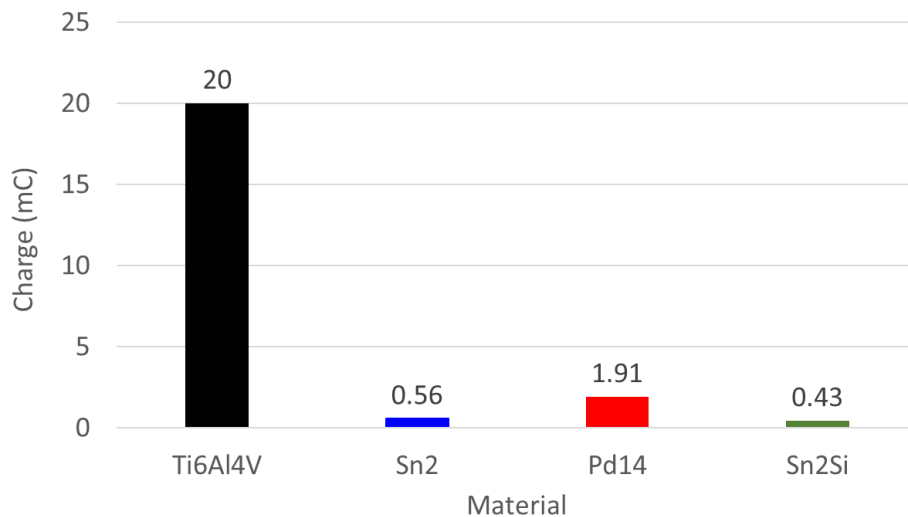


Figure 6-7 Charge accumulated from potentiostatic measurements.

6.6 Effect of load and speed on MACC of Ti6Al4V and metallic glasses

6.6.1 Typical OCP behaviour

Figure 6-8 shows a preliminary experiment to explore changes in potential during MACC experiments (MACC potential). The test material was Ti6Al4V, with 634 g load and 0.1 rpm rotation speed. It shows that once the rotation started (0.8 ks), the OCP exhibited a sudden and sharp decrease from -0.14 to -0.63 V vs Ag/AgCl. During rotation, the potential changed periodically with time and the duration between two peaks is 10 mins, which is the time for a single rotation of the pin (Figure 6-8 b). During the rotation, the contact area varies leading to changes in the wear damage and corresponding changes are seen in the MACC potential.

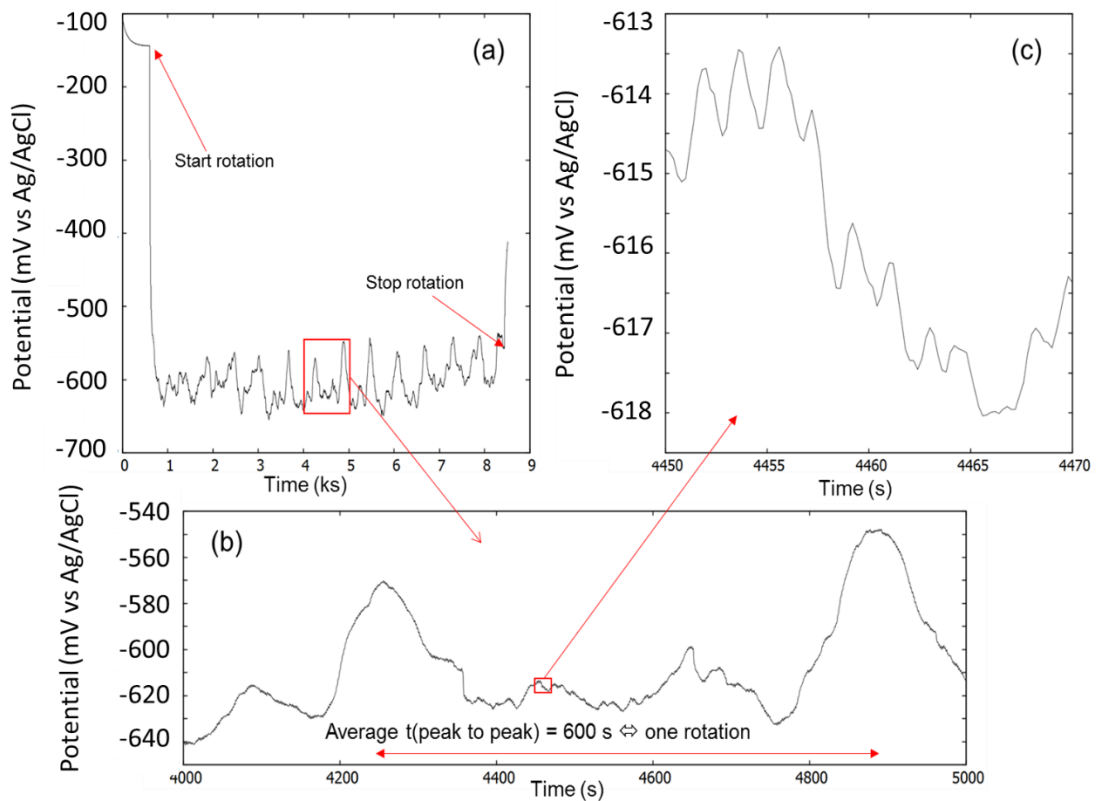


Figure 6-8 MACC potential measurement on Ti6Al4V, load applied was 634 g, rotation speed was 0.1 rpm. Solution: 0.9% NaCl. (b) and (c) are the higher magnified view of (a).

6.6.2 Effect of load and rotation speed on MACC

An experiment was set up to explore the effect of load and rotation speed on the MACC potential. However, during the course of the experiment, the surfaces of the components will change as a function of time as a result of abrasion. In order to take this into account, four repeat experiments were carried out on the same sample. For each experiment, the cup and pin were cleaned, and fresh electrolyte was added. For

experiments 1 and 3, a load of 634 g was applied, and for experiments 2 and 4, a load of 50 g was applied. For all runs, the rotation speed was varied in the same way, with the same speed being applied at the beginning and at the end of the test.

Figure 6-9 (a) shows the change in potential during the course of the four experiments. At the initial rotation speed of 0.1 rpm, it can be seen that the MACC potential is lower (indicating more severe MACC) for run_1 and run_3 (634 g, black and red lines) than for run_2 and run_4 (50 g, blue and green lines), indicating that the effect of load is more significant than the effect of accumulated abrasion. However, the effect of accumulative abrasion can be observed as the MACC potential of run 3 (red) is lower than run 1 (black) and that of run 4 (green) is lower than run 2 (blue). The exceptions are selected and indicated with circles in Figure 6-9 (b).

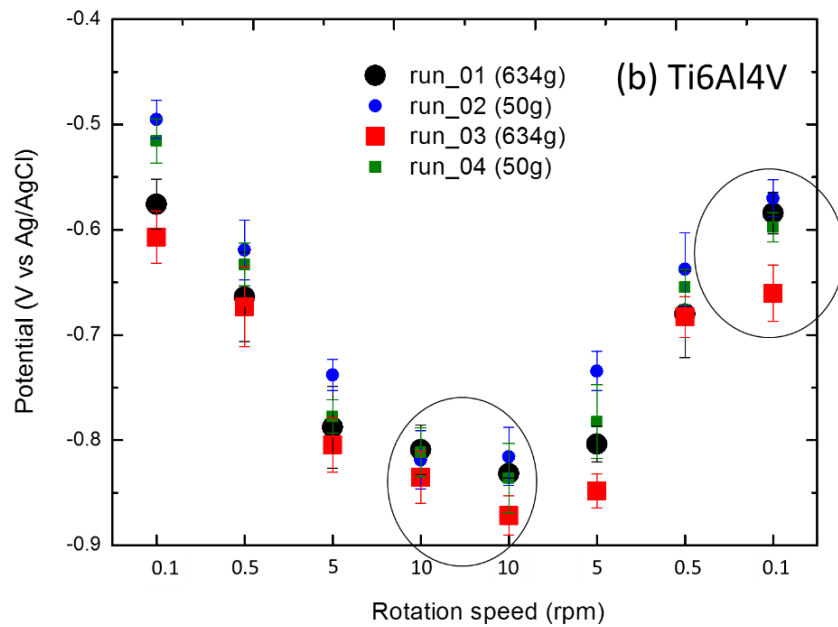
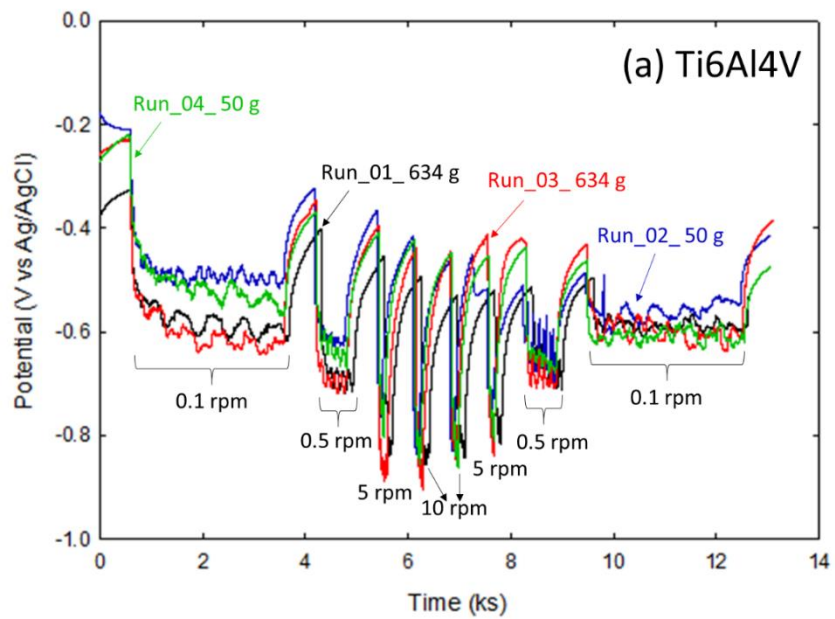


Figure 6-9 (a) OCP of Ti6Al4V versus load and rotation speeds. The load applied follows the order: run_01 (634 g), run_02 (50 g), run_03 (634 g) and run_04 (634 g). In one run, the rotation speed follows the order of 0.1 rpm- 0.5 rpm- 5 rpm- 10 rpm- 10 rpm- 5 rpm- 0.5 rpm- 0.1 rpm. (b) MACC potential (potential during rotation) vs. rotation speed.

Figure 6-10, Figure 6-11 and Figure 6-12 show the OCP values of BMG_Sn2, BMG_Pd14 and BMG_Sn2Si respectively, which were measured with same procedure as used for Ti6Al4V. Similar to Ti6Al4V, the MACC potential of metallic glass samples drops down with higher speeds and a higher applied load, and increased with lower speeds and a lighter load.

The 'repassivation potential' of BMG_Sn2 measured in Figure 4-3 is 81 mV vs SCE (0.13 V vs Ag/AgCl). In Figure 6-10, it is the potential that is reached after MACC (rotation). It is the mixed potential that develops when the anodic current drops as the corrosive solution between the two surfaces in the MACC device diffuses away and the metal surfaces repassivate.

In measurements under anodic polarisation, the pitting potential is the point at which a particular pit is able to grow when the rate of ion production (dissolution) within the pit is larger than rate of ion diffusion out of the pit such that a corrosive solution is maintained within the pit. When the sweep potential is reversed, at some point the rate of ion production is smaller than the rate of ion escape by diffusion, the pit chemistry cannot be maintained, thereby the active dissolution is depressed and repassivation happens.

The difference between the two situations is that in the open circuit MACC tests, the repassivation potential is a mixed potential that depends on the kinetics of both the anodic and cathodic reactions, whereas in the case of potentiodynamic measurements

of the repassivation potential, the value is determined by the anodic reaction in the pit alone. It is therefore difficult to compare the two precisely.

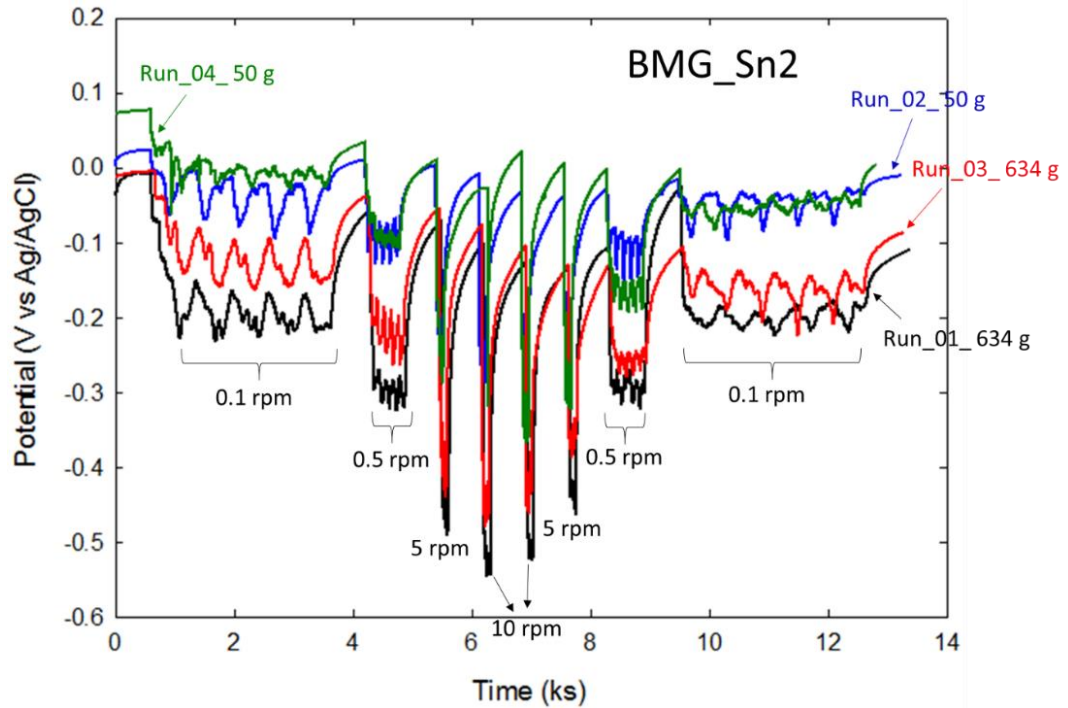


Figure 6-10 MACC potential of BMG_Sn2 versus load and rotation speed. The load applied follows the order: run_01 (634 g), run_02 (50 g), run_03 (634 g) and run_04 (634 g). In one run, the rotation speed follows the order of 0.1 rpm- 0.5 rpm- 5 rpm- 10 rpm- 10 rpm- 5 rpm- 0.5 rpm- 0.1 rpm.

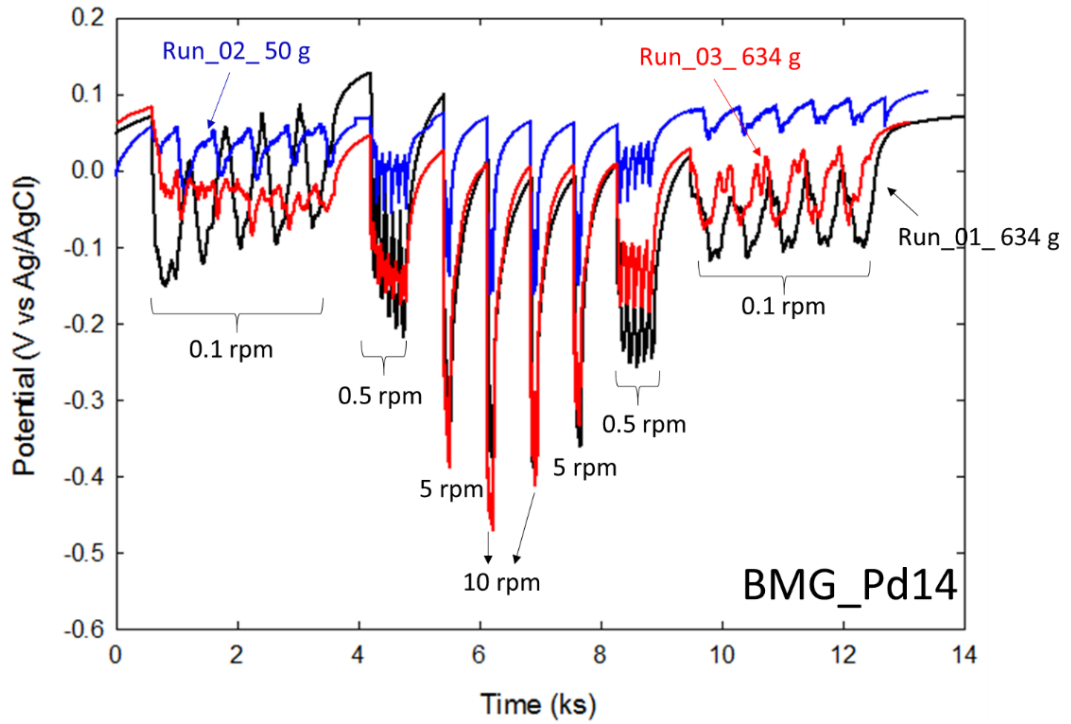


Figure 6-11 MACC potential of BMG_Pd14 versus load and rotation speed. The load applied follows the order: run_01 (634 g), run_02 (50 g), run_03 (634 g). In one run, the rotation speed follows the order of 0.1 rpm- 0.5 rpm- 5 rpm- 10 rpm- 10 rpm- 5 rpm- 0.5 rpm- 0.1 rpm.

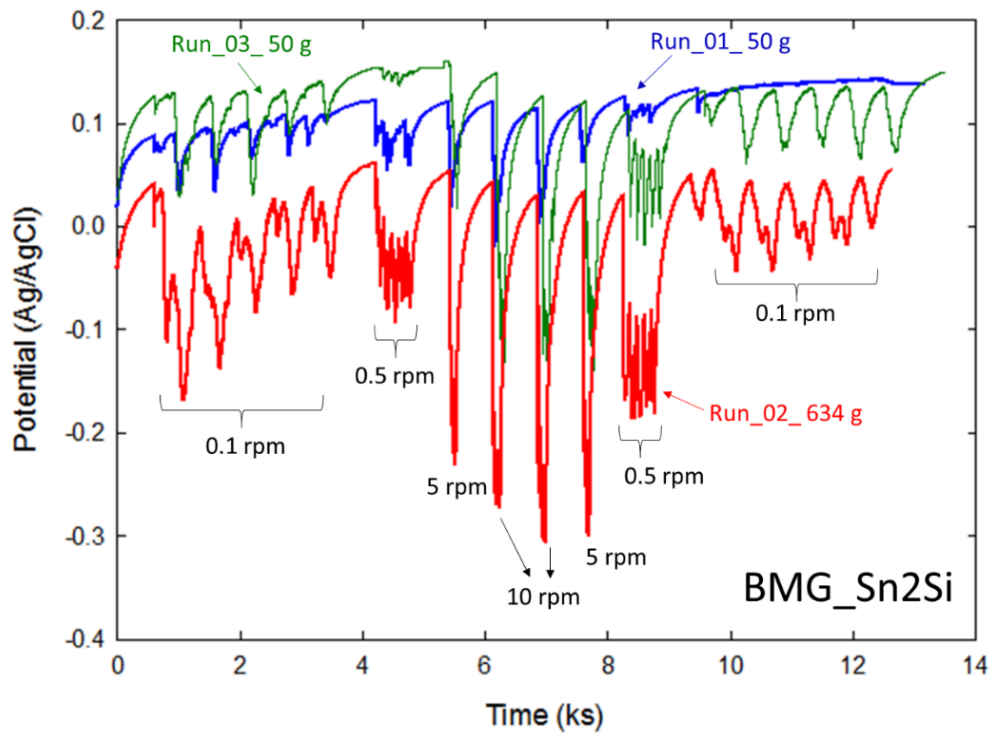


Figure 6-12 MACC potential of BMG_Sn2Si versus load and rotation speed. The load applied follows the order: run_01 (50 g), run_02 (634 g) and run_03 (634 g). In one run, the rotation speed follows the order of 0.1 rpm- 0.5 rpm- 5 rpm- 10 rpm- 10 rpm- 5 rpm- 0.5 rpm- 0.1 rpm.

6.6.3 Time-dependence of MACC potential

To better study the ‘time-dependent effects’, the potential values under the same condition but in a different time sequence were analysed. Specifically, the average values of MACC potentials in each run (y axis), which are under the same loading condition, are plotted against rotation speeds (x axis). The potentials observed in the stage of ‘increasing rotation speed’ (0.1 rpm- 0.5 rpm- 5 rpm- 10 rpm) are connected with solid lines and those in the later stage of ‘decreasing rotation speed’ (10 rpm- 5

rpm- 0.5 rpm- 0.1 rpm) are connected with dashed lines. Figure 6-13 shows the MACC potentials of Ti6Al4V changes with time, loads and rotation speeds. Firstly, both solid and dashed lines exhibit a negative slope, which means the higher the rotation speed is, the lower the potential will be. The dashed line is also consistently below the solid line, indicating that the potentials at later stage (10 rpm- 5 rpm- 0.5 rpm- 0.1 rpm) are less than those at early stage (0.1 rpm- 0.5 rpm- 5 rpm- 10 rpm). This is because the surface becomes increasingly more disrupted with each rotation and it is likely that the contact areas at later stages of the experiment were larger than those seen initially. We can also compare different runs under the same loading conditions. For example, run_01 and run_03, (634 g). Here, we can only compare the potentials at same stage (compare points connected by solid lines or by dashed lines) because each time we used a fresh solution, and the local chemistry would be different at early and later stage. Using this approach, it clearly shows that the potentials in the later run are less than those in early run (e.g. run_03 is below run_01, run_04 is below run_02). These findings strongly indicate the MACC potentials of Ti6Al4V are time-dependant.

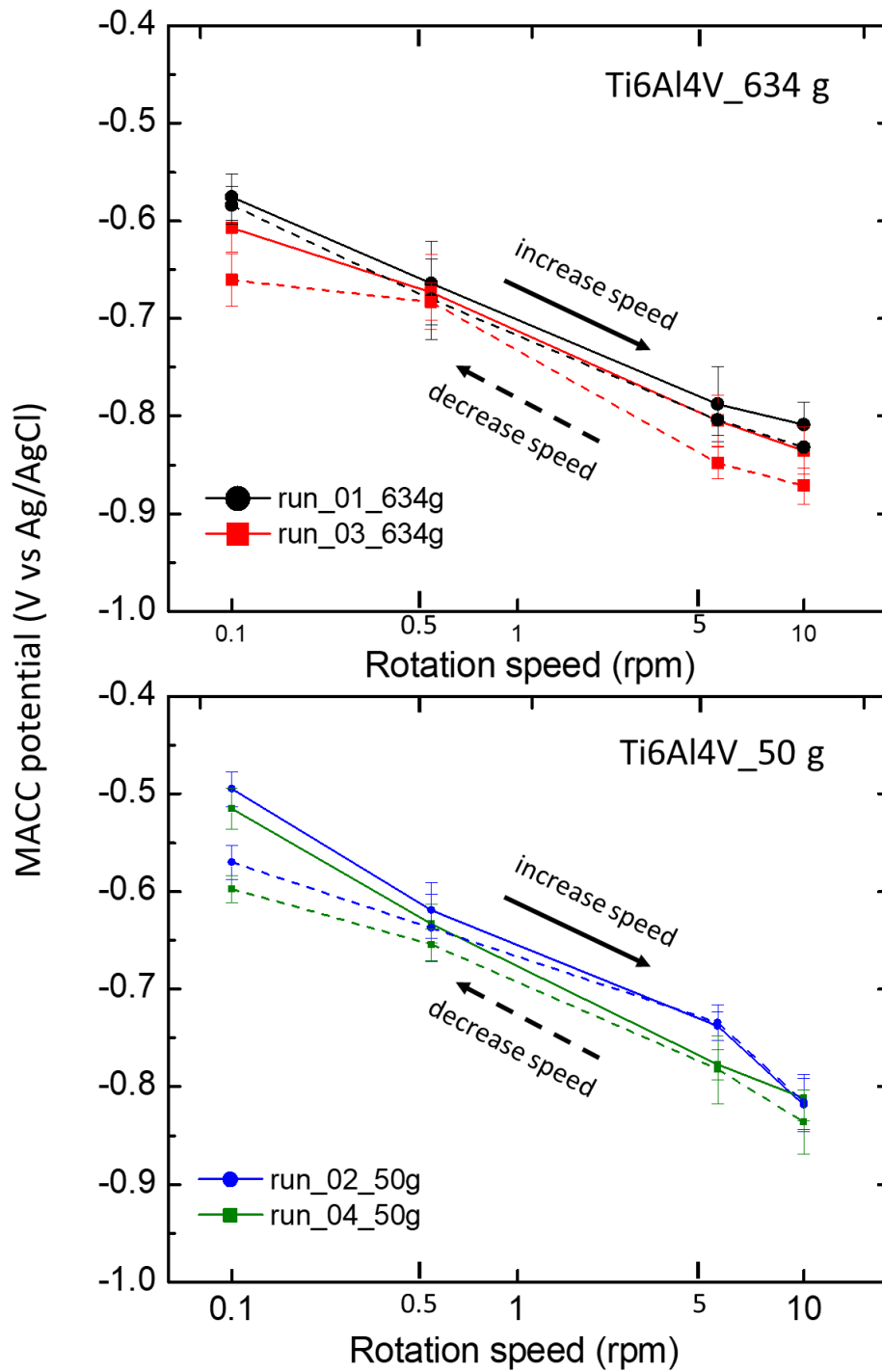


Figure 6-13 MACC potential of Ti6Al4V versus load and rotation speeds. Solid line for increasing speed (0.1 rpm- 0.5 rpm- 5 rpm- 10 rpm) and dashed line for decreasing speed (10 rpm- 5 rpm- 0.5 rpm- 0.1 rpm).

Figure 6-14 shows the MACC potential of BMG_Sn2 changes with time, load, and rotation speed. In common with Ti6Al4V, run_01 and run_03 are under loads of 634 g, while run_02 and run_04 are under loads of 50 g. However, the MACC potential of BMG_Sn2 does not show the same time-dependence as seen for Ti6Al4V. For example, under a load of 634 g, the red lines (run_03) remain above the black lines (run_01). In addition, within one run (e.g. run_01), the potential at the later stage (dashed line) is not always lower than that observed at early time points (solid line). However, the MACC potential still follows a trend that heavier loading or faster rotation lead in general to a lower potential value; for instance, at 0.1 rpm, the MACC potential under a load of 634 g is -0.2 V- -0.1 V vs Ag/AgCl while that under a load of 50 g is -0.1 V- 0 V vs Ag/AgCl.

The MACC potentials of BMG_Pd14 and BMG_Sn2Si, are shown in Figure 6-15 and Figure 6-16 respectively and are similar to that of BMG_Sn2. They also do not show time-dependence with the potentials at early runs or stages overlapping with those in later runs or stages for a consistent load. The data are still in good agreement that heavier loads or faster rotation correlate with a lower potential. Essentially, there is no difference between the three metallic glasses and neither of them show a time-dependency in the MACC potential.

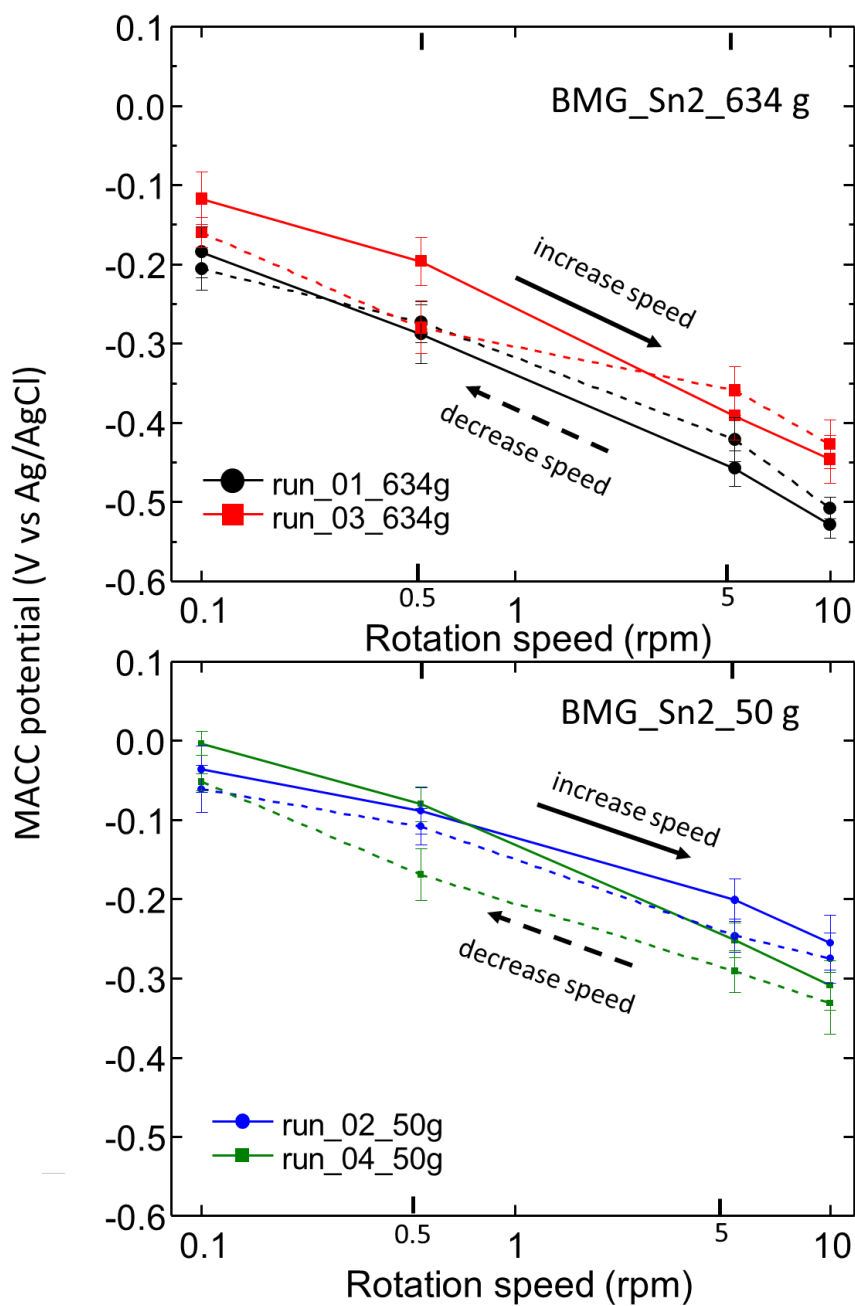


Figure 6-14 MACC potential of BMG_Sn2 versus load and rotation speeds. Solid line for increasing speed (0.1 rpm- 0.5 rpm- 5 rpm- 10 rpm) and dashed line for decreasing speed (10 rpm- 5 rpm- 0.5 rpm- 0.1 rpm).

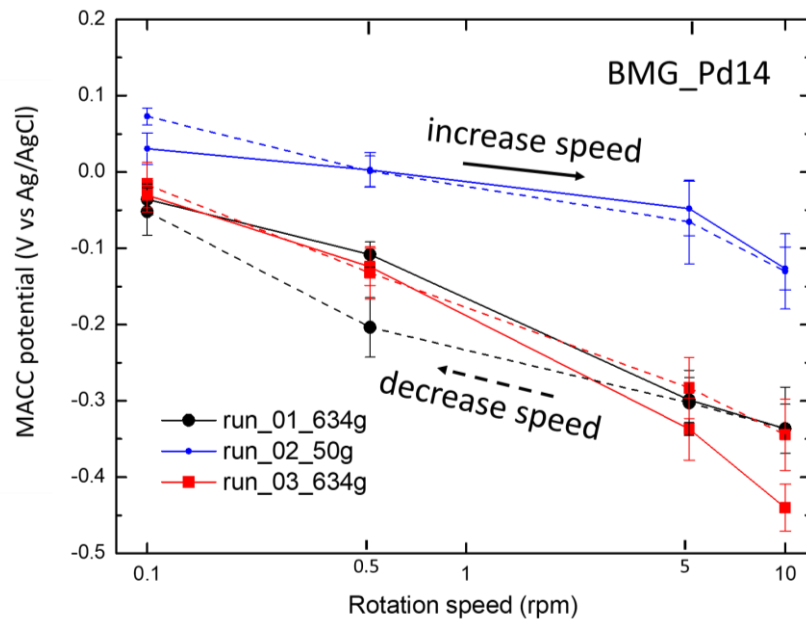


Figure 6-15 MACC potential of BMG_Pd14 versus load and rotation speeds. Solid line for increasing speed (0.1 rpm- 0.5 rpm- 5 rpm- 10 rpm) and dashed line for decreasing speed (10 rpm- 5 rpm- 0.5 rpm- 0.1 rpm).

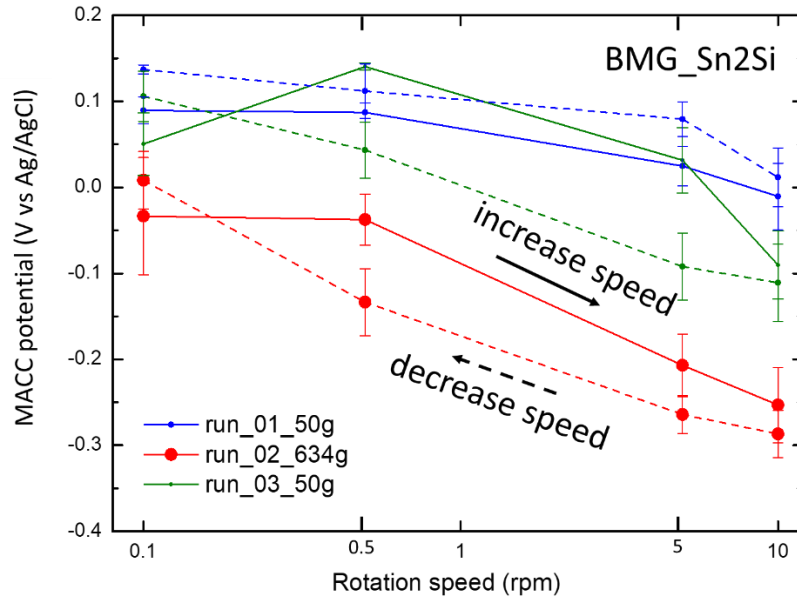


Figure 6-16 MACC potential of BMG_Sn2Si versus load and rotation speeds. Solid line for increasing speed (0.1 rpm- 0.5 rpm- 5 rpm- 10 rpm) and dashed line for decreasing speed (10 rpm- 5 rpm- 0.5 rpm- 0.1 rpm).

6.7 MACC current

The corrosion potential of a device in the body is generally likely to be controlled by the corrosion potential of the passive surface, which is given by the static measurements. This external potential can polarise the active interface in the crevice so that it becomes a net anode, as illustrated in Figure 6-4. It is clear from Figure 6-5 that the cathodic reaction does not appear to be affected by rotation (0.1 rpm). This is not surprising since it would be expected that the cathodic current is due to the reduction of oxygen, and oxygen is likely to be depleted in the crevice between the cup and pin. This means that the net cathodic current measured in the static measurement will be equal and opposite to the anodic current at the same potential during rotation. This is shown in Figure 6-17 (a), where the red dot shows this value.

A reasonable estimate of the corrosion rate in the crevice can then be measured by controlling the potential at the static OCP and then measuring anodic currents flowing during rotation or controlling the potential at the rotation OCP and then measuring cathodic currents flowing in static condition. This measured current is a valid assessment of the MACC current as the cathodic reaction is largely unaffected by rotation.

Figure 6-17 (b) summarizes the MACC currents for all test materials. It is estimated by controlling the potential at the MACC potentials and then measuring currents flowing during static. Under same load (50 g or 634 g) and rotation (0.1 rpm), the MACC currents for BMGs are between 0 to 350 nA while that is 1000 nA- 8000 nA for Ti6Al4V.

In other words, Ti6Al4V would release at least 22 times as much metal ions as BMGs in the case that implants have same dimensions.

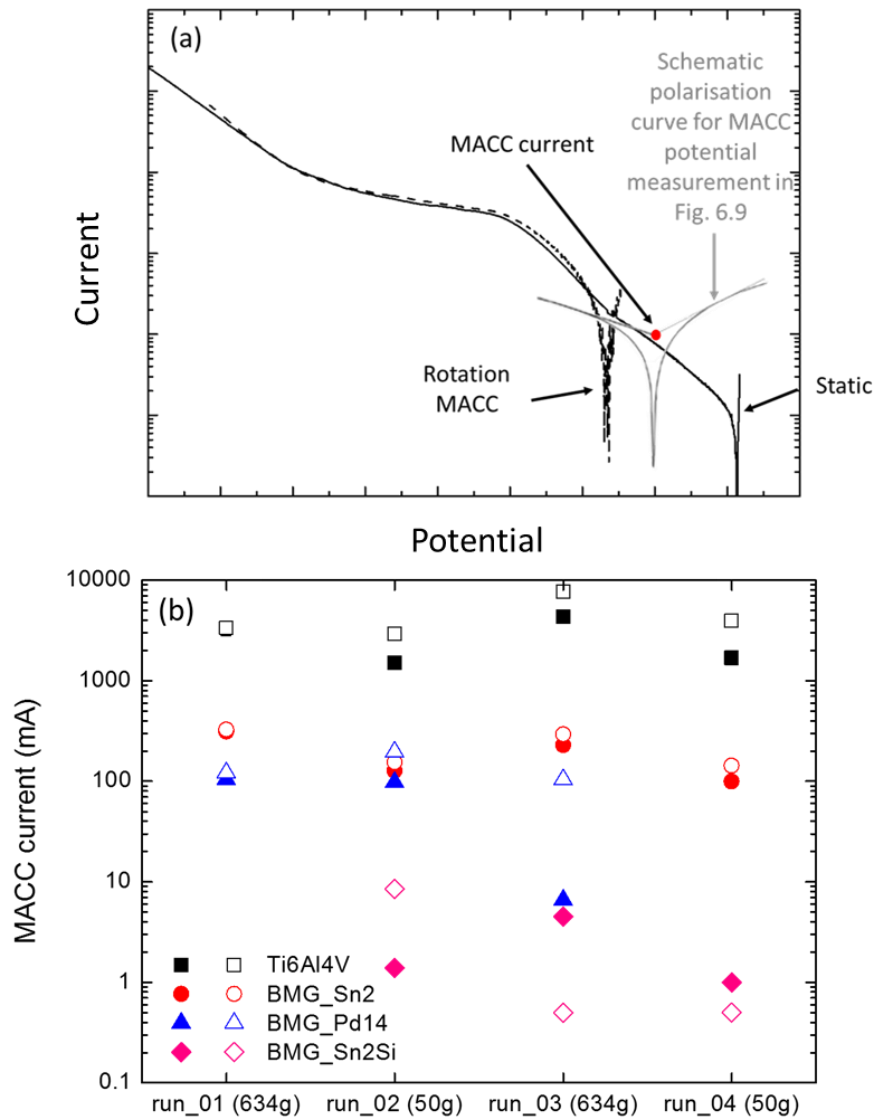
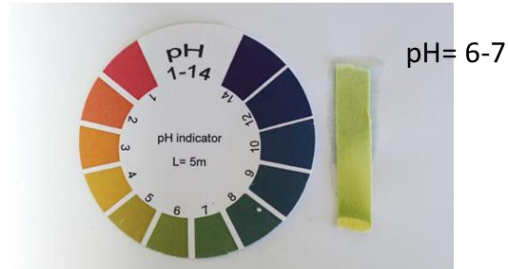


Figure 6-17 (a) Schematic diagram to show how the MACC current was obtained. The cathodic current under static condition can be used to estimate MACC current due to the equivalence of the cathodic current under rotation and static conditions. (b) MACC current for all test materials. Closed symbols for MACC current at 0.1 rpm at early stage, open symbols for MACC current at 0.1 rpm at later stage.

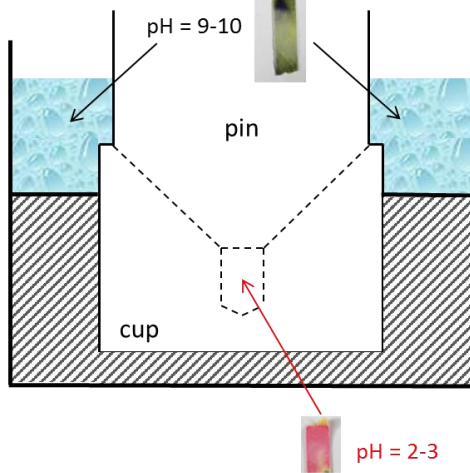
6.8 pH variation

The pH in the crevice formed between the pin and cup of the device was measured by pH indicator paper (Camlab, UK). After run_01 in Figure 6-9, the bulk electrolyte was removed with a syringe, and a small drop of solution was put on the indicator paper. Then the solution in the small cavity between pin and cup was extracted with a microliter syringe, and the pH measured. Figure 6-18 (a) is the photograph of pH paper showing the pH of bulk solution before the experiment. 0.9 wt.% NaCl always shows weak acidity due to the dissolution of CO₂ to the solution. Figure 6-18 (b) and (c) show the pH in cavity of Ti6Al4V sample and BMG_Sn2 sample respectively. The Ti6Al4V sample gave strong acidity (pH= 2-3) in the cavity and alkalinity in bulk solution (pH=9-10). However, with same MACC history, the metallic glass sample showed little change in pH, as seen in (c), the pH was between 6-7 in both the cavity and bulk solution. Note that pH values for all BMG samples were identical.

(a) Bulk solution before test



(b) Ti6Al4V



(c) BMGs

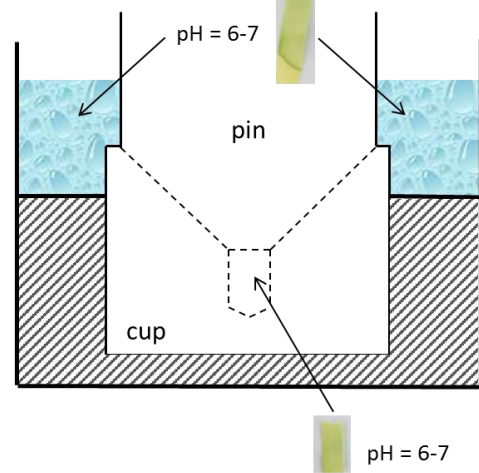


Figure 6-18 (a) is the pH value of solution before experiment started, the solution is in weak acidity. pH variation of (b) Ti4Al4V, (c) BMG samples after OCP measurement in Figure 6-9, load applied during OCP measurement was 634 g, rotation speed was as indicated in Figure 6-9. The pH values of all BMG samples were identical.

6.9 Abrasion damage

The products produced by MACC are important as they have potentially biological relevance if produced clinically. For Ti6Al4V, after 10.5 hours of MACC testing (634 g and 1 rpm), black products were seen to overflow from the cup component and are shown in Figure 6-19 (a). The test was subsequently terminated. For the metallic glasses, under same load and rotation speed, there were no discernible products after 10.5 h, so the test was continued for a longer time (3 days). As shown in Figure 6-19 (b), even after this extended period of testing for the metallic glass the cell remained clear of visual debris. Subsequently, the surface morphologies of samples, including Ti6Al4V and metallic glassed, were compared with their as-received state. Figure 6-20 shows that the as-received samples are shiny and have metallic lustre. After 10.5 h MACC test, the surface of Ti6Al4V was covered with a black layer and has deep scratches. For the metallic glass, only a small central region had corrosion-wear appearance with the most peripheral region keeping its metal-lustre feature. Figure 6-21 and Figure 6-22 show more details of the surface morphologies of Ti6Al4V and BMG_Sn2Si. Clearly, the corrosion products of Ti6Al4V were distributed everywhere on the sample surface and fully filled in the grooves. While for BMG_Sn2Si, only several small areas show corrosion-wear track and most of the as-machined grooves were still preserved.

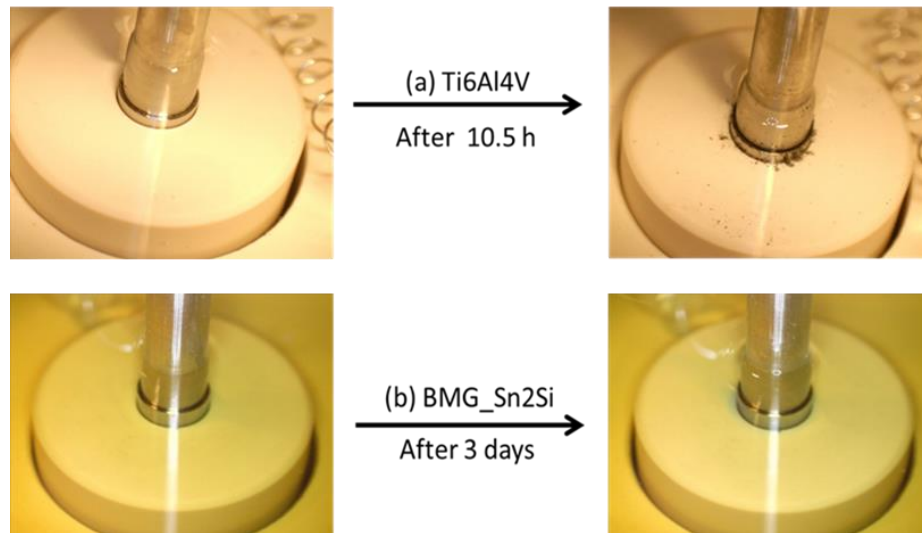


Figure 6-19 The photographs of the MACC cell of (a) Ti6Al4V lasting for 10.5 h and (b) BMG_Sn2Si lasting for 3 days under 634 g load and 1 rpm.

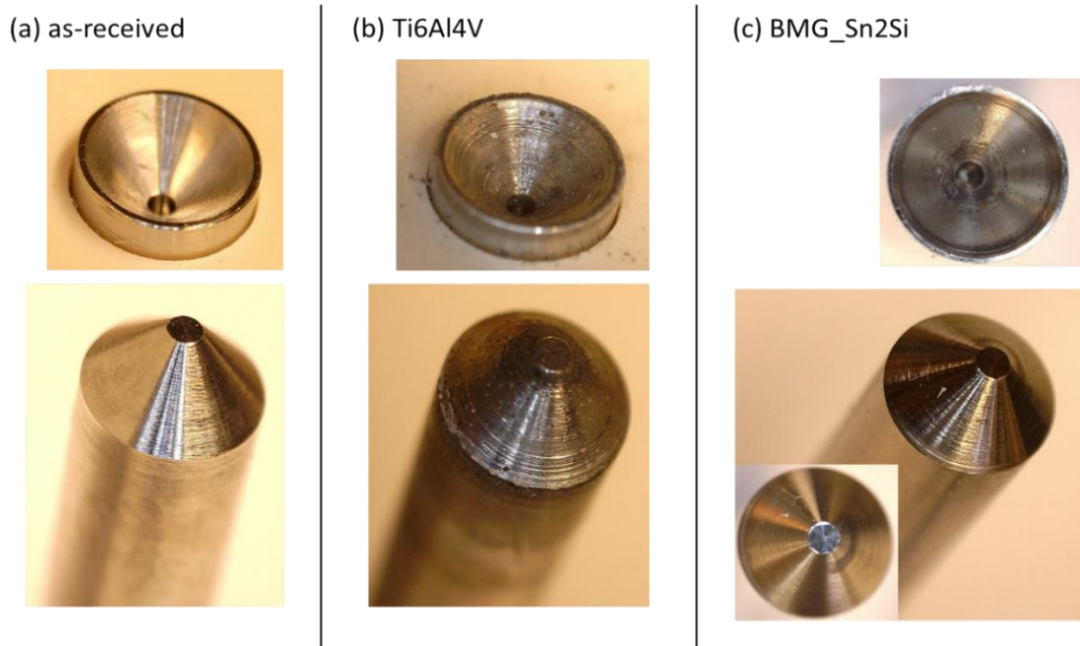


Figure 6-20 The photographs of the uncoupled pin and cup of (a) Ti6Al4V lasting for 10.5 h and (b) BMG_Sn2Si lasting for 3 days under 634 g load and 1 rpm.

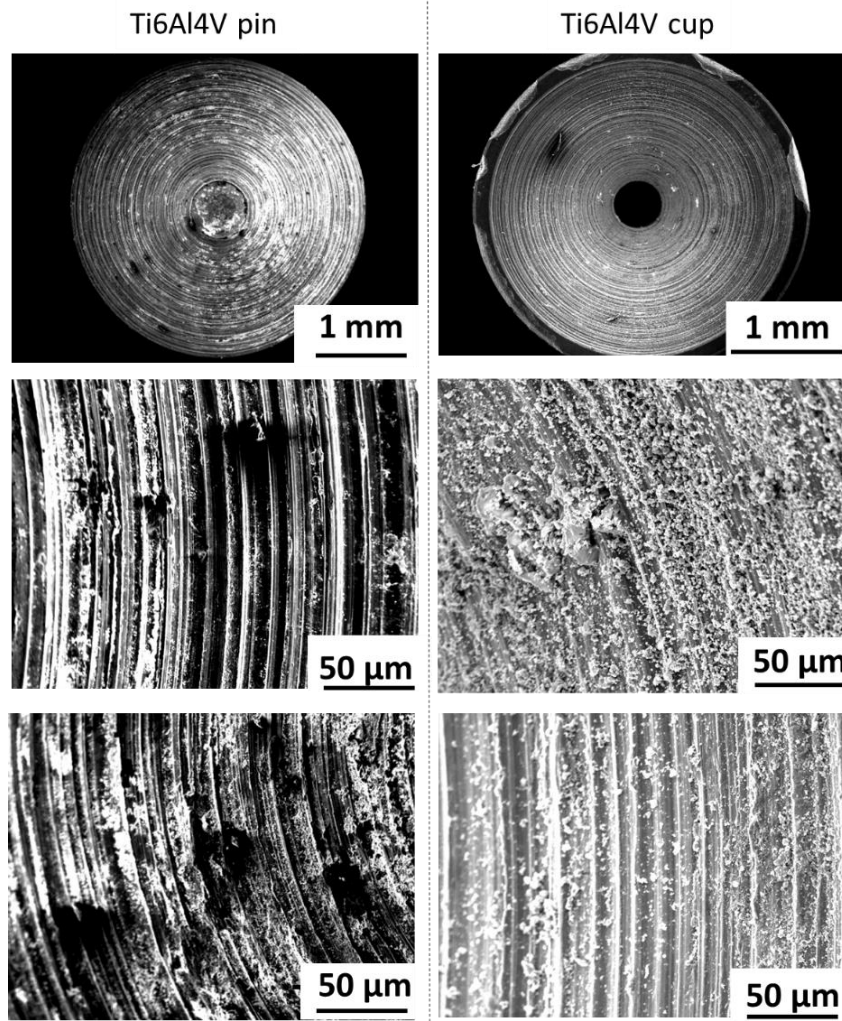


Figure 6-21 SEM images of surface morphologies of Ti6Al4V after 10.5 MACC (634 g, 1 rpm) experiment.

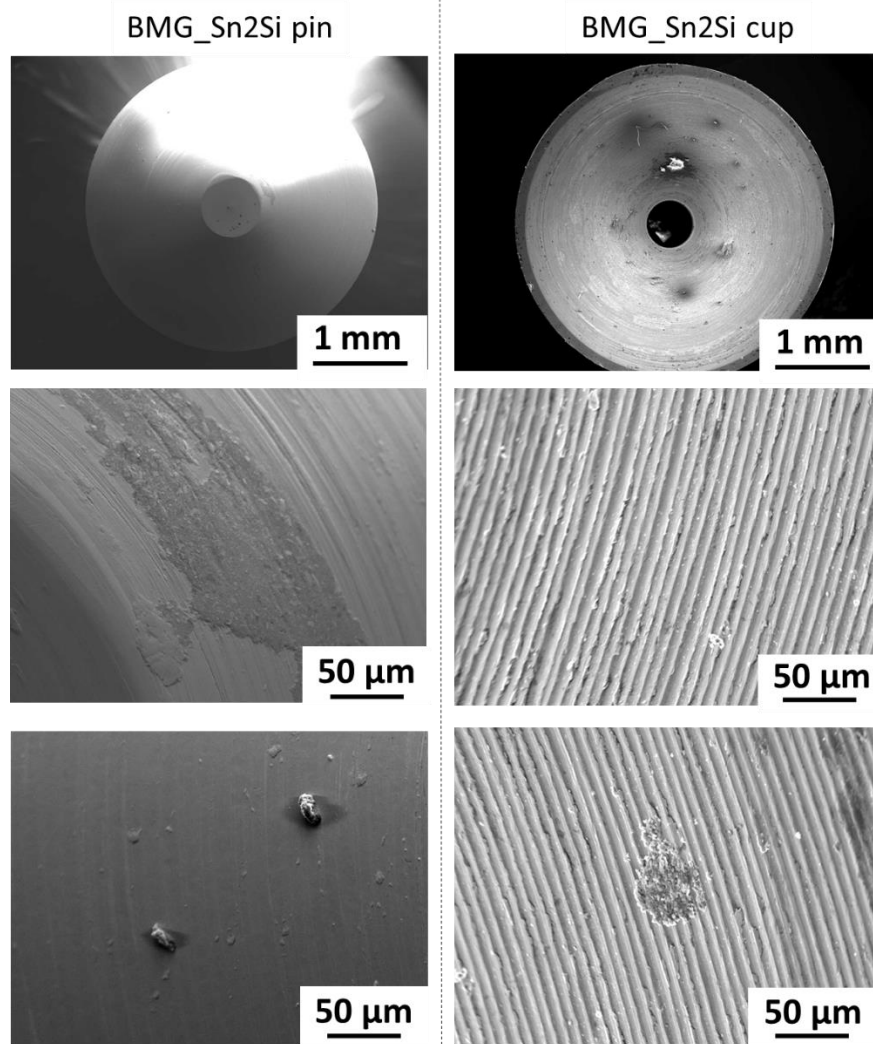


Figure 6-22 SEM images of surface morphologies of BMG_Sn2Si after 3 days MACC (634 g, 1 rpm) experiment.

6.10 Wear debris

The black corrosion products associated with Ti6Al4V can be seen from Figure 6-19 (a). The products were collected and diluted with deionised water (Millipore, >15 MΩcm). After dissolving in deionised water for 12 hours, some insoluble black material remained. One drop of solution was extracted and put on TEM support grid (Agar Scientific, UK) then entirely dried in a clean environment. SEM (JEOL7000, JEOL Ltd.) was used to observe the morphology of products generated by Ti6Al4V, and images are shown in Figure 6-23, revealing that the MACC products are clusters of metallic fragments, micro-meter in scale. The chemical composition was analysed by EDX (Oxford Instrument, UK) and shows that there is considerable amount of oxygen in the products, which may derive from metal oxides or metal hydroxides.

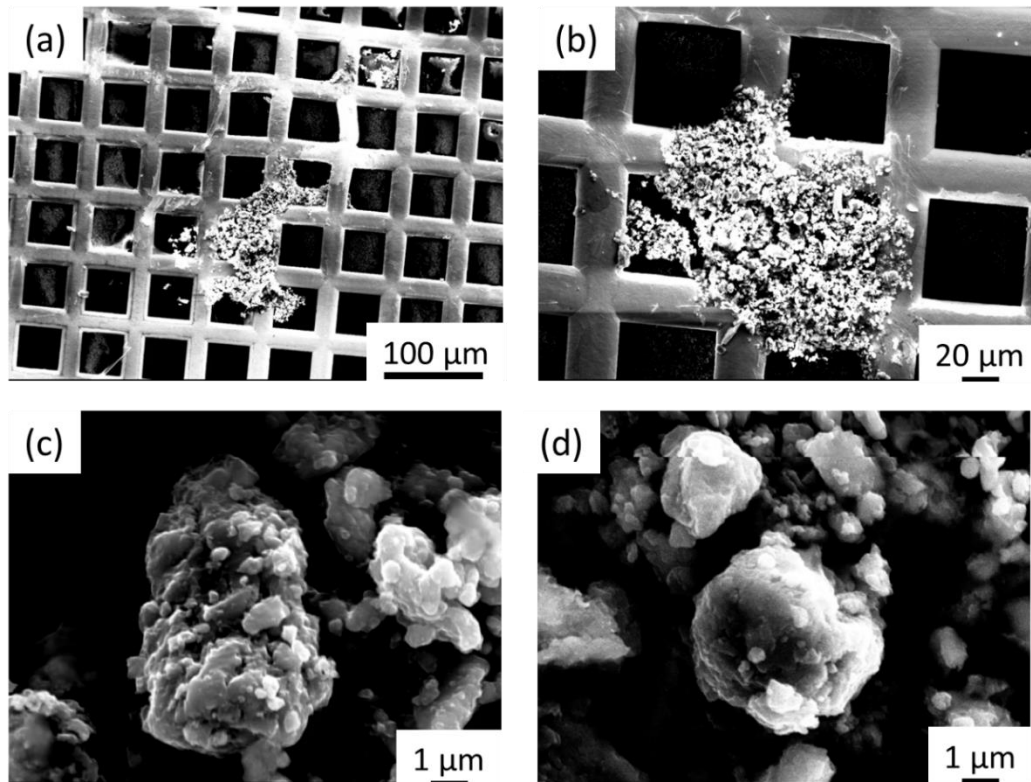
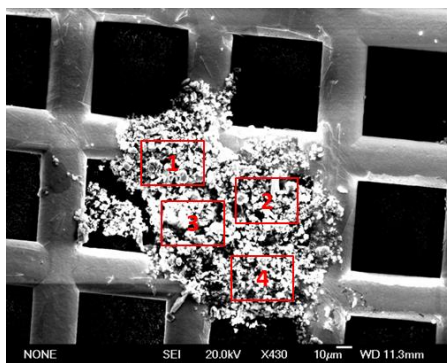


Figure 6-23 Wear debris generated by Ti6Al4V after 10.5 h MACC test, with 634 g load and 1 rpm. The square is TEM supporting grid, made of copper. (c) and (d) is the magnified view of the particles in (a) and (b).



	Au	O	Ti	Al	V	Na	Cl
1		56	37	2	1		1
2		52	40	3	1	1	1
3		58	34	4	1	1	1
4	3	57	33	3	1	1	1

Figure 6-24 Compositional analysis of MACC products from Ti6Al4V, by EDX equipped with JEOL 7000. Unit of all numbers is at.%.

In order to collect reasonable amount of MACC products from metallic glass for characterisation, the test for metallic glasses were continued for a longer period when compared with Ti6Al4V (3 days). After uncoupling the pin and cup, the same procedures were undertaken as for the analysis of Ti6Al4V and in addition further analysis was performed using TEM (TECNAI, FEI). The morphology of nanoparticles generated is shown in Figure 4 (d). With further compositional analysis (Figure 6-26), it was found that oxygen is the main element in the products. When normalising the data to account for increased oxygen and comparing with the nominal alloy composition, it was found that Ti, Zr and Pd were enriched whilst Cu was depleted (minor elements are ruled out for discussion due to their low content).

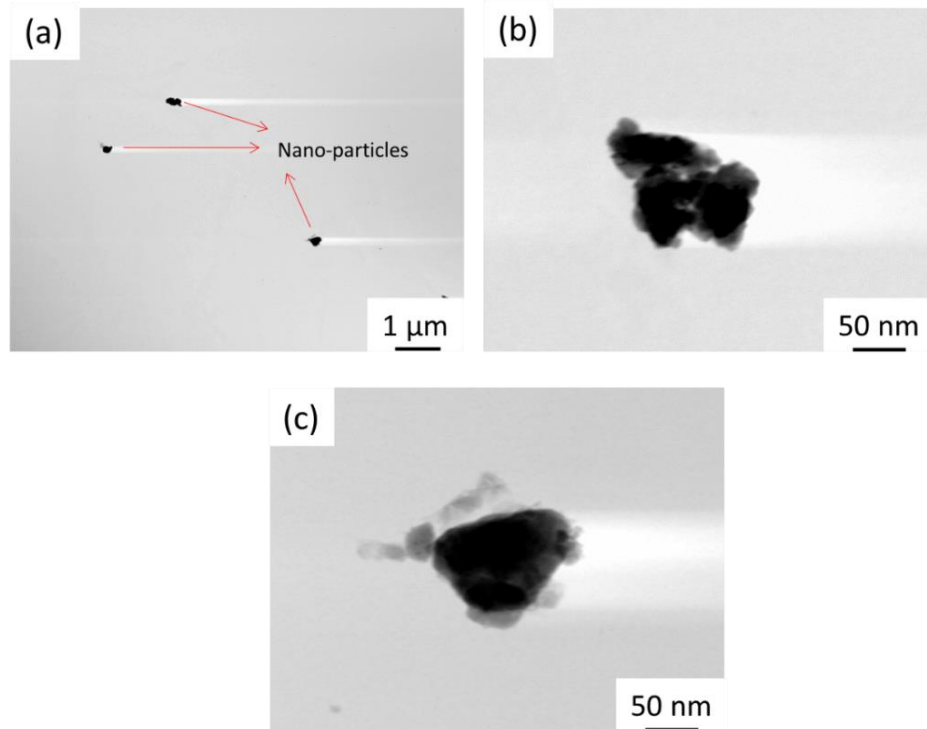
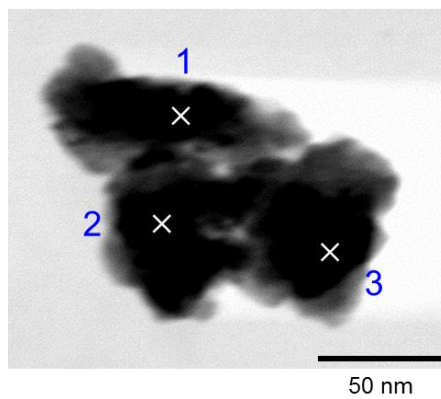


Figure 6-25 Wear debris generated by BMG_Sn2Si after 3 days MACC test, with 634 g load and 1 rpm.



Sp.	O	Ti	Zr	Na	Cu	Pd	Sn	Si	Cl
1	86	9	2	0.7	0.6	0.6	0.3	0	
2	84	9	2	2	1	0.8	0.3	0	0.6
3	82	11	3		3	0.5	0.7	0	

Re-normalized excluding O									
Sp.	Ti	Zr	Na	Cu	Pd	Sn	Si	Cl	
1	66	16	1	4	8	2	1	2	
2	57	12	12	8	5	2	0	4	
3	63	14		16	3	4	0		
Alloy	40	10		33	14	2	1		

Figure 6-26 Compositional analysis of MACC products from BMG_Sn2Si, by EDX equipped with Tecnai. Unit of all numbers is at.%.

The products collected are the mixture of insoluble corrosion products and wear debris. The corrosion products could be some insoluble or supersaturated metal oxides, or some components with high thermodynamic stability. The wear debris, theoretically have same composition with test alloys, and they could derive from the mechanical fretting or the adjacent pits (also known as undercutting mechanism) [220].

6.11 MACC resistance

All the samples were sent back to their original manufacturer (Anthogyr, France) to re-machine the sample surfaces. To study how the corrosion resistance of Ti6Al4V and metallic glasses changes before and after long term MACC, several sequential tests were designed as follows:

#1. Static polarisation curves in physiological saline (634 g)

#2. OCP measurement under MACC condition (634 g and 0.1 rpm) for 10 hours

#3. Static polarisation curves in physiological saline again, same with #1

#4. MACC potential measurement for 10 mins, and potentiostatic measurement at (fretting potential+100) mV vs Ag/AgCl

Note that solution was not replaced with fresh media before each #run started.

The data from measurements #1 to #4 are shown in Figure 6-27. #1 is the polarisation curves of the as-machined alloys. The three metallic glasses showed a similar anodic current, and their pitting potential followed the order of BMG_Sn2Si > BMG_Pd14 > BMG_Sn2. Ti6Al4V showed a higher anodic current and kept being passivated until 1 V vs Ag/AgCl. Once fretting commenced as shown in #2, the free potential went through a sudden drop then varied periodically. The drop seen for Ti6Al4V was much larger than that of the metallic glasses, which indicates that rotating caused more corrosion current variation for Ti6Al4V compared with the metallic glasses. After 10-hours

abrasion at 0.1 rpm under 634 g loading, the polarisation curves under static conditions were measured again (#3). If we compare #1 with #3, the effect of 10-ks MACC to Ti6Al4V was more significant because the anodic current for Ti6Al4V in #3 is - 10 times as large as in #1, while it is only 1- 2 times as large as in #1 for metallic glasses.

Figure 6-27 #4 shows the potentiostatic current of all test materials. Similar to the data shown in Figure 6-6, the current measured for Ti6Al4V increased with time, while the currents measured for the BMGs was smaller and was consistent with time. The current increased to -9 μA in #4 while only to -1.5 μA in Figure 6-6. The increased rate cannot be compared directly due to different experimental conditions, for example, the contact area must differ, and the local chemistry in #4 was more aggressive since it had been evolving during tests #1 to #3, and the applied potential was also different. However, the evidence strongly indicates that the anodic current increased for Ti6Al4V as MACC testing proceeded, in contrast to the behaviour observed for the BMG samples.

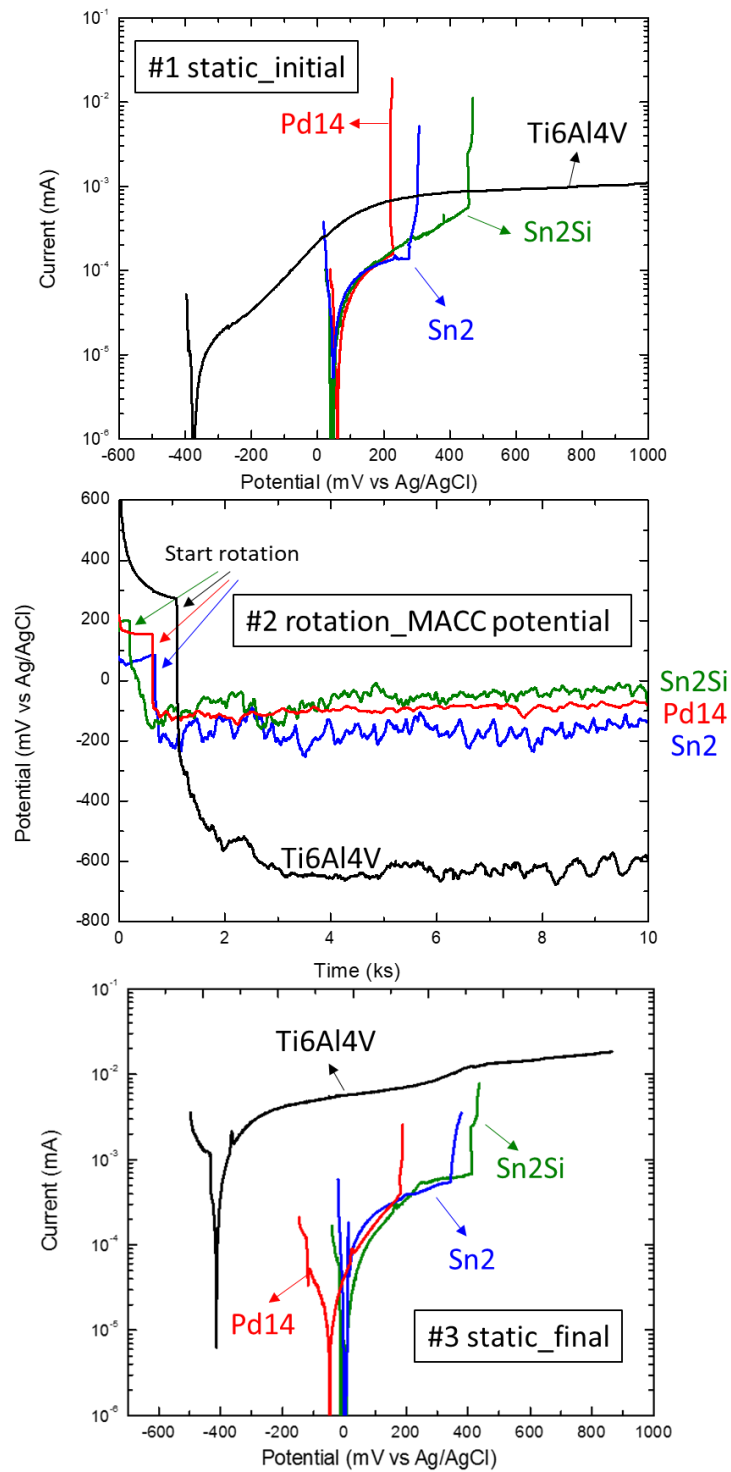
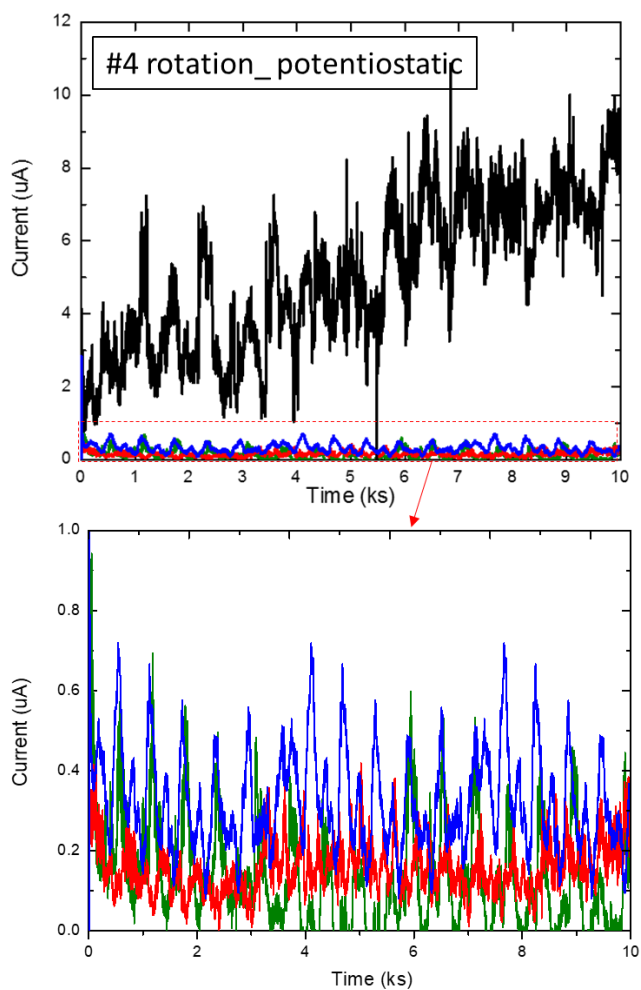


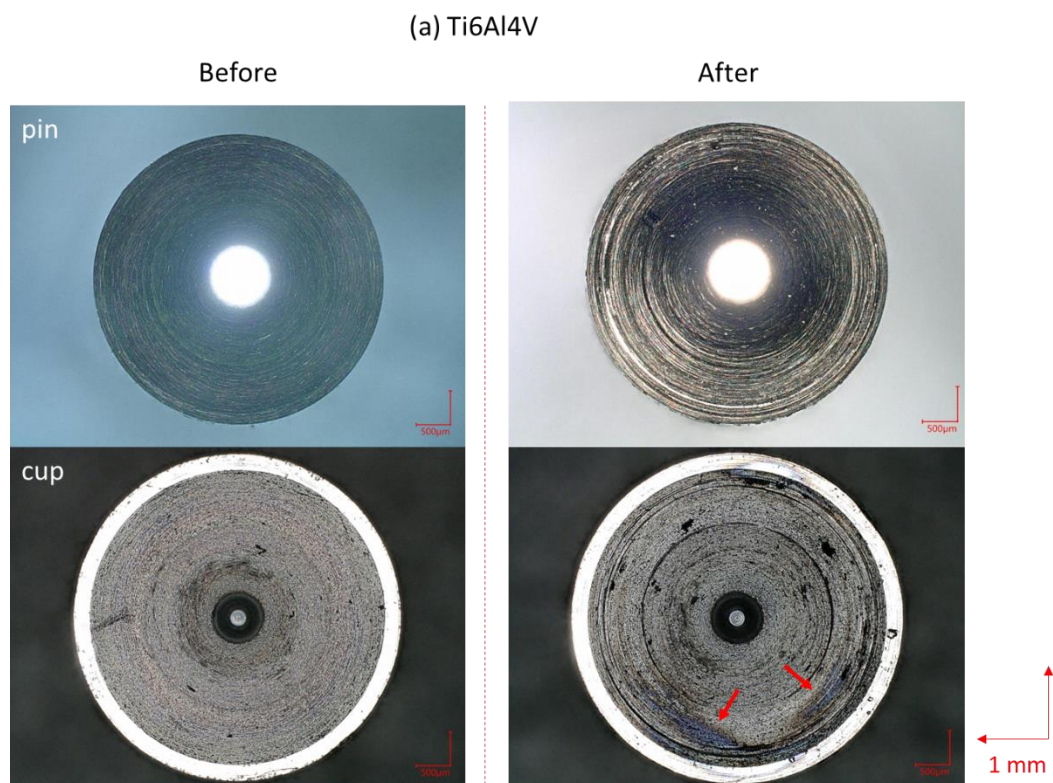
Figure 6-27 #1: Static polarisation curves on Ti6Al4V and metallic glasses. #2: OCP measurements for 3 hours, rotation speed was 0.1 rpm, load was 634 g. #3: repeat of #1.



MACC potential:
 Ti6A4V: -651 mV vs Ag/AgCl
 Sn2: -207 mV vs Ag/AgCl
 Pd14: -187 mV vs Ag/AgCl
 Sn2Si: -74 mV vs Ag/AgCl

Figure 6-28 (continuation of Figure 6-27) #4: MACC potential measured for 10 mins (only end values are shown), potentiostatic measurements at (MACC potential +100 mV) vs Ag/AgCl.

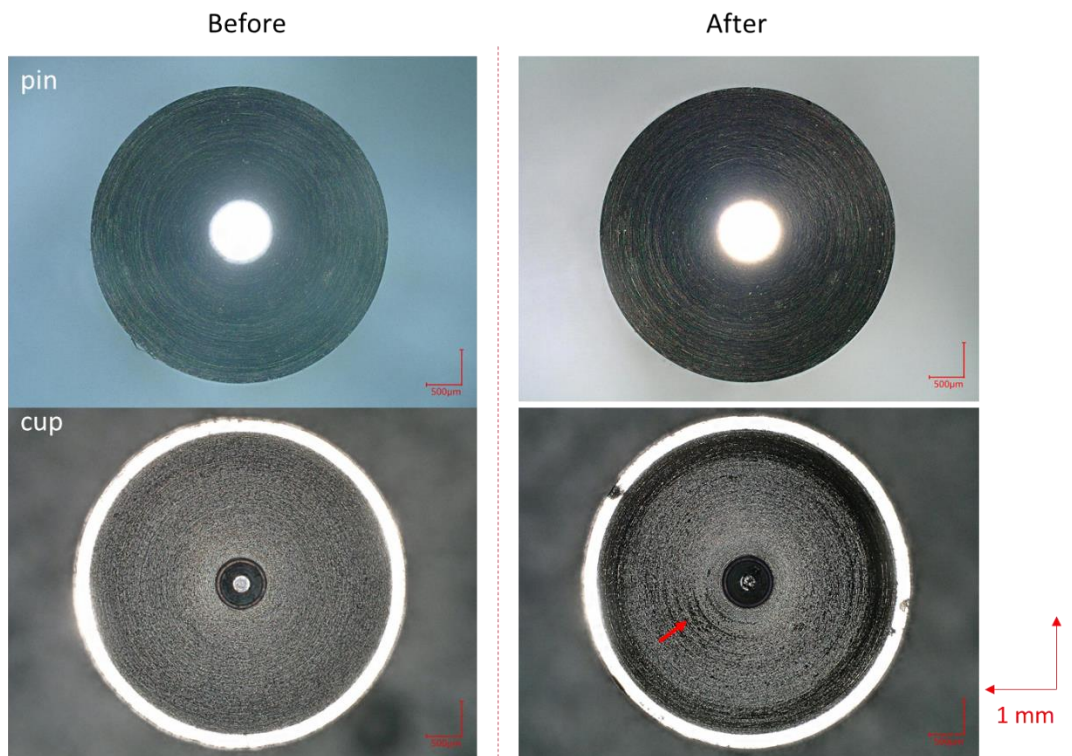
The surface morphologies before and after test #4 were recorded by confocal optical microscope. Not surprisingly, the surface condition of Ti6Al4V exhibited more damage than metallic glasses. Optical microscopy also shows that part of the metal surface of Ti6Al4V was discoloured (labelled by red arrows). This discoloration can be the oxidation of Ti ions, and it was also reported in [94] on a Ti6Al4V retrieved dental implant abutment. On the surface of metallic glasses, the trace of wear-corrosion can also be seen, however, the amount of damages is much less than that on Ti6Al4V. Also, no discoloration was observed on metallic glasses.



(b) BMG_Sn2



(c) BMG_Pd14



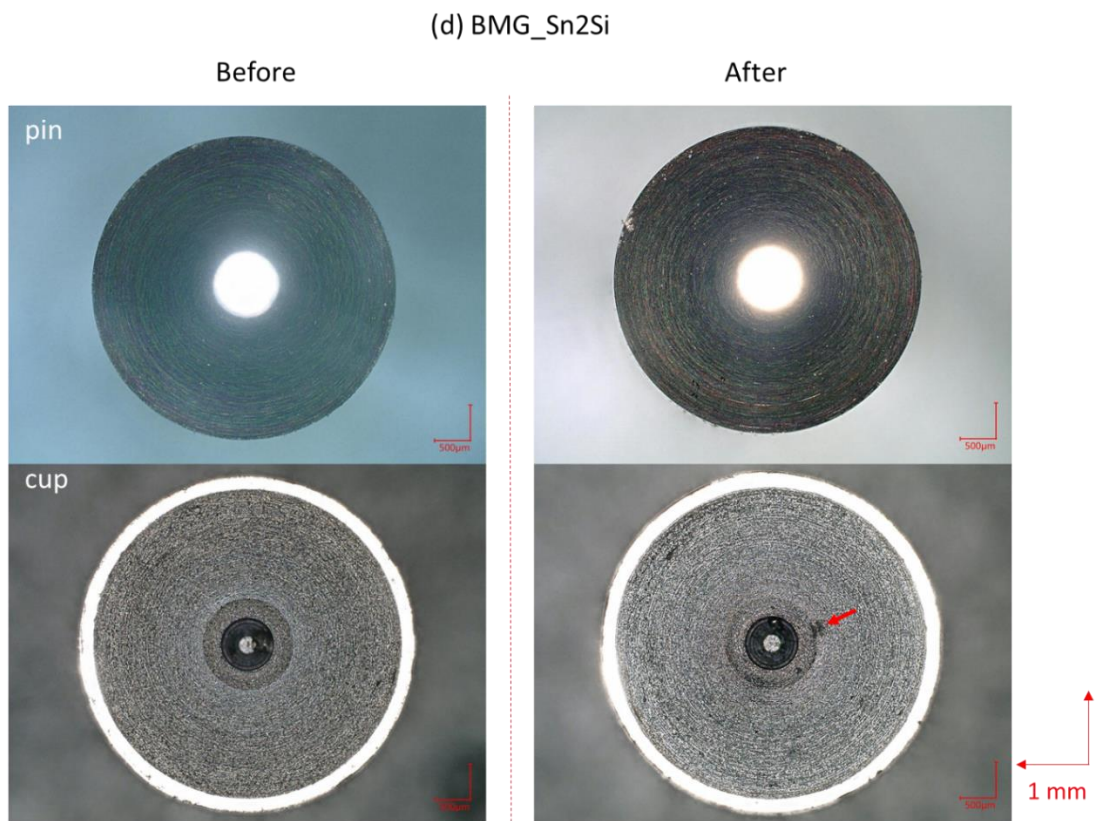


Figure 6-29 Optical microscopy of (a) Ti6Al4V, (b) BMG_Sn2, (c) BMG_Pd14 and (d) BMG_Sn2Si before (re-machined) and after #1 to #4. Red arrows indicate the possible wear/corrosion damaged areas.

6.12 Effect of albumin

For articulating metal surfaces in hip simulators in the presence of albumin, the formation of a 'tribofilm' that lubricates the abrasive surfaces and protects the metal surface from corrosion has been observed [130, 221, 222]. Here, we investigate the effect of albumin (A) on the corrosion behaviour of Ti6Al4V and BMGs under MACC conditions in physiological saline (PS).

Initially, polarisation curves in different solutions (PS, PS+A) were measured under MACC conditions (634 g, 0.1 rpm). BMG_Pd14 was not included here due to its low pitting potential. Figure 6-30 shows the anodic polarisation curves of (a) Ti6Al4V, (b) BMG_Sn2 and (c) BMG_Sn2Si. It is clear that albumin decreases the MACC potential slightly for all test alloys, and albumin postpones pitting for BMG samples. However, it is difficult to distinguish from the polarisation curves how albumin affects the anodic reaction rate and MACC current due to the current variation induced by rotation.

It is interesting to note that the current variation caused by rotation follows the order of: Ti6Al4V > BMG_Sn2 > BMG_Sn2Si, which is correlated with their hardness.

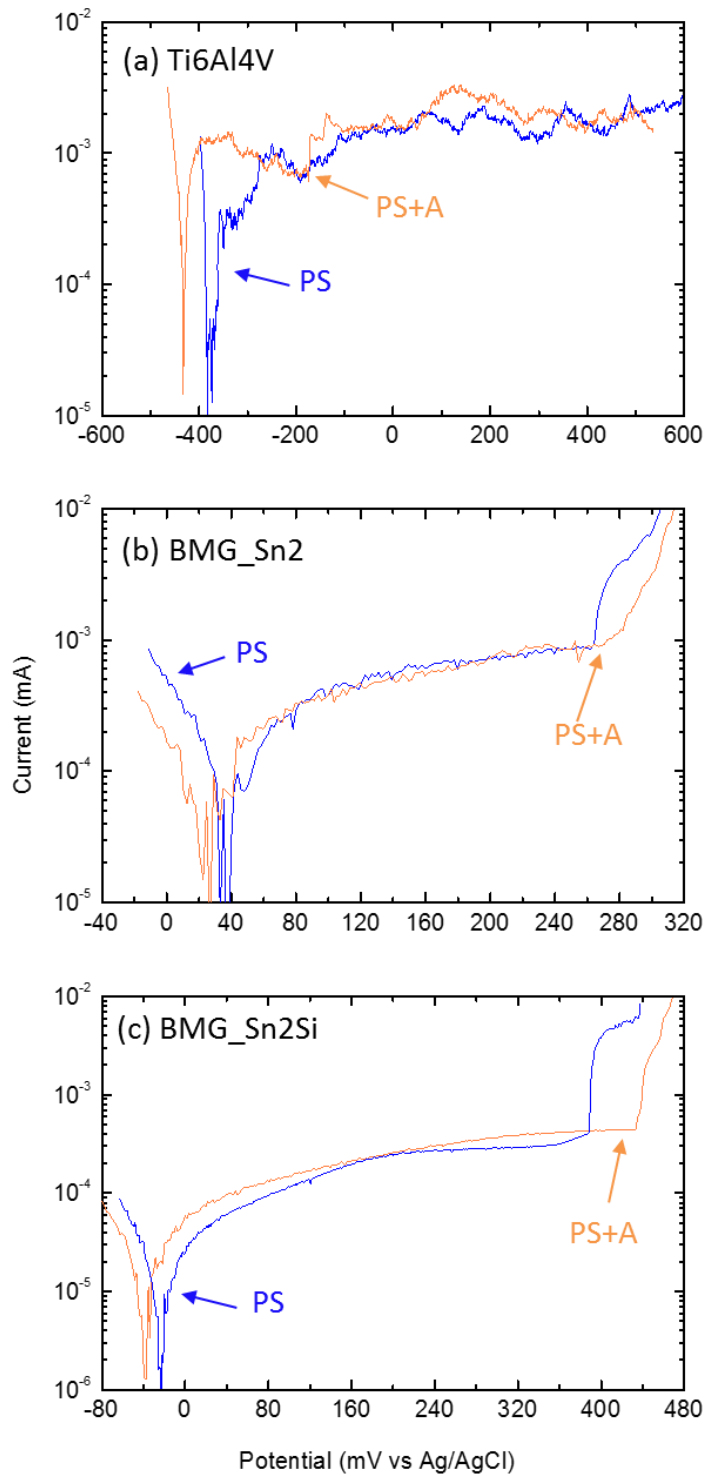


Figure 6-30 Anodic polarisation curve of (a) Ti6Al4V, (b) BMG_Sn2 and (c) BMG_Sn2Si, rotation speed was 0.1 rpm, load was 634 g.

Following these procedures, potentiostatic measurements were carried out at 200 mV vs Ag/AgCl so all samples were in their passive state. In order to control for the effect of gradually increasing wear damage, the rotation was carried out for periods of 1 h, and then the solution was removed, and fresh solution added before continuing. A sequence was used in which typically two measurements were made in the same solution to investigate changes with time between the samples, and then two more measurements were made with a different solution. Figure 6-31 shows the initial set of measurements for BMG_Sn2. It can be seen that the currents were very high at the beginning and then dropped quickly and varied in a small range (0.1 μ A- 0.2 μ A). Further repeats carried out either in PS or in PS+A solutions on Ti6Al4V, BMG_Sn2 and BMG_Sn2Si can be found in the Appendix (Figure 9-1, Figure 9-2 and Figure 9-3).

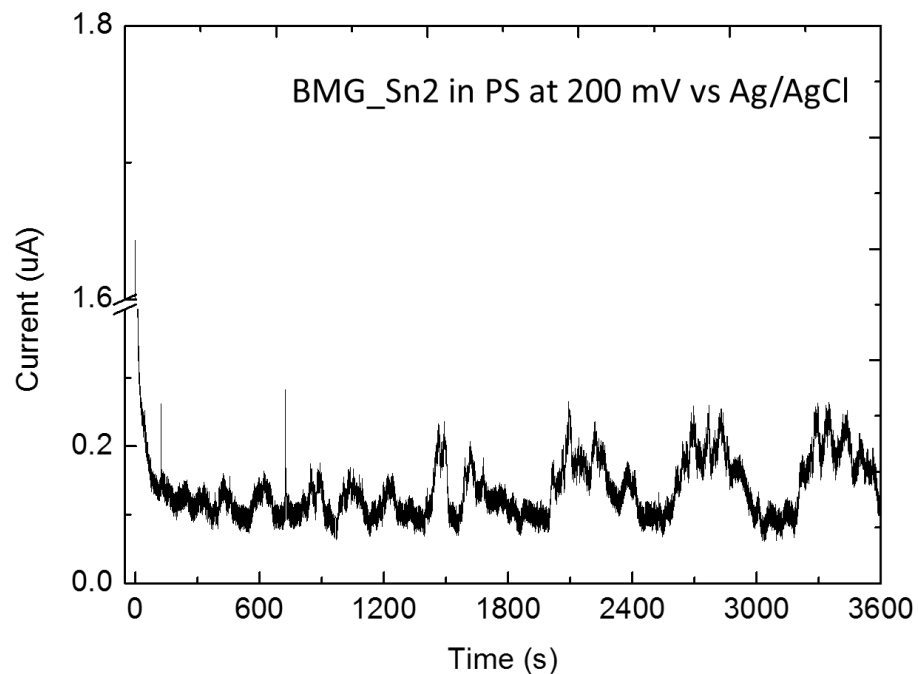


Figure 6-31 A potentiostatic measurement on BMG_Sn2 at 200 mV vs Ag/AgCl in PS.

The accumulated charge was calculated by integrating currents with time (Appendix Part B) and is shown in Figure 6-32. There was significant variation in the charge passed for the solutions for all three samples. There was also significant variation in the charge for successive measurements using the same (fresh) solution. However, comparison of adjacent measurements with and without albumin generally show a lower charge in the presence of albumin. In order to evaluate whether the effect of albumin was significant, a repeat measures statistical test was used (repeat measures ANOVA- using a Greenhouse-Geisser correction) comparing pairs of data for each of the four potential sequences (PS followed by PS, PS followed by PS+A, PS+A followed by PS+A, and PS+A followed by PS). Post-hoc tests ($\alpha=0.05$) were used to identify differences between specific sequences. The results are shown as p values next to the bar charts. For Ti6Al4V there was a significant decrease in the charge when PS+A followed PS when compared with the other sequences. However, no significant effect is observed for the two BMGs.

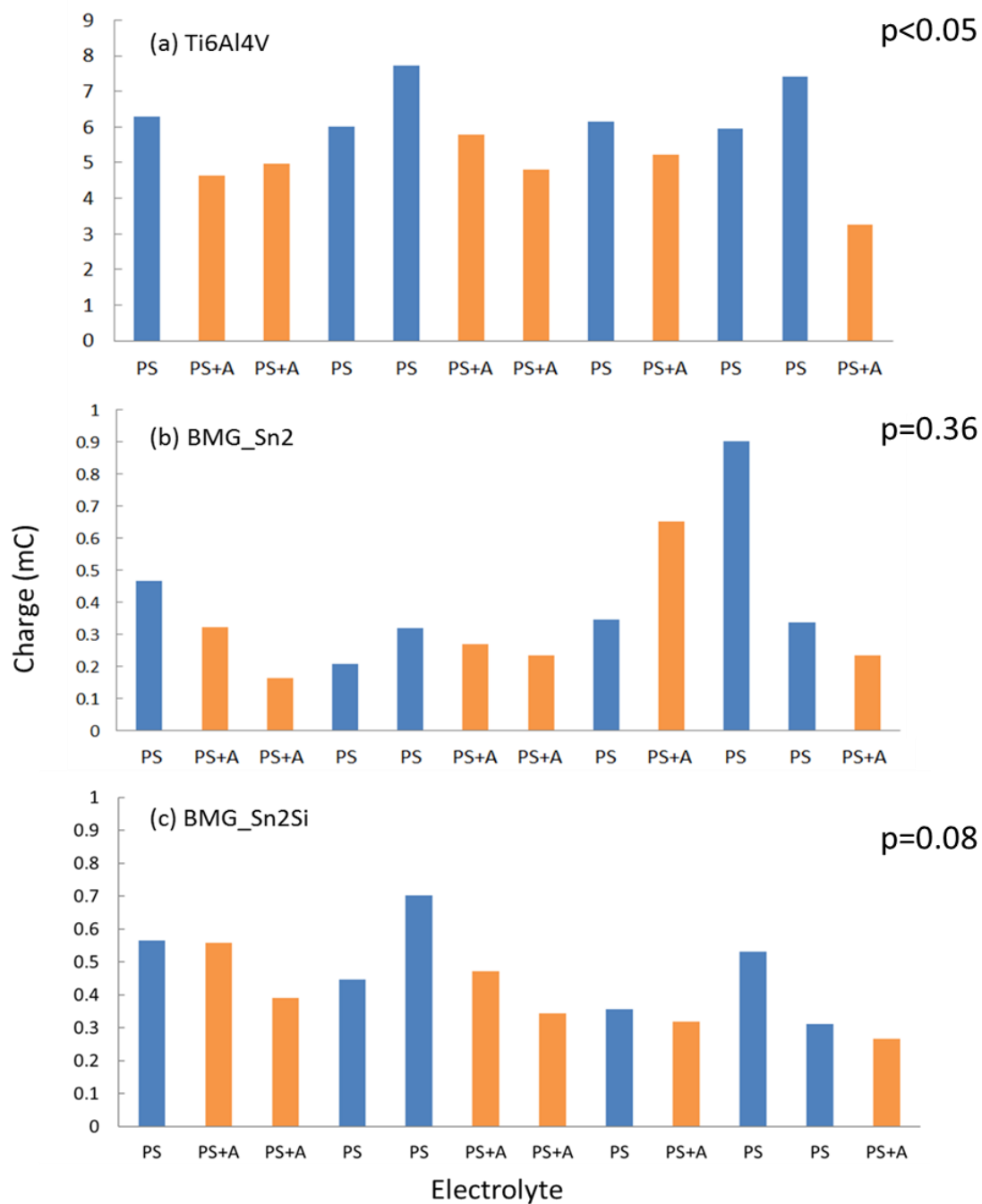


Figure 6-32 Charge calculated from potentiostatic measurements (200 mV vs Ag/AgCl) for 1 hour in 0.9% NaCl (PS) and 0.9% NaCl+4% albumin (PS+A) for (a) Ti6Al4V, (b) BMG_Sn2 and (c) BMG_Sn2Si. Load applied was 634 g and rotation speed was 0.1 rpm.

6.13 Discussion

6.13.1 MACC device

Existing approaches for measuring MACC have used methods such as pin-on-disc measurements, but the macroscopic movements involved flush away the corrosive acidic solution adjacent to the abraded surface permitting repassivation of the metal, and thus underestimating the effect of local acidity on MACC. The device presented in this paper overcomes this problem by maintaining the highly acidic solution in the crevice, and enables capture of wear debris and corrosion products, which may be particularly valuable for studying the effect of such species on adjacent tissue.

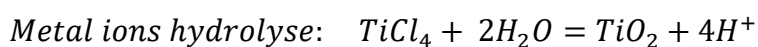
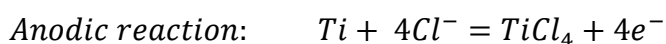
The method is also capable of quantitative comparison of the risk of MACC via direct measurement of charge passed in measurements where the applied potential is controlled. It also gives more subtle information about the risk of corrosion of real devices. As indicated above, the corrosion potential of a device in the body is generally likely to be controlled by the corrosion potential of the passive surface, which is given by the static measurements. This external potential can polarise the active interface in the crevice so that it becomes a net anode, as illustrated in Figure 6-4. A reasonable estimate of the corrosion rate in the crevice can then be measured by controlling the potential at the static OCP and then measuring currents flowing during rotation. This measured current is a valid assessment of the anodic current as the cathodic reaction is largely unaffected by rotation (Figure 6-5).

This new device has been used to demonstrate the relative risk of MACC for Ti6Al4V compared with that for BMGs, which are potential replacements for Ti in small dental implants. BMGs have higher hardness than Ti6Al4V (Table 6-2) leading to a greater resistance to mechanical damage. Electrochemical testing has consistently shown that Ti alloys are highly resistant to pitting corrosion, whereas Ti-based BMGs have clear pitting potentials, and so have often been regarded as more of a corrosion risk. However, Figure 6-3 shows clearly that the pitting potentials of the BMGs are substantially higher than the expected OCP, so the risk of pitting is small, but comparison of the behaviour under MACC conditions indicates that Ti6Al4V is a much greater corrosion risk in terms of susceptibility to MACC under relatively realistic conditions.

The new device also provides a means of producing simulated wear debris and corrosion products that can be used to evaluate the effect of such species on tissue adjacent to implants.

6.13.2 Acidity in cavity for Ti6Al4V

For Ti6Al4V, as the passive film is damaged, the underlying Ti is oxidised and Ti ions hydrolyse, which causes the acidification. Meanwhile, the cathodic reaction is oxygen reduction, which generates OH⁻. The possible reaction is as follows:



Cathodic reaction: $O_2 + 4e^- + 2H_2O = 4OH^-$

Therefore, the direct evidence for the occurrence of MACC is the acidity in crevice and the alkalinity in bulk solution. In theory, a metallic glass sample cannot be immune from MACC, however, due to the low accuracy of pH indicator paper, small changes cannot be captured. However, the observation on the Ti6Al4V sample is sufficient to validate this custom set-up, indicating MACC happened in the crevice as we expected.

6.13.3 Comparison of MACC resistance between BMGs and Ti6Al4V

Section 6.2 shows CT scans of dental implant, as well as SEM images of the contacting and non-contacting surfaces. It is clear that contact surface shows signs of mechanical deformation, which may well be exacerbated by mechanical load during mastication following initial deformation during implantation. This represents a potential site for MACC. It is evident from the orthopaedic and dental device [94] literature that Ti alloys may show susceptibility to MACC. This view is strongly supported by the visual observations and electrochemical measurements, where Ti6Al4V shows significant high currents, high charges and associated pH changes in the surrounding solution.

As shown in section 6.6.3, the MACC potential of Ti6Al4V shows strong time-dependence while none of BMG samples show that. This is because the poor wear resistance leads to more damage on passive film of Ti6Al4V, and more underlying metal gets oxidised and generates more H^+ . The accumulation of local acidity and the increasingly worse surface condition is the main reason for time-dependence for

Ti6Al4V. In comparison, BMG samples have good wear resistance, the damage area in each run is random, and the pH did not show significant changes in the crevice.

Compared with Ti6Al4V, less wear debris and corrosion products produced during MACC by metallic glasses is another advantage to be used as dental implants. Previous literatures revealed that bad osseointegration and severe inflammation are associated with corrosion products [1]. Additionally, the pits and plastic deformation generated by MACC can act as initiation points of cracks, which severely reduces the structural integrity of implanted materials [98].

6.13.4 Effect of albumin

It is very clear that the environment in the body is far more complex than physiological saline, with species such as proteins and reactive oxygen species and many other species that can affect corrosion behaviour [32, 33]. The new device has also been used to evaluate the effect of albumin on MACC. This experiment highlights the challenges of quantifying subtle effects with this device. However, the data do give an indication that the presence of proteins may slightly decrease the risk of MACC. This behaviour is consistent with the work such as that of Neville and co-workers who have shown albumin can form complex organometallic/oxides under tribological contacts and it lubricates the metallic sample surface [100, 129].

The effect of albumin on BMGs during MACC had no statistically significant difference, this is due to the inconsistency of the contact surface area of BMGs.

6.14 Conclusion

A new device has been developed that can provide quantitative information on mechanically-assisted crevice corrosion (MACC) and generate realistic wear debris and corrosion products.

The MACC device demonstrated that Ti-based BMGs ($\text{Ti}_{40}\text{Zr}_{10}\text{Cu}_{34}\text{Pd}_{14}\text{Sn}_2$, $\text{Ti}_{40}\text{Zr}_{10}\text{Cu}_{36}\text{Pd}_{14}$, and $\text{Ti}_{40}\text{Zr}_{10}\text{Cu}_{33}\text{Pd}_{14}\text{Sn}_2\text{Si}$) are considerably more MACC-resistant than Ti6Al4V, which is evidenced by: 1) MACC current of Ti-based BMGs are one order of magnitude lower than that of Ti6Al4V, 2) surface condition of BMGs is much better than that of Ti6Al4V, accordingly, much less MACC products were produced by BMGs. Thereby Ti-based BMGs are potentially suitable for small dental implants.

The masticatory force (load) applied on implants and mismatch (rotation) between modular components can accelerate MACC for both Ti6Al4V and Ti-based BMGs.

MACC of Ti6Al4V can get increasingly worse with time, which is another potential risk of Ti6Al4V used as small dental implants.

It has also been shown that albumin may have a small effect in mitigating MACC in Ti6Al4V, while there is no significant effect on Ti-based BMGs.

7 General discussion and future work

7.1 General discussion

7.1.1 Use of bulk metallic glasses to replace Ti Alloys for small dental implants

This work evaluates the potential for replacing Ti alloys with Ti-based BMGs for small dental implants. The idea to employ BMGs to replace conventional Ti alloys in this application has been proposed previously due to the superior mechanical properties of BMGs [54, 55]. However, in previous work, the greater susceptibility of BMGs to pitting has been considered as a potential risk in comparison with the good pitting resistance of Ti alloys. [54, 56, 223, 224] Nevertheless, the significant difference in the corrosion potential and pitting potential for BMGs in the different solutions investigated in this work suggests that the risk of pitting may be low. Furthermore, there is a concern that the main risk in small modular dental implants may be an increase in MACC [29]. If this is the case, MACC is much more of a risk for Ti-based alloys compared with BMGs as shown in the MACC tests in the current work.

7.1.2 MACC testing

MACC is not only a potential problem for dental implants but is also a known risk for other orthopaedic implants, particularly where Ti alloys are used [225, 226]. The new device established in this work is more realistic than existing tests such as pin-on-disc measurements since it retains the local chemistry, and it also provides a method to

quantify MACC by measuring the current flowing, which was not achievable in previous work. Nevertheless, the device still has several limitations that needs to be overcome. Firstly, the high manufacturing tolerance required for test pieces is difficult to achieve with the current design and results in significant scatter in the data. More precise fabrication needs to be developed to improve the alignment of the pin and cup. Secondly, the one-directional rotation movement of the pin is not representative of the reciprocating movements seen at dental implant connections. This can be updated by changing the relative motion direction between the pin and cup.

In addition to the device itself, consideration should be given to the most appropriate testing solution. This work has shown that the presence of albumin causes a slight decrease in the current flowing, but other species present in the extracellular fluid, including chelating agents and other reactive oxygen species (ROS) may cause greater effects.

7.1.3 Structural relaxation and elemental substitution

The as-cast bulk metallic glasses must be further processed (e.g. laser cutting) to obtain dental components. In such a process, the elevated temperature is likely to cause some structural relaxation of the outer surface of BMGs. This may not be a concern for BMGs if the heat involved is not great since we found that BMGs with some degree of structural relaxation are slightly more resistant to corrosion. However, if there is significant crystallisation, then the corrosion behaviour may become worse.

Ga can be an alternative element to substitute for Cu, up to 10 at.%, without compromising corrosion resistance. The optimised composition of Ga-containing BMGs suggested by S. Bera et. al was $Ti_{40}Zr_{10}Cu_{34}Pd_{14}Ga_2$ due to its better combination of compressive strength and glass forming ability [18]. Further work can be conducted on $Ti_{40}Zr_{10}Cu_{34}Pd_{14}Ga_2$ to investigate how MACC, extracellular protein and ROS affect the corrosion behaviour of it.

There is a minor compositional difference between $Ti_{40}Zr_{10}Cu_{34}Pd_{14}Sn_2$ and $Ti_{40}Zr_{10}Cu_{33}Pd_{14}Sn_2Si$. Addition of 1 at.% Si increases the hardness significantly, which may have caused the decreased susceptibility to MACC. It has been reported that the hydrogen reduction reaction rate is much lower on metalloid surfaces than on noble or transition metal surfaces [227], so from a kinetics point of view, alloying Si may also be effective in lowering corrosion rate. In addition, Si is a biocompatible element [228]. Further investigation of the role of metalloid elements may lead to further optimisation of a Ti-Zr-Cu-Pd system.

7.2 Future work

7.2.1 MACC products characterisation followed by cell culture

Metal ions and metallic fragments surrounding orthopaedic and dental implants have been found [27, 229], and are often associated with increased inflammatory reactions [41], greater alveolar bone loss and poorer osseointegration [11, 12, 132]. The bone loss results in implant displacement (loosening) [71, 133-136], which may give rise to

MACC, which will in turn generate more metal ions and fragments. Therefore, MACC products need to be identified and their biological effects should be carefully evaluated. In situ characterisation, by e.g. synchrotron X-Ray diffraction and spectroscopy might be conducted if an appropriate in situ cell could be designed. In addition, a comparison can be made between MACC and 'artificial pit' tests. Pd nanoparticles from $Ti_{40}Zr_{10}Cu_{34}Pd_{14}Sn_2$ were found in 'artificial pit' tests [149], also Pd is the only element that was enriched in pits, so it is possible that if MACC takes place for enough long time, Pd nanoparticles will also be generated. In short, the knowledge on the MACC products can guide the biological modelling which is crucial to predict the long-period biological responses.

MACC increasingly worsens with time for Ti6Al4V, while it shows little dependence with time on BMGs over the timescales used in the current work. This may be because the current loads and rotation are not great enough to cause sufficient damage to the BMG surfaces. The mastication force of an adult is normally 70-150 N [33], which is significantly larger than 0.49 N (50 g) and 6.2 N (634 g) used in the present work. In future work, higher loads that are closer to mastication forces should be applied to test the MACC behaviour of BMGs.

7.2.2 Effect of albumin and H_2O_2

Previous work has shown that the effect of albumin on corrosion of Ti6Al4V in H_2O_2 -containing solution is a time-dependent process: after ~22h, albumin starts to dissolve the Ti- H_2O_2 products, which releases more Ti compounds to surrounding tissues [14].

This phenomenon arises to the question whether the interaction between BMGs and H₂O₂+ albumin may also be time-dependent. This suggests that longer-term experiments may be important in validating the use of BMGs for dental implants.

It is difficult to evaluate the effect of H₂O₂ on the corrosion behaviour of BMG_Sn₂ through electrochemical measurements due to the current flowing from the oxidation of H₂O₂. This could be validated by directly measuring metal ions release through other techniques, e.g. inductively coupled plasma atomic emission spectroscopy [230].

However, it should be noted that a cellular study indicated that superoxide stabilizes at ~25 μM and H₂O₂ is in the even lower range in neutrophils [231], which is much lower than the H₂O₂ concentration used in this work (0.1 wt.% ≈ 2.9 × 10⁻² M). Thus ROS may not be a significant risk at realistic levels.

Most of the test solutions used for corrosion of biomaterials, e.g. Hanks solution, phosphate-buffered saline and simulated body fluid, do not consist of any protein or ROS. The measured corrosion rate in the solutions absence of protein and ROS may be different from in-vivo corrosion. This work provides evidence that albumin and H₂O₂ should be considered when conducting in-vitro corrosion tests. Furthermore, the current work investigated the corrosion of alloys used as dental implants, so consideration should also be given to the corrosion behaviour of the alloys used here in artificial saliva.

8 References

1. Geetha Manivasagam, D.D.a.A.R. Biomedical Implants: Corrosion and its Prevention - A Review. *Recent Patents on Corrosion Science* 2010, 2, 40-54.
2. Shemtov-Yona, K. and D. Rittel. An Overview of the Mechanical Integrity of Dental Implants. *Biomed Res Int* 2015, 2015, 547384.
3. Sun, Y., et al. Comparison of mechanical behaviors of several bulk metallic glasses for biomedical application. *Journal of Non-Crystalline Solids* 2014, 406, 144-150.
4. Fengxiang Qin, Z.D., Xinmin Wang, Guoqiang Xie and Akihisa Inoue. Ti-based Bulk Metallic Glasses for Biomedical Applications. *Biomedical Engineering, Trends in Materials Science* 2011, 11, 249-268.
5. S. L. Zhu, X.M.W., F. X. Qin, and A. Inoue A new Ti-based bulk glassy alloy with potential for biomedical application. *Materials Science and Engineering: A* 2007, 459, 233-237.
6. Zhu, S.L., X.M. Wang, and A. Inoue. Glass-forming ability and mechanical properties of Ti-based bulk glassy alloys with large diameters of up to 1cm. *Intermetallics* 2008, 16, 1031-1035.
7. Zhu, S.L., et al. New TiZrCuPd quaternary bulk glassy alloys with potential of biomedical applications. *Materials Transactions* 2007, 48, 2445-2448.
8. SATOSHI FUKUZAKI, H.U., AND KAZUYA NAGATA. Adsorption of Bovine Serum Albumin onto Metal Oxide Surfaces. *JOURNALS OF FERMENTATION AND BIOENGINEERING* 1996, 81, 163-167.
9. Bernard M. Babior, R.S.K., and Joh T. Cumtite. Biological defense mechanisms: the production by leukocytes of superoxide, a potential bactericidal agent. *The Journal of Clinical Investigation* 1973, 52, 741-744.
10. N. Broggini, L.M.M., J.S. Hermann, R. Medina, R.K. Schenk, D. Buser, and D.L. Cochran. Peri-implant Inflammation Defined by the Implant-Abutment Interface. *Journal of Dental Research* 2006, 85, 473-478.
11. N. Broggini, L.M.M., J.S. Hermann, R. Medina, R.K. Schenk, D. Buser, and D.L. Cochran. Peri-implant Inflammation Defined by the Implant-Abutment Interface. *J Dent Res* 2006, 85, 473-478.
12. N. Broggini, L.M.M., J.S. Hermann^{1,3}, R.U. Medina, T.W. Oates, R.K. Schenk, D. Buser, J.T. Mellonig and D.L. Cochran. Persistent Acute Inflammation at the Implant-Abutment Interface. *J Dent Res* 2003, 82, 232-237.
13. Yu, F., Addison, O. and Davenport, A. J. A synergistic effect of albumin and H₂O₂ accelerates corrosion of Ti6Al4V. *Acta Biomaterialia* 2015, 26, 355-65.
14. Zhang, Y., et al. Time-dependent Enhanced Corrosion of Ti6Al4V in the Presence of H₂O₂ and Albumin. *Sci Rep* 2018, 8, 3185.
15. Qin, F., et al. Corrosion Behavior of Ti-Based Metallic Glasses. *Materials Transactions* 2006, 47, 1934-1937.
16. Qin, F., et al. Fabrication and Corrosion Property of Novel Ti-Based Bulk Glassy Alloys without Ni. *Materials Transactions* 2007, 48, 515-518.

17. Calin, M., et al. Designing biocompatible Ti-based metallic glasses for implant applications. *Mater Sci Eng C Mater Biol Appl* 2013, 33, 875-83.
18. Bera, S., et al. Tuning the glass forming ability and mechanical properties of Ti-based bulk metallic glasses by Ga additions. *Journal of Alloys and Compounds* 2019, 793, 552-563.
19. C. Suryanarayana, A.I., *Bulk Metallic Glasses*. London: CRC Press, . Vol. 1. 2011. 204.
20. Tailleart, N.R., et al. Effect of thermally induced relaxation on passivity and corrosion of an amorphous Al–Co–Ce alloy. *Corrosion Science* 2012, 59, 238-248.
21. C.A.C. Souza, F.S.P.a.C.S.K. INFLUENCE OF STRUCTURAL RELAXATION AND PARTIAL DEVITRIFICATION ON THE CORROSION RESISTANCE OF Fe78B13Si9 AMORPHOUS ALLOY. *Scripta Materialia* 1998, 39, 329–334.
22. F.F. Marzo, A.R.P., M.M. Vega. Effect of irreversible structural relaxation on the electrochemical behavior of Fe78–xSi13B9Cr(x=3,4,7) amorphous alloys. *Journal of Non-Crystalline Solids* 2003, 329, 108-114.
23. Pitting Corrosion of Titanium The Relationship Between Pitting Potential and Competitive Anion Adsorption at the Oxide Film/Electrolyte Interface. *Journal of The Electrochemical Society* 2000, 147, 1376-1381.
24. S. Virtanen, a.C.C. Metastable and Stable Pitting Corrosion of Titanium in Halide Solutions. *Corrosion Science* 2004, 60, 643-649.
25. Jeremy L. Gilbert, C.A.B.a.J.J.J. In vivo corrosion of modular hip prosthesis components in mixed and similar metal combinations. The effect of crevice, stress, motion, and alloy coupling. *Journal of Biomedical Materials Research* 1993, 27, 1533-1544.
26. Gilbert, J.L., et al. In vivo oxide-induced stress corrosion cracking of Ti-6Al-4V in a neck-stem modular taper: Emergent behavior in a new mechanism of in vivo corrosion. *J Biomed Mater Res B Appl Biomater* 2012, 100, 584-94.
27. Addison, O., et al. Do 'passive' medical titanium surfaces deteriorate in service in the absence of wear? *J R Soc Interface* 2012, 9, 3161-4.
28. M. Uo, K.A., A. Yokoyama, M. Ishikawa, K. Tamura, Y. Totsuka, T. Akasaka, F. Watari. X-ray absorption fine structure (XAFS) analysis of titanium-implanted soft tissue. *Dental Materials Journal* 2007, 26, 268-273.
29. Karpavicius, D., et al. The determination of pH of peri-implant crevicular fluid around one-piece and two-piece dental implants: A pilot study. *Clin Exp Dent Res* 2019, 5, 236-242.
30. Jacobs, J.L.G.a.J.J. The Mechanical and Electrochemical Processes Associated with Taper Fretting Crevice Corrosion: A Review. *Modularity of Orthopedic Implants*, ASTM STP 1301, Donald E. Marlowe, Jack E. Parr, and Michael B. Mayor, Eds., American Society for Testing and Materials 1997,
31. Hacisalihoglu, I., et al. Tribocorrosion properties of different type titanium alloys in simulated body fluid. *Wear* 2015, 332-333, 679-686.
32. Lemons JE, D.-M.F. *Biomaterials for dental implants*. Contemporary implant dentistry 1999, St Louis, 271-302.

33. Scully, C., *Oxford Handbook of Applied Dental Sciences*. 2003, Oxford: Oxford University Press.
34. Jackson, B.J. Small-Diameter Implants: A 7-Year Retrospective Study. *J Oral Implantol* 2017, 43, 125-129.
35. Atsuta, I., et al. Soft tissue sealing around dental implants based on histological interpretation. *J Prosthodont Res* 2016, 60, 3-11.
36. Golovanova, O.A., E.S. Chikanova, and Y.O. Punin. Main features of nucleation in model solutions of oral cavity. *Crystallography Reports* 2015, 60, 438-445.
37. Zani, S.R., et al. Peri-implant crevicular fluid biomarkers as discriminants of peri-implant health and disease. *J Clin Periodontol* 2016, 43, 825-32.
38. Barros, S.P.W., R.; Offenbacher, S.; Morelli, T. Gingival crevicular fluid as a source of biomarkers for periodontitis. *Periodontol* 2016, 2000, 53-64.
39. Khurshid, Z., et al. Human Gingival Crevicular Fluids (GCF) Proteomics: An Overview. *Dent J (Basel)* 2017, 5,
40. HAROLD E. HARRISON, D.C.D., AND HERMAN YANNET THE TOTAL ELECTROLYTE CONTENT OF ANIMALS AND ITS PROBABLE RELATION TO THE DISTRIBUTION OF BODY WATER. *J. Biol. Chem* 1936, 113, 515-529.
41. Muñoz, A.I. and S. Mischler. Electrochemical Quartz Crystal Microbalance and X-Ray Photoelectron Spectroscopy study of cathodic reactions in Bovine Serum Albumin containing solutions on a Physical Vapour Deposition-CoCrMo biomedical alloy. *Electrochimica Acta* 2015, 180, 96-103.
42. Fukuzaki, K.T.a.S. Effect of pH on the adsorption and desorption of human serum albumin at titanium-water interface. 2010, 61, 522-527.
43. Harandi SE, B.P., Easton CD, Singh Raman RK. Influence of bovine serum albumin in Hanks' solution on the corrosion and stress corrosion cracking of a magnesium alloy. *Materials Science and Engineering C* 2017, 80, 335-345.
44. Maskat, M.j.K.a.M.y. Interaction of titanium dioxide nanoparticle with human serum albumin: a spectroscopic approach. *International Journal of Pharmacy and Pharmaceutical Sciences* 2014, 6, 43-46.
45. Carter, X.M.H.a.D.C. Atomic structure and chemistry of human serum albumin. *Nature* 1992, 358, 209-215.
46. Wittmann, C., et al. Hydrogen peroxide in inflammation: messenger, guide, and assassin. *Adv Hematol* 2012, 2012, 541471.
47. Linlin Chen, H.D.a.Y.L. Inflammatory responses and inflammation-associated diseases in organs. *Oncotarget* 2018, 9, 7204-7218.
48. Kim, B.G., et al. Effect of TiO₂ Nanoparticles on Inflammasome-Mediated Airway Inflammation and Responsiveness. *Allergy Asthma Immunol Res* 2017, 9, 257-264.
49. Han, S.G., B. Newsome, and B. Hennig. Titanium dioxide nanoparticles increase inflammatory responses in vascular endothelial cells. *Toxicology* 2013, 306, 1-8.
50. Ying Mu, T.K., Masae Sumita, Akiko Yamamoto, Takao Hanawa. Metal ion release from titanium with active oxygen species generated by rat macrophages in vitro. *Journal of Biomedical Materials Research* 2000, 49, 238-243.

51. Mittal, M., et al. Reactive oxygen species in inflammation and tissue injury. *Antioxid Redox Signal* 2014, 20, 1126-67.
52. M.POURBAIX, *Atlas of electrochemical equilibria in aqueous solutions*. Vol. 5. 1974, Texas: NACE.
53. Fraker, M.A.I.a.A.C. Titanium Alloys as Implant Materials M_ edical Applications of Titanium and Its Alloys: The Material and Biological Issues, ASTM STP 1272, S. A. Brown and J. E. Lemons, Eds., American Society for Testing and Materials. 1996,
54. Xie, G., F. Qin, and S. Zhu. Recent Progress in Ti-Based Metallic Glasses for Application as Biomaterials. *Materials Transactions* 2013, 54, 1314-1323.
55. Gong, P., et al. Review on the Research and Development of Ti-Based Bulk Metallic Glasses. *Metals* 2016, 6, 264.
56. Zhu, S.L., et al. A new Ti-based bulk glassy alloy with potential for biomedical application. *Materials Science and Engineering: A* 2007, 459, 233-237.
57. *Metals Handbook, Vol.2 - Properties and Selection: Nonferrous Alloys and Special-Purpose Materials*, . Vol. ASM International 10th Ed. . 1990.
58. Yamaura, S.-i., et al. Ultrasonic Fatigue of Ti40Zr10Cu34Pd14Sn2 Glassy Alloy. *Open Journal of Metal* 2014, 04, 56-64.
59. <https://www.aaid-implant.org/dental-implants/what-are-dental-implants/>, A.A.o.I.D.A.f.
60. Pjetursson, B.E., et al. A systematic review of the survival and complication rates of implant-supported fixed dental prostheses (FDPs) after a mean observation period of at least 5 years. *Clin Oral Implants Res* 2012, 23 Suppl 6, 22-38.
61. Elias, C.N., et al. Mechanical and clinical properties of titanium and titanium-based alloys (Ti G2, Ti G4 cold worked nanostructured and Ti G5) for biomedical applications. *Journal of Materials Research and Technology* 2019, 8, 1060-1069.
62. Osman, R.B. and M.V. Swain. A Critical Review of Dental Implant Materials with an Emphasis on Titanium versus Zirconia. *Materials (Basel)* 2015, 8, 932-958.
63. Yu, S.Y., C.W. Brodrick, M.P. Ryan, and J.R. Scully. Effects of Nb and Zr alloying additions on the activation behavior of Ti in hydrochloric acid. *Journal of the Electrochemical Society* 1999, 146, 4429-4438.
64. Dyer, C.K.a.J.S.L.L. Reversible reactions within anodic oxide films on titanium electrodes. *Electrochimica Acta* 1978, 23, 1387-1394.
65. Blackwood, D.J., L.M. Peter, and D.E. Williams. Stability and open circuit breakdown of the passive oxide film on titanium. *Electrochimica Acta* 1988, 8, 1143-1149.
66. Rahul Bhola, S.M.B., Brajendra Mishra and David L. Olson. Corrosion in Titanium Dental Implants/Prostheses - A Review. *Trends Biomater. Artif. Organs* 2011, 25, 34-46.
67. SXJTO, G.T.B.a.R.M. OBSERVATIONS OF LOCALISED INSTABILITY OF PASSIVE TITANIUM IN CHLORIDE SOLUTION. *Electrochimica Acta* 1995, 40, CL IBBI- 1888.
68. He, X., J.J. Noël, and D.W. Shoesmith. Temperature Dependence of Crevice Corrosion Initiation on Titanium Grade-2. *Journal of The Electrochemical Society* 2002, 149, B440.

69. H. Satoh, K.S.a.F.K. The Crevice Corrosion Resistance of Some Titanium Materials. *Platinum Metals Rev.* 1987, 31, 115-121.
70. Abdulsalam, M.I. Crevice Corrosion of Titanium in High Temperature-Concentrated Chloride Environments. *Journal of Materials Engineering and Performance* 2007, 16, 736-740.
71. Delgado-Ruiz, R. and G. Romanos. Potential Causes of Titanium Particle and Ion Release in Implant Dentistry: A Systematic Review. *Int J Mol Sci* 2018, 19,
72. Senna, P., et al. Surface Damage on Dental Implants with Release of Loose Particles after Insertion into Bone. *Clin Implant Dent Relat Res* 2015, 17, 681-92.
73. Jackson DR, O.S., Roscoe SG. Electrochemical studies of the adsorption behavior of serum proteins on titanium. *Langmuir* 2000, 16, 5449-5457.
74. Oliva, F.Y., et al. Adsorption of human serum albumin (HSA) onto colloidal TiO₂ particles, Part I. *Journal of Colloid and Interface Science* 2003, 261, 299-311.
75. Cheng, X. and S.G. Roscoe. Corrosion behavior of titanium in the presence of calcium phosphate and serum proteins. *Biomaterials* 2005, 26, 7350-6.
76. Karimi, S., T. Nickchi, and A. Alfantazi. Effects of bovine serum albumin on the corrosion behaviour of AISI 316L, Co-28Cr-6Mo, and Ti-6Al-4V alloys in phosphate buffered saline solutions. *Corrosion Science* 2011, 53, 3262-3272.
77. Huang, H.-H. Effect of fluoride and albumin concentration on the corrosion behavior of Ti-6Al-4V alloy. *Biomaterials* 2003, 24, 275-282.
78. Takemoto, S., et al. Corrosion behavior and surface characterization of titanium in solution containing fluoride and albumin. *Biomaterials* 2005, 26, 829-37.
79. Williams, G.C.F.C.a.D.F. The effects of proteins on metallic corrosion. *Journal of Biomedical Materials Research* 1982, 16, 125-134.
80. Omanovic S, R.S. Electrochemical studies of the adsorption behavior of Bovine Serum Albumin on stainless steel. *Langmuir* 1999, 15, 8315-21.
81. Khan MA, W.R., Williams DF. The corrosion behaviour of Ti-6Al-4V, Ti-6Al-7Nb and Ti-13Nb-13Zr in protein solutions. *Biomaterials* 1999, 20, 631-7.
82. Padilla, N. and A. Bronson. Electrochemical characterization of albumin protein on Ti-6Al-4V alloy immersed in a simulated plasma solution. *J Biomed Mater Res A* 2007, 81, 531-43.
83. Berbel, L.O., et al. Determinants of corrosion resistance of Ti-6Al-4V alloy dental implants in an In Vitro model of peri-implant inflammation. *PLoS One* 2019, 14, e0210530.
84. Karimi S, A.A. Ion release and surface oxide composition of AISI 316L, Co-28Cr-6Mo, and Ti-6Al-4V alloys immersed in human serum albumin solutions. *Mater Sci Eng C Mater Biol Appl* 2014, 40, 435-44.
85. Kotaro Doi, S.M.a.S.F. Metal Dissolution and Repassivation of Ti-6Al-4V Alloy during Rapid Elongation in Simulated Body Fluid including Osteoblast-like Cells. *ECS Transactions* 2013, 50, 1-10.
86. Huang, H.H. and T.H. Lee. Electrochemical impedance spectroscopy study of Ti-6Al-4V alloy in artificial saliva with fluoride and/or bovine albumin. *Dental Materials* 2005, 21, 749-755.

87. Okazaki Y, T.T., Ito Y. Corrosion resistance of implant alloys in pseudo physiological solution and role of alloying elements in passive film. *Materials Transactions, JIM* 1997, 38, 78-84.
88. Penarrieta-Juanito, G., et al. Surface damage of dental implant systems and ions release after exposure to fluoride and hydrogen peroxide. *J Periodontal Res* 2019, 54, 46-52.
89. J. PAN, D.T.a.C.L. ELECTROCHEMICAL IMPEDANCE SPECTROSCOPY STUDY OF THE PASSIVE OXIDE FILM ON TITANIUM FOR IMPLANT APPLICATION. *Electrochim Acta* 1996, 41, 1143-1153.
90. J. Pan, D.T., and C. Leygra. Hydrogen peroxide toward enhanced oxide growth on titanium in PBS solution: Blue coloration and clinical relevance. *Journal of Biomedical Materials Research* 1996, 30, 393-402.
91. Sérgio Luiz de Assis, I.C. The Effect of Hydrogen Peroxide on the Electrochemical Behaviour of Ti-13Nb-13Zr Alloy in Hanks' Solution. *Materials Research* 2006, 40, 425-429.
92. Gilbert, J.L., Buckley, C. A., and Lautenschlager, E. P. Titanium Oxide Film Fracture and Repassivation The Effect of Potential, pH and Aeration. *Medical Applications of Titanium and Its Alloys: The Material and Biological Issues*, ASTM STP 1272 1996, S. A. Brown and J. E. Lemons, Eds., American Society for Testing and Materials, 199-215.
93. Gilbert, J.L.a.J., J.J. The Mechanical and Electrochemical Processes Associated with Taper Fretting Crevice Corrosion: A review. *Modularity of Orthopedic Implants*, ASTM STP 1301, Donald E. Marlowe, Jack E. Parr, and Michael B. Mayor, Eds., American Society for Testing and Materials 1997,
94. Rodrigues, D.C., et al. Titanium Corrosion Mechanisms in the Oral Environment: A Retrieval Study. *Materials (Basel)* 2013, 6, 5258-5274.
95. Manda, M.G., et al. Observations on an in-vivo failure of a titanium dental implant/abutment screw system: a case report. *J Biomed Mater Res B Appl Biomater* 2009, 89, 264-73.
96. Winter, W., D. Klein, and M. Karl. Micromotion of Dental Implants: Basic Mechanical Considerations. *J Med Eng* 2013, 2013, 265412.
97. Noronha Oliveira, M., et al. Can degradation products released from dental implants affect peri-implant tissues? *J Periodontal Res* 2018, 53, 1-11.
98. Souza, J.C.M., et al. Wear and Corrosion Interactions on Titanium in Oral Environment: Literature Review. *Journal of Bio- and Tribo-Corrosion* 2015, 1,
99. Maruyama, N., Kawasaki, H., Yamamoto, A., Hiromoto, S., Imai, H., Hanawa, T. Friction-wear properties of nickel-free Co–Cr–Mo alloy in a simulated body fluid. *Materials Transactions* 2005, 46, 1588-1592.
100. Yan, Y., et al. Tribocorrosion in implants—assessing high carbon and low carbon Co–Cr–Mo alloys by in situ electrochemical measurements. *Tribology International* 2006, 39, 1509-1517.
101. Souza, J.C., et al. Do oral biofilms influence the wear and corrosion behavior of titanium? *Biofouling* 2010, 26, 471-8.

102. Guo, X., et al. Effects of sliding amplitude and normal load on the fretting wear behavior of alloy 690 tube exposed to high temperature water. *Tribology International* 2017, 116, 155-163.
103. Royhman, D., et al. Fretting-corrosion in Hip Implant Modular Junctions: New Experimental Set-up and Initial Outcome. *Tribol Int* 2015, 91, 235-245.
104. M. Karthega, S.T.a.N.R. Effect of pH on the Corrosion Behaviour of Ti6Al4V alloy for Dental Implant Application in Fluoride Media. *Trends Biomater. Artif. Organs*, 2006, 20, 31-34.
105. Ain A. Rozali, N.R.N.M., Mardziah C. Murad, Zuraidah Salleh, Koay M. Hyie. The Effect of pH Value on the Corrosion Behaviour of Ti-6Al-4V and 316L SS Alloys under Physiological Environment. *Chemical Engineering Transactions* 2018, 63, 769-774.
106. Gascoyne, T.C., et al. Corrosion on the acetabular liner taper from retrieved modular metal-on-metal total hip replacements. *J Arthroplasty* 2014, 29, 2049-52.
107. Higgs, G.B., et al. Does Taper Size Have an Effect on Taper Damage in Retrieved Metal-on-Polyethylene Total Hip Devices? *J Arthroplasty* 2016, 31, 277-81.
108. Siljander, M.P., et al. Fretting and Corrosion Damage in Retrieved Metal-on-Polyethylene Modular Total Hip Arthroplasty Systems: What Is the Importance of Femoral Head Size? *J Arthroplasty* 2018, 33, 931-938.
109. Panagiotidou, A., et al. Effect of impact assembly on the interface deformation and fretting corrosion of modular hip tapers: An in vitro study. *J Orthop Res* 2017,
110. Pourzal, R., et al. Does Surface Topography Play a Role in Taper Damage in Head-neck Modular Junctions? *Clin Orthop Relat Res* 2016, 474, 2232-42.
111. S. R. Thomas, D.S., P. D. Latham. Corrosion of cemented titanium femoral stems. *J Bone Joint Surg* 2004, 86, 974-8.
112. Cook, S., Barrack, RL, Clemow, A.IT,. Corrosion and Wear at the Modular Interface of Uncemented Femoral Stems. *J Bone and Joint Surgery* 1994, 76-B, 68-72.
113. Mathew, M.T., et al. Tribocorrosion behavior of CoCrMo alloy for hip prosthesis as a function of loads: a comparison between two testing systems. *Wear* 2011, 271, 1210-1219.
114. Revankar, G.D., et al. Wear resistance enhancement of titanium alloy (Ti-6Al-4V) by ball burnishing process. *Journal of Materials Research and Technology* 2017, 6, 13-32.
115. Budinski, K.G. Tribological properties of titanium alloys. *Wear* 1991, 151, 203-217.
116. LIRERATO CIAVATTA, D.P.a.G.R. ON THE HYDROLYSIS OF THE TITANIUM(W) IN CHLORIDE MEDIA. *Polyhedron* 1985, 4, 15-21.
117. Henry, P., J. Takadoum, and P. Berçot. Tribocorrosion of 316L stainless steel and TA6V4 alloy in H₂SO₄ media. *Corrosion Science* 2009, 51, 1308-1314.
118. F. Assi , H.B. Study of wear-corrosion synergy with a new microelectrochemical technique. *Wear* 1999, 233, 505-514.

119. Contu, F., B. Elsener, and H. Böhni. A study of the potentials achieved during mechanical abrasion and the repassivation rate of titanium and Ti6Al4V in inorganic buffer solutions and bovine serum. *Electrochimica Acta* 2004, 50, 33-41.
120. Scully, D.G.a.J.R. On the Repassivation Behavior of High-Purity Titanium and Selected β , α and $\beta + \alpha$ Titanium Alloys in Aqueous Chloride Solutions. *J. Electrochem. Soc.*, 1996, 143, 1847-1860.
121. T. Hanawa, K.A., K. Asaoka. Repassivation of titanium and surface oxide film regenerated in simulated bioliquid. *Journal of Biomedical Materials Research* 1997, 62, 530-538.
122. Yu, F., *CORROSION OF TITANIUM FOR BIOMEDICAL APPLICATIONS* in *School of Metallurgy and Materials*. 2015, University of Birmingham: Birmingham. p. 219.
123. Ghanbarzadeh, A., et al. A New Asperity-Scale Mechanistic Model of Tribocorrosive Wear: Synergistic Effects of Mechanical Wear and Corrosion. *Journal of Tribology* 2018, 141,
124. M.A. Khan, R.L.W., D.F. Williams. Conjoint corrosion and wear in titanium alloys. *Biomaterials* 1999, 20, 765-772.
125. Dimah, M.K., et al. Study of the biotribocorrosion behaviour of titanium biomedical alloys in simulated body fluids by electrochemical techniques. *Wear* 2012, 294-295, 409-418.
126. Hiromoto, S. and S. Mischler. The influence of proteins on the fretting–corrosion behaviour of a Ti6Al4V alloy. *Wear* 2006, 261, 1002-1011.
127. Runa, M.J., M.T. Mathew, and L.A. Rocha. Tribocorrosion response of the Ti6Al4V alloys commonly used in femoral stems. *Tribology International* 2013, 68, 85-93.
128. Yan, Y., A. Neville, and D. Dowson. Biotribocorrosion—an appraisal of the time dependence of wear and corrosion interactions: II. Surface analysis. *Journal of Physics D: Applied Physics* 2006, 39, 3206-3212.
129. Yan, Y., A. Neville, and D. Dowson. Tribo-corrosion properties of cobalt-based medical implant alloys in simulated biological environments. *Wear* 2007, 263, 1105-1111.
130. Yan, Y., et al. Tribofilm formation in biotribocorrosion – does it regulate ion release in metal-on-metal artificial hip joints? *Proceedings of the Institution of Mechanical Engineers, Part J: Journal of Engineering Tribology* 2010, 224, 997-1006.
131. Ryuichiro Kumazawa, F.W., Noriyuki Takashi, Yukihiro Tanimura, Motohiro Uo, Yasunori Totsuka. Effects of Ti ions and particles on neutrophil function and morphology. *Biomaterials* 2002, 23, 3757-3764.
132. Alrabeah, G.O., et al. The effect of metal ions released from different dental implant-abutment couples on osteoblast function and secretion of bone resorbing mediators. *J Dent* 2017, 66, 91-101.
133. Klimecs, V., et al. Bone Loss around Dental Implants 5 Years after Implantation of Biphasic Calcium Phosphate (HAp/betaTCP) Granules. *J Healthc Eng* 2018, 2018, 4804902.

134. Tae-Ju Oh, J.Y., Carl E. Misch, and Hom-Lay Wang. The Causes of Early Implant Bone Loss: Myth or Science? *J Peridontol* 2002, 73, 322-333.
135. Sanz-Sanchez, I., et al. Effects of lateral bone augmentation procedures on peri-implant health or disease: A systematic review and meta-analysis. *Clin Oral Implants Res* 2018, 29 Suppl 15, 18-31.
136. Shi, J.Y., et al. Peri-implant conditions and marginal bone loss around cemented and screw-retained single implant crowns in posterior regions: A retrospective cohort study with up to 4 years follow-up. *PLoS One* 2018, 13, e0191717.
137. Valerio Sansone, D.P., Marco Melato. The effects on bone cells of metal ions released from orthopaedic implants. A review. *Clinical Cases in Mineral and Bone Metabolism* 2013, 10, 34-40.
138. Shemtov-Yona, K. and D. Rittel. Fatigue of Dental Implants: Facts and Fallacies. *Dent J (Basel)* 2016, 4,
139. Timotius Pasang, M.R., Matthew Prygoski, Russell Wanhill, Rohan Byrnes, Osamu Kamiya, Kiyoshi Tanaka. Fatigue of commercially pure titanium dental implants. *Materials Physics and Mechanics* 2016, 27, 79-89.
140. Liens, A., et al. On the Potential of Bulk Metallic Glasses for Dental Implantology: Case Study on Ti₄₀Zr₁₀Cu₃₆Pd₁₄. *Materials (Basel)* 2018, 11,
141. Tantavisut, S., et al. The novel toxic free titanium-based amorphous alloy for biomedical application. *Journal of Materials Research and Technology* 2018, 7, 248-253.
142. Zhu, S., et al. Effect of Minor Sn Additions on the Formation and Properties of TiCuZrPd Bulk Glassy Alloy. *Materials Transactions* 2012, 53, 500-503.
143. S.L. Zhu, X.M.W., and A. Inoue. Glass-forming ability and mechanical properties of Ti-Based bulk alloys with large diameters of up to 1 cm. *Intermetallics* 2008, 16, 1031-1035.
144. Sypien, A., M. Stoica, and T. Czeppe. Properties of the Ti₄₀Zr₁₀Cu₃₆Pd₁₄ BMG Modified by Sn and Nb Additions. *Journal of Materials Engineering and Performance* 2016, 25, 800-808.
145. Oak, J.-J., et al. Characterization of Surface Properties, Osteoblast Cell Culture in Vitro and Processing with Flow-Viscosity of Ni-Free Ti-Based Bulk Metallic Glass for Biomaterials. *Journal of Biomechanical Science and Engineering* 2009, 4, 384-391.
146. Kokubun, R., et al. In vivo evaluation of a Ti-based bulk metallic glass alloy bar. *Biomed Mater Eng* 2015, 26, 9-17.
147. Qin, F., et al. Corrosion Behavior of a Ti-Based Bulk Metallic Glass and Its Crystalline Alloys. *Materials Transactions* 2007, 48, 1855-1858.
148. M. Naka, K.H.a.T.M. Corrosion behavior of amorphous and crystalline Cu₅₀Ti₅₀ and Cu₅₀Zr₅₀ alloys. *Journal of Non-Crystalline Solids* 1978, 30, 29-36.
149. Gostin, P.F., et al. In Situ Synchrotron X-Ray Diffraction Characterization of Corrosion Products of a Ti-Based Metallic Glass for Implant Applications. *Adv Healthc Mater* 2018, 7, e1800338.

150. Akihisa Inoue, Y.S., Yoshihiko Yokoyama and Tsuyoshi Masumoto. Solidification Analyses of Bulky Zr₆₀Al₁₀Ni₁₀Cu₁₅Pd₅ Glass Produced by Casting into Wedge-Shape Copper Mold. *Materials Transactions, JIM* 1995, 36, 1276-1281.
151. Rong, C. and B. Shen. Nanocrystalline and nanocomposite permanent magnets by melt spinning technique. *Chinese Physics B* 2018, 27,
152. Raghvendra Mohan Srivastava, J.u.E., Wolfgang Loser, Brij Kumar Dhindaw and Ludwig Schultz. Cooling Rate Evaluation for Bulk Amorphous Alloys from Eutectic Microstructures in Casting Processes. *Materials Transactions* 2002, 43, 1670-1675.
153. Illeková, E., M. Jergel, P. Duhaj, and A. Inoue. The relation between the bulk and ribbon Zr₅₅Ni₂₅Al₂₀ metallic glasses. *Mater. Sci. Eng. A* 1997, 226–228, 388–392.
154. H. HABAZAKI, Y.-P.L., A. KAWASHIMA, K. ASAMI and K. HASHIMOTO. THE EFFECTS OF STRUCTURAL RELAXATION AND CRYSTALLIZATION ON THE CORROSION BEHAVIOR OF ELECTRODEPOSITED AMORPHOUS Ni-P ALLOYS. *Corrosion Science* 1991, 32, 1227-1235.
155. Jayaraj, J., A. Gebert, and L. Schultz. Passivation behaviour of structurally relaxed Zr₄₈Cu₃₆Ag₈Al₈ metallic glass. *Journal of Alloys and Compounds* 2009, 479, 257-261.
156. Long, Z., et al. Corrosion Behaviour of [(Fe_{0.6}Co_{0.4})_{0.75}B_{0.2}Si_{0.05}]₉₆Nb₄ Bulk Glassy Alloy in Sulphuric Acid Solutions. *Materials Transactions* 2006, 47, 2566-2570.
157. Wang, Y., et al. In vitro corrosion behaviors of Mg₆₇Zn₂₈Ca₅ alloy: From amorphous to crystalline. *Materials Chemistry and Physics* 2012, 134, 1079-1087.
158. Zhang, L.M., et al. Thermally induced structure evolution on the corrosion behavior of Al-Ni-Y amorphous alloys. *Corrosion Science* 2018, 144, 172-183.
159. Jiang, W.H., et al. Electrochemical corrosion behavior of a Zr-based bulk-metallic glass. *Applied Physics Letters* 2007, 91,
160. Suryanarayana, C., Inoue, A. *Bulk Metallic Glasses*. Boca Raton: CRC Press 2011,
161. Li, C.S., Junji; Matsushida, Mitsuhide; Inoue, Akihisa;. Effect of Sn addition on the glass-forming ability in (Cu₄₀Ti₃₀Ni₁₅Zr₁₀)(100-x)/95Sn_x (x = 0, 2, 4, 6 and 8) alloys. *MATERIALS SCIENCE* 2000, 42, 923-927.
162. Xu, Z., et al. Antimicrobial effect of gallium nitrate against bacteria encountered in burn wound infections. *RSC Advances* 2017, 7, 52266-52273.
163. Verron, E., J.M. Bouler, and J.C. Scimeca. Gallium as a potential candidate for treatment of osteoporosis. *Drug Discov Today* 2012, 17, 1127-32.
164. Zhu, S., et al. Glass-Forming Ability and Thermal Stability of Ti–Zr–Cu–Pd–Si Bulk Glassy Alloys for Biomedical Applications. *Materials Transactions* 2007, 48, 163-166.
165. Zhang, Y., et al. Effect of Zr Addition on the Corrosion of Ti in Acidic and Reactive Oxygen Species (ROS)-Containing Environments. *ACS Biomaterials Science & Engineering* 2018, 4, 1103-1111.

166. A. Mamun, R.S., M.A. Hossain, J.R. Parga, D.L. Cocke, M.Y.A. Mollah. Passive film breakdown during anodic oxidation of zirconium in pH8 buffer containing chloride and sulfate. *Electrochimica Acta* 2001, 46, 3343-3350.
167. Masashi Azuma, Y.N.a.H.T. Oxygen and chlorine evolution on niobium-, zirconium- and other metal-nitride amorphous thin film electrodes prepared by the reactive RF sputtering technique. *J. Electroanal. Chem* 1988, 255, 179-198.
168. Akimoto, T., et al. Evaluation of corrosion resistance of implant-use Ti-Zr binary alloys with a range of compositions. *J Biomed Mater Res B Appl Biomater* 2018, 106, 73-79.
169. M.M. Al-Abdallah, A.K.M., M.A. Al-Qudah and N.A.F. Al-Rawashdeh. Corrosion Behavior of Copper in Chloride Media. *The Open Corrosion Journal* 2009, 2, 71-76.
170. Ochoa, M., M.A. Rodríguez, and S.B. Farina. Corrosion of High Purity Copper in Solutions Containing NaCl, Na₂SO₄ and NaHCO₃ at Different Temperatures. *Procedia Materials Science* 2015, 9, 460-468.
171. Kear, G., B.D. Barker, and F.C. Walsh. Electrochemical corrosion of unalloyed copper in chloride media—a critical review. *Corrosion Science* 2004, 46, 109-135.
172. Arjmand, F. and A. Adriaens. Influence of pH and Chloride Concentration on the Corrosion Behavior of Unalloyed Copper in NaCl Solution: A Comparative Study Between the Micro and Macro Scales. *Materials* 2012, 5, 2439-2464.
173. Qin, C.L., et al. A novel Cu-based BMG composite with high corrosion resistance and excellent mechanical properties. *Acta Materialia* 2006, 54, 3713-3719.
174. Pham, A.N., et al. Fenton-like copper redox chemistry revisited: Hydrogen peroxide and superoxide mediation of copper-catalyzed oxidant production. *Journal of Catalysis* 2013, 301, 54-64.
175. Lucas, J.D.B.a.L.C. Toxicity of copper-based dental alloys in cell culture. *Biomed Research* 1989, 23, 1103-14.
176. Song, Y.H., et al. Cytotoxicity of alloying elements and experimental titanium alloys by WST-1 and agar overlay tests. *Dent Mater* 2014, 30, 977-83.
177. Göran Sjögren, G.S., and Jon E.Dahl. Cytotoxicity of dental alloys, metals, and ceramics assessed by Millipore filter, agar overlay, and MTT tests. *The Journal of Prosthetic Dentistry* 2000, 84, 229-236.
178. Pinto, E.M., D.M. Soares, and C.M.A. Brett. Interaction of BSA protein with copper evaluated by electrochemical impedance spectroscopy and quartz crystal microbalance. *Electrochimica Acta* 2008, 53, 7460-7466.
179. Torres Bautista, B.E., et al. Effect of protein adsorption on the corrosion behavior of 70Cu-30Ni alloy in artificial seawater. *Bioelectrochemistry* 2014, 97, 34-42.
180. Hamadi, L., et al. The use of amino acids as corrosion inhibitors for metals: A review. *Egyptian Journal of Petroleum* 2018, 27, 1157-1165.
181. El Ibrahim, B., et al. Amino acids and their derivatives as corrosion inhibitors for metals and alloys. *Arabian Journal of Chemistry* 2017,
182. Matos, J.B., et al. Effect of cysteine on the anodic dissolution of copper in sulfuric acid medium. *Journal of Electroanalytical Chemistry* 2004, 570, 91-94.

183. Ismail, K.M. Evaluation of cysteine as environmentally friendly corrosion inhibitor for copper in neutral and acidic chloride solutions. *Electrochimica Acta* 2007, 52, 7811-7819.
184. Zhang, D.-Q., et al. Inhibition effect of some amino acids on copper corrosion in HCl solution. *Materials Chemistry and Physics* 2008, 112, 353-358.
185. Zhang, D.-Q., et al. Inhibition of copper corrosion in acidic chloride solution by methionine combined with cetrimonium bromide/cetylpyridinium bromide. *Journal of Applied Electrochemistry* 2011, 41, 491-498.
186. Petrovic, M.B., Simonovic, A.T., Milic, S.M. The effect of cysteine on the behaviour of copper in neutral and alkaline sulphate solutions. *Int. J. Electrochem. Sci* 2012, 7, 9043–9057.
187. Masaharu NAKAGAWA, S.M., Koich UDOH. Corrosion Behavior of Pure Titanium and Titanium Alloys in Fluoride-containing Solutions. *Dental Materials Journal* 2001, 20, 305-314.
188. F. Hua, K. Mon, P. Pasupathi, G. Gordon, and D. Shoesmith. A Review of Corrosion of Titanium Grade 7 and Other Titanium Alloys in Nuclear Waste Repository Environments. *Corrosion Science* 2005, 61, 987-1007.
189. Nakagawa, M., et al. The effect of Pt and Pd alloying additions on the corrosion behavior of titanium in fluoride-containing environments. *Biomaterials* 2005, 26, 2239-46.
190. Handzlik, P. and K. Fitzner. Corrosion resistance of Ti and Ti–Pd alloy in phosphate buffered saline solutions with and without H₂O₂ addition. *Transactions of Nonferrous Metals Society of China* 2013, 23, 866-875.
191. Noriko HORASAWA, H.N., Shigeo TAKAHASHI and Toru OKABE. Behavior of pure gallium in water and various saline solutions. *Dental Materials Journal* 1997, 16 200-208.
192. Holliday, M.A. Extracellular fluid and its proteins: dehydration, shock, and recovery. *Pediatr Nephrol* 1999, 13, 989-995.
193. Call, D. The Role of Albumin and Fluids in the Body. *Veterinary Practice Issues* 2005, 26,
194. Pentti TengvaJII, n.L., w s Sjaqvista nd Hans Eilwing. Titanium-hydrogen peroxide interaction: model studies of the influence of the inflammatory response on titanium implants. *Biomaterials* 1989, 10, 33.
195. WIGFIELD, B.S.A.Y. Evidence for albumin - Cu(I1) - amino acid ternary complex. *CANADIAN JOURNAL OF BIOCHEMISTRY* 1968, 46, 601-607.
196. M. Valko, H.M., and M. Mazur. High-Affinity Binding Site for Copper(II) in Human and Dog Serum Albumins (an EPR Study). *J. Phys. Chem. B* 1999, 103, 5591-5597.
197. Wang, T., et al. Novel Ti-based bulk metallic glasses with superior plastic yielding strength and corrosion resistance. *Materials Science and Engineering: A* 2015, 642, 297-303.
198. Lausmaa J, K.B., Mattsson H. Surface spectroscopic characterization of titanium implant materials. *Applied Surface Science* 1990, 44, 133-46.

199. Kaesche, H., *Corrosion of Metals: Physicochemical Principles and Current Problems*, in *Titanium and Titanium alloys*, H. Kaesche, Editor. 2003, Springer: New York. p. 496.
200. Kusakawa, Y., E. Yoshida, and T. Hayakawa. Protein Adsorption to Titanium and Zirconia Using a Quartz Crystal Microbalance Method. *Biomed Res Int* 2017, 2017, 1521593.
201. F. Contu, B.E., H. Bo`hni. Characterization of implant materials in fetal bovine serum and sodium sulfate by electrochemical impedance spectroscopy. I. Mechanically polished samples. *J Biomed Mater Res.* 2002, 62, 412-421.
202. Zhang, Y., et al. In-Situ Synchrotron X-ray Characterization of Corrosion Products in Zr Artificial Pits in Simulated Physiological Solutions. *Journal of The Electrochemical Society* 2017, 164, C1003-C1012.
203. Tengvall P, B.L., Liedberg B, Elwing H, Lundstrom I. Degradation of Dried Ti-Peroxy Gels Made from Metallic Titanium and Hydrogen Peroxide. *J Colloid Interface Sci* 1990, 139, 575-80.
204. J. Pan, D.T.a.C.L. Electrochemical impedance spectroscopy study of the passive oxide film on titanium for implant application. *Electrochimica acta* 1996, 41, 1143-1153.
205. Sérgio Luiz de Assis, I.C. The effect of hydrogen peroxide on the electrochemical behaviour of Ti-13Nb-13Zr alloy in Hanks' solution. *Materials Research* 2006, 9, 425-429.
206. Zhu, J. Influence of Serum Albumin on Copper Corrosion in Simulated Uterine Fluids. *Journal of Chinese Society for Corrosion and protection* 2000, 20, 81-87.
207. Burstein, P.C.P.a.G.T. Metastable pitting corrosion of stainless steel and the transition to stability. *Royal Society* 1997, 341, 532-557.
208. Liens, A., et al. On the Potential of Bulk Metallic Glasses for Dental Implantology: Case Study on Ti40Zr10Cu36Pd14. *Materials* 2018, 11,
209. S. Shruti, A.J.S., G. Malavasi, G. Lusvardi, L. Menabue, C. Ferrara, P. Mustarelli, and M. V. Regì. Structural and in vitro study of cerium, gallium and zinc containing sol-gel bioactive glasses. *Journal of Materials Chemistry* 2012, 22, 13698-13706.
210. R. M. Srivastava, J.E.W.L., B. K. Dhindaw. and L. Schultz. Cooling Rate Evaluation for Bulk Amorphous Alloys from Eutectic. *Materials Transactions* 2002, 43, 1670-1675.
211. Szewieczek, D. and A. Baron. Electrochemical corrosion and its influence on magnetic properties of Fe_{75.5}Si_{13.5}B₉Nb₃Cu₁ alloy. *Journal of Materials Processing Technology* 2005, 164-165, 940-946.
212. Karl M, T.T. Effect of Cyclic Loading on Micromotion at the Implant-Abutment Interface. *Int J Oral Maxillofac Implants* 2016, 31, 1292-1297.
213. David G. Gratton, B.A.A., and Clark M. Stanford. Micromotion and dynamic fatigue properties of the dental implant-abutment interface. *The Journal of Prosthetic Dentistry* 2001, 85, 47-52.

214. Yao, K.T., et al. Mechanical performance of conical implant-abutment connections under different cyclic loading conditions. *J Mech Behav Biomed Mater* 2019, 90, 426-432.
215. B. Stojanović, C.B., C. Stotter, T. Klestil, S. Nehrer, F. Franek, M. R. Ripoll. Tribocorrosion of a CoCrMo alloy sliding against articular cartilage and the impact of metal ion release on chondrocytes. *Acta Biomaterialia* 2019, 94, 597-609.
216. Sikora, C.L., et al. Wear and Corrosion Interactions at the Titanium/Zirconia Interface: Dental Implant Application. *J Prosthodont* 2018, 27, 842-852.
217. Gilbert, J.L. Corrosion in the Human Body: Metallic Implants in the Complex Body Environment. *Corrosion* 2017, 73, 1478-1495.
218. Christopher A. Schuh, T.C.H., Upadrasta Ramamurty. Mechanical behavior of amorphous alloys. *Acta Materialia* 2007, 55, 4067-4109.
219. Huang, C.H., et al. Electrochemical and biocompatibility response of newly developed TiZr-based metallic glasses. *Mater Sci Eng C Mater Biol Appl* 2014, 43, 343-9.
220. Ghahari, M., et al. Synchrotron X-ray radiography studies of pitting corrosion of stainless steel: Extraction of pit propagation parameters. *Corrosion Science* 2015, 100, 23-35.
221. Yan, Y., et al. Effect of tribology processes on adsorption of albumin. *Surface Topography: Metrology and Properties* 2015, 4,
222. Wang, Z., et al. Effect of proteins on the surface microstructure evolution of a CoCrMo alloy in bio-tribocorrosion processes. *Colloids Surf B Biointerfaces* 2016, 145, 176-184.
223. Oak, J.-J., D.V. Louzguine-Luzgin, and A. Inoue. Investigation of glass-forming ability, deformation and corrosion behavior of Ni-free Ti-based BMG alloys designed for application as dental implants. *Materials Science and Engineering: C* 2009, 29, 322-327.
224. Pang, S., et al. New Ti-based Ti–Cu–Zr–Fe–Sn–Si–Ag bulk metallic glass for biomedical applications. *Journal of Alloys and Compounds* 2015, 625, 323-327.
225. de Moraes, L.S., et al. Systemic levels of metallic ions released from orthodontic mini-implants. *Am J Orthod Dentofacial Orthop* 2009, 135, 522-9.
226. Nautiyal, V.P., et al. Tissue response to titanium implant using scanning electron microscope. *Natl J Maxillofac Surg* 2013, 4, 7-12.
227. Latanision, R.M., J. C. Turn, J. and Compeau, C. R., *The corrosion resistance of metallic glasses*. ICM3, vol. 2 of International Series on the Strength and Fracture of Materials and Structures, ed. K.J.S. Miller, R. F. Vol. 2. 1979: Pergamon Press.
228. Hélder A Santos, E.M., AnuAiraksinen, LuisMBimbo and Jouni Hirvonen. Porous silicon nanoparticles for nanomedicine: preparation and biomedical applications. *Nanomedicine* 2014, 9, 535–554.
229. Alrabeah, G.O., J.C. Knowles, and H. Petridis. The effect of platform switching on the levels of metal ion release from different implant-abutment couples. *Int J Oral Sci* 2016, 8, 117-25.

230. Ogle, K. Atomic Emission Spectroelectrochemistry: A new look at the corrosion, dissolution & passivation of complex materials. *Corrosion and Materials* 2012, 37, 60-67.
231. Winterbourn, C.C., et al. Modeling the reactions of superoxide and myeloperoxidase in the neutrophil phagosome: implications for microbial killing. *J Biol Chem* 2006, 281, 39860-9.

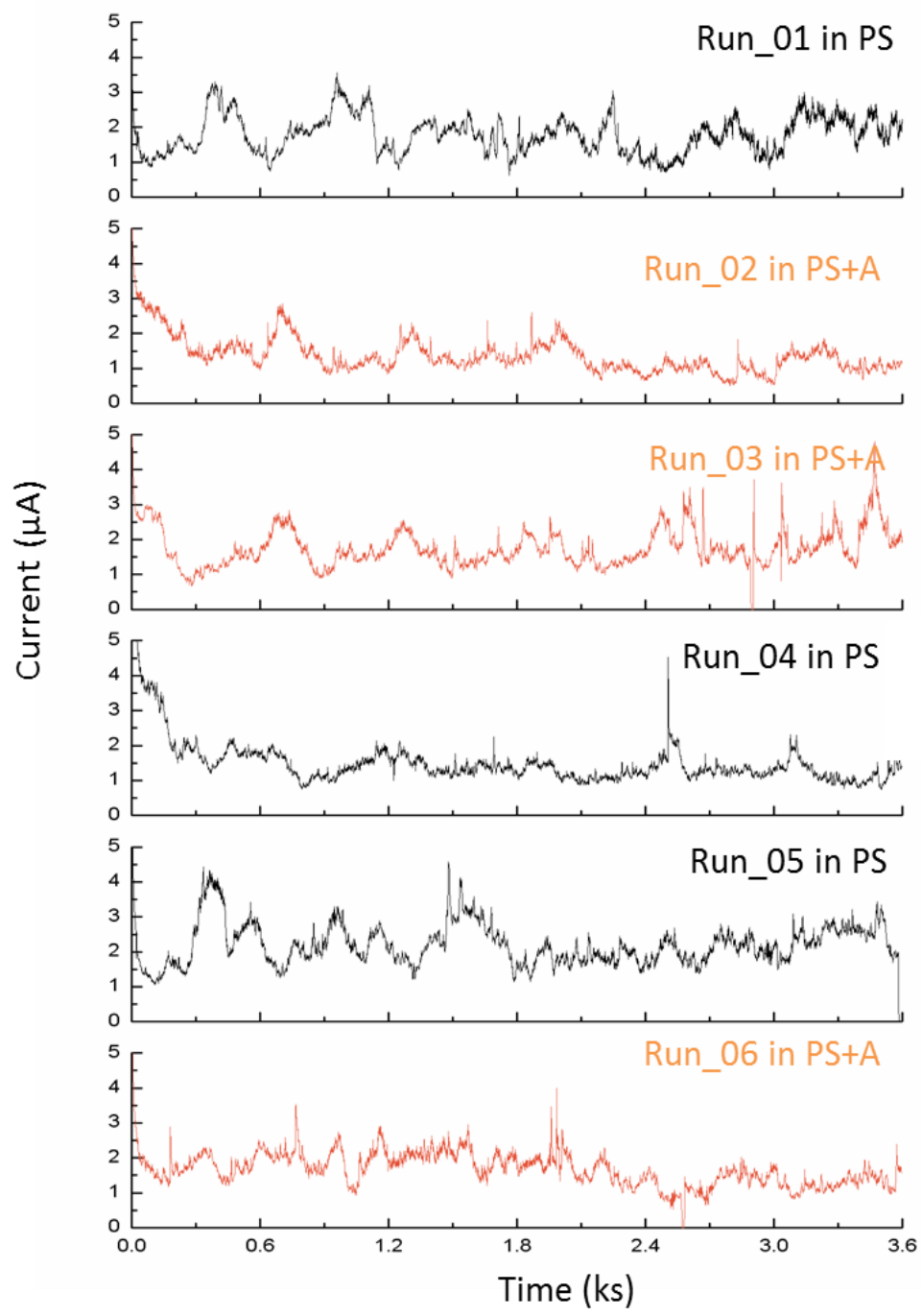
9 Appendix

Part A: Script for calculating the charge in section 6.5:

```
>> [~,sheets] = xlsinfo('C:\Users\qxw487\Desktop\charge.xlsx');
>> for i = 1:length(sheets)
% input time
x{i} = xlsread('C:\Users\qxw487\Desktop\charge.xlsx',sheets{i},'A1:A16000')
% input potentiostatic current
y{i} = xlsread('C:\Users\qxw487\Desktop\albumin.xlsx',sheets{i},'B1:B16000')
% z is integration of x and y
z{i}=trapz(x{i},y{i});
end
```

Part B: Script for calculating the charge in section 6.12:

```
>> [~,sheets] = xlsinfo('C:\Users\qxw487\Desktop\albumin.xlsx');
>> for i = 1:length(sheets)
% input time from 100s to 3600s
x{i} = xlsread('C:\Users\qxw487\Desktop\albumin.xlsx',sheets{i},'A101:A3601')
% input data of fretting current from 100s to 3600s
y{i} = xlsread('C:\Users\qxw487\Desktop\albumin.xlsx',sheets{i},'B101:B3601')
% z is integration of fretting currents
z{i}=trapz(x{i},y{i});
end
```



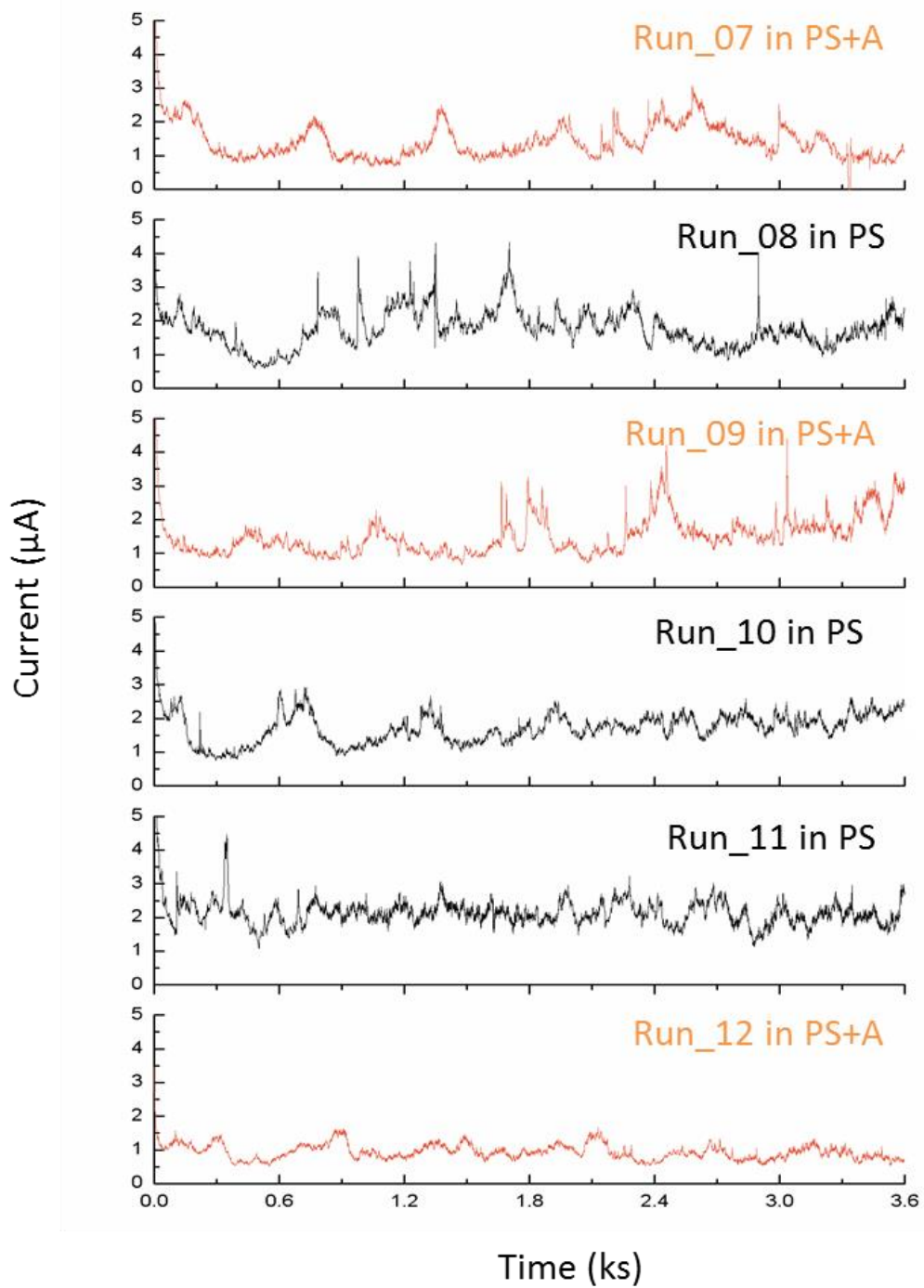
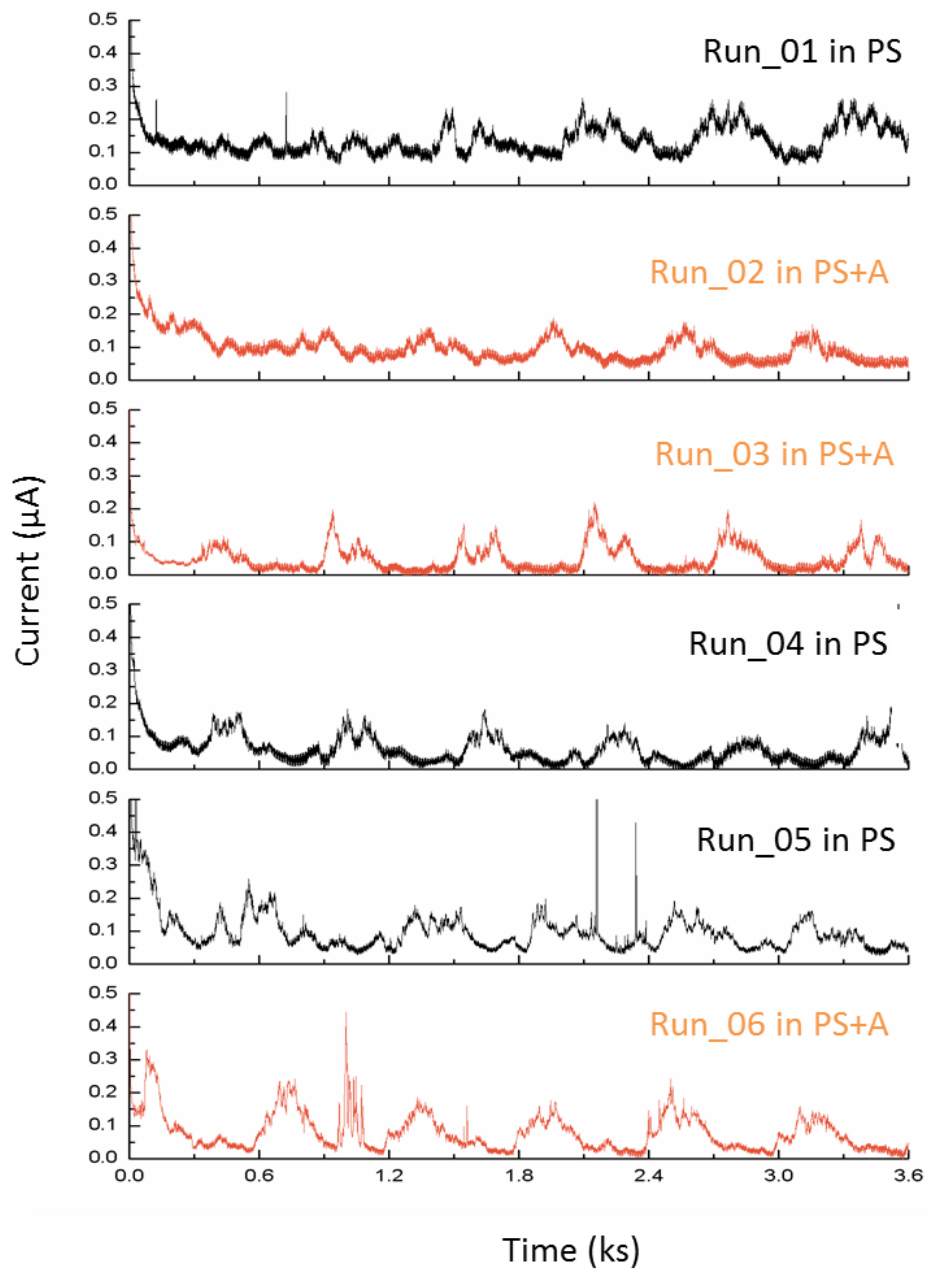


Figure 9-1 Potentiostatic measurements of Ti6Al4V in PS and PS+A, following the sequence of PS – PS+A – PS+A –PS -- PS – PS+A – PS+A –PS – PS+A – PS – PS – PS+A. Load: 634 g. Rotation speed: 0.1 rpm.



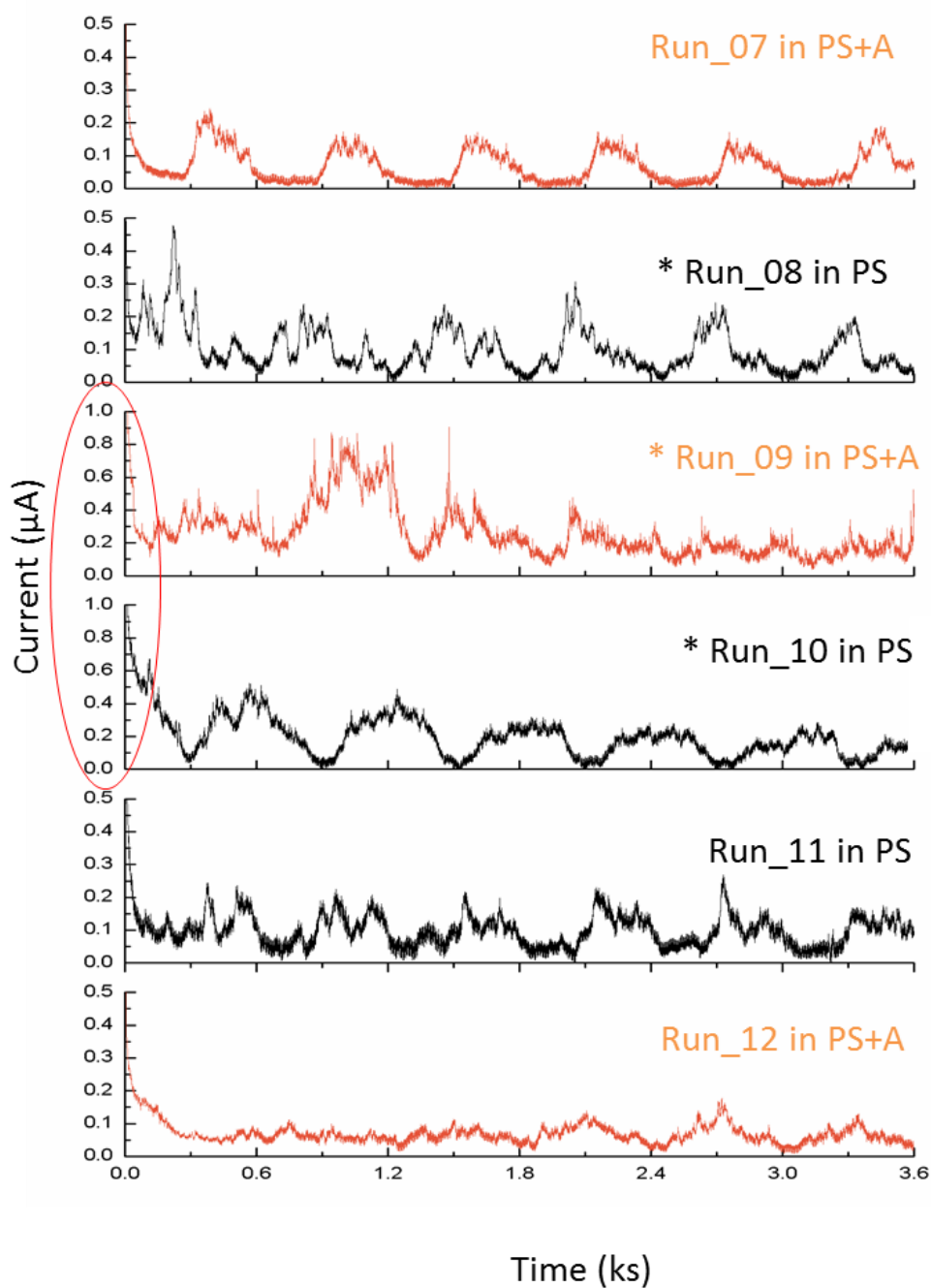
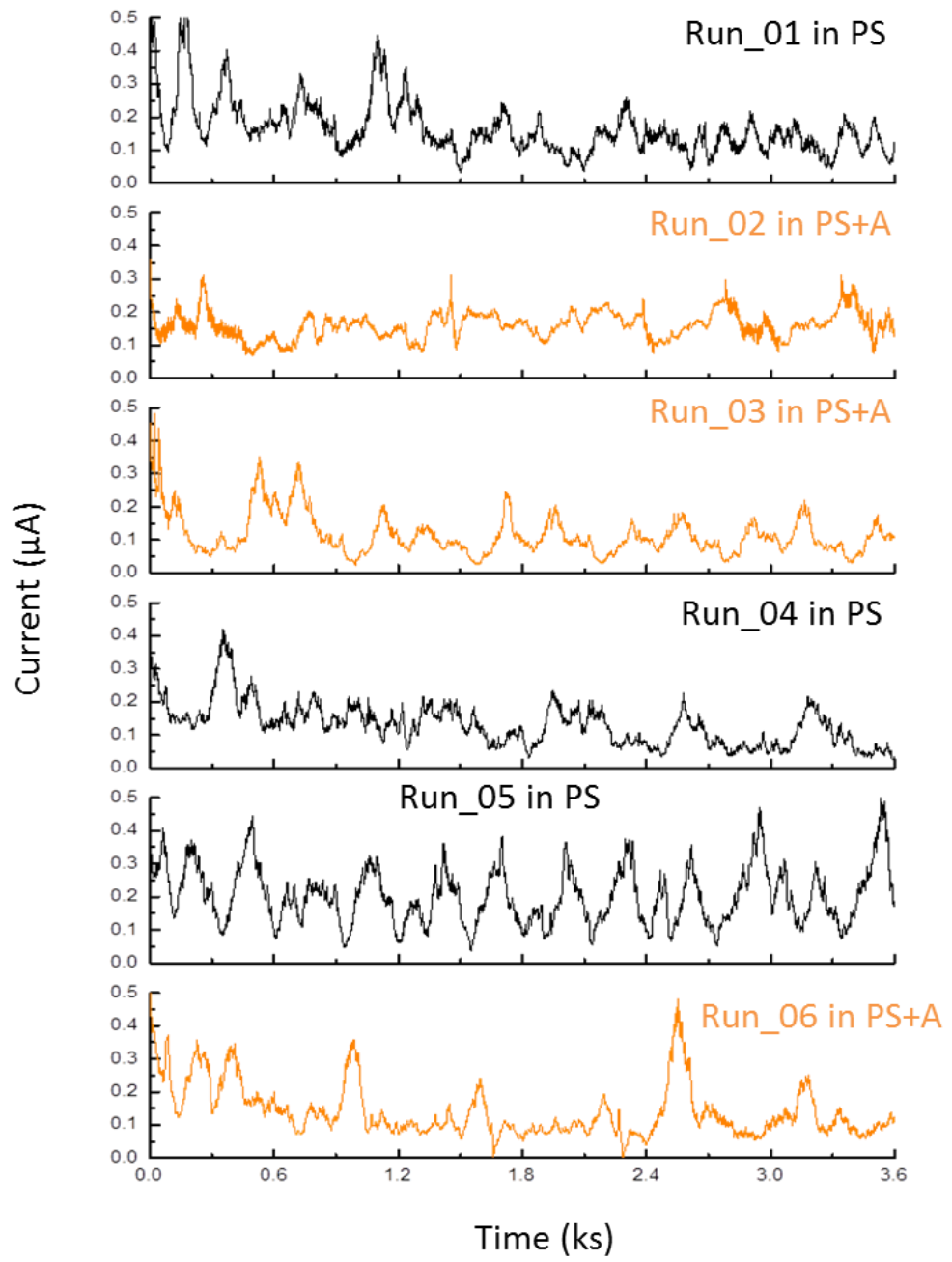


Figure 9-2 Potentiostatic measurements of BMG_Sn2 in PS and PS+A, following the sequence of PS – PS+A – PS+A –PS – PS – PS+A – PS+A –PS – PS+A – PS – PS – PS+A. Load: 634 g. Rotation speed: 0.1 rpm. Potential: 200 mV vs Ag/AgCl. Red circle indicates the larger scale of Y axis.



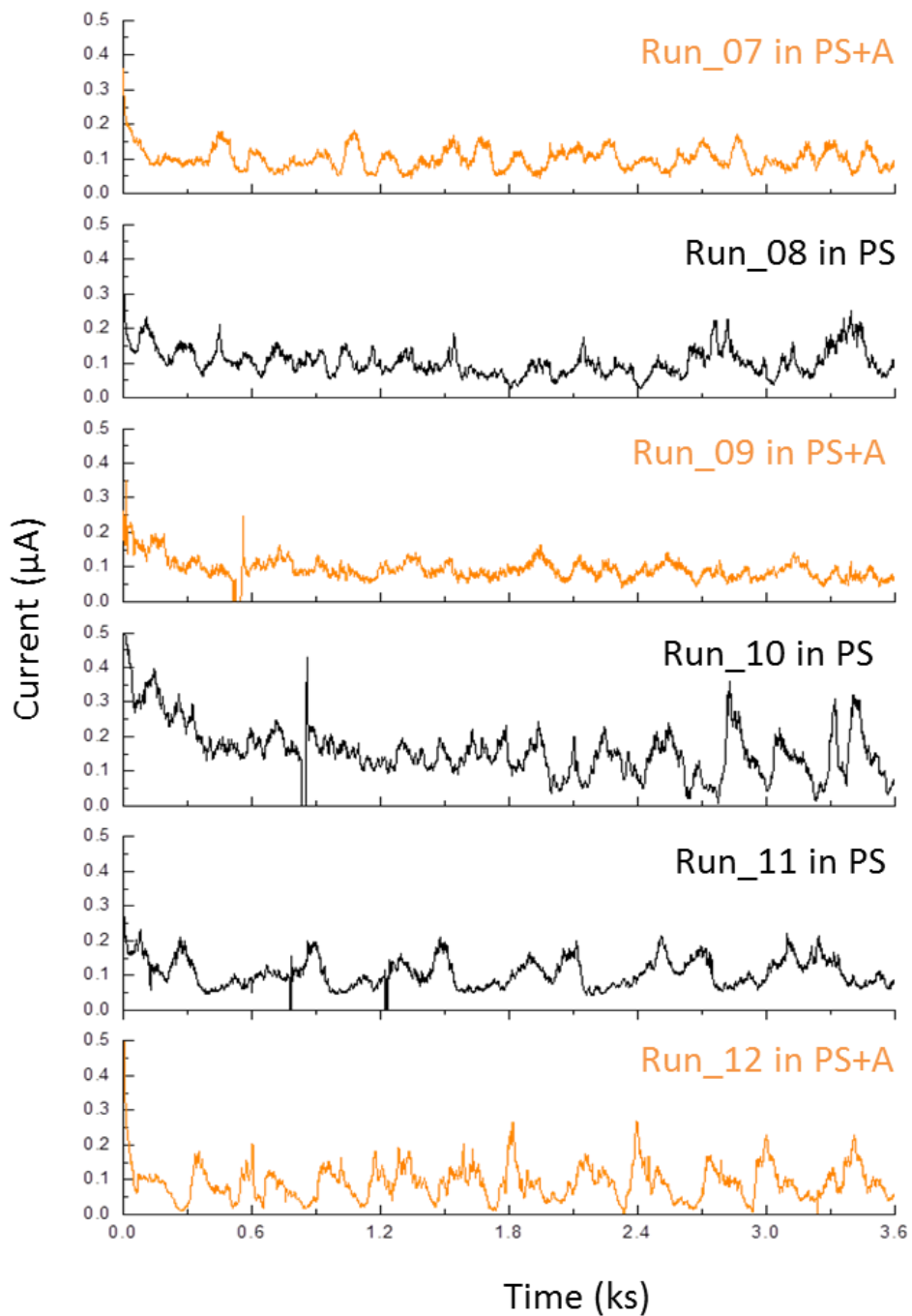


Figure 9-3 Potentiostatic measurements of BMG_Sn2Si in PS and PS+A, following the sequence of PS – PS+A – PS+A –PS -- PS – PS+A – PS+A –PS – PS+A – PS – PS – PS+A. Load: 634 g. Rotation speed: 0.1 rpm. Potential held was at 200 mV vs Ag/AgCl.